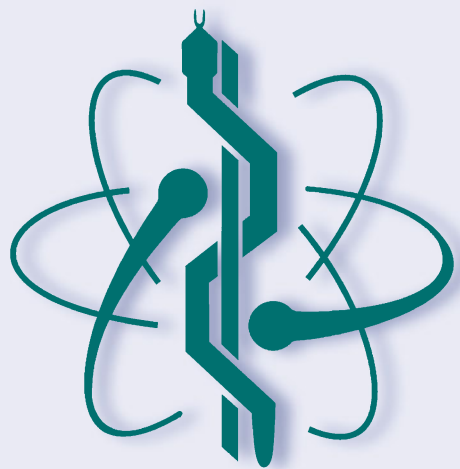


IFMBE Proceedings 97

José de Jesús Agustín Flores-Cuautle · Balam Benítez-Mata ·
Ricardo Antonio Salido-Ruiz ·
Gustavo-Adolfo Alonso-Silverio ·
Guadalupe Dorantes-Méndez ·
Esmeralda Zuñiga-Aguilar · Hugo A. Vélez-Pérez ·
Edgar Del Hierro-Gutierrez ·
Aldo Rodrigo Mejía-Rodríguez *Editors*

XLVI Mexican Conference on Biomedical Engineering

Proceedings of CNIB 2023, November 2–4,
2023, Villahermosa Tabasco, México -
Volume 2: Biomechanics, Rehabilitation
and Clinical Engineering



 Springer

Series Editor

Ratko Magjarević, *Faculty of Electrical Engineering and Computing, ZESOI, University of Zagreb, Zagreb, Croatia*

Associate Editors

Piotr Ładyżyński, *Warsaw, Poland*

Fatimah Ibrahim, *Department of Biomedical Engineering, Faculty of Engineering, Universiti Malaya, Kuala Lumpur, Malaysia*

Igor Lackovic, *Faculty of Electrical Engineering and Computing, University of Zagreb, Zagreb, Croatia*

Emilio Sacristan Rock, *Mexico DF, Mexico*

The IFMBE Proceedings Book Series is an official publication of *the International Federation for Medical and Biological Engineering* (IFMBE). The series gathers the proceedings of various international conferences, which are either organized or endorsed by the Federation. Books published in this series report on cutting-edge findings and provide an informative survey on the most challenging topics and advances in the fields of medicine, biology, clinical engineering, and biophysics.

The series aims at disseminating high quality scientific information, encouraging both basic and applied research, and promoting world-wide collaboration between researchers and practitioners in the field of Medical and Biological Engineering.

Topics include, but are not limited to:

- Diagnostic Imaging, Image Processing, Biomedical Signal Processing
- Modeling and Simulation, Biomechanics
- Biomaterials, Cellular and Tissue Engineering
- Information and Communication in Medicine, Telemedicine and e-Health
- Instrumentation and Clinical Engineering
- Surgery, Minimal Invasive Interventions, Endoscopy and Image Guided Therapy
- Audiology, Ophthalmology, Emergency and Dental Medicine Applications
- Radiology, Radiation Oncology and Biological Effects of Radiation
- Drug Delivery and Pharmaceutical Engineering
- Neuroengineering, and Artificial Intelligence in Healthcare

IFMBE proceedings are indexed by SCOPUS, EI Compendex, Japanese Science and Technology Agency (JST), SCImago. They are also submitted for consideration by WoS.


Proposals can be submitted by contacting the Springer responsible editor shown on the series webpage (see “Contacts”), or by getting in touch with the series editor Ratko Magjarevic.


José de Jesús Agustín Flores Cuautle ·
Balam Benítez-Mata ·
Ricardo Antonio Salido-Ruiz ·
Gustavo Adolfo Alonso-Silverio ·
Guadalupe Dorantes-Méndez ·
Esmeralda Zúñiga-Aguilar ·
Hugo A. Vélez-Pérez ·
Edgar Del Hierro-Gutiérrez ·
Aldo Rodrigo Mejía-Rodríguez
Editors


XLVI Mexican Conference on Biomedical Engineering


Proceedings of CNIB 2023, November 2–4, 2023,
Villahermosa Tabasco, México - Volume 2:
Biomechanics, Rehabilitation and Clinical
Engineering


Editors

José de Jesús Agustín Flores Cuautle 
División de Estudios de Posgrado e
Investigación
Instituto Tecnológico de Orizaba
Orizaba, Mexico


Ricardo Antonio Salido-Ruiz 
Departamento de Bioingeniería Traslacional
Universidad de Guadalajara
Guadalajara, Jalisco, Mexico


Guadalupe Dorantes-Méndez 
Facultad de Ciencias
Universidad Autónoma de San Luis Potosí
San Luis Potosí, Mexico

Hugo A. Vélez-Pérez 
Departamento de Bioingeniería Traslacional
Universidad de Guadalajara
Guadalajara, Mexico

Aldo Rodrigo Mejía-Rodríguez 
Facultad de Ciencias
Universidad Autónoma de San Luis Potosí
San Luis Potosí, Mexico

Balam Benítez-Mata 
Department of Biomedical Engineering
University of California, Irvine
Irvine, CA, USA

Gustavo Adolfo Alonso-Silverio 
Facultad de Ingeniería
Universidad Autónoma de Guerrero
Chilpancingo de los Bravo, Guerrero, Mexico

Esmeralda Zúñiga-Aguilar 
Departamento de Ingeniería Eléctrica y
Computación
Universidad Autónoma de Ciudad Juárez
Ciudad Juárez, Chihuahua, Mexico

Edgar Del Hierro-Gutiérrez
Facultad de Medicina
Universidad Autónoma del Estado de México
Toluca de Lerdo, Mexico

ISSN 1680-0737

ISSN 1433-9277 (electronic)

IFMBE Proceedings

ISBN 978-3-031-46935-0

ISBN 978-3-031-46936-7 (eBook)

<https://doi.org/10.1007/978-3-031-46936-7>

© The Editor(s) (if applicable) and The Author(s), under exclusive license
to Springer Nature Switzerland AG 2024

This work is subject to copyright. All rights are solely and exclusively licensed by the Publisher, whether the whole or part of the material is concerned, specifically the rights of translation, reprinting, reuse of illustrations, recitation, broadcasting, reproduction on microfilms or in any other physical way, and transmission or information storage and retrieval, electronic adaptation, computer software, or by similar or dissimilar methodology now known or hereafter developed.

The use of general descriptive names, registered names, trademarks, service marks, etc. in this publication does not imply, even in the absence of a specific statement, that such names are exempt from the relevant protective laws and regulations and therefore free for general use.

The publisher, the authors, and the editors are safe to assume that the advice and information in this book are believed to be true and accurate at the date of publication. Neither the publisher nor the authors or the editors give a warranty, expressed or implied, with respect to the material contained herein or for any errors or omissions that may have been made. The publisher remains neutral with regard to jurisdictional claims in published maps and institutional affiliations.

This Springer imprint is published by the registered company Springer Nature Switzerland AG
The registered company address is: Gewerbestrasse 11, 6330 Cham, Switzerland

Paper in this product is recyclable.

Preface

The XLVI Mexican Conference on Biomedical Engineering (CNIB 2023), organized by the Mexican Society of Biomedical Engineering (SOMIB), took place at Villahermosa Tabasco, Mexico, on November 2–4. The CNIB 2023 aims to close the gap among academia, industry, and clinics by sharing the latest advances in biomedical engineering and related fields. The conference joins researchers, academics, students, health professionals, and industrials in an enriching environment to discuss and foster the advancements in biomedical engineering.

This book shows various biomaterials developed for biomedical applications. The knowledge related to biomechanics and rehabilitation deserves a special mention. Additionally, some clinical practices are shown, and several applications are developed to assist in this practice.

In this book, the scientific committee presents high-quality papers resulting from a peer review. More than 120 referees performed the screening process under the guidance of the scientific committee. As a result of the strict review process, 28 papers conform to this volume set, representing 40% of the total number of submissions.

All plenary and scientific presenters and distinguished guests from academia, government, health care, industry, and society made this conference one of the leading events in the field. We want to express our gratitude to the scientific committee and the organizing committee for their essential labor, diligence, and optimism leading up to the conference. We would also like to express our gratitude to the session chairpersons, authors, and reviewers for their involvement and essential contributions to biomedical engineering.

It is our hope to inspire all the students to get involved in biomedical engineering and continue working so that this discipline grows. Without each and every one of you, the CNIB 2022 would not have been a success so, many thanks.

Balam Benítez-Mata
Co-chair Program CNIB 2023

José de Jesús Agustín Flores Cuautle
Chair Program CNIB 2023

President of the Mexican Society of Biomedical Engineering Message

Dear readers and collaborators in the field of biomedical engineering,

It is an honor to address you on the occasion of the XLVI Mexican Conference on Biomedical Engineering, an event that symbolizes our collective commitment to the advancement of biomedical engineering. At a time when technology and innovation play an essential role in the development of our country, this congress represents an invaluable opportunity to bring together the brightest and most dedicated minds in this field.

Biomedical engineering plays a fundamental role in merging technology with the health sector. This congress is a showcase for the latest research and developments in this area. The scientific papers that are presented here reflect the hard work and dedication of experts who seek to innovate and contribute to improving health through engineering; by coming together at this event, we create a space to share ideas and establish fruitful collaborations that further advance our field.

This congress is not only a platform for the dissemination of results, but also a space for personal and professional growth. I hope that you find inspiration in the work and that you take the opportunity to establish collaborations that allow you to develop new research.

I appreciate your participation and hope you enjoy and benefit from this event as much as we did organizing it. Together, we are shaping the future of biomedical engineering in Mexico.

Sincerely,

Francisco Javier Aceves Aldrete
President of the Mexican Society of
Biomedical Engineering 2022–2023,
Organizing Committee of the XLVI
Mexican Conference on Biomedical
Engineering

Organization

CNIB 2023 was organized by the Mexican Society of Biomedical Engineering (SOMIB).

Executive Committee

Conference Chair

Francisco Javier Aceves Aldrete

Program Chair

José Jesús Agustín Flores-Cuautle

Scientific Committee

Program Chair

José Jesús Agustín Flores-Cuautle Instituto Tecnológico de Orizaba, México

Program Co-chair

Balam Benítez-Mata University of California Irvine, USA

Session Coordinators

Ricardo Antonio Salido-Ruiz	Universidad Guadalajara, México
Gustavo-Adolfo Alonso-Silverio	Universidad Autónoma de Guerrero, México
Guadalupe Dorantes-Méndez	Universidad Autónoma de San Luis Potosí, México
Esmeralda Zuñiga-Aguilar	Universidad Autónoma de Ciudad Juárez, México
Hugo A. Vélez-Pérez	Universidad de Guadalajara, México
Edgar Del Hierro-Gutierrez	Universidad Autónoma del Estado de México, México
Aldo Rodrigo Mejía-Rodríguez	Universidad Autónoma de San Luis Potosí, México

Awards Committee

Student Competition

Hugo A. Vélez-Pérez

Universidad de Guadalajara, México

Organizing Committee

Organizing Chair

Francisco Javier Aceves Aldrete

Program and Guest

Ximena Ruiz

Workshop

Manuel Nuñez Meza

Exposition Chair

Verónica Castillo

Special Session

Ana Luz Portillo

Students Coordinator

Rodrigo García

Education Committee

Chair

Eduardo Mendez Palos

Industry Committee

Chair

Christopher Bricio

Innovation Committee

Chair

Luis Fernández

Logistics Committee

Chair

Zayra Resendiz

Administrative Support

Nicolle Ramírez
Gabriela Sámano

Local Committee

Chair

Alejandra Casanova

Sponsoring Institution

Mexican Society of Biomedical Engineering (SOMIB)



Referees

Adeodato Israel Botello Arredondo
Adriana Pliego-Carrillo
Agustin Vidal-Lesso
Angel Saucedo Carvajal
Carlos Martinez
Christian Cruz Sosa
Citlalli Tujillo Romero
Claudia Ivette Ledesma-Ramirez
Daniela Ayala Barajas
David Abad
Edgar Del Hierro-Gutiérrez
Edgar Miguel Ramírez
Edson Francisco Estrada Meneses
Erika Guadalupe Meráz Tena
Esmeralda Sarai Zuñiga Aguilar
Fabián Equihua Guillén
Fabian Vazquez
Fausto Cortes
Francisco Aceves
Gemima Lara Hernández
Griselda Argelia Rivera Vargas
Héctor Camacho Montes
Hector Emanuel Martin Alcala
Isela Bonilla-Gutierrez
Javier Castro
Jorge Rodriguez Arce
José Antonio Ruvalcaba
Jose De Jesus Agustin Flores Cuautle
Jose Diaz
Jose Javier Reyes-Lagos
Juan Carlos García-López
Juan Miguel Colores Vargas
Lidia Hortencia Rascón Madrigal
Lucero Guadalupe Burciaga Jurado
Luis Jiménez-Angeles
Marco Octavio Mendoza Gutiérrez
Marcos David Moya Bencomo
Marcos Mendoza Mejia
María de la Luz Mota
Miguel Peña-Castillo
Nelly Gordillo-Castillo
Odin Ramirez-Fernandez
Quetzali Salazar-Mireles

Rafael E. González-Landaeta
Sarai Esmeralda Favela Camacho
Solange Ivette Rivera Manrique
Victor Gómez Flores
Yara Villalobos
Zaira Pineda Rico

Contents

Biomechanics, Rehabilitation, Biomaterials and Tissue Engineering

Inverse Kinematics Analysis of a Novel Osseointegrated Prosthesis Prototype with the Use of the “Montefiori” MRI Based Musculoskeletal Subject Specific Model	3
<i>Antonio Gómez Ruiz, Armando Ladislao López Montes, Alejandro De León Cuevas, Adrian Jefe Elías Jiménez, and Tania Pérez Salazar</i>	
Characterization of Kinematics and Electromyography During Lunges Execution to Assess Knee Performance in Healthy Subjects	15
<i>Leonel González, Arantza Ituarte, Juan Carlos Vera, Felix León, Rafaella Romero, José Javier Reyes-Lagos, and Carlos Cuellar</i>	
Kinematic and Electromyography Analysis of the Knee Function in Non-trained Healthy Subjects Through a Single-Leg Drop Landing Test	25
<i>Arantza Ituarte, Felix León, Juan Carlos Vera, Isamar Duarte, Leonel González, and Carlos Cuellar</i>	
Analysis of Mechanical Behavior of Biomaterials of HA/Ti for Bone Tissue Regeneration Using Finite Element Method	33
<i>María Fernanda Toledo Romo, María Flores Sánchez, Hipólito Aguilar Sierra, and Erick Ramírez Aguilar</i>	
Kinetic and Kinematic Analysis of Gait in a Patient with Transtibial Amputation: A Case Study	48
<i>Karla Martínez, Isabel C. Soto, and Elizabeth Pareja</i>	
Ocular Biomechanics of Glaucoma	57
<i>Yael Osmar Bravo Sustaita, Ximena Berenice Guzmán González, and A. Vidal-Lesso</i>	
Stem Design for Tibial Component of Knee Prosthesis	68
<i>Dorothy Alejandra Almanza-Martínez, Roberto González-Navarrete, and Agustín Vidal-Lesso</i>	

Morphological Evaluation of Freeze-Dried Fish Gelatin and Bovine Gelatin Scaffolds for Tissue Engineering	80
<i>Wendy Meliza Álvarez-Nanguce, Edith Cedillo-Cruz, Alfredo Maciel-Cerda, Patricia Mendoza-Lorenzo, and Roberto Hernández-Córdova</i>	
Experimental Test Bed for Hand Orthotic Actuators Characterization	87
<i>Ángel Iván De Luna-García, Ricardo Cortez, Marco Sandoval-Chileño, Norma Lozada-Castillo, and Alberto Luviano-Juárez</i>	
Lumbar Erector Spinae Activity During Anterior Trunk Flexion of People Who Use the Computer for More Than 30 h a Week	99
<i>Raide Alfonso González-Carbonell, Igor Salinas-Sánchez, and Jesús Manuel Dorador-González</i>	
Biocompatibility In-Vivo Evaluation of Polypyrrole/Iodine Synthesized by Plasma Polymerization	108
<i>Rodrigo Mondragon-Lozano, Hermelinda Salgado-Ceballos, María Guadalupe Olayo, Guillermo Jesús Cruz, Eva González Trujano, Araceli Díaz-Ruiz, Stephanie Sánchez-Torres, Carlos Orozco Barrios, and Angelica Coyoy Salgado</i>	
Exploring the Biological Potential of Hydroxyapatite-Doped with Magnesium: Cytotoxicity and Cell Viability Assessment	115
<i>Rafael Rangel Ibarra, Juan David Olivares Hernández, José Rafael Alanís Gómez, and Fabiola Hernández-Rosas</i>	
Voronoi 3D: A Novel Approach to Design 3D PLA/HAP Printed Scaffolds for Tissue Engineering Applications	122
<i>Salgado-Alvarez Ana Paola, Hernández-Vega Luis Alberto, Alanís-Gómez José Rafael, and Hernández-Rosas Fabiola</i>	
Combating Prosthetic Infections: Synthesis, Characterization, and Evaluation of Magnesium-Doped Hydroxyapatite Nanofibers with Antibacterial Properties	131
<i>Epsiba Lorena Marañón Romero, Ricardo Pascual Alanís Gómez, José Rafael Alanís-Gómez, Kevin José Martínez Arellano, Fabiola Hernández-Rosas, and Rodrigo Velázquez Castillo</i>	
Characterization and Antimicrobial Evaluation of Gadolinium- Doped Hydroxyapatite for Potential Use as Drug Carrier System	139
<i>Cristhian Valencia Arreguin, Luis Fernando Serna Maldonado, Natalia Mora Padron, Ramírez Ortiz, Fernando, Fabiola Hernandez Rosas, José Rafael Alanís Gómez, and Rodrigo Velázquez Castillo</i>	

Wrist-Forearm Differential Kinematics Using Monocular Vision Capture 148
*Alejandro Pescador-Salas, Juan Pablo Rosales-Huie,
Dulce Martínez-Peon, and Ernesto Olguín-Díaz*

Knee Osteoarthritis Therapy Assistance Software 158
*Pérez Alvarado Oscar Eduardo, Solís López Daniel,
and Vargas Martínez Darien Gustavo*

Hand Assessment Device Prototype 169
*Sabrina Sofía Prieto Salazar, Guadalupe Karla Velasco Gómez,
Perla Vanessa Aguilar Mejía, and Marisol Martínez-Alanís*

Determination of the Survival of Recellularized Primary Hepatocytes
in a Wistar Rat Liver Extracellular Matrix 176
*Nelly A. Morales-Guerrero, Alfredo Varela-Echavarría,
Carlos Lozano-Flores, Francisco G. Vázquez-Cuevas,
Esperanza Mata-Martínez, and Hebert Luis Hernández-Montiel*

**Clinical Engineering, Regulations and Innovation and Development
of Technologies for Health, Medical Physics**

An Experimental Study of Induced Maculopathy in Ex-Vivo Tissue
by Laser Pointers 183
*Aurora-Yunuen Cardiel-Espino, Galilea-Fernanda Corral-Valencia,
Manuel Vázquez-Nambo, Carlos-Alberto Trejo-Seráfico,
and Joaquin Esteves-Delgado*

Innovation of Sanitization Procedures for Mechanical Ventilators Using
Six Sigma Methodology 191
Ana Bertha Pimentel-Aguilar and Martha Refugio Ortiz-Posadas

A Technical Assessment Tool to Prioritize Medical Devices Replacement 202
*María de Lourdes Cruz-Hernández, Beatriz Gutiérrez-Sánchez,
and Martha Refugio Ortiz-Posadas*

Innovation of Pre-surgical Orthopedics Process for Patients with Cleft Lip
and Palate Using the Six Sigma Methodology 211
Alitzel Munguía-Crisóstomo and Martha Refugio Ortiz-Posadas







Permanent Changes in Clinical Engineering Procedures Since COVID-19
in OECD Countries 222
*Valeria Chico, Nelly Gordillo-Castillo, Ana Luz Portillo,
and Yara Villalobos*

Relationship Between Neuroarchitecture and Stress Reduction Compared to Conventional Architecture in Healthcare Personnel	232
<i>Mauricio Baez, Sergio Camacho, Bersain Reyes, Antonio Morante, and Miguel Fuentes</i>	
Implementation of QR Codes on Medical Equipment as a Tool for Hospital Management	241
<i>Quetzalli Hidalgo, Sergio Camacho, Bersain Reyes, and Miguel Fuentes</i>	
Examining the Impact of Academic Degree Level on Misinformation Levels Regarding the COVID-19 Pandemic in Mexico: A Social Media Perspective	250
<i>Sarahi Alvarez, Sergio Camacho, and Bersain Reyes</i>	
Design Thinking Methodology Applied for the Development of Remote Teaching Models in Biomedical Engineering	257
<i>Jorge Luis Rodríguez-Medina, Guadalupe Dorantes-Méndez, and Aldo Rodrigo Mejía-Rodríguez</i>	
Author Index	269

**Biomechanics, Rehabilitation,
Biomaterials and Tissue Engineering**



Inverse Kinematics Analysis of a Novel Osseointegrated Prosthesis Prototype with the Use of the “Montefiori” MRI Based Musculoskeletal Subject Specific Model

Antonio Gómez Ruiz¹ , Armando Ladislao López Montes¹  ,
Alejandro De León Cuevas² , Adrian Jefe Elías Jiménez² ,
and Tania Pérez Salazar³ 

- ¹ Departamento de Ingeniería Biomédica, Facultad de Ingeniería, Universidad Anáhuac, Santiago de Querétaro, Querétaro, Mexico
armando.lopez05@anahuac.mx
- ² Laboratorio Universitario de Biomecánica Campus UNAM Querétaro, Mexico City, Mexico
- ³ Unidad Profesional Interdisciplinaria en Ingeniería y Tecnologías Avanzadas, Instituto Politécnico Nacional, Mexico City, Mexico

Abstract. Prosthetic limb models created with 3D software simulators are nowadays a great tool to visualize the motion of existing and novel prosthesis designs. Magnetic resonance image (MRI) based models created with 3D bone surfaces can simulate prostheses with the joint kinematics data obtained from a motion capture system. These simulations also can help us to visualize the features of a prosthetic design before the prosthesis is created. The main objective is to facilitate prosthesis designers with virtual tools to simulate the prosthesis prototypes to decrease the time and resources of the prosthesis design. By using the method designed by Montefiori *et al.* [6], it is possible to simulate the differences between the knee flexion during a gait cycle between the physiological limb and a prototype of a prosthetic leg. The joint kinematics of both limbs can be compared to detect the differences during walking. This research was applied to one test subject, but for further research, this method can be applied to more patients that use prosthetic limbs to develop a database of joint kinematics variables that are essential to improve efficiency in the prosthesis design.

Keywords: Subject-specific · MRI-based model · Osseointegrated prosthesis · 3D-model · Biomechanics · Motion capture system · Optoelectronic

1 Introduction

Balance is the phenomenon where a body’s center of mass (CoM) is vertically over the base of support to retain equilibrium [1]. This balance allows the standing position which is essential for the mobility of an individual. Patients with amputation have challenges to hold a standing position. Consequently, this increases the risk of falling and other injuries caused by the lack of balance [2].

Prosthetics are built as a replacement for the lost limb and the attempt to establish a quality of life for the amputees, the most common prosthesis is the socket prosthesis [3]. However, the surface of this replacement regularly causes pain, and skin injuries, among other issues [3].

Consequently, osseointegrated prostheses were successfully implemented first time in 1990 and, among other existent systems, the Osseointegrated Prostheses for the Rehabilitation of Amputees (OPRA) and Implant Supported Prosthesis Endo/Exo (ISP) prosthesis protocols are available [4] bringing new alternatives. In addition, this kind of prosthesis is directly anchored to the bone, therefore, eliminating the socket inconveniences and providing additional benefits like a larger range of motion (ROM), greater reabsorption of the bone, and leaving behind soft tissue problems [5].

Combining the direct implant of the prosthesis to the bone in a 3D motion capture model allows the previsualization, and simulation of the individuals with their prosthesis. In 2019 similar research was done with a 3D model human, and attached a prosthesis to the musculoskeletal system as we can see in Fig. 1 [14]. They stated that the benefits of doing these methodologies is that we can understand better the gait cycle, kinematics and relations between assistive devices and walking characteristics [14].



Fig. 1. Grabke and teams' musculoskeletal model

Then in 2020 research with a similar methodology was done, using OpenSim and attaching a transfemoral prosthesis to the musculoskeletal model [12]. In that article they measured the ankle moment and ankle angle for dorsiflexion and plantarflexion. But in both cases, they used generic 3D models, instead of having a specific subject model.

The challenge resides in the correct adjustment of the geometrical properties of the prosthesis with the anthropometric properties of each patient. Therefore, this research is aimed to simulate the standing and the gait motion with an MRI-based model to adapt the prosthesis design with the geometrical and motion requirements for a specific patient.

2 Methodology

2.1 Materials and Methods

Software tools such as SolidWorks (2020), NMSBuilder version 2.1, and OpenSim 3.3, were used to perform simulations, material tests, and obtain measurements of the model prosthesis.

Whereas gait analysis data was collected by Montefiori et al. [6] using movement analysis based on infrared optical stereophotogrammetry. An 8-camera system (MX, Vicon Motion System Ltd, UK, 200 Hz) with two force platforms (OR6-6, AMTI, USA, 1000 Hz).

The marker-set was a combination of the Vicon Plugin gait (Vicon Motion System) and the modified Oxford Foot Model (mOFM) protocols, with a total of forty-four markers. A subset of twenty-eight markers was retained during a following MRI exam.

The patient was chosen from the population evaluated by Montefiori et al. [6] and had a virtual amputation with D5 Render software. The novelty of our project is the implementation of MRI based musculoskeletal models (Montefiori et al. [6]) instead of using generic bones models, to evaluate gait cycles of a subject using a novel virtual transfemoral Osseointegrated prosthetic limb prototype to evaluate joint kinematics between a prosthetic and physiological knee.

2.2 Anatomical Model and Segmentation Through MRI

Both the imaging and gait analysis data of the subject were shared by Montefiori et al. [6], following the procedures they described. MRI was used to acquire images of the lower limbs and NMSBuilder to generate the anatomical model, to get the segmentation of every individual bone to create the MRI-based model. Then in the software tools, the physiological left leg was replaced with the prosthesis to test it in the simulation.

2.3 Prosthesis Design

Research

An anchoring system (AS) was required for the osseointegrated part of the prosthesis. Tomaszewski [7] found that there was an advantage in a direct attachment of the prosthesis vs a traditional socket fixation. Two temporal parameters were proposed: the use of the implant after using a socket, or immediately after surgery. The second option has therefore, the design of the screw for the patient.

The use of a socket affects the bone mineral content (BMC) because the bone is not under stress conditions since all the forces are applied to the stump of the patient, so the bone would lose its density and mechanical properties. Nevertheless, with a direct fixation, the bone would be again under stress conditions preventing the loss of bone thickness.

In Tomaszewski's [7] work, there were 2 proposals of design, the implant supported prosthesis (ISP), and the Osseointegrated Prostheses for the Rehabilitation of Amputees (OPRA) implant. The OPRA implant is a titanium pin screwed in the medullary cavity,

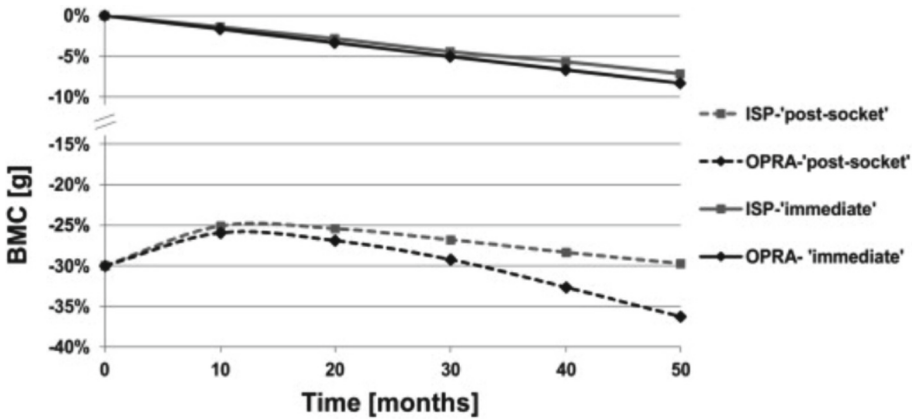


Fig. 2. ISP and OPRA, comparison in BMC loss in Tomaszewski's research [7]

while the ISP is a press-fit implant made of a cobalt-chromium–molybdenum alloy covered with a porous trabecular (PT) metal. The results can be explained in Fig. 2.

The evidence showed that fixation of the implant made immediately after surgery is better than using a socket first, due to being a major loss of BMC and the ISP implant has less BMC loss than the OPRA implant.

Later, models that incorporate the use of springs were sought to help the mechanical system as seen in Fig. 3. It was found information about this in an investigation made by Geeroms [8] where a proposal of using a semi-active actuator with a parallel spring was made. The goal was to achieve similar results for this research.

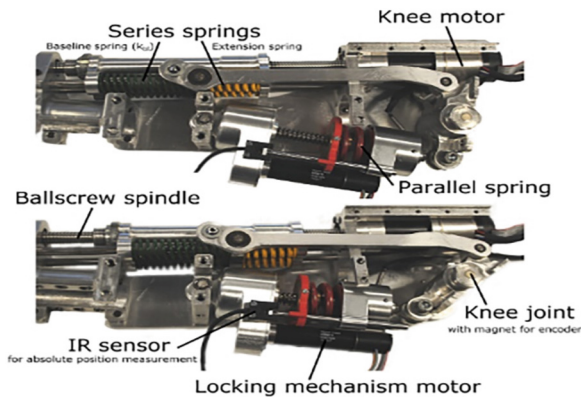


Fig. 3. Spring used in a damped system in a prosthetic leg to improve its functionality [8]

In this design, the concept was to use a semi-active spring system that would improve the gait cycle providing a better flexion and extension. For this case instead, it was agreed to use the spring to have a damped ankle system.

This was an important part of the design since a fixed implant would transmit all the impacts when a person is walking, directly to the bone. Therefore, the spring assists to reduce the impact on the cartilage or the meniscus.

Designing Process

The first step in design was the AS. Based Tomaszewski [7] research, a medical-grade titanium screw that had porous trabecular metal using a cellular solid prototype design was made by our team, as we can see in Fig. 4, and has the properties shown in Table 1.

Table 1. Physical properties of the designed AS SolidWorks®

Density	Mass	Volume	Surface area
4.43 g/cm ³	129.49 g	29.24 cm ³	206.01 cm ²

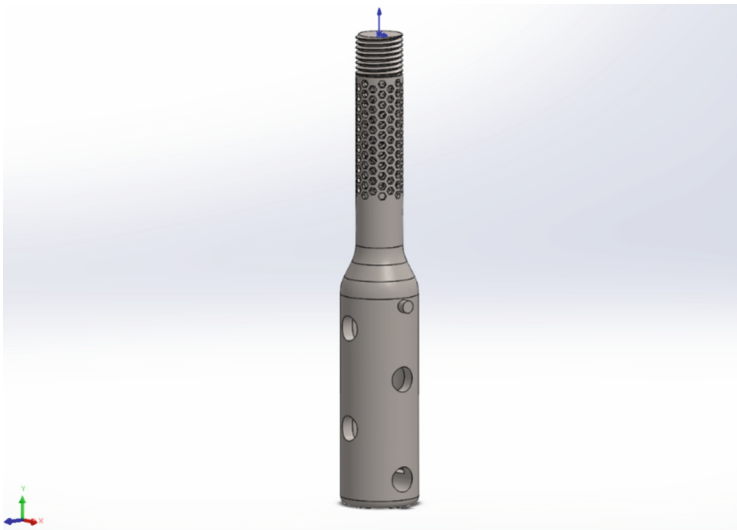


Fig. 4. Model prototype design for AS

The PT area is in the upper part of the piece, anchoring the bone and using the cellular solid form to allow nutrients to travel along the cancellous bone, the lower area will be attached to the prosthetic limb.

After the AS was designed, the rest of the prosthetic leg followed. As a first step, the essential parts and mechanisms were designed for the prosthetic leg and the function of every component. Then we assured that the prototype of the model had the essential components that attempt to replace the leg, knee, calf, and feet. Then the design was adapted to have similar motion ranges on the joints, an efficient feet design that allow a correct gait motion kinematics and a final prototype design was made which is presented in Figs. 5 and 6.



Fig. 5. Final model frontal view.

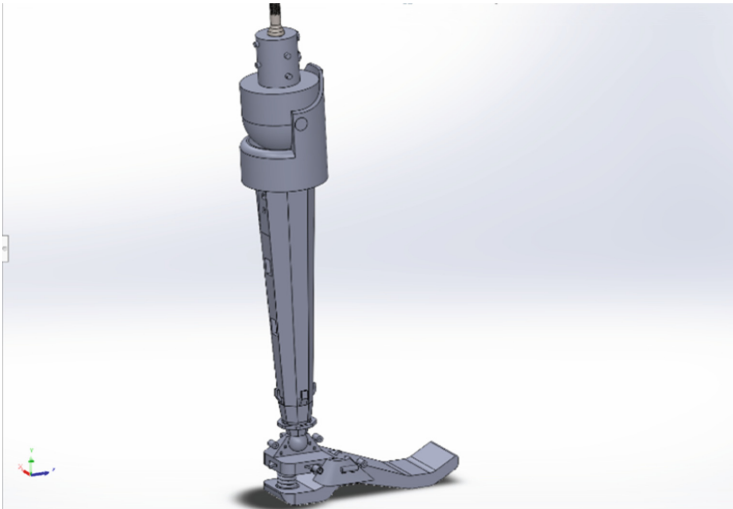


Fig. 6. Final model rear view

The ankle was something challenging because it works as a ball joint, so it has 6° of freedom. To solve this, a ball joint was placed at the top of the feet and designed an assembly mechanism so that the leg and the feet could be attached or be able to be detached for maintenance or repair. Furthermore, a spring was incorporated into

the prosthetic ankle system that would make the feet a damped system as previously discussed.

Exportation and Model Generation

After the design modeling, the 3D surfaces from the prosthetic design were exported to NMSBuilder 2.1 following Montefiori's method [6] to create joints and a musculoskeletal virtual model. The model was scaled for a 1.6 m female patient. The prosthesis was anisotropically scaled on the 3 axes to adjust the height of the participant and the lengths of the original limb. The prosthetic device was adapted to fit the center of rotations of the contralateral limb.

The components of the prosthetic device were scaled to the MRI-based 3d surfaces. The distance of the prosthetic devices was scaled based on the distance between the center of rotation of the hip, knee, and ankle. The 3d surfaces of the prosthetics components were exported to NMS Builder after being scaled to the participant's geometry as shown in Fig. 7.

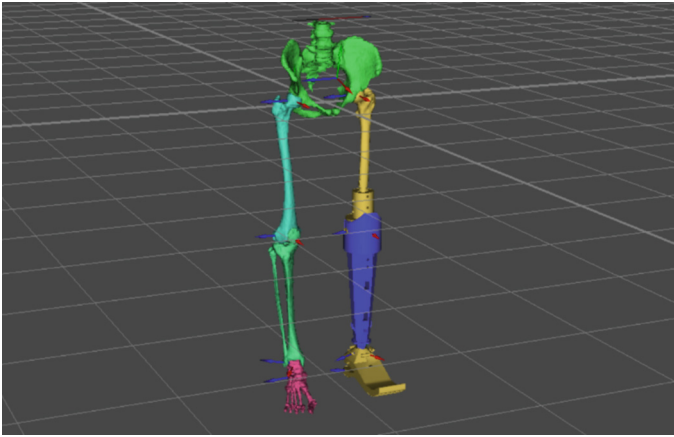


Fig. 7. Simulated model with an adjusted prosthetic leg

In the NMS builder software, the parent and child reference systems of the pelvis, hip, knee, and ankle were created. The hip and ankle were modeled as a ball and socket joint, and the pelvis was simulated as a 6° of freedom joint with 3 rotations and 3 translations. The knee was simulated as a 1° of freedom rotational pin joint.

Exportation to OpenSim 3.3

Taking further Montefiori's methods [6] the model was imported to OpenSim 3.3, which is a computational musculoskeletal motion simulation software. It was very important for the work that the model already had the body, in this case. The anatomical virtual markers that were used for this work were named: RPSI, LPSI, LASI, RASI, RTHI, RKNE, RMFC, RHFB, RSHN, RMMA, RANK, RTUB, LTUB, LMFC, LSHN, LMMA, LANK, LHFB, LKNE, LTHI. Landmarks are represented with spheres (see Fig. 8), as shown in Figs. 9, 10 and 11.

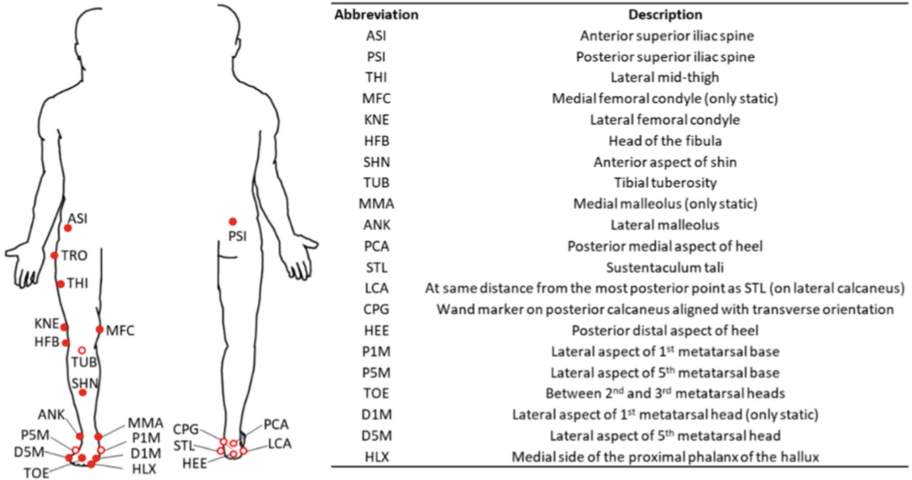


Fig. 8. Anatomical landmarks used for simulation by Montefiori et al. [6]



Fig. 9. Coronal view of the model



Fig. 10. Sagittal view of the model.

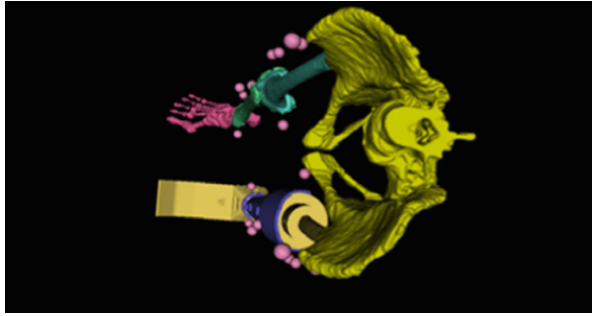


Fig. 11. Axial view of the model

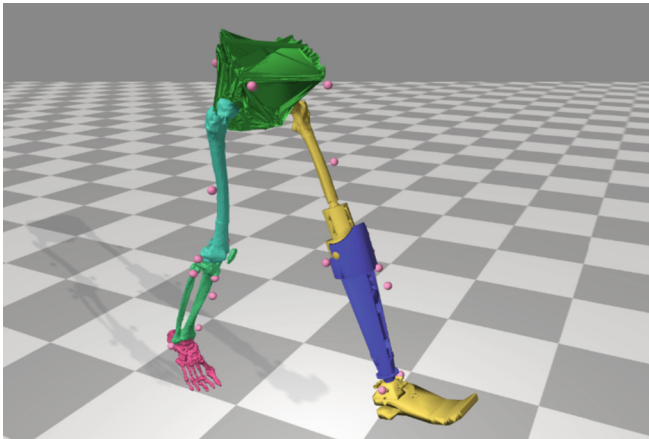


Fig. 12. Model simulation in motion capture

With the landmarks set in their standing position, the joint kinematics was estimated with Opensim 3.3 with the 3D motion coordinates of the anatomical markers that were obtained in an optoelectronic motion capture obtained by Montefiori et al. [6].

The prosthetic device was simulated with a 1° of freedom rotation pin joint for the knee and the ankle as shown in Fig. 12. The model was adapted to have a virtual amputation in the femur.

3 Results

After calculating the joint angles, the differences between the joint kinematics of the prosthetic device knee compared with the physiological knee joint were calculated. The prosthetic leg has a similar range of motion as seen in Fig. 13, but they have variations in the gait motion kinematics. The next graph shows the gait cycle in both legs, and the degrees of the knee in each phase. The phases emphasized are the loading response and the toe off, which involve more knee flexion. For the loading response phase there were 3° approximately of difference while in the toe off phase there were 10° approximately

of difference. This means that in the toe off phase there is a 15% of deviation while in the loading response is an 11% of deviation.

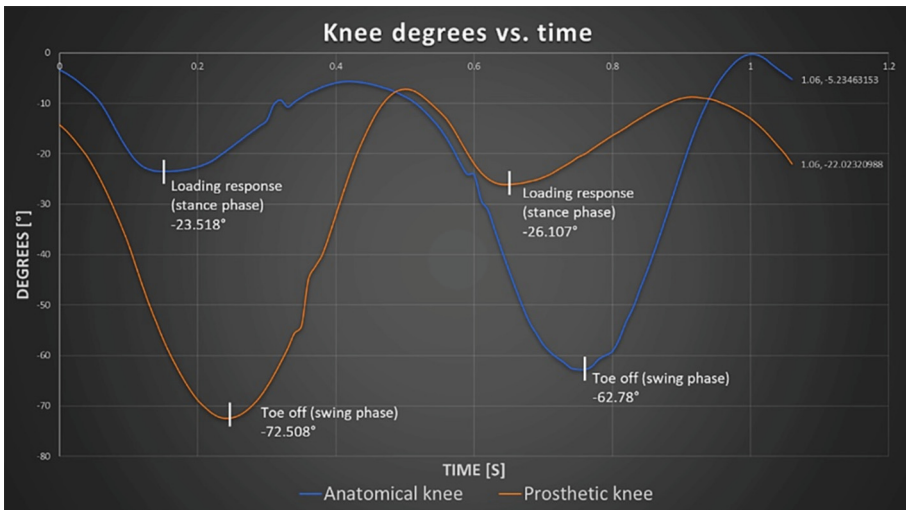


Fig. 13. Angle comparison between both legs

In related works such as Raveendranathan [12] they also had a degree difference; in their case their maximum was of 10°. This could be caused by the scaling of the prosthesis and its components.

4 Discussion

In this research, it has been possible to compare the joint kinematics with software to represent MRI digital surfaces, and simulators to create a 3D model of a transfemoral osseointegrated prosthesis and to estimate the joint kinematics after the prosthesis is integrated into the musculoskeletal MRI based subject-specific model, which have the capability of representing the joint kinematics of a virtual prosthetic prototype. Even though the anatomical leg and the prosthetic leg do not have the same range of motion, musculoskeletal modeling can be used to calculate the range of motion of prosthetic virtual designs to test the geometry, scaling and the joint kinematics that are obtained. The calculation of the joint kinematics can be useful to test the joint angles of the prosthetic limb with different geometrical parameters.

5 Conclusions

This was a preliminary study where it was assumed that the bodies of the proposed prosthetic model were rigid, except for the knee, and where we proposed a method to analyze and evaluate the alignment of the joints between the biological leg and prosthetic limb. Even though the design is a prototype, the gait analysis, and standing joint

kinematics were compared for the prosthetic limb compared with the contralateral limb. Also, in this research we had some limitations, as we worked with an MRI based model, for example, Arnold [13] worked directly with bones from a cadaver giving him more precise models. With this research, further work can take place where different persons that use prostheses are analyzed to evaluate design and functioning. We could also make a database based on the joint kinematic data provided by the simulations done with MRI based musculoskeletal models of a higher sample of participants.

Acknowledgments. We thank Dr. José Rafael Alaniz Gómez Coordinator of the biomedical engineering career at Anáhuac Querétaro University.

Authors A. Elias and A. de Leon thank Ing. Lidia Mendoza, Lic. Horacio Leyva team of the Biomechanical Laboratory and Luis Aguilar, Alejandro Ávalos, Jair García team of the Laboratorio Nacional de Visualización Científica Avanzada [10, 11].

References

1. Ku, P.X., Abu Osman, N.A., Wan Abas, W.A.B.: Balance control in lower extremity amputees during quiet standing: a systematic review. *Gait Posture* **39**, 672–682 (2014)
2. Steinberg, N., Gottlieb, A., Siev-Ner, I., Plotnik, M.: Fall incidence and associated risk factors among people with a lower limb amputation during various stages of recovery—a systematic review. *Disabil. Rehabil.* p. 1778–1787. Taylor and Francis Ltd. (2019)
3. Leijendekkers, R.A., et al.: Comparison of bone-anchored prostheses and socket prostheses for patients with a lower extremity amputation: a systematic review. *Disabil. Rehabil.* p. 1045–1058. Taylor and Francis Ltd. (2017)
4. Thesleff, A., Ortiz-Catalan, M., Brånemark, R.: The effect of cortical thickness and thread profile dimensions on stress and strain in bone-anchored implants for amputation prostheses. *J. Mech. Behav. Biomed. Mater.* **129** Elsevier Ltd. (2022)
5. Hagberg, K., Häggström, E., Uden, M., Brånemark, R.: Socket versus bone-anchored transfemoral prostheses: hip range of motion and sitting comfort. *Prosthet. Orthot. Int.* **29**, 153–163 (2005)
6. Montefiori, E., Modenese, L., di Marco, R., Magni-Manzoni, S., Malattia, C., Petrarca, M., et al.: Linking joint impairment and gait biomechanics in patients with juvenile idiopathic arthritis. *Ann. Biomed. Eng.* **47**, 2155–2167. Springer New York LLC (2019)
7. Tomaszewski, P.K., Verdonschot, N., Bulstra, S.K., Rietman, J.S., Verkerke, G.J.: Simulated bone remodeling around two types of osseointegrated implants for direct fixation of upper-leg prostheses. *J. Mech. Behav. Biomed. Mater.* **15**, 167–175 (2012)
8. Geeroms, J., Flynn, L., Jimenez-Fabian, R., Vanderborght, B., Lefeber, D.: Design and energetic evaluation of a prosthetic knee joint actuator with a lockable parallel spring. *Bioinspir. Biomim.* **12**, 026002 (2017)
9. Brinkmann, J.R., Perry, J.: Rate and range of knee motion during ambulation in healthy and arthritic subjects. *Phys. Ther.* **65**(7), 1055–1060 (1985)
10. Pirker, W., Katzenschlager, R.: Gait disorders in adults and the elderly: a clinical guide. *Wiener klinische Wochenschrift* **129**(3–4), 81–95 (2017)
11. Abbass, S.J., Abdulrahman, G.: Kinematic analysis of human gait cycle. *Coll. Eng. J. (NUCEJ)* **16**, 208–222 (2014)
12. Raveendranathan, V., Carloni, R.: Musculoskeletal model of an osseointegrated transfemoral amputee in OpenSim. In: 2020 8th IEEE RAS/EMBS International Conference for Biomedical Robotics and Biomechatronics (BioRob), pp. 1196–1201. IEEE (2020) November

13. Arnold, A.S., Salinas, S., Hakawa, D.J., Delp, S.L.: Accuracy of muscle moment arms estimated from MRI-based musculoskeletal models of the lower extremity. *Comput. Aided Surg.* **5**(2), 108–119 (2000)
14. Grabke, E.P., Masani, K., Andrysek, J.: Lower limb assistive device design optimization using musculoskeletal modeling: a review. *J. Med. Devices* **13**(4), 040801 (2019)



Characterization of Kinematics and Electromyography During Lunges Execution to Assess Knee Performance in Healthy Subjects

Leonel González¹ , Arantza Ituarte² , Juan Carlos Vera² , Felix León² ,
Rafaela Romero² , José Javier Reyes-Lagos¹ , and Carlos Cuellar³  

¹ Facultad de Medicina, Universidad Anáhuac México, 052786 Huixquilucan, Estado de México, Mexico

² Facultad de Ciencias de la Salud, Universidad Anáhuac México, 052786 Huixquilucan, Estado de México, Mexico

³ Escuela de Ciencias del Deporte, Universidad Anáhuac México, 052786 Huixquilucan, Estado de México, Mexico
carlos.cuellarra@anahuac.mx

Abstract. The knee joint is essential for stability, postural support and as a shock absorber of the body weight when carrying out bipedal physical activity. The lunge exercise is a functional test to evaluate the knee performance, therefore, applying a quantitative evaluation through kinematics and electromyography during lunge execution in non-trained healthy subjects will contribute to establish normative values in males and females for future comparison with diverse knee injuries. The aim of this study was to characterize electromyography parameters and kinematics of the knee while performing lunges bilaterally in healthy non-trained subjects ($n = 70$). A statistical difference between Right Leg vs. Left Leg for RMS, AUC and MNF was found for the pooled data, and between male vs. female just for RMS. The range of movement did not differ significantly between legs or sexes. These results will be used to establish a database in healthy subjects that can be used to compare results vs. subjects with a knee injury.

Keywords: knee joint · kinematics · electromyography · lunge

1 Introduction

During physical activity, involving lower limbs, the knee joint contributes to stabilizing the body and prevents overload during movement [1]. The quadriceps (QM) and hamstring muscles (HM) coactivate to guarantee proper stability when performing knee joint high-impact movement. In addition, HM contraction contributes to reducing the traction of the QM, allowing to keeping better movement control [2].

The probability for an athlete to suffering a knee ligament injury (KLI) is related to leg dominance, i.e., the Dominant Leg (DML) presents the highest prevalence of injury

during movements such as landing or cutting movements due to the DML receives a greater load compared to its counterpart [3]. Moreover, women are 2 to 3 times more vulnerable to suffering a KLI, most frequently the Anterior Cruciate Ligament (ACL) [4]. Electromyography data (EMG) from the muscles directly involved in the knee joint during functional tests provides information about the activation pattern (AP) in the right leg (RL) compared to the left leg (LL) and between male (M) and female (F) [5]. In addition, kinematics assess the Range of Movement (ROM) of the knee to evaluate if there is any limitation involving knee flexion-extension [6].

The lunge exercise is an appropriate functional test to estimate the reaction exerted by the knee in a kinematic and neuromuscular system [7]. This test is used within the rehabilitation plan of subjects with KLI reconstruction to reintegrate it to an optimal and functional level when fulfilling impact physical activities [8]. Studies have been carried out in athletes without a history of KLI, as in [9]. However, non-trained subjects with low physical activity levels have not been considered; consequently, they may exhibit different knee performance compared to trained athletes.

By using EMG and kinematics during lunges, we aimed to characterize Root Mean Square (RMS), Area Under Curve (AUC), Mean Frequency (MNF) and ROM. Data from this study, could be useful to determine the probability of KLI and to establish a database to compare knee performance in subjects with a KLI in future studies.

2 Materials and Methods

Seventy subjects (30 M, 40 F) without history of trauma or musculoskeletal injury in lower limbs participated in this study. Height and weight were measured to determine Body Mass Index (BMI). 65 subjects reported right dominance. The protocol was approved by the Research and Research Ethics Committee of the U. Anáhuac México (202303).

2.1 Lunge Test

Initially, the participant completed a 5 min warm-up. The subject stood with their feet shoulder-width apart. Then, the subject had to step forward with one leg while lowering the body and flexing both legs until the knee of the leg that remained in the starting position was a few centimeters from the ground. Upon reaching the maximum point, the subject had to return to the starting position and alternate the leg. The exercise consisted of 3 repetitions per leg, initiating with RL. Figure 1 shows how the test was performed.

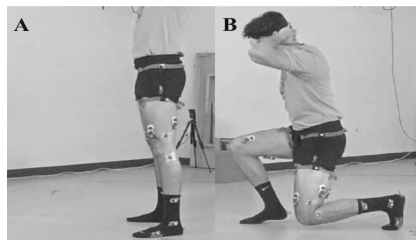


Fig. 1. Lunge test. **A.** Initial test position. **B.** Maximal knee flexion in RL.

2.2 EMG

Eight wireless sensors (FREE EMG, BTS Bioengineering) were used. Paired surface Ag/AgCl electrodes were connected to the sensors and placed bilaterally on the subject's abraded skin in the Vastus Lateralis (VL), Vastus Medialis (VM), Semitendinosus (ST), and Biceps Femoris (BF) as shown in Fig. 2. The signals were recorded with a sampling frequency of 1 kHz and a bandpass filtered (20–450 Hz). MATLAB 2020b was used for off-line data processing. For each lunge, the amplitude of the EMG signal was normalized and segmented for both legs. The RMS, AUC, and MNF parameters were calculated for each lunge.

2.3 Kinematics

Six infrared light cameras (SMART DX, BTS Bioengineering) were used to capture the knee kinematics. The camera's resolution was 1.5 Mpixels. Recordings were sampled at 250 Hz. Seventeen reflective markers were placed bilaterally as follows (Fig. 2): in trochanteric pons, middle area of the thigh, lateral epicondyle, head of the fibula, in the medial area of the fibula, lateral malleolus protuberance, central area of the hindfoot, on the fifth metatarsal, and one at the level of S2.

BTS Bioengineering software was used to record kinematics, and reconstruct the anatomical model from the labeled markers according to their position. Then, a vector was created from the proximal femur to the distal femur, and another from the distal fibula to the proximal fibula, as the union of both vectors represents the ROM of the knee during lunges. The angular trajectory in each leg was plotted and obtained peaks represented the maximum flexion exerted for each repetition. The median value of the flexion of each leg was determined.

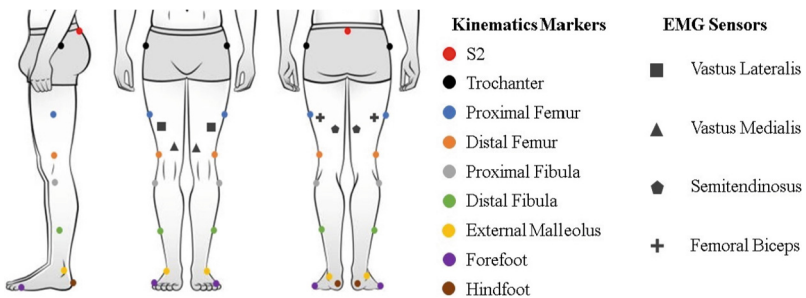


Fig. 2. Lateral, anterior and posterior views of the anatomical position of lower limbs where the markers for kinematics and the sensors for EMG were placed.

2.4 Data Analysis

For RL and LL, the mean value and standard deviation of RMS, AUC, MNF, and ROM were obtained for each participant. Then the limb symmetry index (LSI) was calculated for all parameters as the ratio of the non-DML by the DML. Therefore, $LSI < 1$ indicates higher values for DML. Then, the LSI was used to compare M vs. F. For each subject, the average of the EMG envelope was obtained during lunges from the moment the subject grounded with the leg that took the step until the ascent phase towards the initial position for each leg. A mean envelope was created for each muscle, in both lower limbs to determine the AP of the muscles.

2.5 Statistical Analysis

GraphPad Prism 8.0.2 was used for statistics and graphical representation of the results. A Shapiro-Wilk Test was performed to determine if the data had a normal distribution. If $p > 0.05$, the paired T or unpaired test was applied accordingly. On the contrary, the Wilcoxon test was used instead. For both tests, a value of $p < 0.05$ was considered a statistical difference.

3 Results

The sample ($n = 70$) had a mean of 21 ± 2 years and a mean BMI of 23.7 ± 3.76 . No statistical differences were found between sexes in both age and BMI ($p > 0.05$).

3.1 EMG

First, M and F data were pooled and comparisons between RL and LL for RMS, AUC, and MNF (mean \pm SD) were obtained, as shown in Fig. 3A. The LSI for the same EMG parameters, comparing M vs. F, is shown in Fig. 3B. A significant difference was found in the RMS (mV) comparing both legs in VL (RL, 0.33 ± 0.07 , LL, 0.30 ± 0.02 , $p < 0.001$), VM (RL, 0.33 ± 0.09 , LL, 0.29 ± 0.03 , $p < 0.001$), ST (RL, 0.31 ± 0.07 , LL, 0.28 ± 0.02 , $p = 0.006$) and BF (RL, 0.31 ± 0.06 , LL, 0.29 ± 0.03 , $p < 0.001$). Similarly, in the AUC, statistical differences between legs were found in VL (RL, 773.9 ± 237 , LL, 679 ± 197 , $p < 0.001$), VM (RL, 770.6 ± 269.5 , LL, 667.8 ± 194.5 , $p < 0.001$), ST (RL, 694.2 ± 215.6 , LL, 632.3 ± 195.3 , $p = 0.006$) and BF (RL, 732.7 ± 215.5 , LL, 646.4 ± 190.4 , $p < 0.001$). For the MNF (Hz), significant differences were found in the VL (RL, 89.45 ± 11.74 , LL, 85.19 ± 13.23 , $p = 0.010$); but not in VM (RL, 85.72 ± 9.18 , LL, 86.53 ± 9.09 , $p = 0.412$), ST (RL, 103.4 ± 18.9 , LL, 101.6 ± 16.06 , $p = 0.403$) and BF (RL, 96.19 ± 16.38 , LL, 92.99 ± 15.41 , $p = 0.113$). In summary, differences were found in RMS and AUC in all muscles evaluated, resulting in greater

muscle activation in the RL, considering that 65 subjects reported right dominance. This implies that in the DML, there is a greater coactivation of the QM-HM, compared with the non-DML, as described Ruas CV et al. [2]. By contrast, in MNF, there was only a statistical difference in VL. A higher mean value was also reported for HM compared to QM, as HM requires a higher frequency of contraction to achieve stability in the leg during movement [10].

In addition, VL showed a significant difference in all EMG parameters, possibly because the muscle is not only involved in knee stability but also in hip stability. Thus, during an exercise such as the lunge, the VL works to achieve knee flexion and control the internal rotation of the hip, maintaining functional stability of the limb, as Rojas-Quinchavil G et al. mentioned [11]. By having the VL a double function during the test, this muscle is more sensitive to present a difference in its AP and the moment of muscle fatigue of each subject [12].

Between M and F, the LSI was obtained for RMS, and statistical differences were found in BF (M, 0.96 ± 0.20 , F, 0.88 ± 0.17 , $p = 0.027$), but no for the rest of the muscles: VL (M, 0.89 ± 0.24 , F, 0.87 ± 0.15 , $p = 0.157$), and VM (M, 0.82 ± 0.22 , F, 0.85 ± 0.21 , $p = 0.114$) and ST (M, 0.97 ± 0.20 , F, 0.93 ± 0.19 , $p = 0.881$). In contrast, no statistical differences were found in the LSI of the AUC in VL (M, 0.91 ± 0.30 , F, 0.81 ± 0.23 , $p = 0.355$), VM (M, 0.82 ± 0.27 , F, 0.80 ± 0.25 , $p = 0.7815$), ST (M, 0.99 ± 0.23 , F, 0.92 ± 0.33 , $p = 0.155$) and BF (M, 0.95 ± 0.28 , F, 0.84 ± 0.29 , $p = 0.111$). Similarly, no statistical differences were found in the LSI for the MNF: VL (M, 0.96 ± 0.14 , F, 0.97 ± 0.20 , $p = 0.866$), VM (M, 1.01 ± 0.14 , F, 1.03 ± 0.11 , $p = 0.406$), ST (M, 0.97 ± 0.15 , F, 1.02 ± 0.18 , $p = 0.561$) and BF (M, 0.98 ± 0.16 , W, 0.98 ± 0.15 , $p = 0.989$). According to the previous results, there was only a significant difference in the RMS data for one muscle from the HM group (BF) in males compared to females. This may be related to different altered neuromuscular control strategies and movement patterns of both sexes [13]. For example, Dwyer MK et al. [14], M and F also performed a lunge as a functional test and found a significant difference for the RMS in the gluteus maximus.

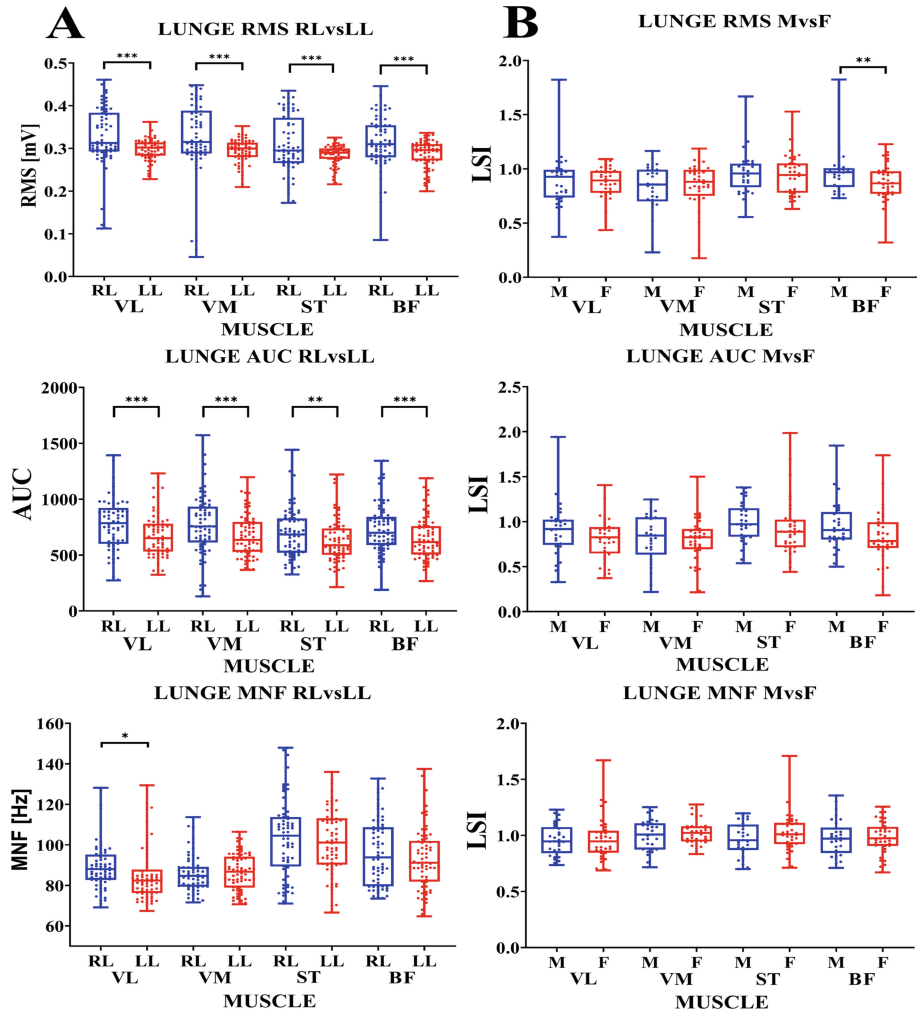


Fig. 3. A. RMS, AUC and MNF comparing RL vs. LL ($n = 65$, 29 M, 36 F). B. M vs. F LSI for RMS, AUC and MNF (* $p < 0.05$, ** $p < 0.01$, *** $p < 0.001$).

Then, a profile of EMG AP during lunge execution is plotted in Fig. 4. This AP is divided into four stages; the first stage shows when the subject grounds; the second stage includes the subject descent (first plateau); the third stage represents the maximum knee flexion and the instant in which the subject gets up (second plateau); the incorporation to the initial position is contained in the fourth stage.

Higher amplitude is shown in QM AP (VL and VM, red and blue lines, respectively), which matches the RMS values. On the other hand, HM exhibited lower amplitude, coinciding with the AUC obtained for both muscle groups, and coincides with the results of MNF, saying that QM is activated to a greater extent during lunges.

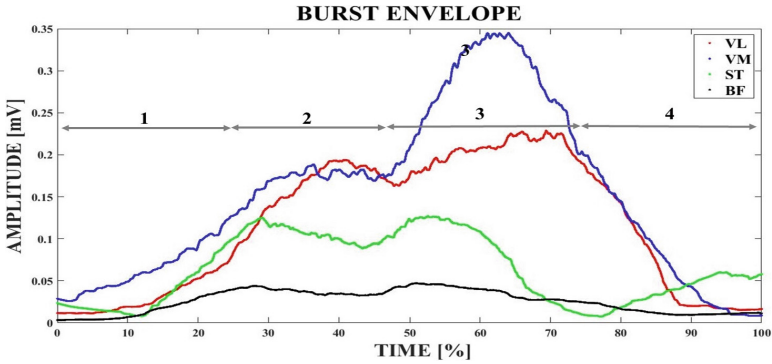


Fig. 4. Mean EMG envelope of the AP for VL, VM, ST and BF ($n = 65$). The mean EMG envelope for all the subjects and both legs was calculated, then it was pooled to represent the AP during a lunge. **1.** Ground contact. **2.** Descent time. **3.** Maximum flexion and push up. **4.** Rise to initial position.

3.2 Kinematics

Kinematics analysis revealed no statistical differences in the ROM for the maximum flexion comparing RL vs. LL (RL, 96.43 ± 9.71 , LL, 97.75 ± 9.16 , $p = 0.5759$). And for ROM LSI (M, 1.01 ± 0.14 , F, 1.01 ± 0.09 , $p = 0.9669$). Statistical data and the trajectory of the maximum and minimum flexion during lunges are shown in Fig. 5A, B respectively.

Knee flexion does not differ significantly between legs and sex. In general, no limitation was identified to execute this test. Similarly, Dwyer MK et al. [14], lunges were used as a functional test to evaluate the knee performance, authors did not find significant differences in control subjects comparing M vs. F.

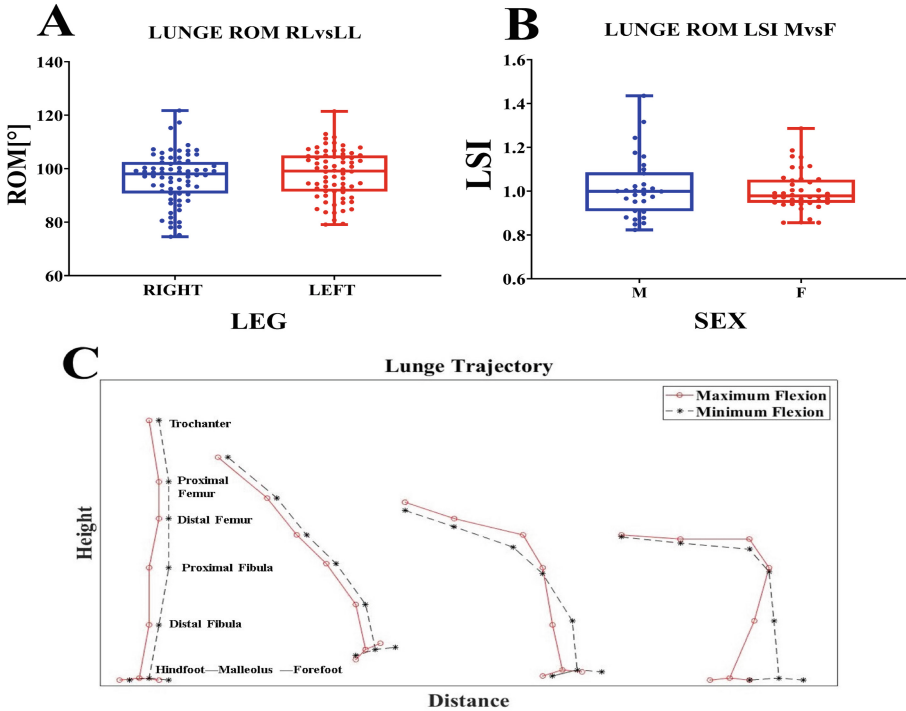


Fig. 5. A. ROM for RL vs. LL, and **B.** M vs. F. ($n = 65$, 30 M, 40 F). **C.** Kinematics trajectory of the RL during lunge execution of two subjects with maximum and minimum flexion (red and black lines respectively). Height and distance were normalized for comparison

4 Conclusion

In this study, the EMG and kinematics activity of the knee joint during lunges were characterized. We observed that for EMG parameters such as RMS, and AUC, a significant difference comparing RL vs. LL in all muscles was found. On the other hand, for MNF, it was statistically different only in VL. RL showed a greater AP, which could be related to the dominance reported in the subjects of this study. VL showed a significant difference in all EMG parameters during lunges, as it is involved in functional control of the hip and knee. Other functional tests in control subjects could determine if the EMG parameters of this muscle are also different when comparing RL vs. LL. For example, Ribeiro G et al. [15], single leg squat was applied in healthy subjects; however, they found no statistical difference in the AP.

For RMS, M showed greater symmetry in both legs in HM, BF being the only one with a significant difference. In contrast, F reported an LSI closer to 1 for the QM. Future experiments could compare EMG parameters of subjects whom suffered a KLI vs. control subjects of the same sex, due to there is a disparity between M and F in some motor control mechanisms that affect the AP in the QM-HM [13].

The EMG envelope of each muscle shown in Fig. 4, reveals the AP of both QM-HM, characterized by two plateaus during lunge execution, in which QM increase in amplitude to a greater extent than the HM.

Based on the kinematics results, where there was no significant difference for the ROM in RL vs. LL and M vs. F. This means that the subjects did not have a limitation flexing with RL or LL and that there was no significant asymmetry in both legs between sexes. These results could suggest that evaluating a subject with a KLI could show a ROM limitation in the injured leg by performing a unilateral functional test such as a lunge. Alkjær T et al. [16] found a significant reduction in the maximum flexion achieved by subjects with ACL injury and controls during lunges.

Our data could contribute to the generation of a database that allows quantitative evaluation from EMG and kinematics in healthy non-trained subjects compared to people who suffered a KLI.








References

1. Zlotnicki, J.P., Naendrup, J.H., Ferrer, G.A., Debski, R.E.: Basic biomechanic principles of knee instability. *Curr. Rev. Musculoskelet. Med.* **9**(2), 114–122 (2016)
2. Ruas, C.V., Pinto, R.S., Haff, G.G., Lima, C.D., Pinto, M.D., Brown, L.E.: Alternative methods of determining hamstrings-to-quadriceps ratios: a comprehensive review. *Sports Med – Open.* **5**(1), 11 (2019)
3. Olivares-Jabalera, J., Fílder-Ruger, A., Dos’ Santos, T., Afonso, J., Della Villa, F., Morente-Sánchez, J., et al.: Exercise-based training strategies to reduce the incidence or mitigate the risk factors of anterior cruciate ligament injury in adult football (soccer) players: a systematic review. *Int. J. Environ. Res. Public Health* **18**(24), 13351 (2021)
4. Ruiz-Pérez, I., López-Valenciano, A., Jiménez-Loaisa, A., Elvira, J.L.L., De Ste, C.M., Ayala, F.: Injury incidence, characteristics and burden among female sub-elite futsal players: a prospective study with three-year follow-up. *PeerJ* **5**(7), e7989 (2019)
5. Coombs, R., Garbutt, G.: Developments in the use of the hamstring/ quadriceps ratio for the assessment of muscle balance. *J. Sports Sci. Med.* **1**, 56–62 (2002)
6. Di Paolo, S., Lopomo, N.F., Della Villa, F., Paolini, G., Figari, G., Bragonzoni, L., et al.: Rehabilitation and return to sport assessment after anterior cruciate ligament injury: quantifying joint kinematics during complex high-speed tasks through wearable sensors. *Sensors* **21**(7), 2331 (2021)
7. Alkjær, T., Simonsen, E.B., Peter Magnusson, S., Aagaard, H., Dyhre-Poulsen, P.: Differences in the movement pattern of a forward lunge in two types of anterior cruciate ligament deficient patients: copers and non-copers. *Clin. Biomech.* **17**(8), 586–593 (2002)
8. Pincivero, D.M., Aldworth, C., Dickerson, T., Petry, C., Shultz, T.: Quadriceps-hamstring EMG activity during functional, closed kinetic chain exercise to fatigue. *Eur. J. Appl. Physiol.* **81**(6), 504–509 (2000)
9. Nagano, Y., Ida, H., Akai, M., Fukubayashi, T.: Effects of jump and balance training on knee kinematics and electromyography of female basketball athletes during a single limb drop landing: pre-post intervention study. *Sports Med. Arthrosc. Rehabil. Ther. Technol.* **3**(1), 14 (2011)

10. Phinyomark, A., Thongpanja, S., Hu, H., Phukpattaranont, P., Limsakul, C.: The usefulness of mean and median frequencies in electromyography analysis. In: Naik, G.R., (ed.) *Computational Intelligence in Electromyography Analysis – A Perspective on Current Applications and Future Challenges* [Internet]. InTech; 2012 [cited 2023 Jun 10]. Available from: <http://www.intechopen.com/books/computational-intelligence-in-electromyography-analysis-a-perspective-on-current-applications-and-future-challenges/the-usefulness-of-mean-and-median-frequencies-in-electromyography-analysis>
11. Rojas-Quinchavil, G., Venegas-Jeldrez, P., Valencia, O., Guzmán-Venegas, R., Araneda, F., Integramédica, C.: Hip and thigh muscular activity in professional soccer players during an isometric squat with and without controlled hip contraction *Actividad muscular de cadera y muslo en jugadores de fútbol profesionales durante una sentadilla isométrica con y sin contracción controlada de cadera*. *Fed Esp Asoc Docentes Educ Física FEADef* **39**, 697–704 (2021)
12. Babadi, N., Roostayi, M.M., Rahimi, A., Baghban, A.A., Sarmadi, A., Roostaei, H.: The effect of different hip rotation angles on electromyography activity of the quadriceps muscle during closed kinetic chain tasks in healthy females. *J. Phys. Ther. Sci.* **30**(8), 1112–1116 (2018)
13. Malinzak, R.A., Colby, S.M., Kirkendall, D.T., Yu, B., Garrett, W.E.: A comparison of knee joint motion patterns between men and women in selected athletic tasks. *Clin. Biomech.* **16**(5), 438–445 (2001)
14. Dwyer, M.K., Boudreau, S.N., Mattacola, C.G., Uhl, T.L., Lattermann, C.: Comparison of lower extremity kinematics and hip muscle activation during rehabilitation tasks between sexes. *J. Athl. Train.* **45**(2), 181–190 (2010)
15. Ribeiro, G., Dionísio, V.C., Almeida, G.L.: Electromyographic activity during one-legged squatting under different foot positions. *Rev Bras Med Esporte.* **13** (2007)
16. Alkjær, T., Smale, K.B., Flaxman, T.E., Marker, I.F., Simonsen, E.B., Benoit Daniel, L., et al.: Forward lunge before and after anterior cruciate ligament reconstruction: faster movement but unchanged knee joint biomechanics. Williams, J.L. (ed.) *PLOS ONE* **15**(1), e0228071 (2020)



Kinematic and Electromyography Analysis of the Knee Function in Non-trained Healthy Subjects Through a Single-Leg Drop Landing Test

Arantza Ituarte¹ , Felix León¹ , Juan Carlos Vera¹ , Isamar Duarte¹ ,
Leonel González² , and Carlos Cuellar³  

¹ Facultad de Ciencias de La Salud, Universidad Anáhuac México, 052786 Huixquilucan, Estado de México, Mexico

² Facultad de Medicina, Universidad Autónoma del Estado de México, 050120 Toluca, Estado de México, Mexico

³ Escuela de Ciencias del Deporte, Universidad Anáhuac México, 052786 Huixquilucan, Estado de México, Mexico

carlos.cuellarra@anahuac.mx

Abstract. Knee joint performance in elite and amateur athletes has been studied; however, scarce information has been reported on non-trained subjects. The single-leg drop landing is used to assess knee biomechanics. A method used to assess knee function is 3D motion capture and superficial electromyography (sEMG). The aim of this study was to analyze kinematics and EMG in lower limbs in healthy, non-trained individuals when performing the single-leg drop landing test. Seventy subjects (30 M, 40 F) were recruited. sEMG was recorded bilaterally in the Vastus Medialis, Vastus Lateralis, Rectus Femoris, and Semitendinosus. Root Mean Square, Area Under the Curve, and Mean Frequency were calculated for both legs. Seventeen reflective markers were placed bilaterally in the lower limbs to assess knee kinematics. Range of motion and angular velocity were determined. A statistical difference between males and females was found in the RMS in the Vastus Medialis ($p = 0.019$). The rest of the sEMG and kinematics parameters evaluated had no statistical differences between the right and left leg and sexes. sEMG and kinematics parameters on healthy populations could be useful to create baseline values to predict knee injuries and compare them with knee-injured populations in future studies.

Keywords: Single-leg drop landing · knee joint · biomechanics · kinematics · electromyography

1 Introduction

The single-leg drop landing (SLDL) is a training drill and a functional test that is often used to measure knee function [1]. The SLDL has shown good reliability in healthy subjects [2], and it is a reliable test to evaluate sex differences in knee biomechanics [3],

interlimb asymmetries post knee ligament reconstruction [4], fatigue-related changes in shock attenuation [5] and knee differences between dominant and nondominant leg [6]. Kinematics and superficial electromyography (sEMG) have been used to measure landing stability [7, 8] and the pattern of muscle activation [9, 10], respectively. To date, the majority of studies have been conducted in the athletic population [2–4, 6, 9, 11, 13, 14]. Data on healthy, non-trained individuals may help to create baseline values useful in future studies. The present study aimed to analyze kinematics and sEMG when performing the SLDL test in non-trained healthy participants.

2 Materials and Methods

Subjects

Seventy healthy subjects (M 30, F 40) between 18–27 years old, with no history of trauma or musculoskeletal injuries were recruited. The Body Mass Index (BMI) was calculated from height and weight. Informed consent was obtained prior to participation. The protocol was approved by the Research and Ethics Committees of the Universidad Anáhuac México (ID 202303).

Procedure

For sEMG recordings, an 8-channel wireless electrode system (FreeEMG, BTS Engineering) was used. Bipolar electrodes were placed bilaterally on the following muscles: Vastus Lateralis (VL) and Vastus Medialis (VM), Biceps Femoris (BF), and Semitendinosus (ST) (Fig. 1). Recordings were acquired at a sampling frequency of 1 kHz and filtered in a range of 20–450 Hz. sEMG parameters analyzed were: Area Under the Curve (AUC), Root Mean Square (RMS), and Mean Frequency (MFr). For kinematics, the SmartDx (BTS Engineering) camera system with six infrared light cameras was used at a sampling frequency of 250 Hz in a working volume of $4 \times 2 \times 2.5$ m. Seventeen reflective markers were placed on the following anatomical landmarks: base of the fifth metatarsal, posterior part of the calcaneus, lateral malleolus, distal fibula, proximal fibula, lateral femoral condyle, proximal femur, greater trochanter, and sacrum (at S2 level) (Fig. 1). The kinematic parameters considered for the analysis were the range of motion (ROM) and angular velocity (AV).

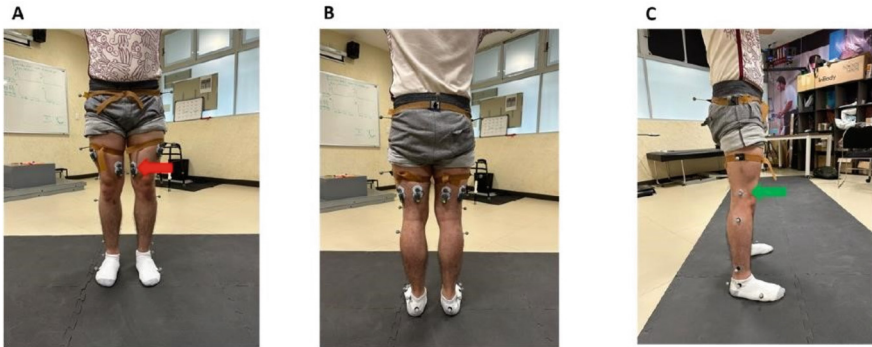


Fig. 1. Placement of sEMG electrodes and reflective markers in a front view (A), Back view (B), and Side view (C). The red and green arrows show sEMG wireless electrodes and reflective markers, respectively.

Single-Leg Drop Landing

First, a 5-min warm-up was carried out by the participant as indicated by a physical therapist. The test was performed in three series of three repetitions, starting with the right lower limb (RLL) followed by the left lower limb (LLL). On a raised platform (30 cm high, 60 cm base, and 40 cm deep), standing on both feet while barefoot, the participant was asked to go down a step. At the moment of landing, the participant was instructed to land strictly on one foot, maintain the balance for 2 s and then lower the contralateral foot to return to bipedal support (Fig. 2).

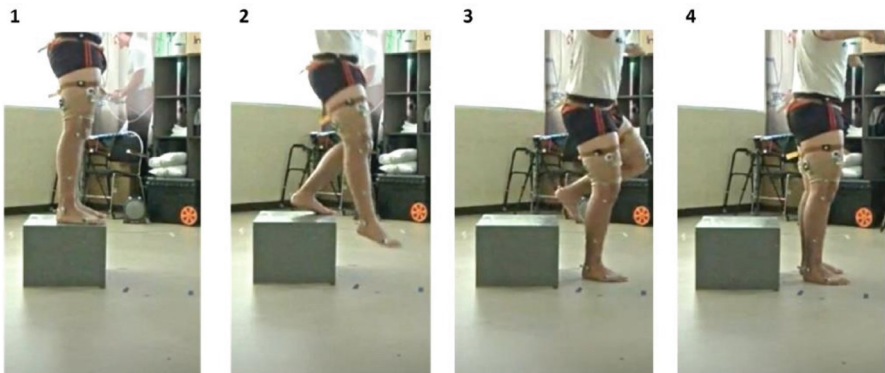


Fig. 2. SLDL sequence. 1. Initial position. The participant with both feet on the box. 2. Drop phase. Participant drops from the box using one foot. 3. Landing phase. Participant lands using one foot and maintains the position for two to three seconds. 4. Final phase. After three seconds the participant lowers the contralateral foot to the ground.

Data Analysis

MATLAB 2020b was used to calculate RMS, AUC, and MFr. The sEMG signal for each muscle and subject was normalized to the amplitude, and for each parameter, the mean value (\pm SD) was obtained. Data from all subjects were pooled (M and F) to compare RLL vs. LLL. BTS Bioengineering software was used for kinematics acquisition and analysis. The analysis of the ROM of each subject was determined as follows: the angular trajectory of two vectors was represented in a graph (one from the proximal femur to the distal femur, the other from the distal fibula to the proximal fibula). The mean value of the maximum flexion reached by each leg during the three repetitions of the SLDL was obtained from the angular trajectory. The resulting ROM of all subjects was pooled to compare RLL vs. LLL. Then, data were pooled for M and F to calculate the limb symmetry index (LSI) for all sEMG and kinematic parameters, as the ratio of the values of the non-dominant leg (NDL) by the dominant leg (DL). If $LSI < 1$, the DL parameter predominates over the NDL.

For statistical analysis, GraphPad 8.0.2 was used. The Shapiro-Wilk test was performed to determine if data were normally distributed. If $p > 0.05$, paired or unpaired T-test was applied accordingly. If data were not normally distributed, the Wilcoxon Test was used instead. For comparisons, $p < 0.05$ was considered.

3 Results

Mean height and weight of the sample was 1.65 ± 0.08 m, and 64.15 ± 12.96 kg, respectively. No statistical differences were found between males and females. The BMI was 23.37 ± 3.37 .

3.1 sEMG

sEMG results are shown in Table 1. No significant differences were found in the RMS, AUC, and MFr when comparing RLL vs. LLL in the pooled data. On the other hand, a significant difference was found in the RMS between males and females in the VM muscle (M 0.92 ± 0.17 ; F 1.02 ± 0.19 , $p = 0.019$). No significant differences between males and females were observed in AUC and MFr in the rest of the muscles evaluated (Table 2). In this context, a recent systematic review showed that men and women athletes have similar activation patterns during jump landing tasks with only the VL showing differences between sexes at post-contact [11], while Xu et al., showed that only the ST displayed a different activation pattern while performing the single leg drop jump [12]. A systematic review and meta-analysis assessed muscle activation patterns between males and females during pre- and post-contact phases of jump-landing task. The subjects performed regular exercises. It was found that men had an earlier VL activation compared to women in the post-contact phase [11]. On the other hand, in men, it was found that quadriceps muscles are active earlier than women's in the pre-contact phase of the jump landings [9]. In a sample of recreational active males, data extracted from sEMGs showed that during the landing phase, VL and VM contributed significantly to muscle force and muscle power [13]. Although no comparisons between males and females was done in the latter study, the modeling based on sEMG could be

used in future studies to extract additional parameters rather than RMS, AUC and MFr. Finally, we found a significant difference in the RMS in males compared to females during the whole jump-landing test. In future studies we could analyze specific phase parameters to extract additional information when comparing sex differences.

Table 1. sEMG parameters in all subjects, comparing the RLL vs. LLL. (n = 65, M 29, F 36).

sEMG Parameters						
	RMS (μV)		AUC ($\mu\text{V}\cdot\text{s}$)		MFr (Hz)	
	Mean	SD	Mean	SD	Mean	SD
RVL	0.25	0.04	516.3	223.1	88.95	17.48
LVL	0.25	0.04	517.9	229.2	90.50	16.35
<i>p value</i>	0.588		0.760		0.337	
RVM	0.24	0.05	500.2	228.1	84.79	14.37
LVM	0.24	0.05	489.4	215.5	85.41	13.3
<i>p value</i>	0.278		0.625		0.775	
RST	0.22	0.04	427.70	197.10	98.25	19.89
LST	0.24	0.04	450.50	176.70	101.90	20.94
<i>p value</i>	0.082		0.254		0.188	
RBF	0.23	0.04	461.6	220.5	98.46	19.65
LBF	0.23	0.04	435.3	163.9	96.56	15.88
<i>p value</i>	0.312		0.346		0.096	

Abbreviations: RMS = Root Mean Square, AUC = Area Under the Curve, MFr = Mean Frequency, SD = Standard Deviation, RVL = Right Vastus Lateralis, LVL = Left Vastus Lateralis, RVM = Right Vastus Medialis, RVL = Right Vastus Medialis, RST = Right Semitendinosus, LST = Left Semitendinosus, RBF = Right Biceps Femoris, LBF = Left Biceps Femoris.

3.2 Kinematics

A representative example of the lower limb trajectory during the SLDL showing maximum and minimum knee flexion in two subjects is presented in Fig. 3. For the pooled data (n = 70), no statistical differences were found when comparing ROM of the RLL ($62.45 \pm 11.84^\circ$) vs. the LLL ($62.70 \pm 13.48^\circ$), or when comparing the LSI of ROM in males and females (M 1.0 ± 0.24 , F 0.98 ± 0.14). Similarly, no statistical differences were found for the mean AV of the RLL ($31.01 \pm 11.27^\circ/\text{s}$) vs. the LLL ($31.27 \pm 11.35^\circ/\text{s}$). The mean LSI of AV for the whole sample was 1.00 ± 0.19 . No statistical differences were found between males and females (M 1.04 ± 0.23 , F 0.97 ± 0.14) in the same LSI parameter.

Table 2. LSI for the sEMG parameters compared by sex (n = 65, M 29; F 36).

sEMG Parameters						
	LSI RMS		LSI AUC		LSI MFr	
	Mean	SD	Mean	SD	Mean	SD
MVL	1.01	0.21	1.03	0.35	1.01	0.22
FVL	1.00	0.15	1.04	0.35	1.01	0.18
<i>p value</i>	0.949		0.942		0.965	
MVM	0.92	0.17	0.94	0.32	1.04	0.20
FVM	1.02	0.19	1.04	0.38	1.01	0.20
<i>p value</i>	0.019		0.221		0.471	
MST	1.066	0.24	1.00	0.38	1.07	0.24
FST	1	0.22	0.98	0.34	1.01	0.21
<i>p value</i>	0.079		0.818		0.264	
MBF	0.99	0.23	0.92	0.29	1.02	0.22
FBF	1.00	0.18	0.98	0.33	0.97	0.14
<i>p value</i>	0.416		0.413		0.927	

Abbreviations: RMS = Root Mean Square, AUC = Area Under the Curve, MFr = Mean Frequency, SD = Standard Deviation, RVL = Right Vastus Lateralis, LVL = Left Vastus Lateralis, RVM = Right Vastus Medialis, RVL = Right Vastus Medialis, RST = Right Semitendinosus, LST = Left Semitendinosus, RBF = Right Biceps Femoris, LBF = Left Biceps Femoris.

Landing maneuvers demand a correct muscle synergy between agonist and antagonist muscles to adequately distribute kinetic energy to the lower limb when executing functional tests [13]. Kajiwara et al. carried out a similar study that evaluated knee biomechanics during a single-leg drop jump while performing a cognitive task on 20 competitive-level athletes who suffered an anterior cruciate ligament rupture [14]. In the kinematics results, the authors reported that the maximum knee flexion angle degree was $40.2^\circ \pm 5.4$. In comparison, our study assessed 70 healthy non-injured subjects, and as stated previously, the maximum knee flexion angle degree was $62.45^\circ \pm 11.84^\circ$ for the right lower extremity and $62.70^\circ \pm 13.48^\circ$ for the left lower extremity. Differences between untrained and trained subjects and anthropometric characteristics may explain this difference. In this context, additional studies in larger samples are warranted. Moreover, the SLDL requires a certain degree of complexity involving an individual's physical activity and proper mental planning; therefore, considering non-physical factors such as kinesiophobia [15] could add information about motor performance during challenging movement tasks.

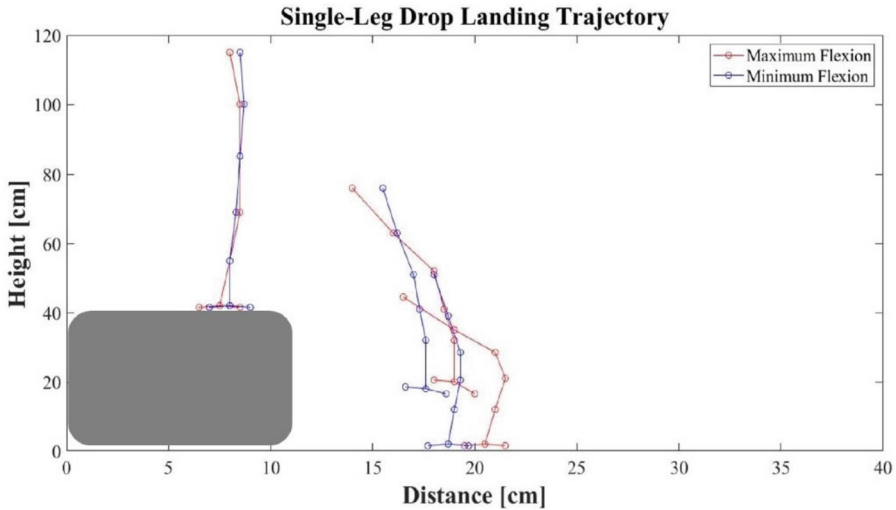


Fig. 3. Lower limb representative trajectories during the SLDL test in two participants. The red line represents a participant that displayed maximum flexion during landing. The blue line represents a participant that displayed minimum flexion during landing. The jumping platform is represented by the gray square.

4 Conclusion

In the present study, a statistical difference was just observed in the VM between males and females in the RMS. The rest of the sEMG and kinematic parameters were not statistically different when comparisons between lower limbs or sexes were made. Scarce information combining sEMG and kinematics during different knee functional tests in non-trained subjects has been published [5, 7, 8, 10, 12]. A healthy population with no history of trauma or musculoskeletal injuries, with normal BMI, was selected with the purpose of establishing normative values for future assessments. The data provided could be useful when comparing healthy and injured populations.





References

1. Dufek, J.S., Bates, B.T.: The evaluation and prediction of impact forces during landings. *Med. Sci. Sports Exerc.* **22**(3), 370–377 (1990)
2. Byrne, A., Lodge, C., Wallace, J.: Test-retest reliability of single-leg time to stabilization following a drop-landing task in healthy individuals. *J. Sport Rehabil.* [Internet]. [cited 2023 Jun 5]; 30(8), 1242–1245 (2021) May 23 <https://journals.humankinetics.com/view/journals/jsr/30/8/article-p1242.xml>
3. Romanchuk, N.J., Del Bel, M.J., Benoit, D.L.: Sex-specific landing biomechanics and energy absorption during unanticipated single-leg drop-jumps in adolescents: implications for knee injury mechanics. *J. Biomech.* **2**(113), 110064 (2020)
4. Vorensky, M., Peredo, D., Colón, W., Rao, S., Kakar, R.S.: Asymmetries in two-dimensional trunk and knee kinematics during a single-leg drop landing post anterior cruciate ligament

- reconstruction. *Int. J. Athl. Ther. Train* [Internet]. [cited 2023 Jun 23]; 1(aop), 1–9 (2023) Jan 17 <https://journals.humankinetics.com/view/journals/ijatt/aop/article-10.1123-ijatt.2021-0108/article-10.1123-ijatt.2021-0108.xml>
5. Tamura, A., Akasaka, K., Otsudo, T., Sawada, Y., Okubo, Y., Shiozawa, J., et al.: Fatigue alters landing shock attenuation during a single-leg vertical drop jump. *Orthop. J. Sports Med.* **4** (2016)
 6. Nakahira, Y., Taketomi, S., Kawaguchi, K., Mizutani, Y., Hasegawa, M., Ito, C., et al.: Kinematic differences between the dominant and nondominant legs during a single-leg drop vertical jump in female soccer players. *Am. J. Sports Med.* **50**(10), 2817–2823 (2022)
 7. Fukaya, T., Mutsuzaki, H., Wadano, Y.: Kinematic analysis of knee varus and rotation movements at the initial stance phase with severe osteoarthritis of the knee. *Knee* **22**(3), 213–216 (2015)
 8. Mannering, N., Young, T., Spelman, T., Choong, P.F.: Three-dimensional knee kinematic analysis during treadmill gait. *Bone Jt Res* [Internet]. [cited 2023 Jun 23]; **6**(8), 514–521 (2017). <https://www.ncbi.nlm.nih.gov/pmc/articles/PMC5579312/>
 9. Ebben, W.P., Fauth, M.L., Petushek, E.J., Garceau, L.R., Hsu, B.E., Lutsch, B.N., et al.: Gender-based analysis of hamstring and quadriceps muscle activation during jump landings and cutting. *J. Strength Cond. Res.* **24**(2), 408–415 (2010)
 10. Nimphius, S., McBride, J.M., Rice, P.E., Goodman-Capps, C.L., Capps, C.R.: Comparison of quadriceps and hamstring muscle activity during an isometric squat between strength-matched men and women. *J. Sports Sci. Med.* **18**(1), 101–108 (2019)
 11. Seyedahmadi, M., Minoonejad, H., Karimizadeh Ardakani, M., Heidari, Z., Bayattork, M., Akbari, H.: What are gender differences in lower limb muscle activity during jump–landing tasks? A systematic review and meta-analysis. *BMC Sports Sci Med Rehabil* [Internet]. [cited 2023 Jun 13]; **14**(1), 77 (2022). <https://doi.org/10.1186/s13102-022-00469-3>
 12. Xu, X., Hu, G., Williams, G.K.R., Ma, F.: Gender comparisons and associations between lower limb muscle activation strategies and resultant knee biomechanics during single leg drop landings. *Biomechanics* [Internet]. [cited 2023 Jun 13]; **2**(4), 562–574 (2022). <https://www.mdpi.com/2673-7078/2/4/44>
 13. Maniar, N., Schache, A.G., Pizzolato, C., Opar, D.A.: Muscle function during single leg landing. *Sci. Rep.* **12**(1), 11486 (2022)
 14. Kajiwara, M., Kanamori, A., Kadone, H., Endo, Y., Kobayashi, Y., Hyodo, K., et al.: Knee biomechanics changes under dual task during single-leg drop landing. *J. Exp. Orthop.* [Internet]. [cited 2023 Jun 13]; **6**, 5 (2019). <https://www.ncbi.nlm.nih.gov/pmc/articles/PMC6367493/>
 15. de Vasconcelos, G.S., da Batista Silva, M.E.C., Nunes, G.S., Viadanna Serrão, F.: Relationship between kinesiophobia, isometric hip and knee torques to pelvic, hip and knee motion during the single-leg drop jump in women with patellofemoral pain: a cross-sectional study. *Knee* **42**, 264–272 (2023)



Analysis of Mechanical Behavior of Biomaterials of HA/Ti for Bone Tissue Regeneration Using Finite Element Method

María Fernanda Toledo Romo¹ (✉) , María Flores Sánchez² , Hipólito Aguilar Sierra² , and Erick Ramírez Aguilar¹ 

¹ Facultad de Ingeniería, Universidad La Salle México, 06140 Cuauhtémoc, Mexico City, Mexico

fer.toledoromo@gmail.com

² Vicerrectoría de Investigación, Universidad La Salle México, 06140 Cuauhtémoc, Mexico City, Mexico

Abstract. This work presents the numerical analysis by FEM of different types of biomaterials based on Hydroxyapatite and Hydroxyapatite-Titanium to estimate the values of maximum stresses in a tibial segment. The mechanical response with respect to an axial applied force of 750N on the tibial plateaus of the bone structure was analyzed. The 3D models were considered static systems. For the numerical analysis, the ANSYS tool was transmitted. The maximum stresses and total deformations in the biomaterials based on Hydroxyapatite and Hydroxyapatite-Titanium are within the range reported in the literature and confirm that the reconstruction of the 3D model used can be a good alternative in the regeneration of bone tissue. In addition, to consider reinforcing them with titanium plates, considerably increasing the stress capacity, which is important in the treatment of implants in long bones.

Keywords: Finite Element Analysis · Bone Tissue Engineering · Hydroxyapatite

1 Introduction

Bones are susceptible to damage from trauma, necrosis, tumors [1], and congenital diseases such as osteoporosis [2]. Loss of skeletal tissue can result in significant morbidity and, furthermore, is typically associated with significant socioeconomic cost [3]. The most viable treatment of a long bone defect is bone grafting, which involves removal of donor bone from a non-load-bearing patient site or filling with a biomaterial [4].

Tissue engineering is widely accepted as an effective way to treat these bone defects [5]. It is also defined as an interdisciplinary field in which engineering principles are applied to bone-related biochemical reactions. Scaffolds, cells, growth factors and their interrelationship in the microenvironment are major concerns in bone tissue engineering [6].

The success of materials for bone tissue engineering focuses on the proper selection of natural biomaterials or biomimetics, such as polymers, ceramics, metals, and composites. In addition, there are different manufacturing technologies such as three-dimensional printing and electrical field-assisted techniques such as electrospinning, which have been used to process these biomaterials for bone tissue engineering [7].

Hydroxyapatite (HA, $\text{Ca}_{10}(\text{PO}_4)_6(\text{OH})_2$) is the main component of bone tissue [8], representing 70% of bone weight, while type I collagen fibrils constitute 20% and water about 10% [9]. HA promotes the growth of bone cells and stimulates the formation of new bone cells [10]. Titanium (Ti), usually grade 5 Ti6Al4V, is commonly used for orthopedic implant applications due to its excellent corrosion resistance, biocompatibility, mechanical strength, and elastic modulus [11].

The HA/Ti combination promotes bone tissue regeneration because Ti acts as a structural support and HA contributes the cells to the bone. The finite element method (FEM) estimates the mechanical behavior of 3D models. It can improve the design process of orthopedic devices, the analysis of tissue growth or the biomechanical behavior of implants, making it very useful in tissue engineering. [12].

This work presents a numerical analysis by finite elements of the mechanical behavior of different hydroxyapatite and hydroxyapatite-titanium biomaterials, for which various forms and concentrations of this material obtained by different techniques were considered, and of which Young's Modulus are reported that they are within the feasible values for long bones such as the tibia or femur. Static structural analyzes of Hydroxyapatite and Hydroxyapatite-Titanium were carried out in 3D models of the tibial segment obtained from the tomographic study of a female patient in which an isotropic linear behavior of the materials was ensured.

2 Materials and Methods

2.1 Biomaterials

Mechanical behavior of composite biomaterials based on HA and HA-Ti was analyzed, since it has been considered one of the best materials to regenerate bone tissue, mainly long bones such as the tibia or femur.

Four HA samples with different grain shapes at different concentrations were used, from which the Young's Modulus and Poisson's Coefficient values were taken, because linear isotropic studies were considered. The first sample was bulk HA (S1) engineering [13], the second sample was HA in HA pellets subjected to nanoindentation experimental tests with a composition of 75/25 (S2) [13], the third sample was an HA composite biomaterial (18.1%) /PLA (Polylactic Acid) (S3), and the fourth sample was a biomaterial composed of HA (35.7%) /PLA (S4). The biomaterials S3 and S4 were obtained by electrospinning [14]. These biomaterials present a diameter distribution from 800 nm to 50 μm and a great diversity of pore sizes with ranges from 10 μm to 100 μm , allowing a favorable network for the case in which bone cells are used [14].

2.2 3D Model Reconstruction

Figure 1a and 1b show the reconstruction of the 3D model of the tibia of a female patient segmented with the Open Source 3D Slicer tool. The area replaced by the HA implant was the tibial shaft due lower extremity fusions experience a lever arm effect, which affects the central area of the tibia [15]. Two 3D models were worked on: the first with Hydroxyapatite and the second with Hydroxyapatite-Titanium. In the latter, CAD models of two plates and five screws designed in the SolidWorks® 2022 Educational Version Software provided by Universidad La Salle México were added. Dimensions of each of the two plates were $150\text{ mm} \times 20\text{ mm} \times 5\text{ mm}$ while for the five screws, they were $\phi 6\text{ mm} \times 40\text{ mm}$.

The cuts and the assembly of the bone structure with the two plates and the five screws were carried out on the Autodesk MeshMixer platform provided by La Salle Mexico University, to continue with the structural analyzes of the bone-implant assembly in the ANSYS Mechanical Software Version 14.5. (ANSYS Inc., Canons-burg, PA, USA) provided by the INR-LGII Biomechanics Laboratory, referring to the implant as each of the HA-based biomaterial samples mentioned in the previous point and analyzed by separate.

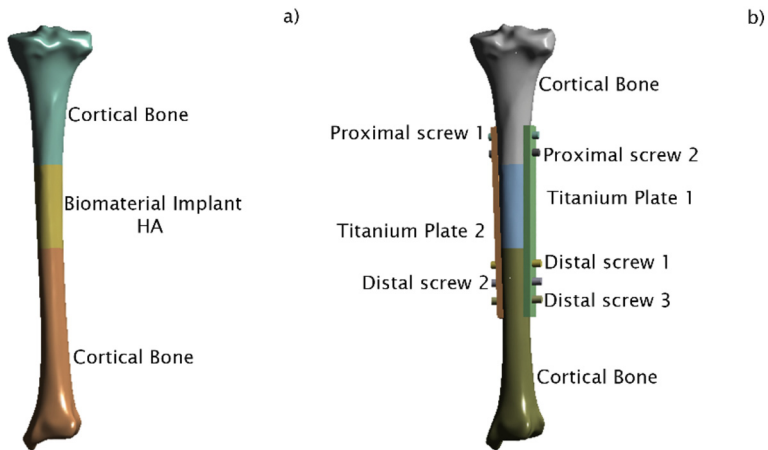


Fig. 1. Reconstruction of the 3D model of the tibia of a female patient a) Cortical bone with HA; b) Cortical bone with HA-Ti plate and screws.

2.3 Finite Element Method

For development of the numerical analysis, the mechanical properties corresponding to each of the pieces of the set were assigned, which determine the behavior of each of these biomaterials, as shown in Table 1. Bonded contact was used because the model was considered as a fixed block and this contact was applied at each of the model interfaces (Bone-HA and Bone-Ti), while size of the element used in the mesh was 1 mm as reported by [16].

Table 1. Mechanical properties applied in Finite Element Model.

Component	Young's Modulus (MPa)	Poisson's Coefficient
Cortical bone	13,000 [17]	0.3
Plates (Ti Grade 5)	114,000 [17]	0.3
Screw (Ti Grade 5)	114,000 [17]	0.3

In addition to the above components, four HA-based biomaterials were used, to which a Modulus of Elasticity value was assigned depending on the HA composition to identify the mechanical behavior of the system. These values are shown in Table 2.

Table 2. Young's Modulus values used (MPa)

Biomaterial Sample	HA compound	Young's Modulus (MPa)
S1	Bulk [13]	102610
S3	18.1% [14]	102.88
S4	35.7% [14]	17.849

For the boundary conditions of model, the inferior articular surface and the articular facet of the medial malleolus were kept fixed; A distributed axial load of 750 N was applied on the tibial plateaus in the -Z direction in all the models (Hydroxyapatite and Hydroxyapatite Titanium) because in the numerical simulation the half support phase of human gait is being represented and, at that instant, the weight of the body falls on one foot, in addition to the average body weight of a person of 75 kg. Results obtained by the finite element simulations show the values of the equivalent stresses and total deformations of the bone-implant set, considering a position of average support for human gait, a moment in which the weight of the body falls on a single lower extremity because the other extremity is not touching the ground at that moment.

A total of eight simulations were carried out: four of them were with only HA biomaterial to replace the diaphysis of the tibia, varying the values of the Modulus of Elasticity of the compound. To the four remaining simulations, two Titanium plates were added to provide support, one on each edge of the tibia (medial and interosseous), in addition to five fixing screws: two proximal and three distal, which were responsible for joining the two plates with the Hydroxyapatite implant. The Modulus of Elasticity values also varied for these four cases.

3 Discussion

3.1 Cortical Bone Model with HA Implant

In the simulations carried out with the HA implants in the diaphysis of the tibia, it can be observed that the maximum stress values increase, while the Modulus of Elasticity values decrease. This indicates a clear behavior of ductility in implants that depends mainly on their mechanical properties.

The minimum value of maximum stress was 25.076 MPa and it was presented in the bulk HA biomaterial (Fig. 2a), which indicates the presence of dislocations and vacancies, as mentioned by Obinna in 2023 [13]; The composition, HA concentration, morphology and, in the last two cases, the combination with PLA are important, because these characteristics cause different stresses in each of the materials. The highest value of maximum stress was of 35.908 MPa in the HA (35.7%)/PLA compound (Fig. 2d), as shown in Fig. 3.

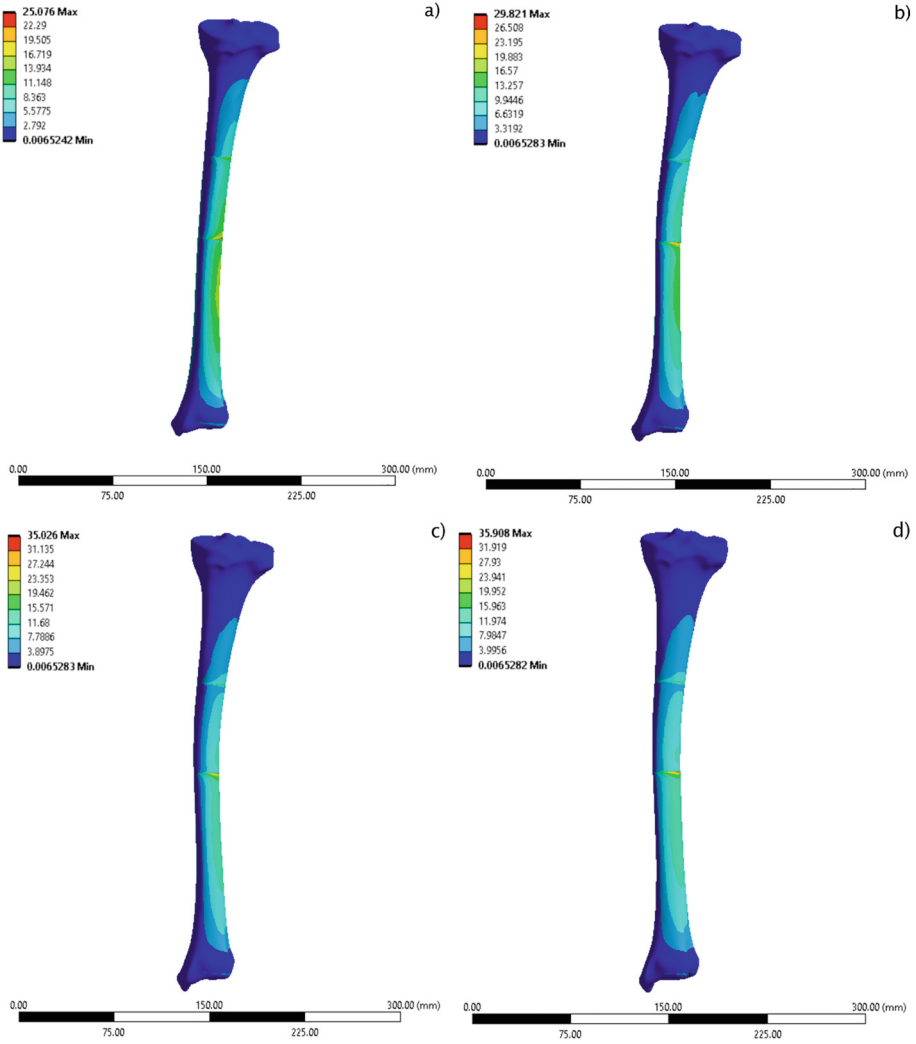


Fig. 2. Maximum stresses in tibia models with HA implant a) Bulk (S1) 25.076 MPa, b) Pellets HA (S2) 29.821 MPa, c) 18.1% HA/PLA (S3) 35.026 MPa, d) 35.7% HA/PLA (S4) 35.908 MPa.

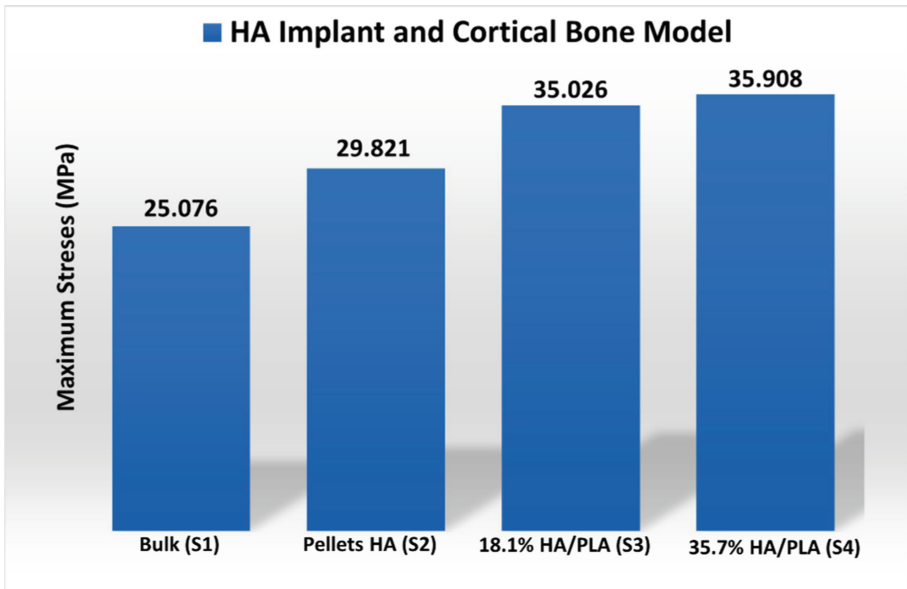


Fig. 3. Maximum stresses values that do not exceed the yield stress of cortical bone reported in the literature (78 to 151 MPa).

Figure 4 shows the values of the total deformations estimated through the simulations, in which deformations increase due to the ductility effect shown by the analyzed models. The lowest value of total deformation was 2.5671 and corresponds to bulk HA (Fig. 4a), demonstrating its main application as a dental coating due to its limited ability to deform [13], while the highest value of total deformation was 448.7 for HA(35.7%)/PLA 35.7% compound (Fig. 4d), which is mainly attributed to the fact that the latter is combined with Polylactic Acid that provides elasticity to the compound, for which it has given good results and continues to be one of the most widely combination used in tissue engineering in long bones (see Fig. 5).

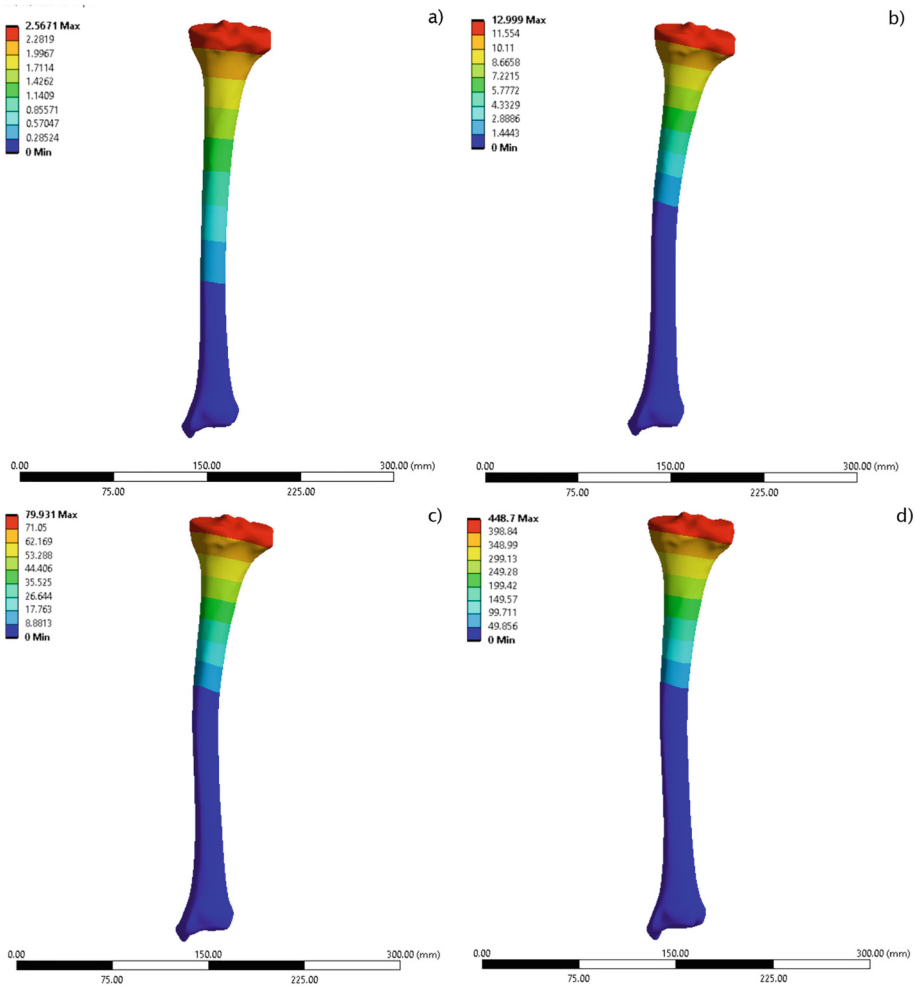


Fig. 4. Total deformations in tibia models with HA implant a) 2.5671, b) 12.999, c) 79.931, d) 448.7.

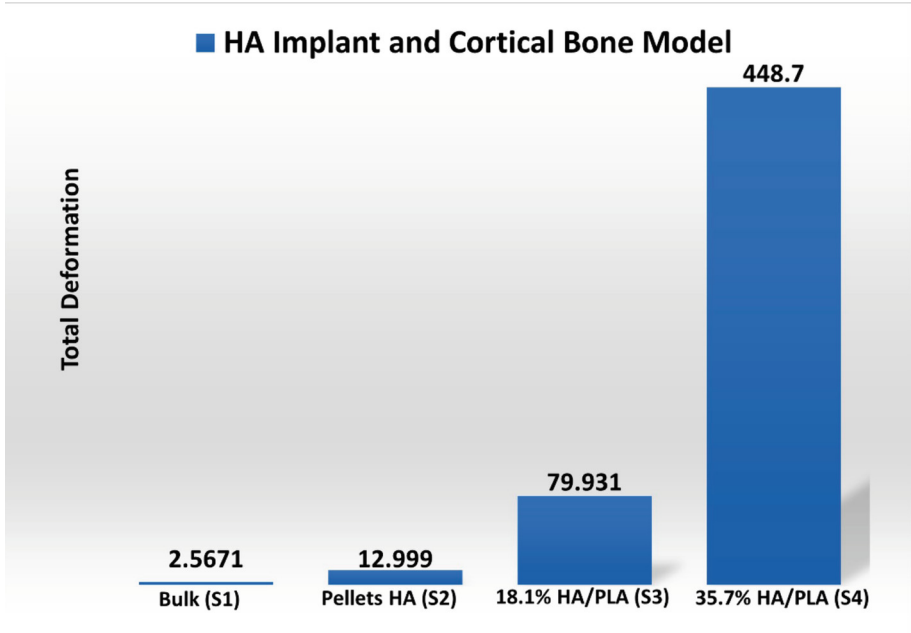


Fig. 5. Total deformations of S1, S2, S3 and S4; changes between these values are shown due to the morphology, composition, and concentration of these materials. Biomaterials S3 and S4 reach higher deformations due to the elasticity provided by PLA.

3.2 Cortical Bone Model with HA-Titanium Implant

In the models of bone-implant assembly (Fig. 6) using the Titanium plates, the maximum stress values increased significantly up to 77.8% compared to the models that only consist of cortical bone with HA implant. The maximum stress for the bulk HA with the titanium plate was 112.9 MPa (Fig. 7a), while the minimum value was 91.2 MPa for the HA (35.7%)/PLA composite (Fig. 7d).

These values show that the rigidity of Titanium is greater than that of cortical bone, therefore, the vertical force along the bone intensified, causing this stress distribution in the tibial diaphysis [18]. In both cases (Hydroxyapatite and Hydroxyapatite-Titanium), the stress values did not exceed the yield stress of cortical bone (78–151 MPa), nor of Titanium (950 MPa) [19, 20].

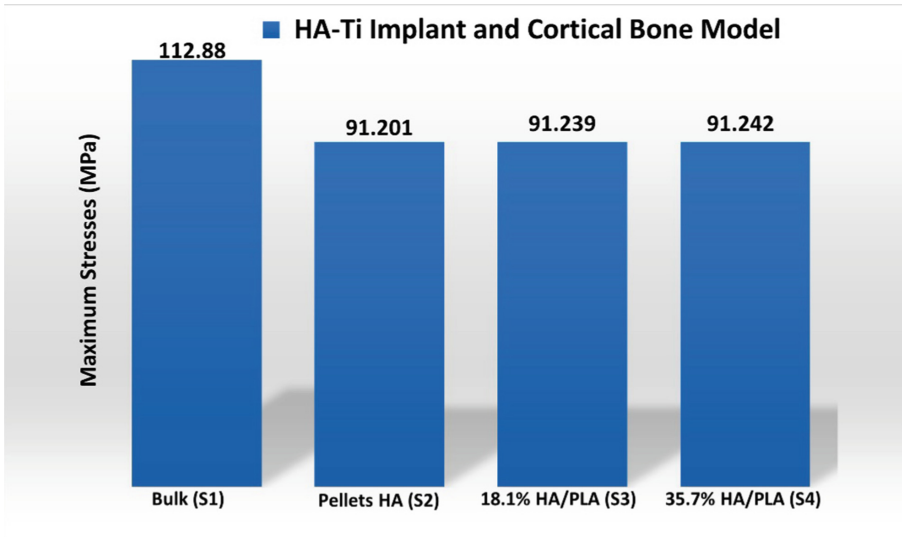


Fig. 6. Maximum stresses of the HA-Ti model that increased by 77.8% compared to the model of cortical bone and HA implant, attributed to the fact that Ti has a greater rigidity than that of cortical bone, in addition to promoting bone consolidation with the implant and function as structural support for the tibia.

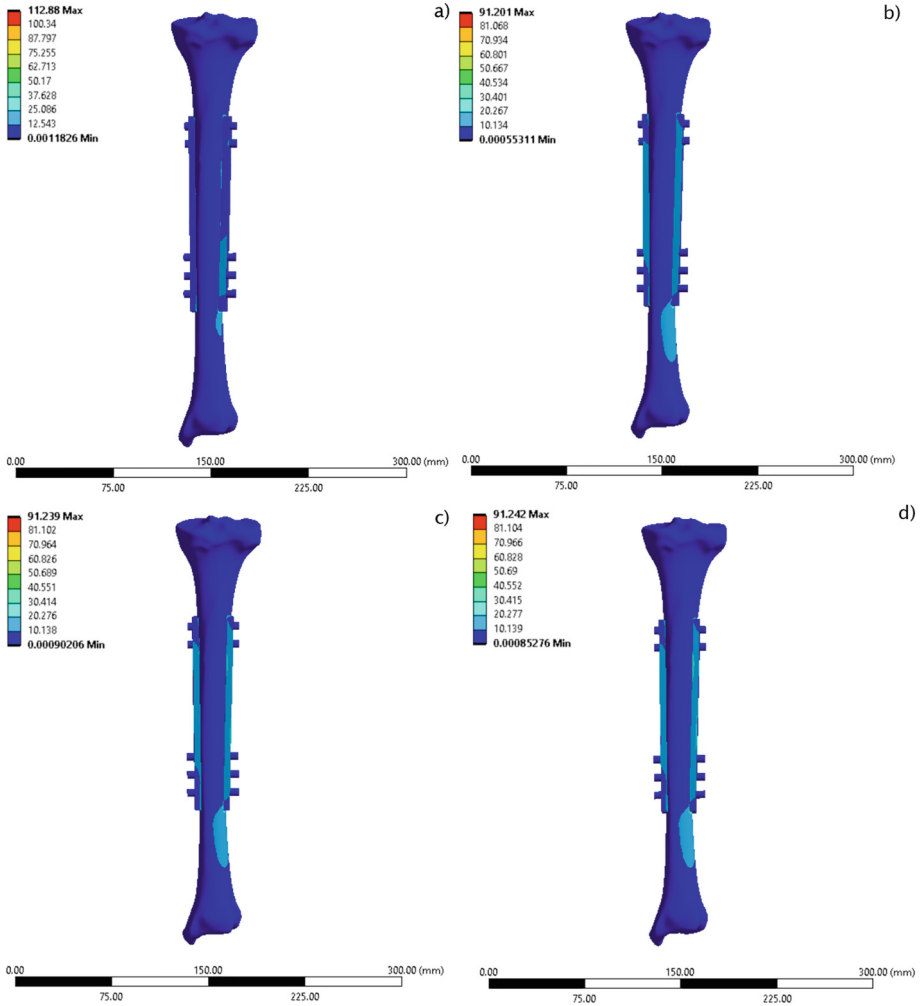


Fig. 7. Maximum stresses in tibia models with HA-Ti implant: a) Bulk (S1) 112.88 MPa, b) Pellets HA (S2) 91.201 MPa, c) 18.1% HA/PLA (S3) 91.339 MPa, d) 35.7% HA/PLA (S4) 91.242 MPa.

Figure 8 shows the total deformations that occurred in these four cases, the values are between 1.5505 and 1.6693 (Fig. 9), therefore, in comparison with the models that use only cortical bone and HA, the deformations decrease considerably up to 99.62%. This is attributed to the fact that the titanium implant that aids cortical bone consolidation with the HA implant also provides structural support to the bone.

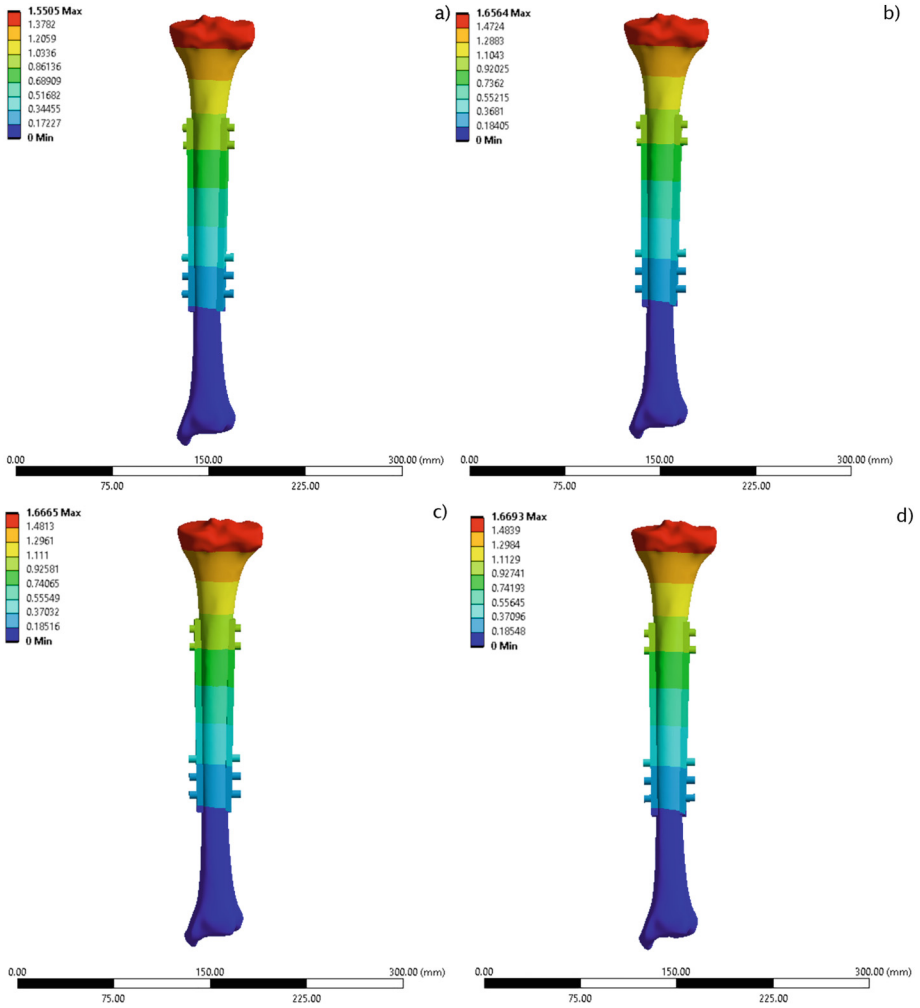


Fig. 8. Total deformations in tibia models with HA-Ti implant a) 2.5671, b) 12.999, c) 79.931, d) 448.7. The values of the deformations are similar due to the Titanium plate.

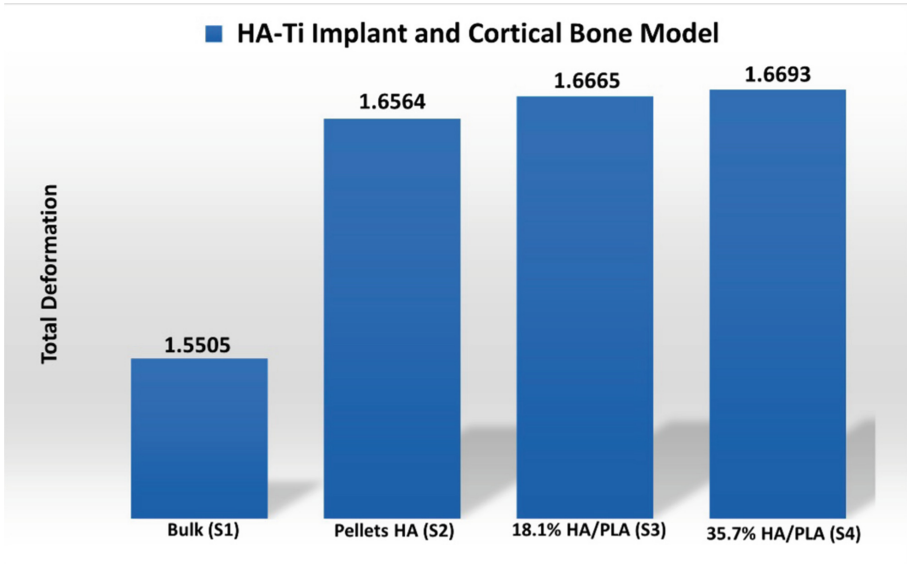


Fig. 9. Total deformations in tibia models with HA-Ti implant a) 1.5505, b) 1.6564, c) 1.6665, d) 1.6693.

4 Conclusions

This work presented the analysis of the mechanical behavior of different biomaterials based on HA which have the objective of replacing a bone defect in the region of the tibial diaphysis. To evaluate the behavior of the complete structure, two models were made, the first made up of HA-cortical bone and the second made up of HA-Ti cortical bone as support. The 3D reconstruction was carried out using design tools and they were evaluated using the Finite Element Method through the ANSYS software, for which Young's Modulus corresponding to each type of HA was used. The results of the models presented different Maximum Stresses: the best were for HA-cortical bone 18.1% HA/PLA (S3) 35.026 MPa, 35.7% HA/PLA (S4) 35.908 MPa; and, for HA-Ti-18.1% HA/PLA (S3) 91.339 MPa, 35.7% HA/PLA (S4) 91.242 MPa and different total deformations: 18.1% HA/PLA (S3) 79.931, 35.7% HA/PLA (S4) 448.7; HA-Ti-18.1% HA/PLA (S3) 1.6665, 35.7% HA/PLA (S4) 1.6693). Each biomaterial responds according to its morphology, composition, and concentration, which influences a certain distribution of vacancies, and, in turn, this influences the stress capacity and the maximum deformation that it can reach. In relation to the porosity of the biomaterials analyzed, it was determined that, due to the distribution of diameters from 800 nm to 50 μm and a pore size of 10 μm to 100 μm , a favorable environment is generated for bone cells to grow and consequently, the biomaterial increases its mechanical resistance.

In addition, it was obtained that the biomaterials containing PLA reached greater stresses compared to the others, which is attributed to the fact that the polymer confers elasticity to the compound and due to this, such a combination continues to be one of the best for regenerating cortical bone tissue, it is also important to mention the fact

that they are biomaterials made with electrospinning, a technique that also continues to give good results for manufacturing viable composite biomaterials for use in Tissue Engineering.

References

1. Turnball, G.: 3D bioactive composite scaffolds for bone tissue engineering. *Bioact. Mater.* **III**, 1 (2017)
2. Zhao, Li., et al.: Bionic design and 3D printing of porous titanium alloy scaffolds for bone tissue repair. *Compos. Part B: Eng.* **162**, 154–161 (2019). <https://doi.org/10.1016/j.compositesb.2018.10.094>
3. Kanczler, J.M., Wells, J.A., Gibbs, D.M.R., Marshall, K.M., Tang, D.K.O., Oreffo, R.O.C.: Chapter 50 - Bone tissue engineering and bone regeneration. In: Lanza, R., Langer, R., Vacanti, J.P., Atala, A. (ed.): *Principles of Tissue Engineering* 5th edn. pp. 917–935. Academic Press (2020) ISBN 9780128184226. <https://doi.org/10.1016/B978-0-12-818422-6.00052-6>
4. Niedhart, C., Pingsmann, A., Jurgens, C., Marr, A., Blatt, R., Niethard, F.U.: Complications after harvesting of autologous bone from the ventral and dorsal iliac crest – a prospective: controlled study. *Z. Orthop. Ihre Grenzgeb.* **141**(4), 481–486 (2003)
5. Bagde, A.D., Kuthe, A.M., Nagdeve, S.R., et al.: Geometric modeling and finite element simulation for architecture design of 3D printed bio-ceramic scaffold used in bone tissue engineering. *J. Indian Inst. Sci.* **99**, 361–374 (2019). <https://doi.org/10.1007/s41745-019-00120-0>
6. Chahal, S., Kumar, A., Hussian, F.S.J.: Development of biomimetic electrospun polymeric biomaterials for bone tissue engineering a review. *J. Biomater. Sci., Polym. Ed.* **30**(14), 1308–1355 (2019). <https://doi.org/10.1080/09205063.2019.1630699>
7. Koons, G.L., Diba, M., Mikos, A.G.: Materials design for bone-tissue engineering. *Nat. Rev. Mater.* **5**, 584–603 (2020). <https://doi.org/10.1038/s41578-020-0204-2>
8. Ribas, R.G., et al.: Current advances in bone tissue engineering concerning ceramic and bioglass scaffolds: a review. *Ceram. Int.* **45**(17), 21051–21061 (2019). <https://doi.org/10.1016/j.ceramint.2019.07.096>
9. Huang, M.-H., Shen, Y.-F., Hsu, T.-T., Huang, T.-H., Shie, M.-Y.: Physical characteristics, antimicrobial and odontogenesis potentials of calcium silicate cement containing hinokitiol. *Mater. Sci. Eng.: C* **65**, 1–8 (2016). <https://doi.org/10.1016/j.msec.2016.04.016>
10. Chen, Y.-W., Ho, C.-C., Huang, T.-H., Hsu, T.-T., Shie, M.-Y.: The ionic products from mineral trioxide aggregate–induced odontogenic differentiation of dental pulp cells via activation of the Wnt/ β -catenin signaling pathway. *J. Endodontics* **42**(7), 1062–1069 (2016). <https://doi.org/10.1016/j.joen.2016.04.019>
11. Ottria, L., Lauritano, D., Andreasi Bassi, M., et al.: Mechanical, chemical and biological aspects of titanium and titanium alloys in implant dentistry. *J. Biol. Regul. Homeost. Agents* **32**(2, suppl 1), 81–90 (2018)
12. Soufivand, A.A., Abolfathi, N., Hashemi, S.A., Lee, S.J.: Prediction of mechanical behavior of 3D bioprinted tissue-engineered scaffolds using finite element method (FEM) analysis. *Addit. Manufact.* **33**, 101181 (2020). <https://doi.org/10.1016/j.addma.2020.101181>
13. Osuchukwu, O.A., et al.: Datasets on the elastic and mechanical properties of hydroxyapatite: A first principle investigation, experiments, and pedagogical perspective. *Data Brief* **48**, 109075 (2023). <https://doi.org/10.1016/j.dib.2023.109075>. PMID: 37020900; PMCID: PMC10068552

14. Flores-Sánchez, M.G., et al.: Effect of a plasma synthesized polypyrrole coverage on poly-lactic acid/hydroxyapatite scaffolds for bone tissue engineering. *J. Biomed. Mater. Res. A* **109**(11), 2199–2211 (2021). <https://doi.org/10.1002/jbm.a.37205>. Epub 2021 Apr 26 PMID: 33904255
15. Abols, Y.: Biomecánica y fisiología articular subastragalina. *EMC - Podología* **11**(1), 1–5 (2009). [https://doi.org/10.1016/S1762-827X\(09\)70689-3](https://doi.org/10.1016/S1762-827X(09)70689-3)
16. Donahue, T.L., Hull, M.L., Rashid, M.M., Jacobs, C.R.: A finite element model of the human knee joint for the study of tibio-femoral contact. *J. Biomech. Eng.* **124**(3), 273–280 (2002). <https://doi.org/10.1115/1.1470171>. PMID: 12071261
17. Kim, W.H., et al.: Optimized dental implant fixture design for the desirable stress distribution in the surrounding bone region: a biomechanical analysis. *Materials (Basel)*. **12**(17), 2749 (2019). <https://doi.org/10.3390/ma12172749>. PMID:31461942;PMCID:PMC6747764
18. Simon, U., Augat, P., Ignatius, A., Claes, L.: Influence of the stiffness of bone defect implants on the mechanical conditions at the interface—a finite element analysis with contact. *J. Biomech.* **36**(8), 1079–1086 (2003). [https://doi.org/10.1016/s0021-9290\(03\)00114-3](https://doi.org/10.1016/s0021-9290(03)00114-3). PMID: 12831732
19. Kundu, J., Pati, F., Shim, J.-H., Cho, D.-W.: Rapid prototyping technology for bone regeneration. In: Narayan, R., (ed.) *Rapid Prototyping of Biomaterials*, pp. 254–284. Woodhead Publishing (2014) ISBN 9780857095992 <https://doi.org/10.1533/9780857097217.254>
20. Bruschi, S., Bertolini, R., Ghiotti, A.: Coupling machining and heat treatment to enhance the wear behaviour of an additive manufactured Ti6Al4V titanium alloy. *Tribol. Int.* **116**, 58–68 (2017). <https://doi.org/10.1016/j.triboint.2017.07.004>



Kinetic and Kinematic Analysis of Gait in a Patient with Transtibial Amputation: A Case Study

Karla Martínez¹ (✉) , Isabel C. Soto^{2,3} , and Elizabeth Pareja^{2,3}

¹ Instituto Tecnológico Metropolitano/Departamento de Ciencias Aplicadas, Medellín, Colombia

karlamartinez287011@correo.itm.edu.co

² Grupo de Investigación E Innovación Biomédica, Instituto Tecnológico metropolitano/Departamento de Ciencias Aplicadas, Medellín, Colombia

³ Laboratorio de Biomecánica E Ingeniería de Rehabilitación, Instituto Tecnológico Metropolitano/Departamento de Ciencias Aplicadas, Medellín, Colombia

Abstract. Transtibial amputation involves the loss of the ankle joint, distal tibia, and fibula, while preserving the knee joint. For this type of amputation, a prosthesis is required to replace the missing limb for the patient to continue their daily activities. However, some patients experience poor prosthetic adaptation, leading to gait abnormalities. A case study was conducted on a patient with left transtibial amputation to evaluate the kinetics and kinematics using baropodometry, accelerometry, and electromyography, aiming to identify potential anomalies experienced by the patient during short walking periods. Static baropodometry analysis indicated that the patient had a greater distribution of body weight on the forefoot, resulting in a forward body displacement and instability. The overall symmetry index was below normal values, indicating differences in gait between the left and right foot. Additionally, the muscle coactivation index was above normal values, indicating excessive muscle contraction and consequently poor muscle coordination.

Keywords: Transtibial amputation · Gait · Baropodometry · Electromyography · Accelerometry

1 Introduction

Transtibial amputation constitutes a significant impairment to the neural, muscular, and skeletal systems, involving the loss of the ankle, distal tibia, and fibula articulation while retaining the knee joint. Individuals with this type of amputation experience challenges in walking and increased energy consumption [1]. Patients with transtibial amputation require a prosthesis that enhances efficiency and gait pattern during both static and dynamic phases. This involves cushioning impacts from body weight and achieving proper prosthetic suspension in the swinging phase as well as stable support during the stance phase [2]. Achieving this involves assessing biomechanical variables such as baropodometry, accelerometry, and electromyography to understand how prosthetic

adaptation occurs in amputee patients. Consequently, there has been a growing focus on prosthetic alignment studies, particularly regarding the impact of socket alignment with the foot and the assessment of associated energy costs [2].

Among baropodometric variables, weight distribution assesses how weight is borne by the prosthetic device and the contralateral limb in an orthostatic position [3]. Additionally, the center of pressure trajectory is associated with postural stability and balance evaluation. On the other hand, ground reaction force (GRF) identifies the effects of misalignment in prosthetic gait, indicating that misalignments increase the load on the contralateral limb and likewise extend the support phase time, as well as causing differences in vertical GRF peaks [4, 5].

Accelerometry evaluation identifies propulsion indices, describing a subject's ability to push the center of mass forward during the single support phase [6]. The symmetry index represents the difference in percentage terms between support and swing phases of the healthy and amputated limbs [7]. The quality index characterizes a single limb, assessing the subject's ability to correctly time and balance their gait cycle between the healthy and amputated limbs [8]. Lastly, pelvic kinematics are assessed in different planes, providing information about inclination, obliquity, and rotation during the gait cycle. Ultimately, muscle coactivation informs about the overall compensatory strategy adopted by amputees in the intact limb, where high values indicate the need for amputees to increase simultaneous activation of multiple muscles for an extended duration. This may lead to compensatory increases in stiffness, force production, and support time [9].

Biomechanical assessments are crucial for prosthesis users as they provide quantitative information about prosthetic adaptation, aiming to improve patient function and prosthetic component effectiveness in terms of user safety and stability [2]. Therefore, the main objective of this study is to evaluate kinetic and kinematic signals of lower limbs using baropodometry, accelerometry, and electromyography during the walking motion in a patient with transtibial amputation.

2 Materials and Methods

A 66-year-old patient with left transtibial amputation was evaluated. The patient reported fatigue when attempting short walks with the prosthetic provided by their healthcare institution. The study took place at the Biomechanics and Rehabilitation Laboratory of the Metropolitan Technological Institute in Medellín, Colombia. The patient participated voluntarily after signing the appropriate informed consent, which was approved by the Ethics Committee of the Metropolitan Technological Institute and adhered to the principles outlined in the Helsinki Declaration (DoH), as recommended by the World Medical Association [10].

2.1 Baropodometry Analysis

The EcoWalk plantar pressure platform (Ecosanit, Arezzo, Italy) was utilized for the study. Data processing was conducted using the EcoFoot 4.0 software developed by the same company, which includes predefined protocols for defining specific characteristics

in both static and dynamic positions. This encompasses weight distribution, calculation of the center of gravity trajectory, and the ground reaction force vector.

For static position data acquisition, the patient stood on the platform, facing a fixed point, with relaxed arms and feet shoulder-width apart for 60 s (see Fig. 1). Subsequently, the patient was instructed to perform a short walk, alternating steps, to ensure recording of at least 4 steps for each foot during the dynamic assessment.



Fig. 1. Static evaluation on the plantar pressure platform.

2.2 Accelerometry and Surface Electromyography (EMG) Analysis

The G-walk inertial sensor (BTS Bioengineering, Milan, Italy) was used for Accelerometry Analysis. This sensor includes an accelerometer (frequency: 4–1.000 Hz), a gyroscope (frequency: 4–8.000 Hz), and a magnetometer. For signal processing, the G-Studio software version 3.2.25.0 developed by the same company was implemented.

This device facilitates the spatial and temporal evaluation of gait parameters, including quality index, propulsion, temporal parameters, and pelvic kinematics.

The inertial sensor was placed at the S1 and S2 vertebrae level, specifically below the line connecting the two dimples of Venus, to align it accurately with the patient's spine. Once the sensor was securely positioned, the patient received instructions to walk along a 6-m path, maintaining a natural pace. You were also asked to perform a wide turn and return to the starting point of the test. This sequence was repeated multiple times, with each repetition lasting no more than 1 min.

To analyze muscle activity using surface electromyography, the wireless electromyograph FREEEMG 1000 (BTS Bioengineering, Milan, Italy) was utilized. This device is equipped with 8 sensors and operates at a sampling frequency of 1000 Hz. For signal processing, the EMG-Analyzer software version 2.10.44.0, developed by the same company, was employed. The calculation of the coactivation index followed the methodologies outlined in previous studies [11, 12]. Electrodes were placed on the right tibialis

anterior, right medial gastrocnemius, right rectus femoris, right semitendinosus, left rectus femoris and left semitendinosus as shown in Fig. 2. After the sensor was stabilized, the patient then walked a 6-m path at a natural pace until reporting fatigue, marking the end of the test.

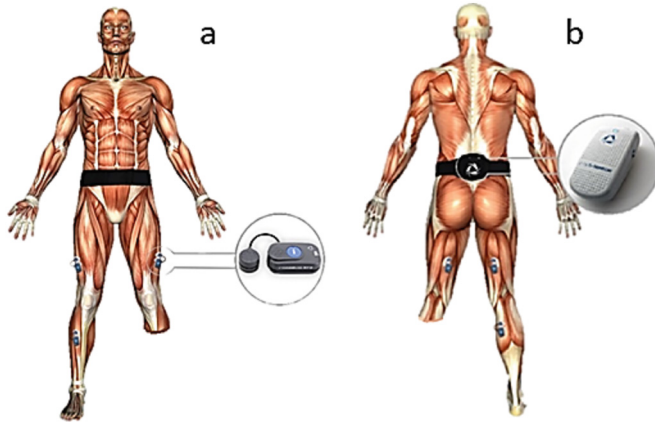


Fig. 2. Positioning of the inertial sensor and electromyography probes. a. Front view. b. Rear view.

3 Results and Discussion

3.1 Baropodometry Analysis

In the static baropodometry results, it's observed that the right foot bears 50.1% of the load, while the left foot carries 49.9%. Furthermore, the left foot has 38.1% of the load on the forefoot, whereas the right foot records 31.3%, totaling 69.4% on the forefoot. These values suggest that the metatarsals bear the majority of the patient's weight, leading to a forward displacement of the center of pressure, causing instability, fatigue, and wear in this area [13].

In the posterior zone, a total load of 30.5% is presented, with an uneven distribution between the feet.

The left foot bears 11.8% of the load, whereas the right foot reaches 18.8%. This discrepancy indicates that the patient doesn't fully support the heel of the prosthetic foot, and there is a force compensation in the right foot's heel (see Fig. 3). It's crucial that the body weight is evenly distributed, with 50% of the load on both lower limbs, as well as anteroposteriorly, to avoid potential discomfort or long-term injuries [6].

In the dynamic analysis, for the left foot, the ground reaction force (GRF) exerted is low (68.9 kPa), representing less than 20% of the total weight. In the rearfoot, there's a percentage of 5.49%, midfoot 2.94%, and forefoot 6.47%. These percentages add up to a total of 14.9% of the total weight, indicating that the patient exerts very little force with their left foot, possibly due to the lack of confidence they feel with the prosthesis.

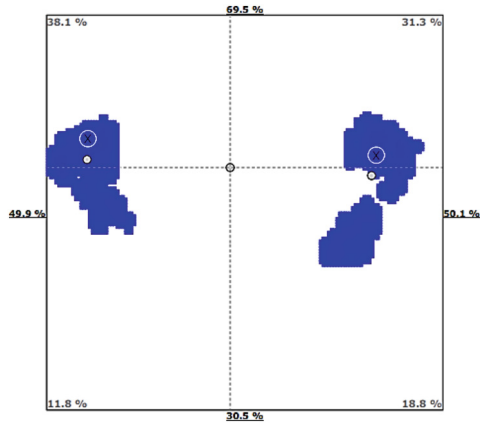


Fig. 3. Distribution of Body Loads

On the other hand, the right foot records a higher force percentage (253.6 kPa). Specifically, there's 15.29% in the rearfoot, 9.80% in the midfoot, and 24.31% in the forefoot, adding up to a total of 48.88% of the total weight. Although all these percentages are below normal values, the right foot shows a higher force percentage compared to the left foot and a longer time in the support phase, which is consistent with findings reported in other studies [5] (see Fig. 4).

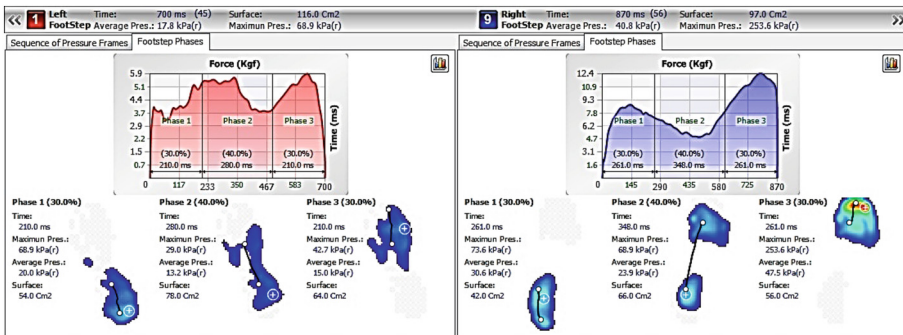


Fig. 4. Ground Reaction Force Vector Graph

3.2 Analysis of Accelerometry and Surface Electromyography

The global symmetry index is 1.7%, indicating that the gait cycle in both feet is not symmetric, as the value is below the normal range [8]. Furthermore, the gait cycle quality index is 88.5% in the right limb and 85.5% in the left limb, indicating that the subject lacks symmetry in accelerating the center of mass similarly during the walking cycle in the right and left feet. The closer the index is to 100, the more symmetrical the gait pattern is [7] (see Table 1).

Table 1. Symmetry gait index.

SIMMETRY GAIT INDEX		Normal Values
Global Symmetry Index	GSI (%) = 1.7	75<GSI<100
Gait Cycle Quality Index	Right Side (%): 88.5	90-100
	Left Side (%): 85.5	

The propulsion index presents a normal value when it's > 5.5 . In the case of this study, the values are slightly higher than the normal range, indicating that the patient has good propulsion, but might not possess all the necessary strength to execute it in the most correct and comfortable manner (see Fig. 5).

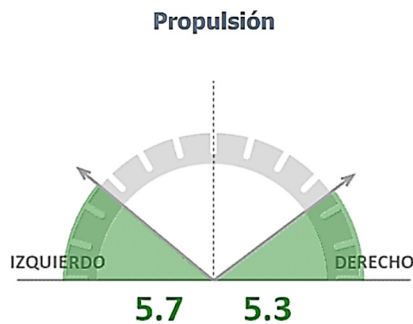
**Fig. 5.** Propulsion

Figure 6 illustrates pelvic kinematics in all three anatomical planes. The graphs feature two continuous lines representing the right side (green) and the left side (red). The gray lines correspond to the normal range. On the right side of the figure, the symmetry index is generated for each evaluated angle, along with maximum and minimum values for each foot, and the range between these values [14].

The inclination displays a symmetry index of 73.7%, indicating alignment issues with the pelvis and a tendency towards positive values, signifying anterior pelvic movement. This relates to maximum metatarsal support and confirms the patient's forward-leaning body posture. In pelvis obliquity, there's a symmetry of 33.5%, with an opposing angular pattern in each limb. The right pelvis remains higher than the left, potentially indicating poor prosthetic adaptation due to gait pattern asymmetry. Finally, in pelvic rotation, a symmetry index of 62.3% is observed, indicating neutral movement (see Fig. 6). Changes in pelvic kinematics might arise from relative compensations due to different prosthetic components. Inclination can be influenced by stability in re-establishing the center of gravity, and obliquity might be influenced by prosthetic adjustments like prosthesis length and suspension system [15].

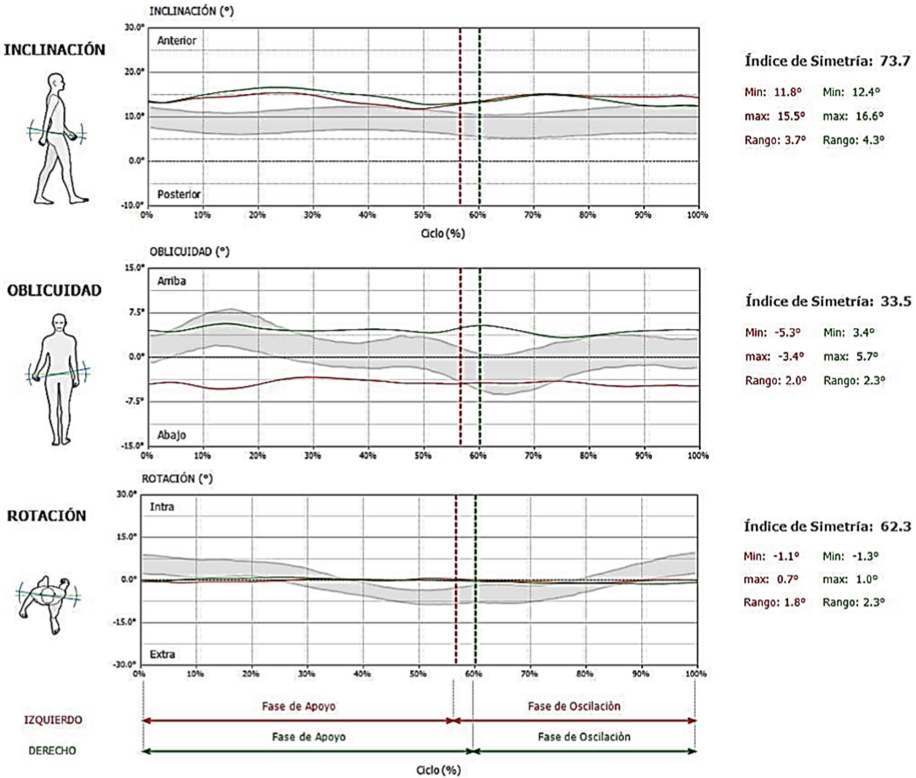


Fig. 6. Pelvic Kinematics

The results of muscular activity can be observed in Fig. 7. The gray band indicates the phase during which each muscle should be activated, and the absence of a band signifies the resting phase of muscular contraction. For the right foot, muscles display activation throughout most of the gait cycle, without clear relaxation during the appropriate phase. This finding is consistent with studies indicating that the intact limb increases simultaneous activation for a longer duration to compensate for stiffness, force production, and support time in the healthy limb [16]. The rectus femoris and semitendinosus muscles show peaks of electrical activity closer to normal values; however, the voltage values obtained are low, suggesting that these muscles might not be generating sufficient force to adequately contribute to the gait cycle. On the other hand, in the left lower limb, the semitendinosus muscle’s activation is not consistent but shows relatively low voltage values, indicating insufficient force generation for a proper gait cycle with the amputated limb. However, the rectus femoris displays better activation and less silence, indicating that this muscle tends to experience faster fatigue, given that it bears the weight of the prosthesis. Consequently, the foot support might be lighter.

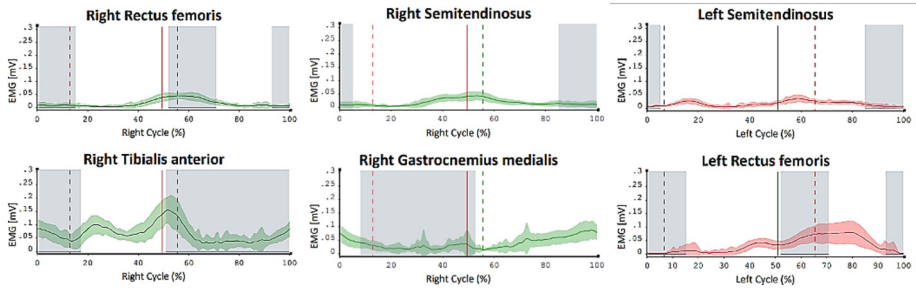


Fig. 7. Muscle Activation Timing

The coactivation index reflects the postural stability of the patient [17]. According to the data reported in Table 2, the coactivation values are higher than normal, indicating that the patient has balance issues during gait.

Table 2. Muscle Coactivation Index.

	Rigth	Left	Normal Values
Stance Phase (%)	64	49.7	< 30
Swing Phase (%)	53.6	79.7	< 50

4 Conclusions

The results of this study revealed altered biomechanical behaviors in both joint and muscular aspects in a patient with transtibial amputation, underscoring the importance of such assessments for proper prosthetic adaptation. The absence of these considerations can lead to muscular fatigue, instability, and gait difficulties, significantly impacting the patient's quality of life. It's important to note that this study was conducted with a single patient, thus further evaluation with a larger amputee population is crucial to obtain comparative results. Moreover, the devices used for measurements necessitate trained personnel to ensure their proper utilization. Despite limitations, this study provides vital insights in biomedicine and rehabilitation, highlighting overlooked health-care research that ensures proper patient prosthetic adaptation and quality of life. These findings advance understanding and stress the need for broader future approaches.


References

1. Sarroca, N., Valero, J., Deus, J., Casanova, J., Luesma, M.J., Lahoz, M.: Quality of life, body image and self-esteem in patients with unilateral transtibial amputations. *Sci. Rep.* **11**(1), 12559 (2021). <https://doi.org/10.1038/s41598-021-91954-1>

2. Chui, K.K., Milagros, J., Sheng-Che, Y., Lusardi, M.M.: *Orthotics and Prosthetics in Rehabilitation*. 4th ed. (2020)
3. da Fontes, C.H.S., et al.: Bodyweight distribution between limbs, muscle strength, and proprioception in traumatic transtibial amputees: a cross-sectional study. *Clinics* **76**, e2486 (2021). <https://doi.org/10.6061/clinics/2021/e2486>
4. Kobayashi, T., et al.: Ground reaction forces during double limb stances while walking in individuals with unilateral transfemoral amputation. *Front. Bioeng. Biotechnol.* **10** (2023) <https://doi.org/10.3389/fbioe.2022.1041060>
5. Cárdenas, A.M., Uribe, J., Font-Llagunes, J.M., Hernández, A.M., Plata, J.A.: The effect of prosthetic alignment on the stump temperature and ground reaction forces during gait in transfemoral amputees. *Gait Posture* **95**, 76–83 (2022). <https://doi.org/10.1016/j.gaitpost.2022.04.003>
6. Bernardini, M., Quarto, G., Del Sole, D., Bernardini, E.: Influences of postural alterations on the hemodynamic of the gait in patients with saphenous incompetence a preliminary study. *Ann. Ital. Chir.* **90**, 545–550 (2019)
7. Winiarski, S., Rutkowska-Kucharska, A., Kowal, M.: Symmetry function – an effective tool for evaluating the gait symmetry of trans-femoral amputees. *Gait Posture* **90**, 9–15 (2021). <https://doi.org/10.1016/j.gaitpost.2021.07.021>
8. BTS Bioengineering. WALK Evaluación de La Coordinación Muscular Durante La Marcha (2020)
9. Tatarelli, A., et al.: Global muscle coactivation of the sound limb in gait of people with transfemoral and transtibial amputation. *Sensors* **20**(9), 2543 (2020). <https://doi.org/10.3390/s20092543>
10. The World Medical Association. Declaración de Helsinki. Investigación médica en seres humanos Mar 21 (2017)
11. Boudarham, J., Hameau, S., Zory, R., Hardy, A., Bensmail, D., Roche, N.: Coactivation of lower limb muscles during gait in patients with multiple sclerosis. *PLoS ONE* **11**(6), e0158267 (2016). <https://doi.org/10.1371/journal.pone.0158267>
12. Chow, J.W., Yablon, S.A., Stokic, D.S.: Coactivation of ankle muscles during stance phase of gait in patients with lower limb hypertonia after acquired brain injury. *Clin. Neurophysiol.* **123**(8), 1599–1605 (2012). <https://doi.org/10.1016/j.clinph.2012.01.006>
13. Contreras, L.A.L., Ramírez, M.Á.G., G.S.P.: Distribución de presión plantar en pacientes con amputación transtibial unilateral (2018)
14. Izzo, R., Bertoni, M., Cejudo, A., Giovannelli, M., VardeI, C.H.: The global symmetry index, symmetry index, quality index and kinematics of the gait cycle with the synchronized contribution of the latest generation magneticinertial and electromyographic technology. Practical surveys and planning hypotheses for the revision of gesture. *J. Phys. Educ. Sport* **22**(5), 1258–1270 (2022)
15. Valle, M.S., et al.: Use of a single wearable sensor to evaluate the effects of gait and pelvis asymmetries on the components of the timed up and go test, in persons with unilateral lower limb amputation. *Sensors* **22**(1), 95 (2021). <https://doi.org/10.3390/s22010095>
16. Varrecchia, T., et al.: Common and specific gait patterns in people with varying anatomical levels of lower limb amputation and different prosthetic components. *Hum. Mov. Sci.* **66**, 9–21 (2019). <https://doi.org/10.1016/j.humov.2019.03.008>
17. Olaya Mira, N., Soto Cardona, I.C., Martínez Osorno, L.V., Mercado Díaz, D.R., Henao Ceballos, L.M.: Evaluating the effect of a water exercise routine on the postural stability of the elderly. *Colomb Med.* **52**(3), e2014537 (2021). <https://doi.org/10.25100/cm.v52i3.4537>



Ocular Biomechanics of Glaucoma

Yael Osmar Bravo Sustaita, Ximena Berenice Guzmán González,
and A. Vidal-Lesso^(✉) 

Universidad de Guanajuato División de Ingeniería Campus Irapuato Salamanca, Carretera
Salamanca-Valle de Santiago Km 3.5+1.8 Comunidad de Palo Blanco, 36885 Salamanca,
Guanajuato, México
agustin.vidal@ugto.mx

Abstract. In this study, deformations, and principal stresses in ocular tissues, especially in the optic disc, under glaucoma conditions were investigated. Four models with different parameters were developed, and their results were compared. Although the models did not yield quantitatively similar results, critical areas in the tissues were found. In these result values, the possibility of the presence of glaucoma exists, contributing to the early detection of this disease. Deformation in ocular tissues and an increase in principal stresses in the optic disc under glaucoma conditions were demonstrated. This indicates that optic nerve cells lose their mechanical properties due to the presence of stress concentrators, affecting cellular nutrition and potentially leading to cell death over time. Despite the quantitative differences, the models shared critical areas due to the geometry of the eye. These findings expand the understanding of the effects of glaucoma on ocular tissues.

Keywords: glaucoma · optic nerve · deformation

1 Introduction

Glaucoma is recognized as a common condition that can cause vision loss and progressive blindness. It is estimated that approximately 45 million people worldwide suffer from glaucoma [1]. Understanding the deformations of the human eye in glaucoma and identifying the critical areas of principal stresses within its tissues, especially in the optic nerve, which is profoundly affected by this disease. It is crucial for advancing the knowledge in this field. In this project, finite element methods were employed to investigate these deformations and stress patterns. By utilizing finite element analysis, it becomes possible to conduct a comprehensive quantitative assessment of the intricate biomechanical conditions surrounding the optic nerve head (ONH). This analysis takes into account crucial factors, including the complex three-dimensional geometry of the eye, the specific biomechanical properties of ocular tissues, and the boundary and loading conditions [2].

Glaucoma is an eye disease that progresses over time, leading to a gradual decline in vision. It is known for its subtle symptoms, often going unnoticed, and the possibility of sudden and significant vision loss [3]. The primary underlying factor is the instability of

aqueous humor drainage through the trabecular meshwork, located in the anterior chamber of the eye, leading to increased intraocular pressure and the gradual degeneration of the retina [1]. The retina is composed of ganglion cells and a nerve layer [5], with a particular emphasis on the axons as they transmit processed signals from the retina to the optic nerve, as mentioned by Xie [1].

In glaucoma, deformation of the optic cup, also known as the optic disc, occurs in multiple directions, resulting in tearing and excavation of the tissue. This excavation hinders the transmission of signals from the retina to the brain, further contributing to vision impairment [6].

Glaucoma encompasses two main classifications: open-angle glaucoma and closed-angle glaucoma. Open-angle glaucoma, also known as primary or chronic glaucoma, develops gradually as the eye's drainage channels become increasingly obstructed over time. This obstruction prevents proper fluid outflow from the eye, resulting in elevated intraocular pressure [4]. On the other hand, closed-angle glaucoma occurs due to the blockage of aqueous humor flow [3].

Regarding research related to the biomechanical analysis of the eye, Sigal [7] conducted a systematic analysis where finite element modeling was employed to investigate how the biomechanical environment within the optic nerve head (ONH) influences the loss of retinal ganglion cells in glaucoma. Twenty-one factors were evaluated, including biomechanical properties of ocular tissues, intraocular pressure (IOP), and geometric factors. The five most influential factors in ONH biomechanical responses were scleral stiffness, eye radius, lamina cribrosa stiffness, IOP, and scleral shell thickness. Variations in scleral properties had a greater impact on stresses and deformations in the ONH than direct IOP effects, suggesting individual scleral properties could be glaucoma risk factors.

Another study was conducted by Grytz [8]. The objective was to characterize material properties of posterior and peripapillary sclera from human donors and investigate strains as control mechanisms for mechanical stability. Posterior scleral shells from donors aged 57–90 were subjected to IOP elevations (5–45 mmHg), measuring displacements using laser speckle interferometry. Eye-specific finite element models were generated based on measured geometry and thickness. Inverse numerical analyses identified material parameters using a microstructure-based formulation incorporating crimp response and anisotropic architecture of scleral collagen fibrils. Adaptation of material properties produced models fitting overall and local deformations of posterior scleral shells. Nonlinear scleral stiffening with increasing IOP was linked to collagen fibril uncrimping, predicting an aligned fibril ring around the scleral canal.

The study proposed in this work encompassed two main scenarios: the eye under normal pressures and the eye affected by glaucoma. By comparing these scenarios, our goal was to discern the distinctive characteristics associated with glaucomatous conditions. To facilitate this analysis, we developed four different models, each representing a specific set of parameters.

Using these models, we aim to unravel both the differences and similarities in the obtained results. By exploring variations in stress distribution and deformation patterns among the models, our objective is to gain insights into the biomechanical mechanisms underlying glaucoma progression.

2 Methodology

To analyze this disease, it is necessary to model the human eye and to achieve this, the tissues of the sclera, lens, retina, and optic nerve, which are the most critical areas of the eye, were represented. The optic nerve is particularly susceptible to the effects of glaucoma, which is why the methodology employed in this research is presented in Fig. 1.

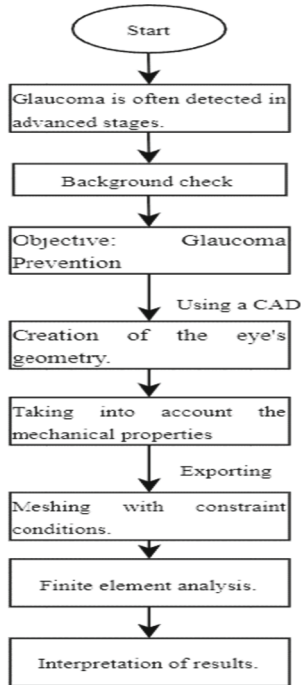


Fig. 1. Flow diagram.

2.1 Model

The initial phase of the study involved investigating the dimensions of the human eye. However, due to the absence of standardized dimensions, four distinct solid models were created to explore significant variations within each model. These models, illustrated in Fig. 1, incorporate measurements expressed in millimeters. They were developed based on equations derived from nonlinear quantum mechanics and calculated using numerical methods [13].

To design the lens, an ellipse was drawn with a major diameter of 11.07 mm, a minor diameter of 3.55 mm, and a curvature thickness of 0.3 mm [14]. The thickness of the sclera was uniformly set at 0.67 mm [15]. These parameters were kept consistent across the four models represented in Fig. 2. The thicknesses of the other tissues will be mentioned below. By providing a detailed explanation of the model development process, readers will gain insights into the considerations and methodology used to capture variations in the dimensions of the human eye.

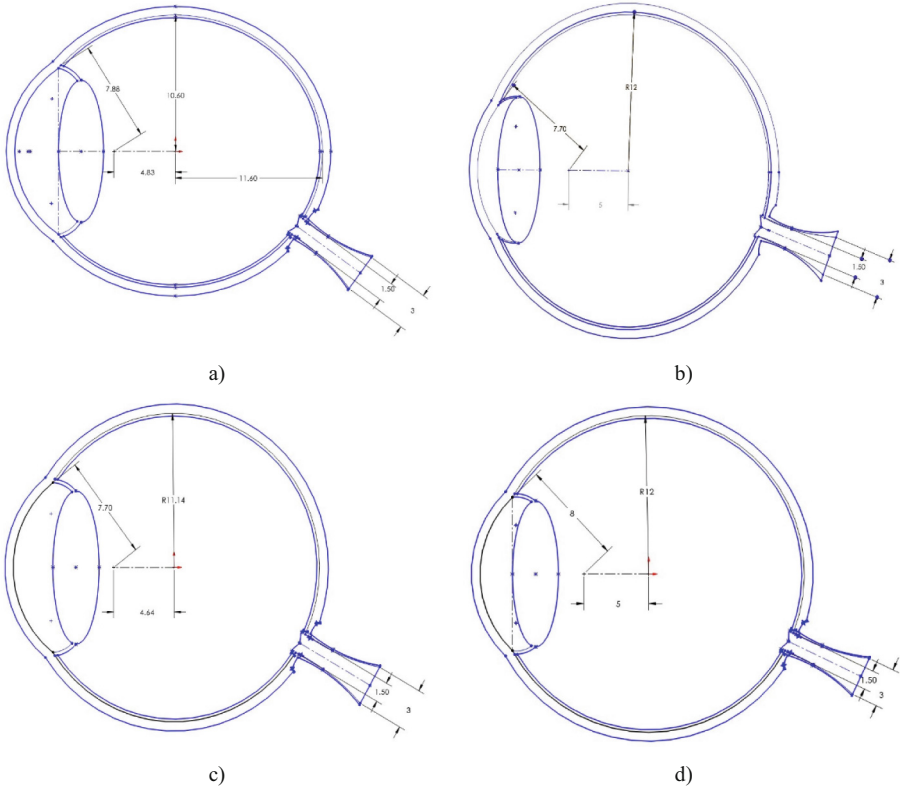


Fig. 2. Geometry of the 2D model: a) Model 1 [9] b) Model 2 [10] c) Model 3 [11] d) Model 4 [12].

2.2 Optic Nerve Geometry

The geometry of the optic nerve, especially the optic disc, is highly complex and highly dependent on the age of the individual. This is because the eye is still growing, making it difficult to parameterize its geometry. Accessing the interior of the ocular eye is challenging, and the dimensions are limited. Additionally, the equipment currently used may introduce errors, making it challenging to establish a defined range for tissue parameterization [13].

Having mentioned the above, Table 1 presents the dimensions used to model the optic nerve. These parameters were employed for all four models, and Fig. 3 illustrates the geometry model for Model 1.

Table 1. Geometry Parameters [7].

Name	Unit	Average
Scleral canal thickness	mm	0.4
Retinal layer thickness	mm	0.2
Scleral thickness	mm	0.67
Pia mater thickness	mm	0.12
Laminar curvature	mm	0.2
Angle of canal wall (horizontal)	deg	60
Peripapillary border height	mm	0.25
Cup depth	mm	0.33

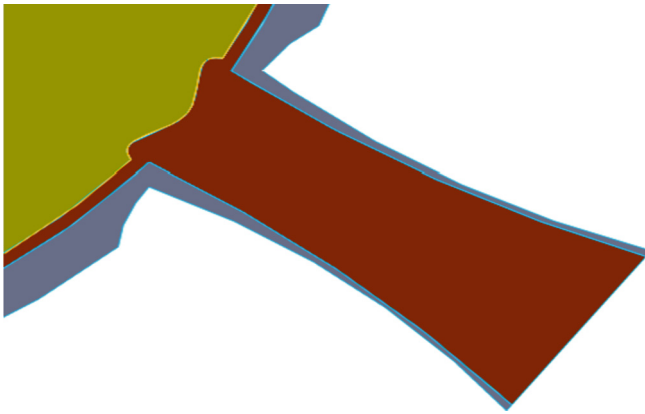


Fig. 3. The geometry of the optic nerve in Model 1.

2.3 Mechanical Properties of Ocular Tissues

The mechanical properties of the eye exhibit significant variations based on factors such as age, intraocular pressure, and individual-specific characteristics [8]. Table 2 provides an overview of the average mechanical properties assigned to each tissue. Specifically, the properties of the sclera are derived from human sources, while the remaining properties are obtained from mammals, predominantly pigs, due to their close resemblance to human eye tissues.

Table 2. Mechanical Properties of Tissues.

Factor	Unit	Average	Reference
Elastic modulus of the sclera	MPa	25.025	[8]
Poisson's ratio	--	0.416	[8]
Elastic modulus of the retina	MPa	0.05	[7]
Poisson's ratio of the retina	--	0.45	[7]
Ultimate strength of the retina	MPa	0.99	[7]
Elastic modulus of the crystalline lens	MPa	3.3	[14]
Poisson's ratio of the crystalline lens	--	0.45	[7]
Elastic modulus of the optic nerve	MPa	0.05	[7]
Poisson's ratio of the optic nerve	--	0.45	[7]
Ultimate strength of the optic nerve	MPa	0.99	[7]

It is crucial to consider the diverse mechanical behaviors of ocular tissues when simulating the eye's response to external stimuli. By incorporating specific mechanical properties of the tissue, the models can better capture the complex biomechanical interactions within the eye.

2.4 Finite Element Analysis for Deformations and Principal Stresses

The simulation was conducted using ANSYS Workbench software. Initially, to capture the intricate interactions among ocular tissues, the solid model geometries were subdivided into three main tissues: the sclera, the crystalline lens, and the retina. This deliberate subdivision was chosen to accurately reflect the functional and anatomical nature of the eye. Furthermore, the retina tissue was expanded to encompass the optic nerve due to its collaboration in visual processing [5], and its mechanical properties' resemblance to those of the retina. This expansion facilitated the capture of the inherent relationship between optical function and biomechanical response.

In the meshing stage of the model, the utilization of "tetrahedral elements" was favored. These elements possess a particular aptitude for adapting to irregular surfaces, as found within the eye. With the aim of optimizing computational efficiency, individual meshes were implemented for each component: the sclera, crystalline lens, retina, and optic nerve.

Following the completion of mesh creation, a mesh quality evaluation, akin to an inspection process, was carried out. The objective of this evaluation was to ensure the suitability of the mesh for the intended calculations. As a result of this process, final meshes comprising 143,252 elements for model 1, 236,869 elements for model 2, 149,298 elements for model 3, and 169,702 elements for model 4 were obtained. Figure 4 illustrates the meshing of model 4.

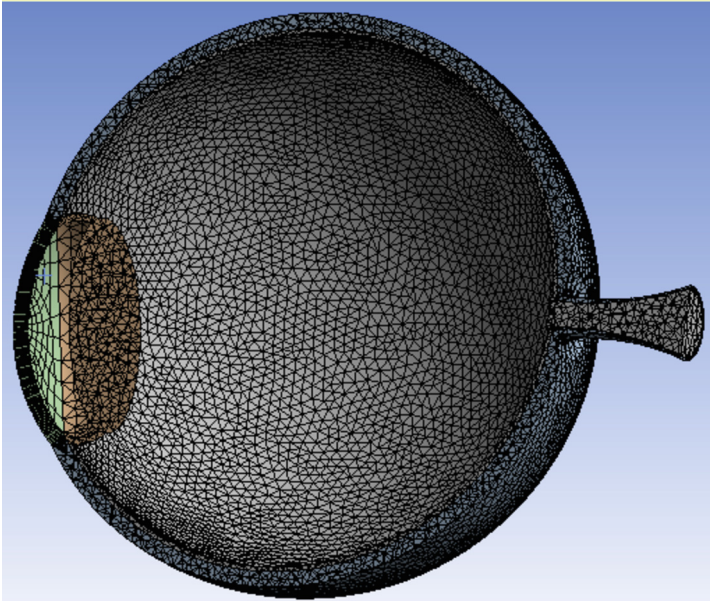


Fig. 4. Visual Representation of Meshing in Model 4.

For the imposition of constraints, in relation to tissue interactions, the condition was established that contacts between them remained immobile and adhered. This decision was grounded in the necessity to simulate the biomechanical coupling conditions existing within the eye, thus enabling a realistic analysis of how stresses and deformations are transmitted between tissues in response to applied pressures and forces.

In determining motion constraints, the choice was made to restrict movement solely at the base of the optic nerve. This choice was based on ocular anatomy and its inherent motion, ensuring that the model accurately reflected the distribution of loads and constraints under real-life conditions.

The simulation of volumetric changes and mechanical responses of the eye to glaucoma was addressed by introducing pressures into the vitreous chamber and anterior chamber. These pressures were applied to induce changes in ocular volume and simulate the characteristic increase in the context of the disease. Two scenarios were considered: one representing normal ocular conditions with an average intraocular pressure of 16.3 mm Hg, and another simulating glaucoma with a pressure of 33 mm Hg [3].

3 Results

Next, in Fig. 5, the results of the total deformation of model 1 in the glaucoma case are shown. As observed in the image, the maximum reached zones are in the retina tissue. These maximum deformations were similar for the other models. The deformations achieved for each case are shown in Fig. 6, where each one increased by 51%. Model 4 reached the highest deformation, with a value of 0.024 mm.

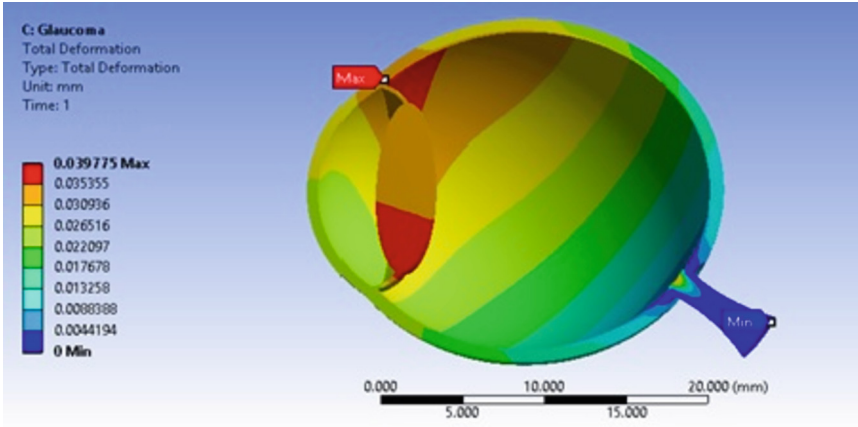


Fig. 5. Total eye deformation.

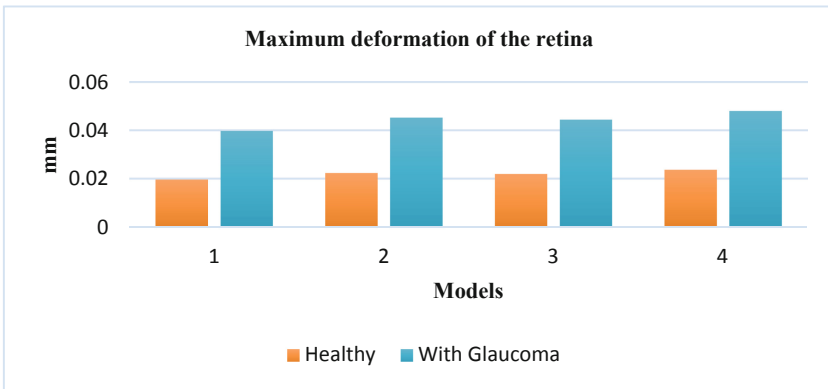
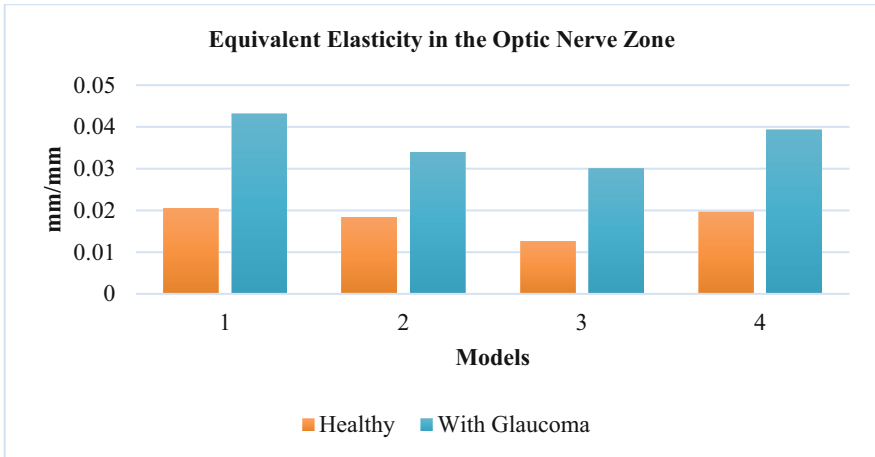


Fig. 6. Maximum Deformation of the Retina in the Healthy and Glaucoma Cases.

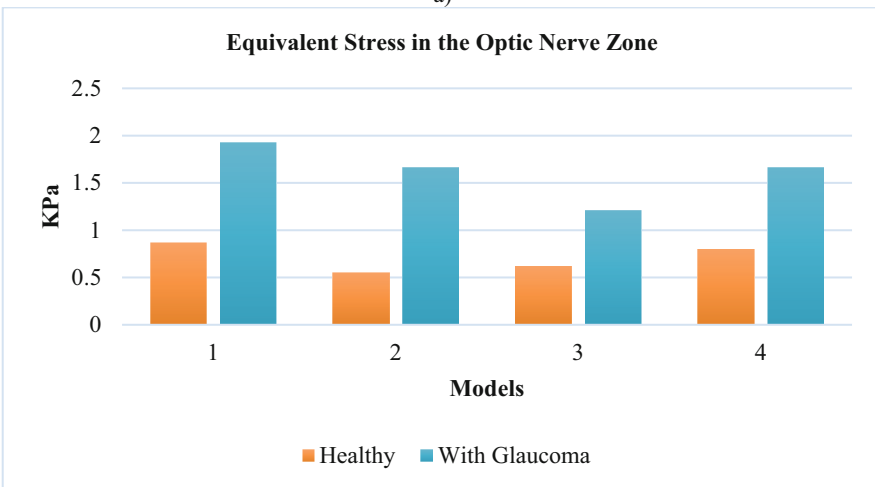
In Fig. 7, the analytical results in the optic nerve zone are presented. In part a) of the figure, the obtained deformation when the eye operates under normal pressures is shown.

In case b), where the pressure operates under glaucoma conditions, in model 1 an increase of 110% was obtained compared to the normal conditions, in model 2 an increase of 85%, in model 3 an increase of 137%, and in model 4 an increase of 100%. Model 3 achieved the highest increase in deformation with 0.017 mm/mm.

In part b) of the figure, the stresses increased by more than 50%, with model 3 showing the highest increase of 202%, resulting in an increase of 0.58 kPa. It is also important to mention that these stresses were the maximum throughout the geometry in all four models, and they were found in the same zone, as shown in part a) of Fig. 8.



a)



b)

Fig. 7. Structural analysis for the two cases: a) Equivalent Elasticity in the Optic Nerve Zone, b) Equivalent Stress in the Optic Nerve Zone.

In part b) of Fig. 8, the zone of maximum equivalent stress is observed, located in the sclera tissue. This maximum zone was also similar to that of the other models. Therefore, the quantitative results of the maximum equivalent stresses located in this zone are shown in the diagram of Fig. 9. These results showed an increase of 51% for each model, except for model 3, which had an increase of 33%.

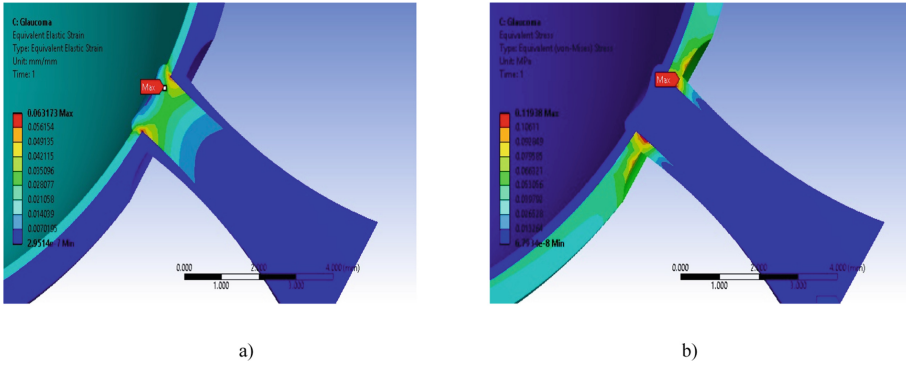


Fig. 8. Results of Model 1: a) Equivalent Elasticity, b) Equivalent Stress.

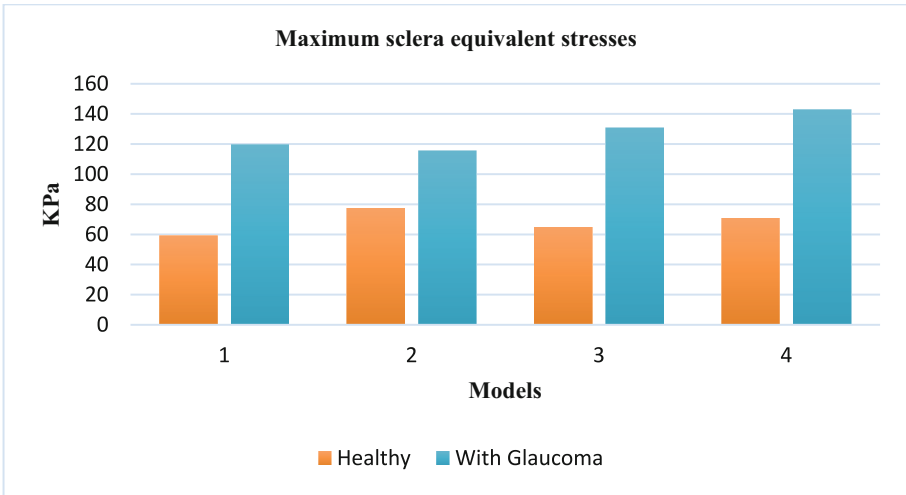


Fig. 9. Maximum equivalent stresses.

4 Conclusions

This study observed the deformation of ocular tissues, specifically in the region of the optic disc, under glaucoma conditions, accompanied by an increase in principal stresses. This indicates that the mechanical properties of optic nerve cells are compromised due to the presence of stress concentrators, which impede proper cellular nutrition and ultimately lead to cell death over time.

Furthermore, it is noteworthy that the four models produced distinct quantitative results. However, the qualitative findings exhibited similarities, with maximum stress concentrations consistently occurring in the same regions. For example, part b) of Fig. 6 demonstrates that the sclera experiences the highest stress concentrations. Additionally, the retina consistently exhibited maximum deformation in all models, as shown in part a) of Fig. 6. Based on these observations, it can be concluded that the identified critical

zones are consistent among the four analyzed models due to the inherent geometry of the eye.

These findings contribute to a better understanding of the biomechanical behavior of the eye under glaucoma conditions and emphasize the importance of identifying and addressing stress concentrators to mitigate the detrimental effects of the disease. Further research and exploration of treatment strategies targeting these critical zones are justified to develop effective interventions for glaucoma management.




Acknowledgments. This project owes its success to the invaluable assistance provided by Alicia Natalia Ruíz Ramos for her collaboration in the research and contribution to the design of the four models used in this study. We are deeply grateful to her.

References

1. Xie, L., et al.: Potential biomarkers for primary open-angle glaucoma identified by long noncoding RNA profiling in the aqueous humor. *Am. J. Pathol.* **189**(4), 739–752 (2019)
2. Wang, X., et al.: Finite element analysis predicts large optic nerve head strains during horizontal eye movements. *Invest. Ophthalmol. Vis. Sci.* **57**(6), 2452–2462 (2016)
3. Chan, M.P., et al.: Glaucoma and intraocular pressure in EPIC-Norfolk Eye Study: cross sectional study. *Bmj.* **358**, j3889 (2017)
4. Whitmore, L.A., Medley, R.: *Cómo entender y vivir con glaucoma* (2013)
5. Tortora, G.J., Derrickson, B.: *Principios de anatomía y fisiología*. Médica Panamericana (2013)
6. Sivaswamy, J., Krishnadas, S., Chakravarty, A., Joshi, G., Tabish, A.S.: A comprehensive retinal image dataset for the assessment of glaucoma from the optic nerve head analysis. *JSM Biomedical Imaging Data Papers* **2**(1), 1004 (2015)
7. Sigal, I.A.: Interactions between geometry and mechanical properties on the optic nerve head. *Invest. Ophthalmol. Vis. Sci.* **50**(6), 2785–2795 (2009)
8. Grytz, R., et al.: Material properties of the posterior human sclera. *J. Mech. Behav. Biomed. Mater.* **29**, 602–617 (2014)
9. Pérez, V.V., de Fez Saiz, D., Verdú, F.M.M.: *Óptica fisiológica: modelo paraxial y compensación óptica del ojo*. Universidad de Alicante (2003)
10. Atchison, D.A., Smith, G.: *Optics of the Human Eye*. Optics of the Human Eye (2000)
11. Puell, M.: *Óptica fisiológica. El sistema óptico del ojo y la visión binocular*. [Internet]. Versión Digital: 1-4135-6363-5. Universidad Complutense de Madrid: ISBN (2006). Citado 27 Jul 2015
12. Gonzalez, G.D.: *Modelo del ojo humano basado en matrices ABCD* (2008)
13. Calderín Pérez, B., Carbonell, G., Alfonso, R., Landín Sorí, M., Nápoles Padrón, E.: Aplicabilidad de la simulación computacional en la biomecánica del disco óptico. *Revista Archivo Médico de Camagüey* **19**(1), 73–82 (2015)
14. Khan, A., Pope, J.M., Verkicharla, P.K., Suheimat, M., Atchison, D.A.: Change in human lens dimensions, lens refractive index distribution and ciliary body ring diameter with accommodation. *Biomed. Opt. Express* **9**(3), 1272–1282 (2018)
15. Norman, R.E., et al.: Dimensions of the human sclera: Thickness measurement and regional changes with axial length. *Experimental Eye Research* **90**, 277–284 (2010)



Stem Design for Tibial Component of Knee Prosthesis

Dorothy Alejandra Almanza-Martínez, Roberto González-Navarrete ,
and Agustín Vidal-Lesso  

Universidad de Guanajuato, Salamanca, Guanajuato, México
agustin.vidal@ugto.mx

Abstract. Knee arthroplasty is one of the most successful operations in joint replacement but it is not free of failures. Mechanical loosening of the tibial component is one of the major causes of knee prosthesis failure. Optimizing the tibial stem can help not only provide better stability but also better anchorage and less loosening. Stems with different physical characteristics exist in the market to help improve these problems. In this work, a methodology for the proposal of a tibial stem was developed and compared with the experimental data of a commercial one. Different models of stems with modifications in their geometry were proposed, and results of stresses and deformations in the cortical and trabecular bone were obtained through finite element analysis. In the deformations of the proposed stem, the results were below the experimental data and within the normal physiological range. And in the stresses, the magnitude of the final model was up to 6 times lower than the commercial model.

Keywords: Stems · Finite element · Knee prosthesis · Optimization · Stress analysis

1 Introduction

Osteoarthritis is the most common joint disorder. Knee prosthesis is used to relieve pain and restore function in patients with knee osteoarthritis who do not respond well to non-invasive treatment. The most frequent reason for revision total knee replacement within the first two years after surgery was generally mechanical failure. Among all causes of failure, the main one was polyethylene wear (25%), followed in frequency by aseptic loosening (24.1%), instability (21.2%), infection (17.5%), arthrofibrosis (14.6%), malalignment (11.8%), extensor mechanism deficiency (6.6%), avascular necrosis of the patella (4.2%), periprosthetic fracture (2.8%) and resurfacing of the patella (0.9%). [1]. Therefore, since the main reason for revision of knee prosthesis replacement is loosening due to mechanical failure, it is necessary to find a way to reduce this percentage. In this project we will propose a tibial stem design that allows the transfer of axial loads in a homogeneous way and that avoids absorbing the torsional torques that can be induced by a bad balance of the ligaments, generating little concentration of efforts, and thus avoiding mechanical loosening. Once the proposed final model is obtained, it can be compared with a commercial model and the results can be analyzed.

2 Materials and Methods

The study was made according to the next methodology shown in Fig. 1.

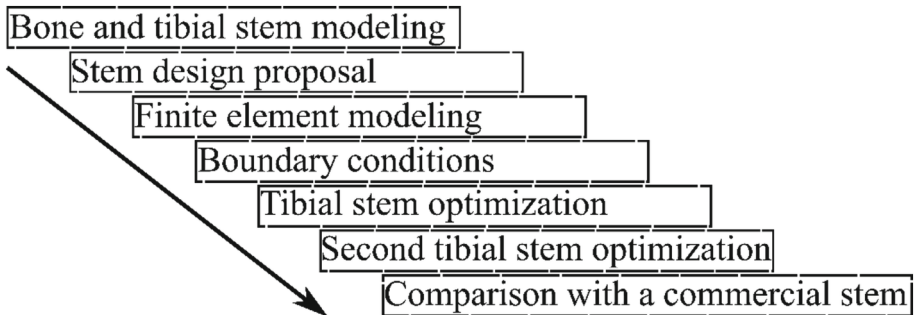


Fig. 1. Methodology used.

2.1 Bone and Tibial Stem Modeling

The CAD models of the tibial bone were obtained from a general assembly of the leg bones obtained from a scan, as shown in Fig. 2a). This assembly was worked to leave only the tibial bone (see Fig. 2b). Tibial bone was cut parallel to the tibial plateau, removing approximately 10 mm along the axis in coronal plane and tilting 2° in sagittal plane. The separation between the cortical and trabecular bone was made, duplicating the cortical bone, and scaling it to a smaller proportion, this was determined according to the thickness of the cortical bone [2], see Fig. 2c) and 2d).

Finally, an initial CAD model of the tibial component was obtained, and a stem was created on the undersurface of the component, as shown in Fig. 2e). This is a simple cylindrical stem with a diameter of 11 mm and a length of 30 mm, dimensions based on commercially available stems [3–5].

2.2 Stem Design Proposal

The creation of the stem designs was through proposals with different geometries and were evaluated considering three parameters: bone removal, machining for bone removal, and simplicity of the design.

Finally, only three of the initial proposals were selected for analysis, see Fig. 3.

Among these options are cylindrical, X-shaped projection and a trapezoidal stem. For the dimensions of the stems, we started from an initial value, some according to the literature [3–5] and others were proposed. The selected stems were then inserted into the trabecular bone, as shown in Fig. 3d, 3e, and 3f, considering the coronal plane and the sagittal plane for alignment with the tibia.

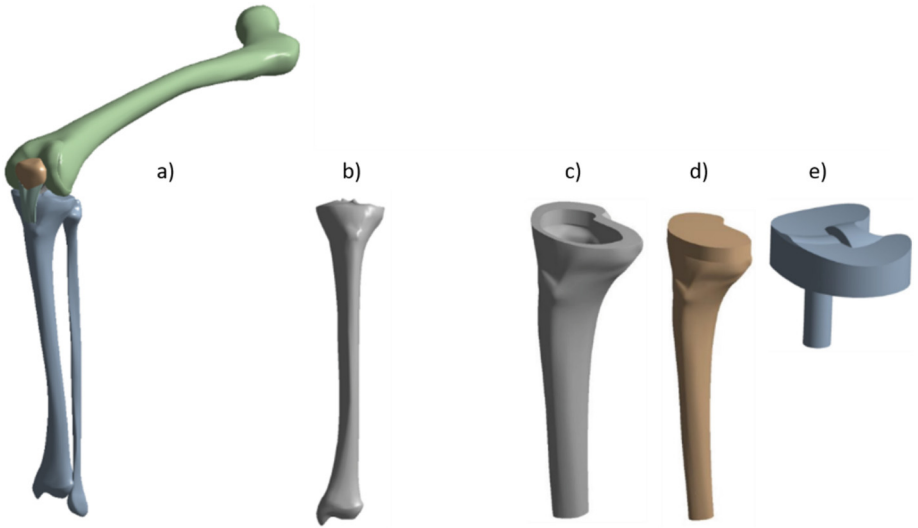


Fig. 2. CAD models: a) tibia-femur assembly, b) tibial bone, c) tibial cortical bone, d) tibial trabecular bone, e) tibial component of knee prosthesis.

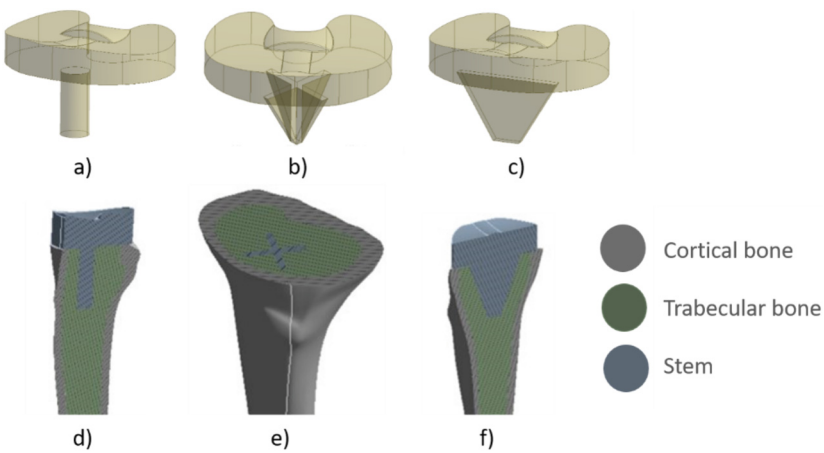


Fig. 3. Initial tibial stems: a) cylindrical, b) X-shaped projection, c) trapezoidal, d) cylindrical stem anchorage, e) X-shaped stem anchorage, f) trapezoidal stem anchorage.

2.3 Finite Element Modeling

For Finite Element (FE) modeling, ANSYS Workbench™ version 19.1 software was used. The components were modeled as orthotropic for the cortical and trabecular bone, and tibial insert as isotropic. The bonded contact type was considered to simulate the bone growth around the stem. The properties of these components are shown in Tables 1 and 2.

Table 1. Orthotropic properties for cortical bone [6].

E_1 (GPa)	6.9
E_2 (GPa)	8.5
E_3 (GPa)	18.4
G_{12} (GPa)	2.4
G_{13} (GPa)	3.6
G_{23} (GPa)	4.9
V_{12}	0.49
V_{13}	0.12
V_{23}	0.14

Table 2. Isotropic properties for computational models [5].

Part	Young modulus (MPa)	Poisson ratio
Trabecular bone ($\rho = 0.3\text{g/cm}^3$)	80	0.3
Trabecular bone ($\rho = 0.9\text{g/cm}^3$)	2,500	0.3
Trabecular bone (Ti-6Al-4V)	107,000	0.3

Elasticity modulus depends on the bone density and varies significantly if is low or high [7], in this work two densities will be taken: 0.3 g/cm^3 and 0.9 g/cm^3 .

The mesh size was decided using the Skewness meshing metric with a maximum value of 1, using element 187 of quadratic order.

2.4 Boundary Conditions

The analysis was performed at “Midstance” walking stage. Due to dynamic effects during the walking cycle, the body load can rise up to three times [8], therefore, the weight of an average person equivalent to 80 kg was selected, and the applied load was 2,352 N distributed on the upper surface 50%:50% medial: lateral condyle of the tibial component with the direction of the vertical axis of the tibia, see Fig. 4.

Displacements of the tibial bone were restricted: cortical and trabecular; in the lower section, simulating that it is fixed to the ground.

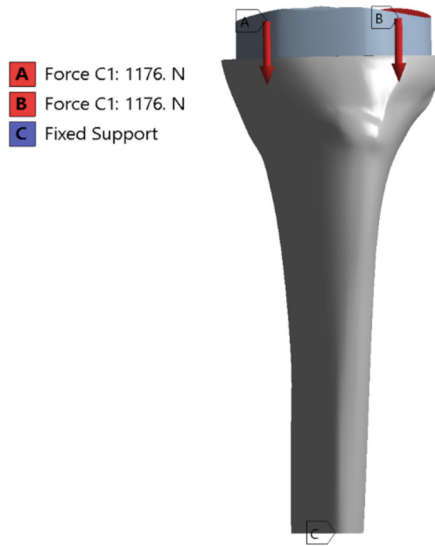


Fig. 4. Boundary conditions.

3 Results

3.1 Optimization of Tibial Stems

Once the proposed stem models were obtained, changes in geometry such as length, fillets, chamfers, and mass reduction were considered based on case study simulations. Three cases were analyzed depending on the body load distribution on the lateral and medial condyles: case 1 “normal” 50% - 50%, case 2 “valgum” 0% - 100% and case 3 “varum” 100% - 0%, respectively.

Figure 5 shows the different case studies case 2 the load was applied at an angle of 163° and in case 3 at an angle of 186° , both with respect to the vertical axis [9].

Simulations were focused on analyzing the study cases with each stem design. We began by analyzing the maximum principal stresses, due to their orthotropic behavior, in the cortical bone, as shown in Table 3.

Table 3 shows the results for each case and the density of the bone, highlighting its maximum principal stress value. These maxima are below the yield stress magnitude, which is approximately 178 MPa [7].

The second analysis was respect to the von Mises stresses, due to its isotropic behavior, of the trabecular bone, see Table 4.

Where the yield stress for trabecular bone at a density of 0.9 g/cm^3 and 0.3 g/cm^3 is 40 MPa and 5.4 MPa, respectively [7].

Results show that there is no significant difference in the stresses between the three stem designs; these stresses are below the yield stress, both for cortical bone and trabecular bone.

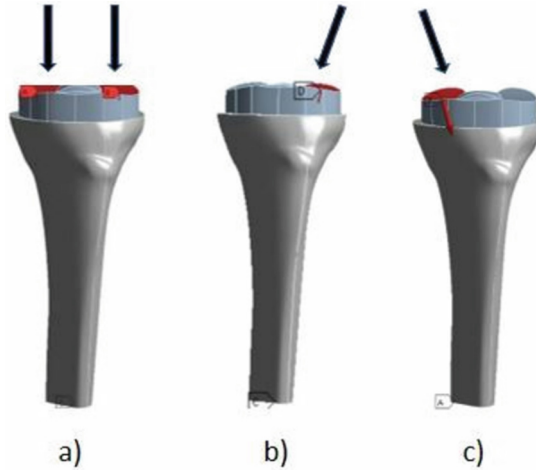


Fig. 5. Case studies: a) case 1, b) case 2, c) case 3).

Table 3. Maximum principal stresses [MPa] of cortical bone.

Stem						
	Cylindrical		X-shaped		Trapezoidal	
Density	0.9 g/cm ³	0.3g/cm ³	0.9 g/cm ³	0.3g/cm ³	0.9 g/cm ³	0.3g/cm ³
Case 1	3.93	6.41	4.86	5.82	4.51	5.68
Case 2	100	93.81	82.15	84.69	84.92	101.28
Case 3	114	81.56	88.58	93.61	94	145.84

Table 4. Von Mises stresses [MPa] in trabecular bone.

Stem						
	Cylindrical		X-shaped		Trapezoidal	
Density	0.9 g/cm ³	0.3g/cm ³	0.9 g/cm ³	0.3g/cm ³	0.9 g/cm ³	0.3g/cm ³
Case 1	3.14	0.42	3.26	0.22	3.19	0.22
Case 2	7.78	0.3	7.63	0.29	7.51	0.28
Case 3	13.98	0.55	13	.052	13.5	0.5

It was concluded that the stem design did not significantly impact the magnitude of the stresses in the bones. It was then decided to analyze how changes in the geometry of each stem affected the bone-stem interface.

In Table 5, it is observed that the maximum von Mises stresses occur at the density of 0.9 g/cm^3 , so it could be considered as the critical density, and this parameter will be used for further analysis of stem design.

Table 5. Von Mises stresses [MPa] at the bone interface.

Stem						
	Cylindrical		X-shaped		Trapezoidal	
Density	0.9 g/cm^3	0.3 g/cm^3	0.9 g/cm^3	0.3 g/cm^3	0.9 g/cm^3	0.3 g/cm^3
Case 1	2.10	0.42	2.36	0.35	1.89	0.20
Case 2	2.22	0.26	2.88	0.27	1.31	0.19
Case 3	1.86	0.31	3.62	0.43	2.11	0.22

To reduce stress concentrations, we considerer to make modifications to the proposed stems by creating fillets at the corners as well as at the bottom of the geometry. When making these changes and inserting the stem into the bone, we realized that there could be a cavity at the bone-stem interface, as shown in Fig. 6, using the cylindrical stem as an example.

In Fig. 6, depending on the operation performed on the stem, a cavity may remain at the interface, causing the results to vary.

Based on this information, we began to perform the analyses focusing on the interface considering bone growth (BG) around each stem and without bone growth.

In Fig. 7, the results of the analysis, with the load and boundary conditions of the stance phase explained above, are shown in a general way, in section b) the results are shown without considering changes in the geometry of the stem (without fillets) in order to have a reference, sections c) and d) show the results considering these changes in the geometry of the stem as well as considering the bone growth or not, respectively around the stem.

In general, the stem designs with and without fillets are very small, with maximum stresses of 6 MPa. The addition of fillets in the stem resulted in an increase of stresses in the contact zone with respect to without using fillets and only considering BG, with an increased range of 1 to 3 MPa.

Since in none of these cases the stresses endanger the integrity of the bone, and considering that the useful life of the prosthesis is approximately 15 years, enough time for BG to be produced, the analysis will be considered more for the BG part, but without discarding the analyses without BG.

From the analysis, it was also concluded that increasing the length of the stem helps to reduce the magnitude of the stress at the interface, but with it also there is greater bone removal, which weakens the bone structure and can generate osteolysis, so there is no mechanical justification for increasing the stem, we will work with the lengths obtained from the literature.

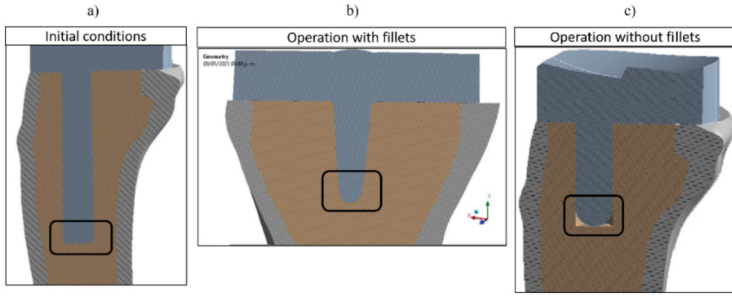


Fig. 6. Fillet operation at the bone-stem interface.

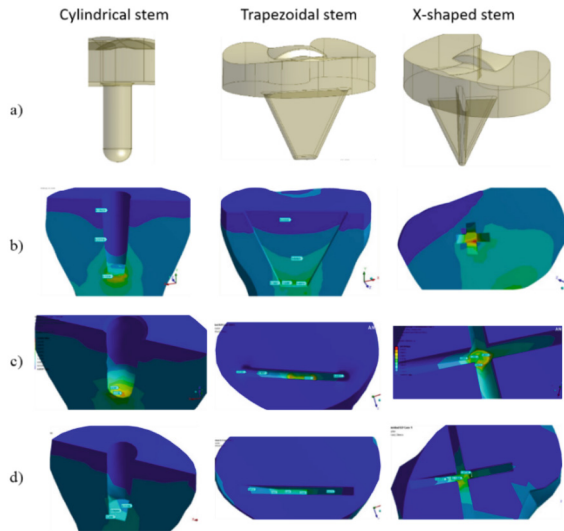


Fig. 7. Qualitative stress analysis at the bone-stem interface: a) 1st modification of the stem, b) without fillets, c) with fillets and BG, without fillets and BG.

3.2 Second Tibial Stem Optimization

For this second stage, the previous designs were considered and an alternative was made for each design. For the cylindrical stem, in addition to adding the pegs to prevent rotating the stem, we reduce the material by making it hollow. For the other 2 stems, we also tried to reduce material in safe low stress zones, approximately zero based on the analysis previously performed.

It was considered to remove material in the stem area to reduce costs and machining, in addition to the fact that in the future there will be bone tissue growth in these voids and it will have a stronger anchorage.

In Fig. 8, the stress results of the different alternatives are shown, each column corresponds to the stem with its respective design alternative and each row represents

state in the stem and in the bone-stem interface considering with and without BG around the stem.

In all cases, the stress concentration is in the lower zone of the bone-stem interface, and they are higher with BG than without BG, these stress ranges are between 1 to 5 MPa, which is a value far from the yield stress.

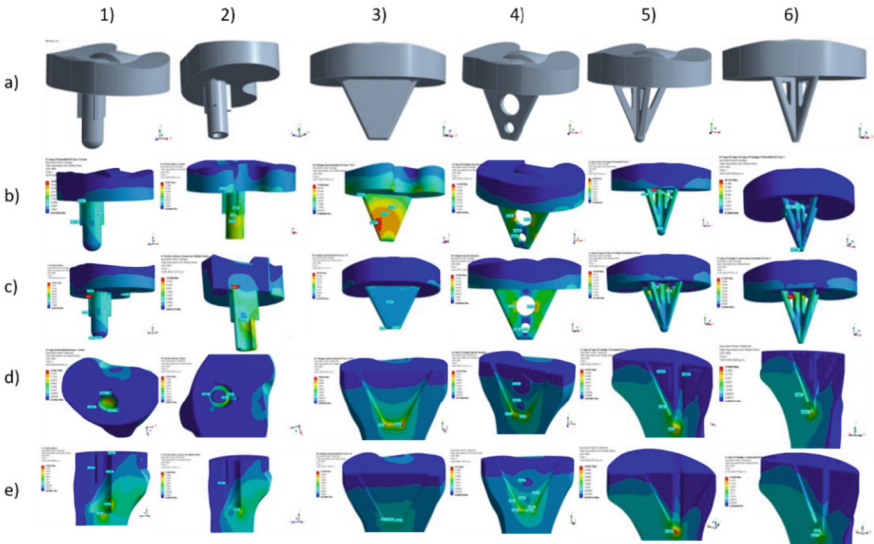


Fig. 8. Qualitative Stress comparison at the bone-stem interface: a) 2nd modification of the stem, b) stresses at the stem considering BG, c) stresses at the stem without considering BG, e) stresses at the bone-stem interface without considering BG.

From these 6 designs, there is no significant difference in the stress analysis, therefore, a selection parameter that was considered to reduce the alternatives was the contact area and the volume of the stem. The greater the contact area at the interface, the greater the anchorage, and the smaller the stem volume, the lower the bone removal (see Table 6).

Table 6. Contact area and volume of tibial stem designs.

Stem	Contact area (mm ²)	Volume (mm ³)
1)	1,291.80	36,587.00
2)	1,682.10	36,259.00
3)	1,622.00	35,791.00
4)	1,510.20	35,367.00
5)	1,939.50	35,753.00
6)	1,825.00	35,550.00

From this information, 2 of the 6 designs were selected by these parameters; stem 4) and stem 6). These stems will be used to compare the analysis with a commercial stem.

3.3 Comparison with a Commercial Stem

For the comparison with a commercial stem, we used the information of the article by Cawley D. et al. [5], which investigates the stresses and distributions in the tibia using a Genesis II type knee prosthesis, the experimental results will be compared with the numerical results of this work.

For this comparison, we worked with the same material properties and loading conditions as the article mentioned above. Firstly, the maximum and minimum deformations were analyzed in the same section views and at the same distances of the cortical bone and trabecular bone as that of the article.

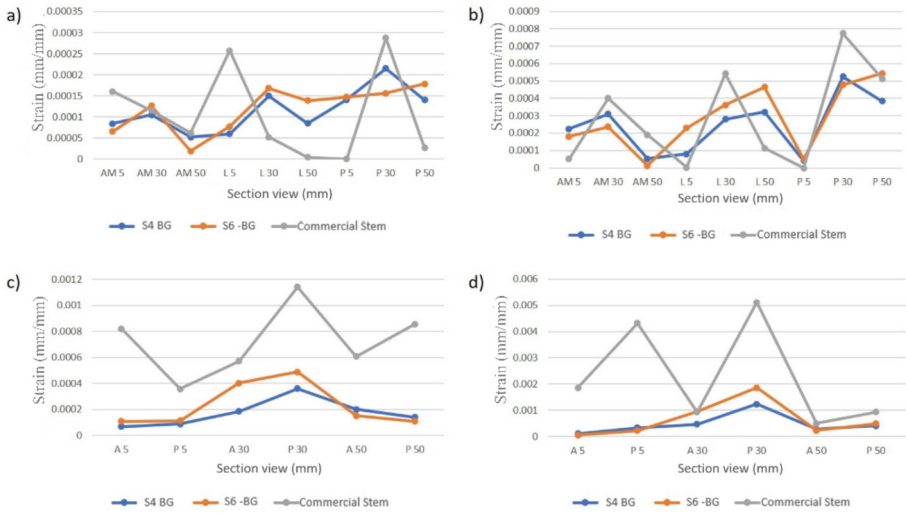


Fig. 9. Maximum deformations of the commercial stem and computational proposals in: a) cortical bone and c) trabecular bone; and minimum deformations: b) cortical bone and d) trabecular bone

In Fig. 9, the comparison of the deformations between the commercial stem and the proposed stems (S4 BG and V6 -BG) is shown, where AM5, L5, and P5 refer to antero-medial, lateral, and posterior, respectively, and 5 mm from the tibial cut, and so on.

Figure 10 shows the comparison of stress distribution between the different stems with the different section views: medial (M), lateral (L), anterior (A), and posterior (P).

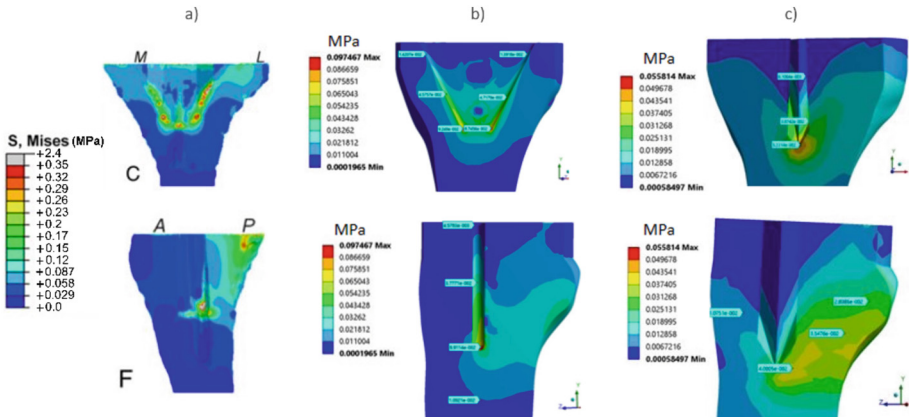


Fig. 10. Von Mises stresses in different section views in trabecular bone: a) commercial stem, b) stem no. 4 with BG, and c) stem no. 6 without BG.

4 Discussion and Conclusions

In this work, the methodology for the optimization of the knee prosthesis stem was developed. Starting from the basic stem design and modifying them from numerical simulations of pathologies suffered by patients in the knee joint. As these case studies progressed, two stages of stem analysis emerged. The first stage is that upon insertion of the stem, there may be some voids in the contact zone (interface) with the bone due to the geometry of the stem (no bone growth), subsequently, the bone will grow filling these cavities, defining stage 2 as with bone growth.

These analyses were compared against experimental data from a commercial Genesis II type stem. The results compared were the maximum and minimum deformations in the cortical and trabecular bone, and the von Mises stresses at the bone-stem interface.

The results in Fig. 9, show that the maximum and minimum deformations in the cortical and trabecular bone have a similar trend along the points where they were taken, being generally lower than that of the proposed stems staying within the zone of the normal physiological range (50 and 1500 $\mu\epsilon$) [10].

The maximum experimental stresses are 0.35 MPa while those of the proposed stems are 0.09 MPa for stem no. 4 and 0.05 MPa for stem no. 6, in the M-L view, and the stresses are concentrated at the bottom and sides of the stem.

With these results, the stresses and deformations at the interface were reduced compared to those proposed with a commercial stem, as future work remains to compare with other types of stems to observe how the proposed stems behave.







References

1. The Ninth Annual Report of the AJRR on Hip and Knee Arthroplasty (2022)
2. Maeda, K., Mochizuki, T., Kobayashi, K.: Cortical thickness of the tibial diaphysis reveals age and sex-related characteristics between non-obese healthy young and elderly subjects

- depending on the tibial regions. *J Exp Orthop.* **7**(1), 78 (2020 Oct 6). <https://doi.org/10.1176/s40634-020-00297-9>
3. Completo, A., Fonseca, F., Simoes, J.A.: Strain shielding in proximal tibia of stemmed knee prosthesis. *J. Biomech.* **41**, 560–566 (2008)
 4. Rastetter, B., Wright, S.: The influence of tibial component malalignment of bone strain in revision total knee replacement. In: Proceedings of the Institution of Mechanical Engineers, Part H: Journal of Engineering in Medicine **230**(6) (2016)
 5. Cawley, D., Kelly, N., McGarry, J.: Full and surface tibial cementation in total knee arthroplasty: a biomechanical investigation of stress distribution and remodeling in the tibia. *Clin. Biomech.* **27**(4), 390–397 (2012)
 6. Donahue, T., Hull, M., Rashid, M., Jacobs, C.: A finite element model of the human knee joint for the study of tibio-femoral contact. *J. Biomech. Eng.* **124**(3), 273–280 (2022). Jun
 7. Mow, V.C., Hayes, W.C.: Basic orthopaedic biomechanics and mechano-biology, 3rd Edition. Lippincott Williams & Wilkins Philadelphia (2005). 0-7817-3933-0
 8. Quílez, M., Pérez, M., Seral-García, B.: Biomechanical study of the tibia in knee replacement revision. *Revista Española de Cirugía Ortopédica y Traumatología* **59**(5), 365–371 (2015)
 9. Vidal, A., Lesso, R., Rodriguez, R.: Analysis, simulation and prediction of contact stresses in articular cartilage of the knee joint (2007). <https://doi.org/10.2495/BIO070061>
 10. Scott, C., Biant, L.: The role of the design of tibial components and stems in knee replacement



Morphological Evaluation of Freeze-Dried Fish Gelatin and Bovine Gelatin Scaffolds for Tissue Engineering

Wendy Meliza Álvarez-Nanguce¹ , Edith Cedillo-Cruz² ,
Alfredo Maciel-Cerda² , Patricia Mendoza-Lorenzo¹ ,
and Roberto Hernández-Córdova¹  

¹ División Académica de Ciencias Básicas, Universidad Juárez Autónoma de Tabasco,
C.P. 86690 Cunduacán, Tabasco, México
roberto.hernandezc@ujat.mx

² Instituto de Investigaciones en Materiales, Universidad Nacional Autónoma de México,
C.P. 04510 Ciudad de México, México

Abstract. Scaffolds are three dimensional porous structures with interconnected pores intended for tissue regeneration. In this work, scaffolds from fish gelatin and bovine gelatin were obtained by freeze-drying method. Gelatin solutions were frozen at different temperatures to evaluate their effect on the morphology and pore size of the obtained scaffold. The chemical composition of the material was evaluated by FTIR analysis. Scanning Electron Microscopy (SEM) was used to observe the cross-section of the scaffolds. These images were utilized to perform a surface morphological analysis. The morphological characterization was carried out with ImageJ software, obtaining the average pore diameter, average orthogonal pore area and surface porosity. It was found that the freezing temperature is determinant in the structural morphology of the scaffolds regardless of the gelatin species, obtaining average pore sizes ranging from 106.32 μm to 220.54 μm , making them suitable for Tissue Engineering applications.

Keywords: Fish Gelatin · Scaffold · Morphology

1 Introduction

Scaffolds for Tissue Engineering are three-dimensional structures that must be highly porous. They should have interconnected pores to allow cell proliferation and possess sufficient mechanical integrity to support cell cultures, they must be degradable at body temperature, biocompatible to ensure tissue integration and its degradation should be not toxic [1]. Interconnected porous net of a scaffold allow cells to spread to the innermost spaces, promote cell migration and differentiation, and facilitate the mass transport of nutrients and waste [2].

Freeze-drying is a versatile and widely used method for the manufacture of porous scaffolds. This process involves freezing a polymer solution, reducing pressure and allow

sublimation of solvent crystals. The freezing temperature control the rate growth of the solvent crystals and the size of this crystals determine the pore size of the solid structure conformed by the solidified polymer [3]. In addition to temperature, there are other parameters that control the pores size of the scaffold such as the nature of polymer, the viscosity, and the concentration of the solution.

Gelatin is extensively used for the manufacture of freeze-drying scaffolds due to its gelling properties. Gelatin is derived from collagen present in animal tissues; it is composed of amino acids such as glycine, proline and hydroxyproline. The main source of gelatin for food and pharmaceutical applications has been from mammals such as bovine and porcine; however, in recent years these sources have been replaced by fish gelatin. The trend for this change is due to the increase in vegetarianism, the appearance of bovine spongiform encephalopathy, foot-and-mouth disease, and swine flu; in addition to the fact that it can be obtained from fishing activities wastes, thus producing a circular economy benefit [4, 5]. In the manufacture of scaffolds, fish gelatin can provide a pore size of around 200 μm [6].

In this work, we used fish gelatin and bovine gelatin to produce scaffolds by freeze-drying method. We seek to know how temperature affects the morphology of the three-dimensional structure of scaffolds and determine if fish gelatin scaffolds are structurally comparable to bovine gelatin scaffolds. A comparative morphological analysis of the scaffold structures was conducted, and the pore size and surface porosity were determined.

2 Methodology

2.1 Materials

In this study gelatin and distilled water were used. Fish skin gelatin and bovine gelatin were obtained from Sigma-Aldrich.

2.2 Methods

Scaffolds Fabrication. For obtaining comparable scaffolds, we prepared solutions of each gelatin (fish and bovine) at the same concentration. Gelatin solutions were prepared in water at 0.65% w/w with continuous stirring for 30 min at 55 °C. The solutions obtained were placed in polytetrafluoroethylene cylinder molds and proceeded to freeze. To evaluate the effect of temperature over morphology of the obtained scaffolds we used two freezing temperatures at -10 °C and -40 °C for 24 h. Subsequently, they were lyophilized for another 24 h. Upon completion, the scaffolds were stored to avoid contact with air and labeled as GP for fish gelatin and GB for bovine gelatin.

Fourier Transform Infrared Spectroscopy (FTIR). Samples were analyzed on ATR-FTIR mode, using the Thermo Scientific Nicolet 6700 spectrometer. A small sample was cut from the scaffold and placed at ATR device, obtaining the spectrum in the interval from 4000 to 400 cm^{-1} .

Scanning Electron Microscopy (SEM). Scaffold structure was visualized in a LEICA Stereoscan 440 equipment at 20 kV. Samples of scaffold were cut and quenched in liquid nitrogen, subsequently the samples were cracked to analyze the cross section. Samples were mounted in a sample holder to be covered with a thin layer of gold prior to observation.

Scaffold Morphology Analysis. Morphological analysis was performed on SEM images. About 10 to 25 measurements were made per scaffold. The pore diameter, the pore orthogonal area and the surface porosity were determined. Measurements were made by digital image analysis using ImageJ software.

Statistical Analysis. Measurements are presented as mean \pm standard deviation. Analysis of variance (ANOVA) with Tukey's test was performed. Statistical significance is considered when $p < 0.05$. In figures, error bars correspond to standard deviation.

3 Results and Discussion

Figure 1 shows the FTIR spectrum of the scaffolds with bands characteristic for gelatin. It was possible to determine that the scaffold fabrication process did not influence the chemical composition of either of the two types of gelatins. The peak at 3270.9 cm^{-1} correspond to amide-A group, representing stretching N-H linked to H-bonding signals, the peak at 1629.3 cm^{-1} correspond to amide-I group due to C = O stretching and H-bonding with COO^- [7]. Both peaks are similar for fish and bovine gelatin. For differentiation between gelatin types, we can observe the peak around 1520 cm^{-1} corresponding to amide-II group, which is slightly more intense for fish [8].

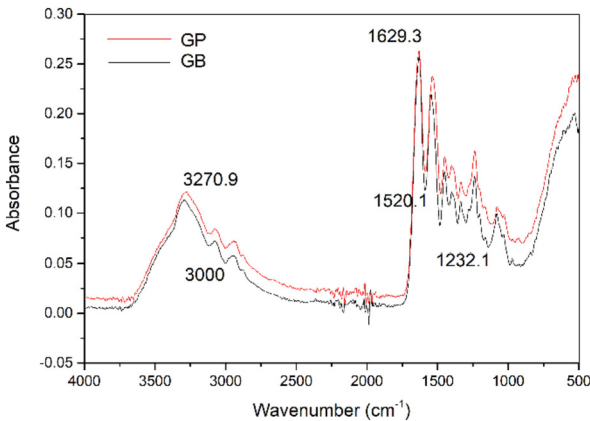


Fig. 1. ATR-FTIR gelatin scaffolds spectrum.

Images from SEM are showed in Fig. 2. Highly porous structures with irregular pore shapes and different pore sizes are observed. It is possible to identify that the scaffolds obtained at a temperature of $-10\text{ }^{\circ}\text{C}$ presented larger pores and greater wall

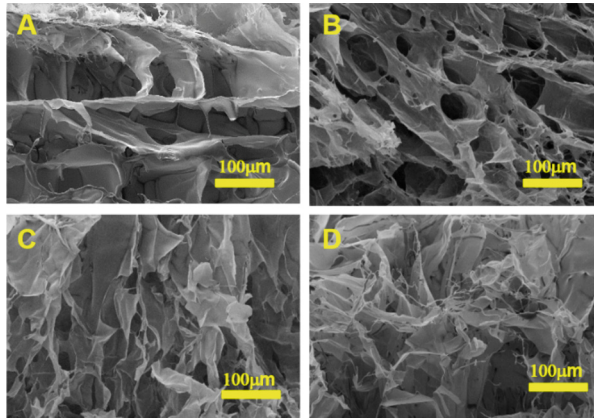


Fig. 2. Scaffolds scanning electron microscopy. A and B are samples treated at $-10\text{ }^{\circ}\text{C}$ corresponding to GP and GB, respectively. C and D are the samples treated at $-40\text{ }^{\circ}\text{C}$ corresponding to GP and GB, respectively.

thickness than their counterparts obtained at $-40\text{ }^{\circ}\text{C}$. It was observed that, at higher freezing temperatures, the variability between pore sizes increased.

The results of the morphological analysis are presented in Table 1. It was observed that the scaffolds obtained at a temperature of $-10\text{ }^{\circ}\text{C}$ have larger diameters than those obtained at $-40\text{ }^{\circ}\text{C}$, regardless of the type of gelatin. The GP sample presented a greater dispersion in the pore diameters compared to the GB sample for both thermal treatments, which indicate that the chemical structure of the fish gelatin different from bovine gelatin (showed in FTIR spectrum) can influence the morphologic structure of the scaffold. Figure 3 shows the result of the statistical analysis of the pore diameter measurements.

Table 1. Scaffold structure morphology assessment.

Temperature ($^{\circ}\text{C}$)	Diameter (μm)		Orthogonal area (μm^2)	
	GP	GB	GP	GB
-10	220.54 ± 113.85	176.54 ± 35.58	26058.13 ± 24135.88	21086.01 ± 16559.94
-40	119.68 ± 50.22	106.32 ± 33.29	9776.12 ± 6035.37	8995.46 ± 3184.79

Another way to characterize the morphological structure of the scaffolds is through the pore areas, orthogonal to the observation plane. This measure makes it possible to parameterize the dimensions of the pores regardless of the irregularity of their geometric shapes. The result of this measurement is presented in Table 1. Figure 4 presents the result of the statistical analysis. A greater dispersion of the measurements of the areas between gelatin types and in function of temperature is observed, although the statistical analysis only showed a significant difference for the GB samples with respect to the freezing temperature.

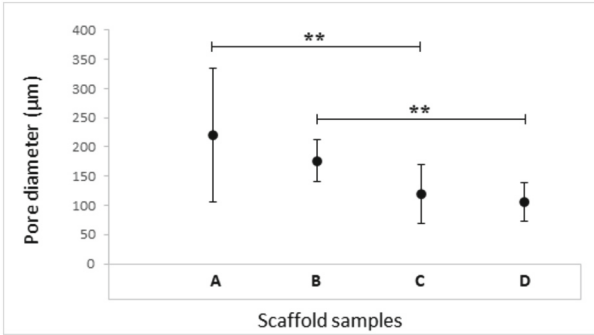


Fig. 3. Pore diameter statistical comparative analysis. A and B correspond to the -10 °C treatment for GP and GB respectively; C and D correspond to the -40 °C treatment for GP and GB, respectively. ** indicates statistical significance ($p < 0.01$, one-way ANOVA with Tukey's test).

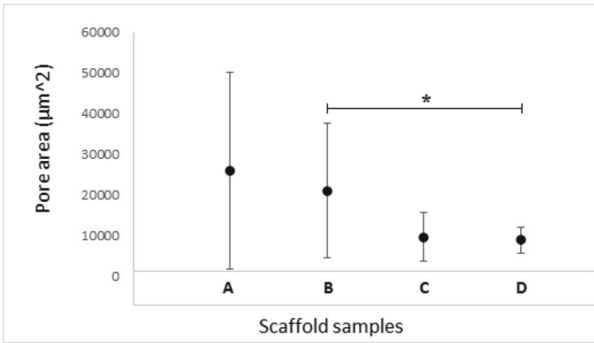


Fig. 4. Orthogonal pore area statistical comparative analysis. A and B correspond to the -10 °C treatment for GP and GB respectively; C and D correspond to the -40 °C treatment for GP and GB, respectively. * Indicates statistical significance ($p < 0.05$, one-way ANOVA with Tukey's test).

Figure 5 shows the measurement of surface porosity. The surface porosity increases when the freezing temperature decreases. The scaffolds obtained at -40 °C presented greater porosity because the formation of water crystals occurs more quickly, so there is no opportunity for the crystals to grow, in consequence smaller pores are obtained and therefore there is a greater number of pores on the surface.

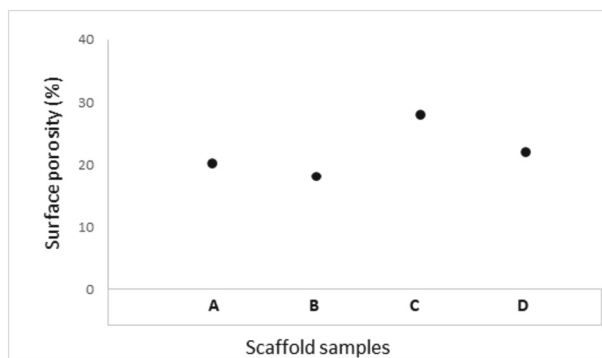


Fig. 5. Scaffolds surface porosity analysis. A and B correspond to the $-10\text{ }^{\circ}\text{C}$ treatment for GP and GB respectively; C and D correspond to $-40\text{ }^{\circ}\text{C}$ treatment for GP and GB, respectively.

4 Conclusions

Relationship with statistical significance was found between the freezing temperatures and the pore sizes of the scaffolds for both gelatin types. At $-10\text{ }^{\circ}\text{C}$, a difference of 1.84 and 1.66 times the pore size was obtained for the GP and GB samples, respectively. Although a significant difference was not reached between the two gelatin species, higher values were observed in pore sizes and a greater dispersion of sizes for the fish gelatin sample. An increase in the concentration of the solutions could lead to a different behavior in the comparison between gelatin species because the higher the concentration, the higher the viscosity, interfering with the speed of crystal formation and affecting the morphology of the scaffold pores. By controlling the processing temperature, it is possible to obtain scaffolds that meets to morphological needs for the regeneration of a specific tissue. We conclude that temperature determine the pore size obtaining bigger pores at higher temperatures, and in terms of structural morphology the fish gelatin scaffolds are statistically comparable to bovine gelatin scaffolds.

References

1. Mohammadi, H., Sepantafar, M., Muhamad, N., Bakar Sulong, A.: How does scaffold porosity conduct bone tissue regeneration?. *Adv Eng Mater* **23**(10), 1–19 (2021). <https://doi.org/10.1002/adem.202100463>
2. Blaudez, F., Ivanovski, S., Ipe, D., Vaquette, C.: A comprehensive comparison of cell seeding methods using highly porous melt electrowriting scaffolds. *Materials Science and Engineering C* **117**(April), 111282 (2020). <https://doi.org/10.1016/j.msec.2020.111282>
3. Grenier, J., Duval, H., Barou, F., Lv, P., David, B., Letourneur, D.: Mechanisms of pore formation in hydrogel scaffolds textured by freeze-drying. *Acta Biomater.* **94**, 195–203 (2019). <https://doi.org/10.1016/j.actbio.2019.05.070>
4. Lv, L.C., Huang, Q.Y., Ding, W., Xiao, X.H., Zhang, H.Y., Xiong, L.X.: Fish gelatin: The novel potential applications. *J. Funct. Foods* **63**(January) (2019). <https://doi.org/10.1016/j.jff.2019.103581>

5. Karim, A., Bhat, R.: Fish gelatin: properties, challenges, and prospects as an alternative to mammalian gelatins. *Food Hydrocolloids* **23**(3), 563–576 (2009). <https://doi.org/10.1016/j.foodhyd.2008.07.002>
6. Uranga, J., Etxabide, A., Cabezudo, S., de la Caba, K., Guerrero, P.: Valorization of marine-derived biowaste to develop chitin/fish gelatin products as bioactive carriers and moisture scavengers. *Science of the Total Environment* **706** (2020). <https://doi.org/10.1016/j.scitotenv.2019.135747>
7. Nur Hanani, Z.A., Roos, Y.H., Kerry, J.P.: Use of beef, pork and fish gelatin sources in the manufacture of films and assessment of their composition and mechanical properties. *Food Hydrocolloids* **29**(1), 144–151 (2012). <https://doi.org/10.1016/j.foodhyd.2012.01.015>
8. Cebi, N., Durak, M.Z., Toker, O.S., Sagdic, O., Arici, M.: An evaluation of Fourier transforms infrared spectroscopy method for the classification and discrimination of bovine, porcine and fish gelatins. *Food Chem.* **190**, 1109–1115 (2016). <https://doi.org/10.1016/j.foodchem.2015.06.065>



Experimental Test Bed for Hand Orthotic Actuators Characterization

Ángel Iván De Luna-García¹ , Ricardo Cortez¹ , Marco Sandoval-Chileño² , Norma Lozada-Castillo¹  , and Alberto Luviano-Juárez¹ 

¹ Instituto Politécnico Nacional – UPIITA, Avenue IPN 2580, Col. Barrio La Laguna Ticomán, 07340 Ciudad de México, Mexico

nlozadac@ipn.mx

² Instituto Politécnico Nacional – UPIEM. 17, 69121, Unidad Profesional, Avenue Wilfrido Massieu, Adolfo López Mateos S/N, Nueva Industrial Vallejo, 07738 Ciudad de México, Mexico

Abstract. The present article shows the implementation of a bilateral control scheme as an option to be implemented on a hand orthosis. The reference signal is computed using a measurement of the position of the phalanx based on a flexible sensor, the measurements are used to estimate positions of a 3DoF robot based on a polynomial approximation. The estimated positions are used to compute the inverse kinematic to provide positions of the orthosis, this is verified using the Matlab Robotic Toolbox that verifies how the robot reaches the same position of the phalanx.

Keywords: Hand orthosis · Bilateral Control · Robotics · Movement analysis

1 Introduction

The development of orthotic devices has been increasing thanks to the recent introduction of alternative manufacturing processes, new sensing technologies, alternative applications in industrial processes, etc. [1]. The successful development of orthotic systems is closely related to a multidisciplinary design approach that must involve aspects such as biomechanics, the final use, the user conditions, the user satisfaction, the capacity of the user to perform movements or the capacity of generating movement intention bio signals, among other important conditions [2]. Another important aspect in the synthesis of an orthotic device concerns the validation tests that must be performed in preliminary design steps (capacity of assistive movement generation) in which the dimensions of the device, size, weight, the workspace, and the velocity/force capacity can be assessed for possible re-designs, materials/actuator changes, among others. There is a wide variety of hand orthosis proposals based on different actuators and manufacturing approaches which may demand evaluation platforms for its analysis.

In this article, it is proposed a set of two modules for the force/position characterization for actuators in orthotic systems. The first module consists of a bilateral control platform to evaluate the supporting force in an orthotic device through a bilateral force control. The second module deals with the kinematic characterization of the movements

in a hand orthotic device by means of flex sensors and a computational validation of the direct cinematic of the finger's articulations based on the Matlab Robotics Toolbox. The article is divided as follows: Sect. 2 presents each module and its forming elements as well as its principles of operation. The evaluation of each module is described in Sect. 3, providing some motivational results. Finally, some concluding remarks and some proposals for future work are provided.

2 Materials and Methods

Orthotic devices can be useful to assist the user in providing extra force support in grasping tasks, where force and position control are necessary. To assess the capacity of the actuators in force/position control, especially when an obstacle or any disturbing element is present implies a validation platform for the actuators. In this work, the proposal is given for direct current motors taking as reference the proposal reported in [3].

Considering that hand orthotic devices may involve the control of each finger separately [4] or the complete hand movement from an individual global actuating force [5], both cases usually demand a kinematic analysis of the fingers/hand concerning mainly the flexion and extension movements, which can be carried out through different sensing approaches. The proposed measurement approach is based on the use of flex sensors along with pressure sensors and Inertia Measurement Units to provide extra movement conditions to describe possible discrete events (important to develop hybrid biomechanical models [6]). The description of each module is given in the following subsections.

2.1 Bilateral Control Characterization

Control systems in which the feedback from the robot (orthotic device) to the person who controls it are called bilateral because the movement and force commands do not just flow from the operator to the robot, but the robot slave also reflects forces back to the operator [7]. Figure 1 illustrates the bilateral control for a one degree of freedom pendular mechanism, where the subindex m is given for the master system (human) and s is denoted for the slave system (orthosis) which receives the environmental forces that are reflected to the user. The control task is that the slave system must follow the reference position (here denoted as q_m), the environmental forces are reflected to the master system and then the force compensation must be implemented in a simultaneous manner.

Let us assume that each finger/hand is locally expressed as a single rotational pendulum system controlled by a direct current motor (for the case of a different nature actuator, the dynamic model must be modified to match the kind of actuator). This system is duplicated for, both, master, and slave systems. Thus, the simplified mathematical model of the control system is given by [3]:

$$\begin{aligned} \ddot{q}_m &= k_v V_m(t) - \xi_m(q_m, \dot{q}_m, t) \\ \ddot{q}_s &= k_v V_s(t) - \xi_s(q_s, \dot{q}_s, t) \end{aligned} \quad (1)$$

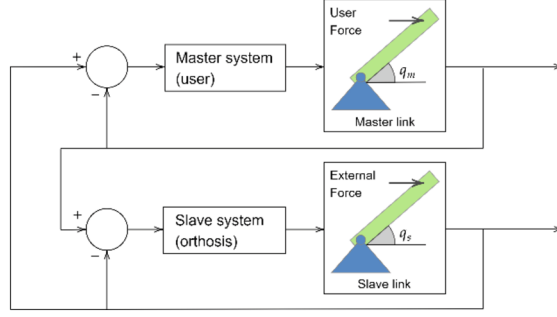


Fig. 1. Schematic of a bilateral control

here, k_v is the gain control depending of the motor parameters (contra electromotive force constant, gear reduction ratio, armature resistance, rotor shaft/gear train lumped inertia), V_m, V_s are the control inputs in terms of the voltage input (see [8]), and ξ_s, ξ_m are the disturbance terms that include internal effects such as non-modeled dynamics, gravity terms, friction effects, possible nonlinearities of the system; and external elements such as the external forces for the orthosis and the user force input as well. The gain parameter can be experimentally computed by system identification methods such as the Matlab system identification toolbox [9] and the disturbances must be estimated online for the bilateral control input through an extended state observer of PI nature [10].

To construct the extended state observers, let us express the master and slave systems (1) in a space state representation:

$$\begin{aligned}\dot{q}_{m1} &= q_{m2} \\ \dot{q}_{m2} &= k_v V_m(t) - \xi_m(q_{m1}, q_{m2}, t) \\ \dot{q}_{s1} &= q_{s2} \\ \dot{q}_{s2} &= k_v V_s(t) - \xi_s(q_{s1}, q_{s2}, t)\end{aligned}\quad (2)$$

where $q_{m1} = q_m, q_{m2} = \dot{q}_m, q_{s1} = q_s,$ and $q_{s2} = \dot{q}_s$ respectively. The PI extended state observers are expressed as:

$$\begin{aligned}\dot{\hat{q}}_{m1} &= \hat{q}_{m2} + \lambda_{m2}(q_{m1} - \hat{q}_{m1}) \\ \dot{\hat{q}}_{m2} &= k_v V_m(t) + \lambda_{m1}(q_{m1} - \hat{q}_{m1}) + \hat{\rho}_m \\ \hat{\rho}_m &= \lambda_{m0}(q_{m1} - \hat{q}_{m1}) \\ \dot{\hat{q}}_{s1} &= \hat{q}_{s2} + \lambda_{s2}(q_{s1} - \hat{q}_{s1}) \\ \dot{\hat{q}}_{s2} &= k_v V_s(t) + \lambda_{s1}(q_{s1} - \hat{q}_{s1}) + \hat{\rho}_s \\ \hat{\rho}_s &= \lambda_{s0}(q_{s1} - \hat{q}_{s1})\end{aligned}\quad (3)$$

where $\hat{q}_{mi}, \hat{q}_{si}, i = 1, 2$ are the estimates of $q_{mi}, q_{si}, \hat{\rho}_m$ is the estimate of ξ_m and $\hat{\rho}_s$ is the estimate of ξ_s respectively. The injection gains $\lambda_{mi}, \lambda_{si}, i = 0, 1, 2$ are set to satisfy that the linear dominant injection error dynamics (expressed in the Laplace domain).

$$\begin{aligned}s^3 + \lambda_{m2}s^2 + \lambda_{m1}s + \lambda_{m0} \\ s^3 + \lambda_{s2}s^2 + \lambda_{s1}s + \lambda_{s0}\end{aligned}\quad (4)$$

have its roots deep in the left half of the complex plane (Hurwitz condition), which ensures that the estimation errors are ultimate bounded whose bounds are closely related to the choice of the injection gains [10]. Finally, the bilateral control is given as follows. Let us define the tracking error between slave and master systems as $\varepsilon := q_{s1} - q_{m1}$. For the slave system (orthotic device), the control consists of a Proportional Derivative with disturbance compensation (Active Disturbance Rejection) of the form:

$$u_s = -k_{ps}\varepsilon - k_{ds}\left(\dot{\hat{q}}_{s1} - \dot{\hat{q}}_{m1}\right) - \hat{\rho}_s \quad (5)$$

with positive gains k_{ps} , k_{ds} , and for the master system (user) the force control is given by:

$$u_m = k_f \hat{\rho}_s \quad (6)$$

where the force sensitivity gain k_f is a positive constant that must be tuned according to experimental tests in which the main user defines the most suitable value (which is not recommended of high gain nature to avoid possible instabilities).

2.2 Module for Position/Force Measurement

Since the problematic related to the position measurements of the hand remains as an open problem because the existence of a high variability from the anthropometric dimensions of the people, which implies the implementation of a rigid structure used to measure the angular positions from the phalanx is not a feasible solution to the problem. A solution is the implementation of a glove that have an embedded instrumentation that allows the estimation of the positions on real-time.

The embedded position estimation on the glove is proposed with the use of a flexible resistive sensor FlexSensor that allows an estimation of the angular changes on the phalanx, the way the sensor is attached to the glove is shown on Fig. 2.

Since this sensor is based on the changes over their resistive value, an instrumentation related to the variable is implemented. In this case, a voltage divider scheme is proposed as shown on Fig. 3 where R_s is the FlexSensor.

The data acquisition is performed using the STM32F407DISCOVERY compiled on Matlab/Simulink with the Waijung package, this uses the ADC module with 12-bits definition. A data acquisition channel to the PC using serial communication with a sampling time of 0.005 seconds is implemented.

A set of experiments are given to determine the range of values from the sensor, this shows a minimal value of $7K\Omega$ and a maximum value of $13K\Omega$, considering this information the resistor value R_2 corresponds to $34K\Omega$. Considering a voltage input from $3.3V$ the output voltage is computed by,

$$\frac{3.334K\Omega}{R_s + 34K\Omega} \quad (7)$$

This implies the range of voltage that corresponds to the movement on the hand are [2.0856 V, 2.7324 V], this information is used to determine the reference signal on the bilateral control scheme. However, given the high frequency noise in the sensor, a digital



Fig. 2. Glove with embedded FlexSensor for position measurement from the phalanx.

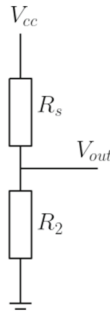


Fig. 3. Voltage divider for instrumentation of the FlexSensor.

version of a low-pass 3th Bessel filter with a cut-off frequency of 60 Hz is implemented. The filter transfer function is

$$H(s) = \frac{15}{\left(\frac{s}{\omega_c}\right)^3 + 6\left(\frac{s}{\omega_c}\right)^2 + 15\frac{s}{\omega_c} + 15} \quad (8)$$

The cut-off frequency given on radians corresponds to $\omega_c = 376.991 \text{ rad/s}$, such the transfer function is

$$H(s) = \frac{8.03 \times 10^8}{s^3 + 2261.95s^2 + 2.13 \times 10^6s + 8.03 \times 10^8} \quad (9)$$

Since the implementation is performed on the Matlab/Simulink environment is not necessary to perform a discretization of the filter.

To implement this data as position reference on the hand orthosis is necessary define the mechanical structure based on the Denavit-Hartenberg convention. The phalanx could be expressed as a 3DoF robot with the parameters given on Table 1, this implies all the rotation axis remains on the same direction. The values of l_1 , l_2 and l_3 varies depend of the phalanx of the orthosis that is considered. Noticed that this model is valid for all the phalanx except for the thumb, that requires an independent analysis.

Table 1. Denavit-Hartenberg parameters of the 3DoF phalanxs from the hand orthosis.

Link	θ_i	d_i	a_i	α_i
1	q_1	0	l_1	0
2	q_2	0	l_2	0
3	q_3	0	l_3	0

Considering the implementation of the Homogeneous Transform matrices on the Denavit-Hartenberg methodology the direct kinematics of the system could be computed as follows:

$$\begin{aligned} x &= l_1 \cos(q_1) + l_2 \cos(q_1 + q_2) + l_3 \cos(q_1 + q_2 + q_3) \\ y &= l_1 \sin(q_1) + l_2 \sin(q_1 + q_2) + l_3 \sin(q_1 + q_2 + q_3) \\ z &= 0 \end{aligned} \quad (10)$$

However, a simplification that only considers a grip task could consider that the first phalanx possesses a fixed angular position that allows to describe the direct kinematics as,

$$\begin{aligned} l_3 \cos(q_3) &= \cos(q_3)x + \sin(q_3)y - l_2 \\ l_3 \sin(q_3) &= -\sin(q_3)x + \cos(q_3)y \end{aligned} \quad (11)$$

The inverse kinematics could be estimated based on the following operations,

$$\begin{aligned} B &= \text{atan}(x, y) \\ L &= \frac{x}{\cos(B)} \\ q_2 &= \text{atan}\left(\frac{l_3 \cos(q_2) + l_2}{L}, \frac{l_3 \sin(q_2)}{L}\right) \\ q_3 &= \text{atan}\left(\pm \sqrt{1 - \frac{x^2 y^2 - l_2^2 - l_3^2}{2l_2 l_3}}, \frac{x^2 y^2 - l_2^2 - l_3^2}{2l_2 l_3}\right) \end{aligned} \quad (12)$$

Since the inverse kinematics provides the angular positions required to reach a desired position on the axis x and y , it is necessary to propose a relationship that describes the position measured by the sensor to these coordinates. At first step a gain of 1.5151 is applied to the voltage measured by the sensor to create an equivalent range of the ADC to $[0V, 5V]$, this modifies the range of the output voltages from the instrumentation to $[3.61 V, 4.14 V]$.

Once this change of scale is implemented a polynomial approximation is proposed based on a 4th order expression as follows,

$$\begin{aligned} x &= 0.5596V^4 - 6.547V^3 + 20.68V^2 - 2.96 \times 10^{-15}V - 53.39 \\ y &= 1.265V^4 - 13.04V^3 + 38.17V^2 + 8.60 \times 10^{-13}V - 93.82 \end{aligned} \quad (13)$$

This polynomial allows to compute a position of the orthosis based on the measured position on the glove, the relationship between the voltage and the positions is shown on Fig. 4.

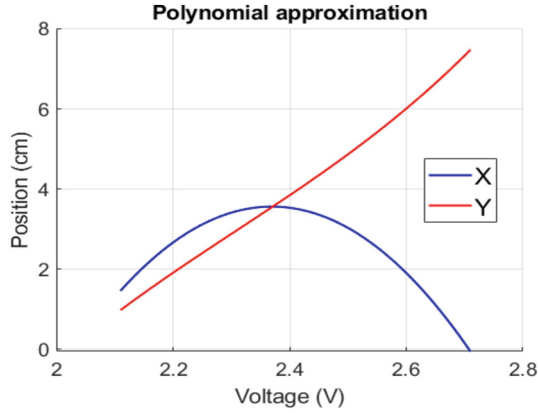


Fig. 4. Polynomial approximation of the positions based on the measured voltage.

3 Results

3.1 Bilateral Control Test Bed

The platform (Fig. 5) consists in two PLA-based penduli, the structures include a Pololu 12 V dc motor with gear reduction of 150. The master pendulum has a length of 5 cm and the slave one has a length of 12 cm. Both motors are supplied by a L298 driver and the control law is implemented in a STM32F407VG discovery embedded card, which was programmed in Matlab/Simulink through the Waijung blockset [11] using a 4th Runge-Kutta method sampled each 1 ms (Fig. 6). The electronic system was validated through Proteus (Fig. 7). The bilateral control scheme was assessed by introducing a user-based trajectory to be tracked by the slave system while the environmental force effects feedback the user system. Figure 8 shows the position response of the slave system (q_s) with respect to the master movement (q_m) where the slave response can track accurately the master reference. The control constants were $k_p = 300$, $k_d = 70$ (slave controller) and $k_f = 35$ was the force sensitivity constant for the master system. The observer gains were $\lambda_{m2} = 29$, $\lambda_{m1} = 156$, and $\lambda_{m0} = 180$ (same values for the slave system).

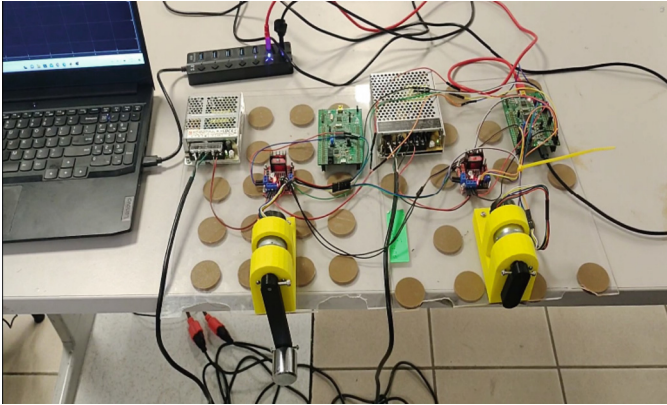


Fig. 5. Bilateral control test bed.

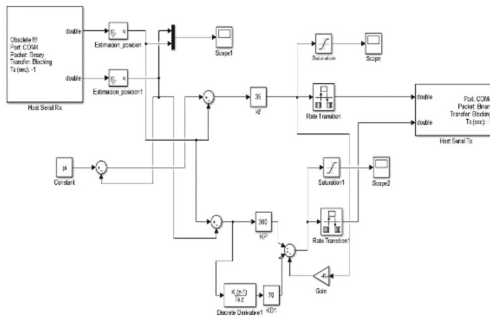


Fig. 6. Bilateral control Simulink programming framework.

3.2 FlexSensor Characterization

The implementation of the characterization from the FlexSensor provides information about the positions of the sensor. The voltage on the sensor corresponds to change on the position of the phalanx, must be noticed that the data possesses measurement noise that must be eliminated. A comparison between the original and the filtered data shown on Fig. 9 allows to see that the implementation of the 3rd order Bessel filter allows the elimination of the measurement noise without generate a deformation on the signal. This implies the filtered data is feasible to be used for the computation of the reference tracking signal on the bilateral control.

3.3 Orthosis Position Estimation

To verify that the computed values produce a shape of the phalanx on the orthosis similar to the shape of the phalanx on the hand these positions are used to compute the inverse kinematics and with the estimated angular positions a simulation using the Robotics Toolbox of Matlab is performed.

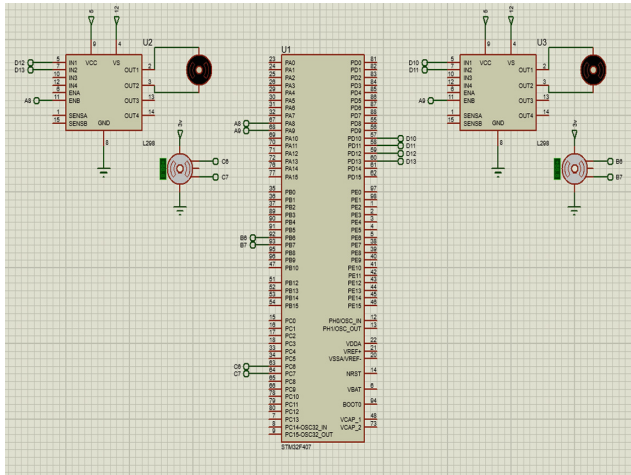


Fig. 7. Bilateral control proteus simulation.

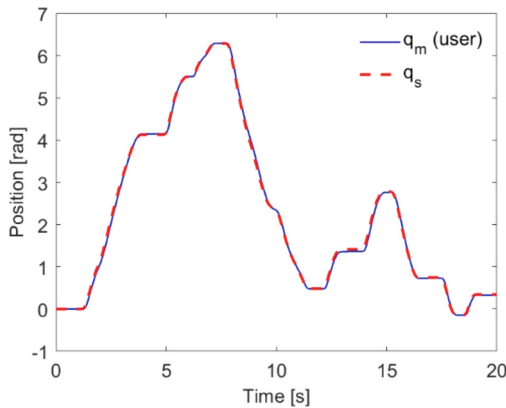


Fig. 8. Bilateral control experimental results.

The implementation uses the data given on Table 1 to configure the simulation and considers that $q_1 = 0$ as the position of the first link is fixed. The correspondence between both elements is shown Fig. 10, on this could be noticed that for the position when the phalanx is extended the correspondence between both positions fulfil the expected results.

Moreover, Fig. 11 shows that the positions for a grip task corresponds between the phalanx position and the equivalent orthosis. This allows to verify that the measurement of the positions performed with the FlexForce is a feasible way to determine the positions of the orthosis.

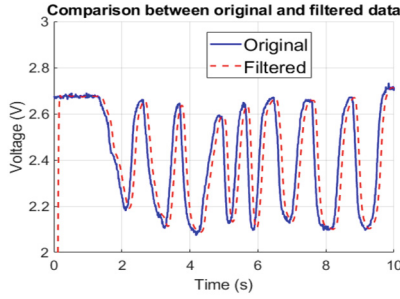


Fig. 9. Comparison between the original and the fitted data.

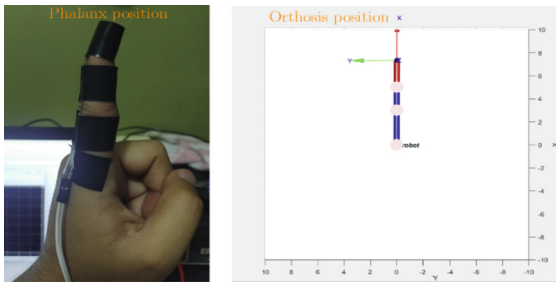


Fig. 10. Extended phalanx and the corresponding estimated position to the orthosis based on the inverse kinematics.

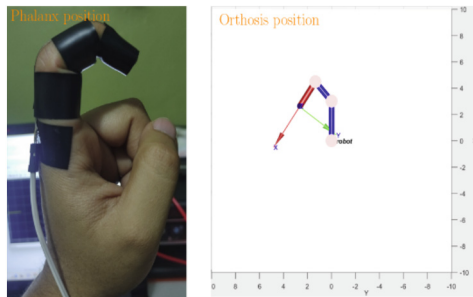


Fig. 11. Grip on phalanx and the corresponding estimated position to the orthosis based on the inverse kinematics.

4 Discussion

The presented results are a first step in the general development of a haptic hand, which is not fully competitive with complete reported schemes such as in [4–6]. However, the perspectives of the presented work would offer the following advantages: Concerning [4], our proposal needs fewer sensing signals (neither a training process) to provide an accurate bilateral control, the presented embedded processing is more accurate and fast regarding the one in [5]. Finally, the model of [6] can be used along with the

presented bilateral control proposal with disturbance compensation to improve both tracking schemes.

5 Conclusions and Future Work

The developed work allows to conclude the following statements:

- The Bilateral scheme provides an adequate methodology to control an orthosis structure because provides force feedback to the user.
- The implementation of a glove with a FlexSensor is an option to measure the positions of the phalanx.
- The data acquired with the FlexSensor requires a filtering process to provide a feasible signal for their use on an orthosis application.
- The reference for the actuators from a 3DoF orthosis for grip tasks can be estimated based on the phalanx measurements when an inverse kinematics is applied.

As future work it is necessary the instrumentation of all the phalanx of the orthosis and the implementation of the estimated positions as a reference signal on a real-time implementation. The computation of the inverse kinematics could be improved to consider 3DoF to assure other tasks could be implemented.

Acknowledgments. This research was funded by Secretaría de Investigación y Posgrado IPN under Grant Numbers 20231585, 20232388, 20231157, 20230472.




References

1. Bos, R.A., et al.: A structured overview of trends and technologies used in dynamic hand orthoses. *J. Neuroeng. Rehabil.* **13**(1), 1–25 (2016)
2. Portnoy, S., et al.: Automated 3D-printed finger orthosis versus manual orthosis preparation by occupational therapy students: preparation time, product weight, and user satisfaction. *J. Hand Ther.* **33**(2), 174–179 (2020)
3. Hernández-Melgarejo, G., Castañeda, L.A., Luviano-Juárez, A., Chairez, I.: Bilateral output-based control of a Master-Slave mechanical system: an active disturbance rejection approach. In: 2016 American Control Conference (ACC), pp. 5284–5289. IEEE, Italy (2016)
4. Zhu, M., Sun, Z., Zhang, Z., Shi, Q., He, T., Liu, H., Lee, C.: Haptic-feedback smart glove as a creative human-machine interface (HMI) for virtual/augmented reality applications. *Sci. Adv.* **6**(19) (2020)
5. Repullo Menéndez, M.: Desarrollo de un guante háptico con realimentación táctil. Bachelor Thesis. Escuela Técnica Superior de Ingenieros Industriales (UPM), Spain (2021)
6. Wang, Z., Qiu, Y., Zheng, X., Hao, Z., Liu, C.: Biomechanical models of the hand-arm system to predict the hand gripping forces and transmitted vibration. *Int. J. Ind. Ergon.* **88**, 103258 (2022)
7. Nagatsu, Y., Hashimoto, H.: Bilateral control by transmitting force information with application to time-delay systems and human motion reproduction. *IEEJ J. Ind. Appl.* **10**(2), 165–177 (2021)
8. Spong, M.W., Hutchinson, S., Vidyasagar, M.: *Robot Modeling and Control*. John Wiley & Sons (2020)

9. Ljung, L., Andersson, C., Tiels, K., Schon, T.B.: Deep learning and system identification. *IFAC-PapersOnLine* **53**(2), 1175–1181 (2020)
10. Sira-Ramírez, H., Luviano-Juárez, A., Ramírez-Neria, M., Zurita-Bustamante, E.W.: *Active Disturbance Rejection Control of Dynamic Systems: A Flatness Based Approach*. Butterworth-Heinemann (2017)
11. Hmidet, A., Hasnaoui, O.: Waijung blockset-STM32F4 environment for real time induction motor speed control. In: 2018 IEEE 5th International Congress on Information Science and Technology (CiSt), pp. 600–605. IEEE (2018)



Lumbar Erector Spinae Activity During Anterior Trunk Flexion of People Who Use the Computer for More Than 30 h a Week

Raide Alfonso González-Carbonell^(✉) , Igor Salinas-Sánchez ,
and Jesús Manuel Dorador-González 

Escuela Nacional de Estudios Superiores Unidad Juriquilla, Universidad Nacional Autónoma de México, Querétaro 76230, México
raideglez@unam.mx

Abstract. College communities engage in more mental than physical activities, working for more than 30 h per week in sitting postures in front of computers, and it can lead to low back pain (LBP). The aim of this work was to study the LES (longissimus and multifidus) muscle activity during anterior flexion of the trunk of people involved in higher education activities who use the computer for more than 30 h a week. The lumbar muscle electromyographic activity during anterior flexion of the trunk was evaluated in 41 subjects (22 with LBP/19 without LBP) that work at the UNAM Campus Juriquilla. As results, the Flexion-relaxation phenomena was not observed in healthy participants, and myoelectric silence was not present in the multifidus muscle of LBP group. Multifidus FRR was lower than average in both groups and lower than longissimus FRR. The muscles at L4-L5 vertebrae are at higher risk of asymptomatic muscle disorders and perhaps passive structures damage as well.

Keywords: Low Back Pain · Flexion-Relaxation Phenomenon · electromyography

1 Introduction

College communities engage in more mental than physical activities, typically adopting a sedentary posture for long hours. In addition, most of their tasks require prolonged sitting time at a computer. Previous studies found that sitting postures at a computer have been related to musculoskeletal disorders [1, 2]. Among people who work for at least four hours per day at a computer, the prevalence of pain was about 55% [3] while Yue et al. [4] found the prevalence of low back pain (LBP) of 45.6%. Hanna et al. [5] investigated the association between sedentary lifestyle and LBP in college employees and found that 61.2% suffered from LBP.

Clinicians recommend measurement of trunk muscle electromyographic surface activity (EMG) as a tool to evaluate the spine function. Healthy people when flex the spine forward (cervical or lumbar spine), at the maximum flexion (peak of flexion angle,

maintenance phase) the EMG activity of the erector spinae muscles decrease at values lower than the EMG activity in the neutral position (standing), which is known as flexion-relaxation phenomenon (FRP) [6]. But in people with LBP, the EMG activity of lumbar erector spinae (LES) muscles continues still during the maintenance phase, the expected myoelectric silence and in consequence FRP are absent [7, 8]. According to [9] there are EMG differences between people with and without LBP at the maintenance phase. The FRP was found to have a strong effect and good accuracy in discriminating patients with LBP from control subjects, so it can be considered as a biomarker for the presence of LBP [10–12].

Furthermore, other indexes like flexion relaxation ratio (FRR) index are used to assess the FRP, it is a ratio between the Peak of EMG activity of the erector spinae muscles during flexion movement and the EMG activity of the erector spinae muscles during maintenance phase [10]. In general, healthy, or asymptomatic people showed higher FRR than people with chronic LBP. According to [13] computer workers with low values of FRR have potential risk of asymptomatic muscle disorders prior to the occurrence of pain at the cervical spine, but the sitting posture of cervical spine is different than lumbar spine, then the question that arises is How is the behavior of FRP and FRR at lumbar spine among people who use the computer for more than 30 h a week? The objective of this work was to study the LES (longissimus and multifidus) muscle activity during anterior flexion of the trunk of people involved in higher education activities who use the computer for more than 30 h a week.

2 Materials and Methods

2.1 Participants

Individuals from the Universidad Nacional Autónoma de México (UNAM) Campus Juriquilla community with at least 30 h of computer use per week and aged between 18 and 65 years were invited to participate in the study. Individuals with a medical history of accidents or cardiovascular or cerebrovascular disease, fibromyalgia, rheumatoid arthritis, herniated disk, whiplash, pregnancy, or those who declined to participate in the study were excluded. The Frequent Activities and Job Conditions questionnaires and the Brief Pain Inventory (BPI) were used to assess the severity of pain and its impact on functioning [14]. An experienced physiotherapist carried out a manual exploration for confirming participants self-selected pain zones.

The procedure for assessing trunk flexion relaxation was explained. From standing position, participants flexed the trunk with the knees extended up to reach the maximum voluntary flexion, remaining about 5 s and then returned to standing position. This procedure was repeated three times. This protocol was approved by the Institutional Bioethics committee from UNAM Campus Juriquilla. Participants who signed the informed consent form were enrolled in the study (Table 1).

Table 1. Characteristics of subjects.

Subject (n = 41)	
M/F, n	22/19, 41
Age in years: mean (SD)	42 (14)
Occupation: Academics/Administrative Staff/Students	14/15/12
LBP/Non-LBP	22/19

M: male; F: female; LBP: Low Back Pain

2.2 Data Acquisition

Kinematic parameters were recorded using an IMU (G-Sensor, BTS Bioengineering, Italy). Surface electromyography (sEMG) data were recorded using the FreeEMG 1000, (BTS Bioengineering, Italy). Bipolar Ag/AgCl pre-gelled bipolar electrodes (circular shape, 11 mm diameter; 25 mm center-to-center distance, see Fig. 1) were used. Before placement of the electrodes, the skin was cleaned with 5% denatured ethyl alcohol, following the recommendations of the guidelines for the use of surface electromyography for noninvasive assessment of muscles (SENIAM). The IMU was placed at the level of the line passing under the angle of the scapula. The sEMG electrodes were placed on the skin bilaterally to the spine at the longissimus (LF12 left and RT12 right) and multifidus (LF45 left and RT45 right) following the direction of the muscle fibers.

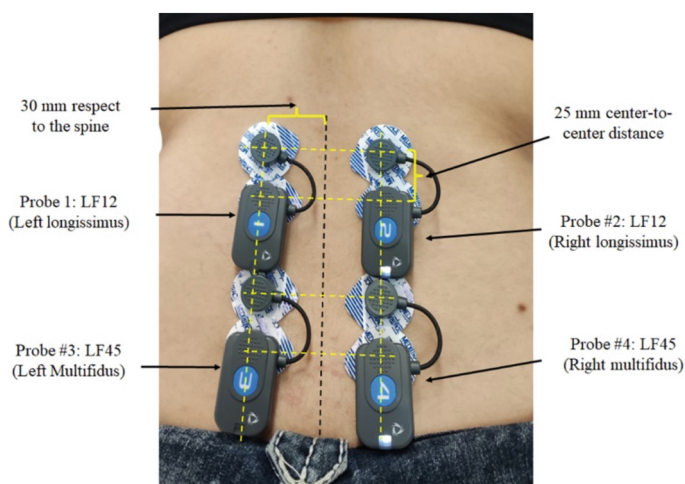


Fig. 1. EMG probes and electrodes placement bilateral at 3 cm respect to the spin and at the longissimus erector spinae (LF12 left and RT12 right) and multifidus (LF45 left and RT45 right) following the muscle fibers.

2.3 Data Analysis

The IMU and sEMG signals were sent via wireless connection to a computer. EMG Analyzer software (BTS Bioengineering, Italy) was used to acquire, process, elaborate the reports and extract the information of the tests. To eliminate noise in the sEMG signals, a bandpass filter (10–500 Hz) was used. The sEMG signals were rectified, and the root mean square (RMS) was calculated in 99 ms windows. Muscle activity during the standing phase, peak muscle activation during flexion, and muscle activity during maximum flexion (maintenance) on both sides were selected. Then, the flexion-relaxation ratio (FRR) index was calculated as follows (1):

$$FRR = \frac{\text{Peak of muscle activity during anterior flexion movement}}{\text{Muscle activity during maintenace}} \quad (1)$$

Data was saved in CSV format and used as input to a series of scripts written using the R software (R Foundation for Statistical Computing, Vienna, Austria) for the statistical analysis. The significant level was set at 0.05. The normality of the data was tested using the Shapiro-Wilk test. The unpaired t Test was utilized to determine whether there was a difference between LBP and non-LBP unpaired groups.

3 Results and Discussion

In this study the lumbar erector spinae activity was studied during anterior flexion of the trunk of people involved in higher education activities who use the computer for more than 30 h a week. BPI revealed the 53.6% of participants reported suffering from LBP, with a mild pain severity and low impact on daily life. Other areas mentioned by participants were the neck and shoulder. Participants were divided into LBP and non-LBP groups.

During the anterior flexion of the trunk with the knees extended, LES controlled the movement with an eccentric contraction; peaks of angular velocity and RMS EMG muscle activity were observed at 50% to 60% of the peak angle of the trunk flexion (Fig. 2). According to [15] the trunk flexion took place mainly in the lumbar segments of the spine at 50%. The lumbar spine reached its maximum range of motion at 75% to 85% of trunk flexion, then the final trunk flexion occurred at the level of the pelvis (lumbar pelvic rhythm). At peak of trunk flexion (maintenance phase), the participant remained for approximately 5 s. Finally, extension occurred with a concentric contraction, a second peak of angular velocity and also a peak of RMS EMG muscle activity was observed [6].

During maintenance, passive soft tissues and vertebrae provide most of the support for the spine, in healthy people a low LES activity is required to maintain this posture [10], and it should be lower than RMS during standing [10]. In Fig. 2c the thick blue line (RMS EMG during maintenance) is below the horizontal red dot line (RMS EMG during standing), meaning the presence of FRP.

In this study, people without LBP showed lower RMS of LES during standing than the LBP group ($p > 0.05$). This behavior indicated that people without LBP required a lower recruitment of LES muscle fibers to maintain the upright position. FRP was observed in the longissimus of LBP group, muscles activity of maintenance phase was lower than standing, but in the multifidus the myoelectric silence was not showed. Surprisingly, the non-LBP group did not show the FRP; both the longissimus and multifidus had greater muscle activation in the maintenance phase than in the standing position. Table 2 shows the LES muscles activity and the kinematics during the trunk flexion-extension movement of the trunk.

More than 70% of people included in the study reported sedentary activities, adopting uncomfortable for more than 10 min suffered fatigue in their lower back during their workday. According to [16] in sitting posture the muscles activity is low and the passive structure support the load and guide lumbar joints, exposition to this conditions may modify the mechanical properties of the tissue (creep viscoelasticity) and therefore onset of EMG activity of FRP. Alteration in the passive spinal structure and in the relative length of muscles (LES, hip, and hamstring) affect the range of motion of lumbar spine and the coordination of trunk and hip movements, hence muscle activity is needed during maintenance phase to stabilize the trunk [9]. Prior studies analysed the EMG activity during the sitting position and they suggest that FRP is present [17, 18], but standing to forward bending FRP were more robust, and slumped sitting FRP were less consistent.

Longissimus FRR was higher than normal (2.98) in all participants ($p > 0.05$). However, multifidus FRR was lower than normal (7.21) in both groups ($p > 0.05$). It was expected that multifidus FRR was higher longissimus FRR, but it was not obtained. This result permit inference that muscles at L4-L5 vertebrae are at higher risk of asymptomatic muscle disorders and perhaps passive structures as well. The presence of mild pain influenced the peak velocity value during flexion and extension motion, non-LBP group shows higher peak of velocity during flexion and extension. The difference was significant for the peak value of velocity during extension ($p < 0.05$).

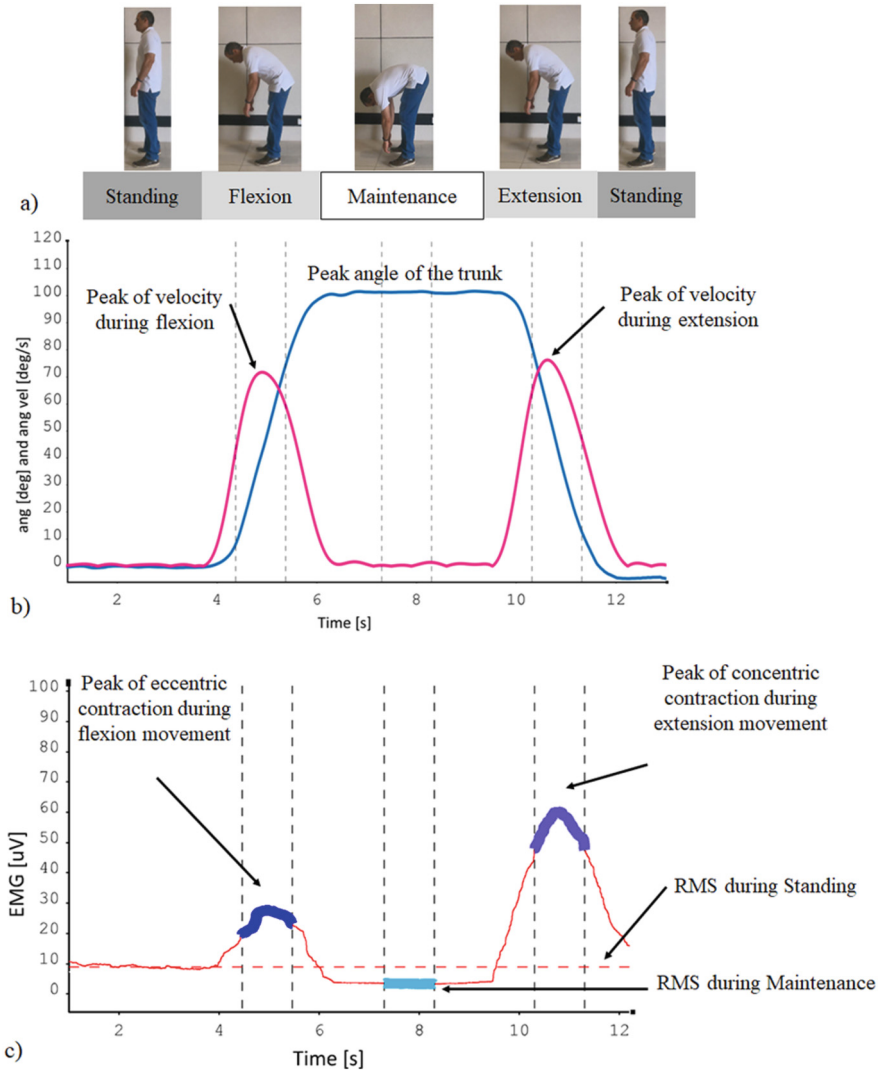


Fig. 2. Representative example of lumbar erector spinae activation of a Subject control #14 during the trunk flexion and extension: a) sequence of the trunk movement, b) angular displacement [deg] and angular velocity graphs [deg/s], and c) RMS EMG of right multifidus with presence of FRP.

During sitting, the legs are flexed, and the length of hamstring is lower than in knee extension. This posture may conduce to hamstring contraction. According to [6] increased hamstring stiffness can lead to decrease the mobility of the lumbar pelvic rhythm and consequently the peak angle of anterior flexion of the trunk. Poor trunk flexibility provokes changes in the onset of lumbar and hamstring muscles, and even asymptomatic people are at risk of LBP [15].

Table 2. Mean and standard deviation of lumbar erector spinae activation during flexion extension movement of the trunk. Reported p-values represent the comparisons of media's groups LBP and non-LBP from unpaired t Tests.

	non-LBP mean (SD)	LBP mean (SD)	p-value
Age [years]	41(15)	42(14)	0.530
RMS Maintenance LF12 [uV]	7.378(9.596)	5.142(3.688)	0.092
RMS Standing phase LF12 [uV]	6.346(4.268)	7.816(7.189)	0.361
RMS Maintenance RT12 [uV]	7.811(10.268)	5.371(4.278)	0.042
RMS Standing phase RT12 [uV]	6.399(4.438)	9.883(15.251)	0.193
RMS Maintenance LF45 [uV]	8.758(8.676)	9.707(10.518)	0.667
RMS Standing phase LF45 [uV]	5.309(2.413)	6.035(4.037)	0.093
RMS Maintenance RT45 [uV]	7.634(6.180)	9.242(8.801)	0.357
RMS Standing phase RT45 [uV]	6.349(3.042)	7.009(6.387)	0.337
FRR LF12 (Normal > 2.98)	5.486(3.559)	5.729(3.139)	0.406
FRR RT12 (Normal > 2.98)	6.656(4.840)	5.297(5.006)	0.328
FRR LF45 (Normal > 7.21)	4.428(3.284)	4.755(3.447)	0.432
FRR RT45 (Normal > 7.21)	5.218(3.931)	4.928(4.067)	0.937
Peak of velocity during flexion [deg/s]	108.6(32.4)	97.69(21.4)	0.242
Peak of velocity during extension [deg/s]	115.4(29.6)	102.3(15.3)	0.008
Flexion angle of the trunk during maintenance [deg]	111.1(18.3)	112.1(25.5)	0.651

Individuals with chronic pain were not studied, and the difference in pain scale between the two groups was not significant, so the characteristics of the two groups were similar. This is a possible explanation for why there was no significant difference between the groups in activation of the erector spinae muscle of the lumbar spine in the standing position and maximum anterior flexion.

4 Conclusions

More than 70% of people included in the study reported sedentary activities, feeling uncomfortable for more than 10 min and suffered fatigue in their lower back during their workday, and 53.6% of participants reported suffering from LBP, with a mild pain severity and low impact on daily life. Individuals with chronic pain were not studied, and the difference in pain scale between the two groups was not significant, so the characteristics of the two groups were similar. No flexion-relaxation phenomena were observed in healthy participants, and myoelectric silence was not present in the multifidus muscle of LBP group. Multifidus FRR was lower than normal in both groups and lower than longissimus FRR. The muscles at L4-L5 vertebrae are at higher risk of asymptomatic muscle disorders and passive structures damage as well.

Acknowledgments. This research was supported by UNAM-DGAPA PAPIIT TA100723. The views expressed herein are those of the authors.

Conflict of Interest. Authors have no conflict of interest to declare.

References

1. Ming, Z., Närhi, M., Siivola, J.: Neck and shoulder pain related to computer use. *Pathophysiology* **11**(1), 51–56 (2004)
2. Żywień, U., Barczyk-Pawełec, K., Sipko, T.: Associated risk factors with low back pain in white-collar workers—a cross-sectional study. *J. Clin. Med.* **11**(5), 1275 (2022)
3. Sadeghian, F., Raei, M., Amiri, M.: Persistent of neck/shoulder pain among computer office workers with specific attention to pain expectation, somatization tendency, and beliefs. *Int. J. Prev. Med.* **5**(9), 1169–1177 (2014)
4. Yue, P., Liu, F., Li, L.: Neck/shoulder pain and low back pain among school teachers in China, prevalence and risk factors. *BMC Public Health* **12**(1), 789 (2012)
5. Hanna, F., Daas, R.N., El-Shareif, T.J., et al.: The relationship between sedentary behavior, back pain, and psychosocial correlates among university employees. *Front. Public Health* **7**, 1–7 (2019)
6. Kim, C., Gwak, G., Kwon, O.: Comparison of the flexion-relaxation ratio of the hamstring muscle and lumbopelvic kinematics during forward bending in subjects with different hamstring muscle flexibility. *Physic. Ther. Korea* **24**(4), 1–10 (2017)
7. Alschuler, K.N., Neblett, R., Wiggert, E., et al.: Flexion-relaxation and clinical features associated with chronic low back pain: a comparison of different methods of quantifying flexion-relaxation. *Clin. J. Pain* **25**(9), 760–766 (2009)
8. Ramezani, M., Kordi Yoosefinejad, A., Motealleh, A., et al.: Comparison of flexion relaxation phenomenon between female yogis and matched non-athlete group. *BMC Sports Sci. Med. Rehab.* **14**(1), 14 (2022)
9. Colloca, C.J., Hinrichs, R.N.: The biomechanical and clinical significance of the lumbar erector spinae flexion-relaxation phenomenon: a review of literature. *J. Manipulative Physiol. Ther.* **28**(8), 623–631 (2005)
10. Gouteron, A., Tabard-Fougère, A., Bourredjem, A., et al.: The flexion relaxation phenomenon in nonspecific chronic low back pain: prevalence, reproducibility and flexion–extension ratios. A systematic review and meta-analysis. *Eur. Spine J.* **31**, 136–51 (2021)
11. Schinkel-Ivy, A., Nairn, B.C., Drake, J.D.M.: Evaluation of methods for the quantification of the flexion-relaxation phenomenon in the lumbar erector spinae muscles. *J. Manipulative Physiol. Ther.* **36**(6), 349–358 (2013)
12. Rose-Dulcina, K., Genevay, S., Dominguez, D., et al.: Flexion-relaxation ratio asymmetry and its relation with trunk lateral ROM in individuals with and without chronic nonspecific low back pain. *Spine* **45**(1), E1–E9 (2020)
13. Pinheiro, C.F., dos Santos, M.F., Chaves, T.C.: Flexion-relaxation ratio in computer workers with and without chronic neck pain. *J. Electromyogr. Kinesiol.* **26**, 8–17 (2016)
14. Moretti, A., Menna, F., Aulicino, M., et al.: Characterization of home working population during COVID-19 emergency: a cross-sectional analysis. *Int. J. Environ. Res. Public Health* **17**(17), 6284 (2020)
15. Takahashi, Y., Yamaji, T.: Comparison of effects of joint flexibility on the lumbo-pelvic rhythm in healthy university students while bending the trunk forward. *J. Phys. Ther. Sci.* **32**(3), 233–237 (2020)

16. Howarth, S.J., Glisic, D., Lee, J.G., et al.: Does prolonged seated deskwork alter the lumbar flexion relaxation phenomenon? *J. Electromyogr. Kinesiol.* **23**(3), 587–593 (2013)
17. Morl, F., Bradl, I.: Lumbar posture and muscular activity while sitting during office work. *J. Electromyogr. Kinesiol.* **23**(2), 362–368 (2013)
18. Schinkel-Ivy, A., Nairn, B.C., Drake, J.D.: Quantification of the lumbar flexion-relaxation phenomenon: comparing outcomes of lumbar erector spinae and superficial lumbar multifidus in standing full trunk flexion and slumped sitting postures. *J. Manipulative Physiol. Ther.* **37**(7), 494–501 (2014)



Biocompatibility In-Vivo Evaluation of Polypyrrole/Iodine Synthesized by Plasma Polymerization

Rodrigo Mondragon-Lozano¹(✉) , Hermelinda Salgado-Ceballos² ,
María Guadalupe Olayo³ , Guillermo Jesús Cruz³ , Eva González Trujano⁴ ,
Araceli Díaz-Ruiz⁵ , Stephanie Sánchez-Torres² , Carlos Orozco Barrios¹ ,
and Angelica Coyoy Salgado¹

- ¹ Unidad de Investigación Médica en Enfermedades Neurológicas, Instituto Mexicano del Seguro Social, Consejo Nacional de Humanidades Ciencia y Tecnología, Ciudad de México 06720, México
ruy.lozano@gmail.com
- ² Unidad de Investigación Médica en Enfermedades Neurológicas, Instituto Mexicano del Seguro Social, Ciudad de México 06720, México
- ³ Departamento de Física, Instituto Nacional de Investigaciones Nucleares, Ocoyoacac 52750, México
- ⁴ Laboratorio de Neurofarmacología de Productos Naturales, Instituto Nacional de Psiquiatría, Ciudad de México 14370, México
- ⁵ Departamento de Neuroquímica, Instituto Nacional de Neurología y Neurocirugía, Ciudad de México 14269, México

Abstract. Polypyrrole is recognized as a biocompatible material. Plasma polymerization is a technique that enables the synthesis of polymers utilized in certain biomedical applications. In this work, the biocompatibility of Polypyrrole/Iodine synthesized by plasma was explored through the determination of the median lethal dose and subacute systemic toxicity in-vivo murine models. The findings indicated that the median lethal dose was not reached even at a dose of 13.6 mg/Kg in Swiss-Webster mice. No mortality occurred throughout the 14-day observation period, neither persistent adverse effect or significant changes in body weight or relative organ weights. In relation to subacute systemic toxicity, transient behavioral changes indicative of stress and pain were observed in Wistar rats following administration of a 20 mg/Kg dose, these changes resolved within a period of 1 h. Additionally, an elevation in transaminase levels was detected. However, these alterations did not affect the overall clinical condition. In conclusion, the conducted investigations did not reveal any potential for systemic toxicity of Polypyrrole/Iodine up to a dose of 20 mg/Kg, which is 30 times higher than the therapeutic dose used in pre-clinical studies. Therefore, it can be considered safe for use.

Keywords: Biocompatibility · in-vivo · Polypyrrole/Iodine · Plasma Polymerization

1 Introduction

The biocompatibility of Polypyrrole synthesized by chemical and electrochemical methods has been extensively studied in various applications, from substrate for cell culture medium, to biosensor and drug releaser, to being tested as a strategy in tissue regeneration, obtaining an adequate performance in each application [1].

The plasma polymerization technique has advantages over other methods of polymer synthesis, mainly the fact that it is not necessary the intervention of other reagents to carry out the reaction, in this sense, the Pyrrole monomer has also shown outstanding characteristics in terms of biocompatibility [2]. Additionally, the iodine doping process contributes to the increase of electrical conductivity, besides favoring antibacterial activity [3].

Although detailed information regarding the structure of Polypyrrole synthesized by chemical or electrochemical methods has been published, the structure of plasma synthesized Polypyrrole remains unclear and is highly dependent on the reaction parameters [4]. However, it is known that the plasma polymerization method is characterized by a high degree of crosslinking and branching [2].

In previous studies by this research group, the use of Polypyrrole/Iodine has been demonstrated as a treatment for spinal cord injury, yielding favorable biological response and functional recovery in rats. Although the doses examined thus far have shown neuroprotective and neuroregenerative therapeutic responses (0.66 mg/Kg) [5, 6] devoid of significant adverse effects. This study investigates the dosage at which Polypyrrole/Iodine exhibits toxicity.

In this work, the biocompatibility of plasma-synthesized PPy/I was explored to determine the dosage at which Polypyrrole/Iodine exhibits toxicity, [7] in order to identify a safety margin between the therapeutic dose and the minimum toxic dose, had been accomplished by determining the mean lethal dose and evaluating the subacute systemic toxicity in in-vivo murine models.

2 Methods

2.1 Polypyrrole/Iodine Synthesis and Characterization

PPy/I was synthesized in a tubular plasma reactor and characterized according to a previous work [5]. The monomer employed for polymerization was Pyrrole (Sigma-Aldrich®, CAS-No: 107-97-7, product No: 131709), with Iodine as the dopant (Sigma-Aldrich®, CAS-No: 7553-56-2, product No: 207772). Reactions began in the gas phase, concluding as solid-phase thin films on the internal reactor surface. Following synthesis, the PPy/I was subjected to a grinding and subsequently autoclaved using steam under a pressure of 1.5×10^6 Pa at a temperature of 120 °C for a duration of 15 min. The morphology study of the surface was performed with a JEOL JSM-5900LV (Peabody, Massachusetts, USA) scanning electron microscopy (SEM) before sterilization and after sample preparation.

2.2 Sample Preparation and Doses

Sample preparation was carried out according ISO 10993-12:2012 [8]. In order to determine the doses to be tested, therapeutic dose of PPy/I that has been used in previous works [5, 6] was taken into account as reference (0.66 mg/Kg). In all experiments the via of administration was intraperitoneal in a single dose, saline was used for preparing a suspension with PPy/I and as vehicle.

2.3 Experimental Animals

All experimental procedures were conducted following the Mexican general law of health regulations for research and science [DOF 02-04-2014] [9], as well as the Mexican guidelines for animal care and handling [NOM-062-ZOO-1999] [10] with the register protocol (R-2015785-060) at Instituto Mexicano del Seguro Social. Every attempt was made to mitigate animal discomfort and minimize the number of animals used.

2.4 Median Lethal Dose

Female Swiss-Webster mice (average 24 g) were divided in groups with different doses: Vehicle (300 μ l and 600 μ l of Saline) and Polypyrrole/Iodine (6.6 mg/Kg and 13.2 mg/Kg) and a Control group consisting of healthy individuals [11]. Behavior was reported with a Functional Observational Battery (FOB) for determining adverse effects [12] within the first 24 h, besides body weight was recorded up to 14 days. Finally, they were euthanized, macroscopic necropsy was performed and organs weighed were registered.

2.5 Subacute Systemic Toxicity

The evaluation of subacute systemic toxicity was carried out in female Wistar rats (average 230 g) were divided in groups: Control, Vehicle (1 ml of Saline) and Polypyrrole/Iodine (20 mg/Kg), changes in behavior were recorded for 24 h after administration with a FOB [12]. After a 14-day follow-up period, euthanasia was carried out, and blood samples were collected for subsequent blood cytometry and blood biochemistry analyses, finally, organs were also extracted and weighed.

3 Results

3.1 Polypyrrole/Iodine Synthesis and Characterization

Figure 1, shows SEM micrographs of PPy/I. Morphologically, the polymer is formed by fine rough particles of variable size with irregular shapes and multiple edges (mean 4.2 μ m) resulting from grinding, Fig. 1A. The micrograph in Fig. 1B presents the PPy/I after the sterilization process and sample preparation, it is observed that the particles have coalesced forming a mostly smooth surface without edges and with pores.

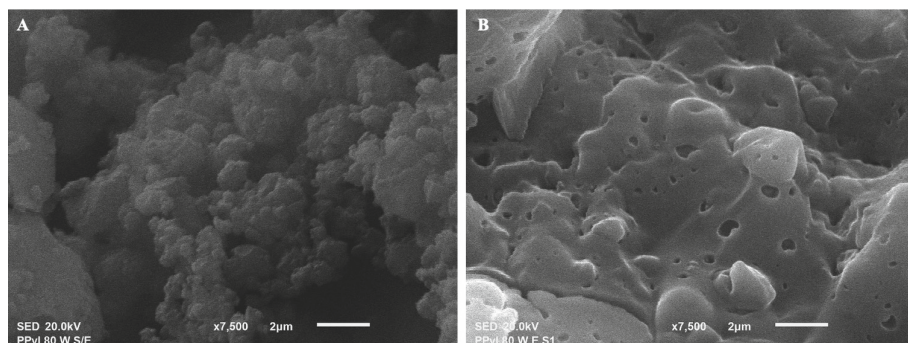


Fig. 1. Polypyrrole/Iodine synthesized by plasma micrographs SEM. A. PPy/I before sterilization. B. PPy/I after sterilization

3.2 Median Lethal Dose

A maximum dose of 13.6 mg/kg was achieved using a volume of 600 μ l. Behavioral recordings conducted over a 24-h period revealed that animals receiving Saline exhibited hypokinesia (up to 75%) and lordosis (up to 25%) behaviors, which subsided within the first hour. In contrast, animals treated with Polypyrrole/Iodine shown hypokinesia (up to 83%) and lordosis (up to 83%) behaviors that persisted for two hours before returning to normal behavior. There were shown changes in body weight around 1%. No deaths occurred in either group of mice, and there were no presented severe side effects during the 14-day follow-up period. After animal euthanasia, a gross necropsy was performed, no abnormalities have been found and their organs (brain, heart & lungs, liver, kidneys and spleen) had been dissected and weighed Table 1. No significant statistical differences were observed between experimental groups and relative organ weights. Two-way ANOVA ($p = 0.6816$).

Table 1. Bodyweight change and relative organ weight percentage, Swiss-Webster mice. Mean \pm SD.

Group	Bodyweight (g) Day 14	Weight Change (%)	Relative organ weight (%)				
			Brain	Heart & Lungs	Liver	Kidneys	Spleen
PPy/I (6.6 mg/Kg)	26.38 \pm 0.50	1.02	1.60 \pm 0.09	1.50 \pm 0.27	5.08 \pm 0.66	1.22 \pm 0.10	0.62 \pm 0.12
PPy/I (13.2 mg/Kg)	27.98 \pm 1.75	1.04	1.52 \pm 0.10	1.45 \pm 0.26	4.94 \pm 0.26	1.20 \pm 0.10	0.63 \pm 0.08
Saline (300 μ l)	28.10 \pm 0.31	1.01	1.53 \pm 0.12	1.42 \pm 0.13	5.06 \pm 0.38	1.47 \pm 0.41	0.68 \pm 0.18
Saline (600 μ l)	28.20 \pm 0.42	1.03	1.46 \pm 0.07	1.42 \pm 0.13	5.28 \pm 0.02	1.47 \pm 0.41	0.80 \pm 0.18
Control	24.99 \pm 2.28	1.08	1.55 \pm 0.10	1.17 \pm 0.11	6.71 \pm 0.97	1.43 \pm 0.16	0.77 \pm 0.15

3.3 Subacute Systemic Toxicity

Throughout the 14-day duration of the study, all experimental animals had survived. In the Polypyrrole/Iodine group, lethargy events had been observed (up to 70%), but they had resolved within 60 min after administration. A 1% increase in bodyweight had been observed in all experimental groups.

Following euthanasia, the spleen, kidneys, brain, liver, heart, and lungs had been dissected. No evidence of hemorrhage or fluid accumulation in the thoracic or abdominal cavity had been detected in any of the individuals. In all cases, the organs were positioned and located as expected and did not exhibit enlargement or deformities. No significant difference was found in the relative organ weights. Two-way ANOVA ($p = 0.2056$).

The values of blood cytometry and blood biochemistry test analytes were compared to standardized reference values based on strain, sex, and age range in healthy individuals [13, 14]. According to cytometry analysis, no findings of anemia or evidence of erythropathy were observed. Regarding the leukocyte series, no alterations in the quantity or distribution of cell populations (Neutrophils, Basophils, Eosinophils, Lymphocytes, Monocytes) were detected that could suggest bacterial infection, inflammation, parasitosis, or allergies. Additionally, no morphological changes such as reactive lymphocytes or toxic neutrophils were reported. Finally, the platelet series exhibited values within the normal reference range, and there was no evidence of hemorrhage.

In the biochemical analysis, the glycemic (Glucose) and lipid (Triglycerides, Cholesterol) profiles did not exhibit values outside the reference range in any case. In the liver profile (Total Bilirubin, Direct Bilirubin, Indirect Bilirubin, ALT, AST, ALP), an increase in transaminases (ALT, AST, and ALP) was observed in the Polypyrrole/Iodine group, while the Saline group only showed an increase in ALP. The Control group exhibited increases in Direct Bilirubin, ALT, and ALP parameters. In the renal profile (Urea, Creatinine), the Control group demonstrated increases in both parameters, while the Saline and PPy/I groups only showed an increase in Urea. Plasma proteins (Albumin) did not manifest any values outside the reference range in any group. Finally, electrolytes (Sodium, Chloride, Potassium, Calcium and Phosphorus) solely exhibited an increase in Phosphorus for the experimental groups Saline and PPy/I, relative to the reference values Table 2. Values of serum biochemical parameters, Wistar rats.

Table 2. Values of serum biochemical parameters, Wistar rats. Mean.

Analyte	Reference	Control	Saline (1 ml)	PPy/I (20 mg/Kg)
Glucose (mmol/L)	4.89–8.96	8.85	6.9	7.75
Triglycerides (mmol/L)	0.18–1.98	1.45	1.3	1.9
Cholesterol (mmol/L)	0.6–2.51	1.915	1.71	1.91

(continued)

Table 2. (continued)

Analyte	Reference	Control	Saline (1 ml)	PPy/I (20 mg/Kg)
Total Bilirubin ($\mu\text{mol/L}$)	1.2–3.6	2.5	1.35	1.85
Direct Bilirubin ($\mu\text{mol/L}$)	0.51–1.2	1.3	0.7	0.9
Indirect Bilirubin ($\mu\text{mol/L}$)	0.34–2.22	1.2	0.65	0.95
Alanine Aminotransferase (ALT) ($\mu\text{mol/(s}\cdot\text{L)}$)	0.23–1.07	1.35	1.07	1.4
Aspartate Aminotransferase (AST) ($\mu\text{mol/(s}\cdot\text{L)}$)	1.07–3.7	2.68	3.04	4.43
Alkaline Phosphatase (ALP) ($\mu\text{mol/(s}\cdot\text{L)}$)	0.3–1.03	2.86	3.33	3.06
Urea (mmol/L)	5.84–6.94	8.5	8.05	8.2
Creatinine ($\mu\text{mol/L}$)	26.52–53.05	55.5	48	53
Albumin (mmol/L)	0.56–0.87	0.68	0.59	0.65
Sodium (mmol/L)	135–146	139.5	137	136.5
Chloride (mmol/L)	97–106	105	102	105.5
Potassium (mmol/L)	5.3–7.5	7.35	8.4	9.35
Calcium (mmol/L)	2.37–3.02	2.66	2.39	2.56
Phosphorus (mmol/L)	1.46–3.07	2.2	2.43	2.37

4 Conclusions

Prior research indicates that plasma polymerization generated Polypyrrole structures exhibit branching and crosslinking, in contrast to those generated through conventional methods, conversely, the surface appears smoother in comparison [2]. However, in this work it was observed that after the sterilization process the particles fuse and pores are formed on the surface. Some works in this regard mention that the presence of pores can contribute to the compatibility of polymers such as Polypyrrole [15], with the advantage that plasma polymerization does not involve other reagents that could affect its performance.

Comparing the biological response of Polypyrrole/iodine from this work with other polymers synthesized by conventional methods [16], it is found that they have an adequate biocompatible response, however they require purification processes before being used

The biocompatibility evaluation of the plasma-synthesized Polypyrrole/Iodine has demonstrated good tolerance up to a dose of 13.6 mg/Kg, as evidenced by the absence of mortality in the experimental animals. Furthermore, no significant changes in body weight or relative organ weight percentage were observed, and no severe adverse effects were detected. In terms of subacute systemic toxicity, a maximum dose of 20 mg/Kg was administered without statistically or biologically significance increase in frequency or severity of adverse effects or alterations in blood cytometry or blood biochemistry






parameters. Therefore, doses up to 20 mg/Kg of plasma-synthesized Polypyrrole/Iodine can be deemed safe for use.

References

1. Wang, X., et al.: Evaluation of biocompatibility of polypyrrole in vitro and in vivo. *J. Biomed. Mater. Res.* **68**(3), 411–422 (2004)
2. Wang, J., et al.: Comparative study of chemically synthesized and plasma polymerized pyrrole and thiophene thin films. *Thin Solid Films* **446**(2), 205–217 (2004)
3. Moulay, S.: Molecular iodine/polymer complexes. *J. Polym. Eng.* **33**(5), 389–443 (2013)
4. Li, C., et al.: Fabrication and structural characterization of plasma polymerized polypyrrole thin film. *Surf. Coat. Technol.* **320**, 206–212 (2017)
5. Mondragon-Lozano, R., et al.: Delayed injection of polypyrrole doped with iodine particle suspension after spinal cord injury in rats improves functional recovery and decreased tissue damage evaluated by 3.0 Tesla in vivo magnetic resonance imaging. *Spine J.* **17**(4), 562–573 (2017)
6. Sánchez-Torres, S., et al.: Recovery of motor function after traumatic spinal cord injury by using plasma-synthesized polypyrrole/iodine application in combination with a mixed rehabilitation scheme. *J. Mater. Sci. Mater. Med.* **31**(58), 1–18 (2020)
7. Lewis, R.W., et al.: Recognition of adverse and nonadverse effects in toxicity studies. *Toxicol. Pathol.* **30**(1), 66–74 (2002)
8. International Organization for Standardization: Biological Evaluation of Medical Devices—Part 12: Sample Preparation and Reference Materials. *ISO 10993-12*, 2012 (2012)
9. Reglamento de la ley general de salud en materia de investigación para la salud. *Diario oficial de la federación*. DOF 02-04-2014 (2014)
10. Norma Oficial Mexicana: Especificaciones técnicas para la producción, cuidado y uso de los animales de laboratorio. *Diario oficial de la federación*, secretaría de agricultura, ganadería, desarrollo rural, pesca y alimentación, NOM-062-ZOO-1999 (2001)
11. Van den Heuvel, M.J., et al.: The international validation of a fixed-dose procedure as an alternative to the classical LD50 test. *Food Chem. Toxicol.* **28**(7), 469–482 (1990)
12. Mathiasen, J.R., et al.: The Irwin test and functional observational battery (FOB) for assessing the effects of compounds on behavior, physiology, and safety pharmacology in rodents. *Curr. Protoc. Pharmacol.* **83**(1), 1–18 (2018)
13. Vigneshwar, R., et al.: Sex-specific reference intervals for Wistar albino rats: hematology and clinical biochemistry. *Indian J. Anim. Health* **60**, 58–65 (2021)
14. Giknis, M.L.A., et al.: Clinical laboratory parameters for CrI: Wi(Han) rats. Charles River Laboratories. <https://www.criver.com/> (2008)
15. Fonner, J.M., et al.: Biocompatibility implications of polypyrrole synthesis techniques. *Biomed. Mater.* **3**(3), 034124 (2008)
16. Ramanaviciene, A., et al.: Biocompatibility of polypyrrole particles: an in-vivo study in mice. *J. Pharm. Pharmacol.* **59**(2), 311–315 (2007)



Exploring the Biological Potential of Hydroxyapatite-Doped with Magnesium: Cytotoxicity and Cell Viability Assessment

Rafael Rangel Ibarra¹ , Juan David Olivares Hernández² , José Rafael Alanís Gómez¹ , and Fabiola Hernández-Rosas³  

¹ Faculty of Biomedical Engineering, Anáhuac Querétaro University, 76246 El Marqués, México

² Institute of Neurobiology, National Autonomous University of Mexico, Campus Juriquilla, 76230 Querétaro, Mexico

³ Research Center, Anáhuac Querétaro University, 76246 El Marqués, México
fabiola.hernandez86@anahuac.mx

Abstract. Hydroxyapatite (HAp) is a bioceramic material of great interest in the field of tissue engineering and bone regeneration due to its high biocompatibility and bioactivity in the human body. HAp has been doped with different elements including magnesium, strontium, silver, among others. Particularly, magnesium-doped hydroxyapatite (HAp-Mg) appears to have high potential in biomedical applications. Therefore, it is relevant to characterize its biological compatibility and cytotoxicity. In this study, an *in vitro* model of fibroblasts obtained from chicken embryos was used to evaluate the effect of HAp-Mg on cell viability. HAp doped with 2% magnesium was synthesized using the Microwave-Assisted Hydrothermal Method. Subsequently, X-ray diffraction analysis was performed to characterize the HAp-Mg samples. Morphological and microstructural characterization of HAp-Mg was carried out using scanning electron microscopy (SEM). To evaluate the effect of HAp-Mg on cell viability, primary cultures of fibroblasts from 10-day-old chicken embryos (ED10) were obtained. The cultures were treated with different concentrations of HAp-Mg (0.1–100 µg/ml) for 24 h. Cell viability and cytotoxicity were then evaluated using MTT and AlamarBlue assays. The results revealed that the tested concentrations of HAp-Mg did not present significant cytotoxic effects. These findings suggest that HAp-Mg has excellent biological compatibility and can be considered as a promising material for biomedical applications.

Keywords: Hydroxyapatite · Biological Assay · Biomaterials · Tissue Engineering

1 Introduction

There are different conditions that hinder bone regeneration or repair, whether from fissures, fractures or genetic malformations; Furthermore, the characteristic selfrepairing capacity of this tissue depends on the type of bone to which it belongs; for example,

flat bones such as those in the region of the skull and face have a lower tendency for osteoblast differentiation due to their intramembranous ossification, so their regeneration is slower than that of long bones. Despite the fact that bone tissue has a high tendency to differentiation and repair, to avoid adverse effects of the aforementioned morphophysiological conditions, it is necessary to find ways to improve and accelerate these osteogenic processes. Once its cell viability and cytotoxicity have been verified, a good alternative to solve these problems is the use of hydroxyapatite nanoparticles [1]. Hydroxyapatite (HAp) belongs to the group of phosphate minerals with a chemical formula of: $[Ca_{10}(PO_4)_6(OH)_2]$ and is found in the human body as carbonated apatite deficient in calcium when the bone is in the process of mineralization [2]. It is a bio-ceramic material of great interest in regenerative medicine given its high biocompatibility and bioactivity in the human body and can be obtained synthetically as hydroxyapatite nanofibers by the microwave-assisted hydrothermal method [3]. HAp has been doped with different elements including magnesium, titanium, silver, among others [4, 5]. Particularly, magnesium-doped HAp (Mg-HAp) appears to have high potential in biomedical applications. Magnesium ions are directly involved in numerous biological mechanisms; for example, they are an important part of the regulation of ion channels, they participate in DNA stabilization and in the activation and stimulation of cell growth and proliferation enzymes [6]. In this study, we sought to successfully dope hydroxyapatite nanofibers with magnesium and analyze their structural properties and biological compatibility in the chicken embryo model because the presence of magnesium in the chemical structure of hydroxyapatite can positively influence the expression of genes associated with osteoblast differentiation, which promotes the production and mineralization of the bone matrix [6]. Additionally, magnesium has the potential to enhance cell adhesion on the surface of doped hydroxyapatite, thus facilitating the interaction of cells with the implanted material. Better cell adhesion is essential for successfully colonizing bone cells on the implant surface, which is crucial for forming functional bone tissue [4]. On the other hand, the magnesium released from the doped hydroxyapatite can act as a regulator of cell activity and bone remodeling processes since magnesium ions can influence the activity of osteoclasts and osteoblasts, thus helping to maintain a proper balance between bone formation and resorption [4, 5]. Magnesium can also enhance the deposition of hydroxyapatite crystals and the formation of bonds between the particles of the material, resulting in a stronger and more resistant bone matrix, thus favoring hydroxyapatite-induced bone remineralization [5]. Thus, it is relevant to characterize hydroxyapatite's chemical, structural, and biological properties doped with magnesium, which will be evaluated *in vitro*. Therefore, our research question becomes: How does the integration of magnesium into the chemical structure of synthetic hydroxyapatite affect cellular viability, biocompatibility, and the creation of functional bone tissue when employing a chicken embryo animal model?

2 Material and Methods

2.1 Nano Hydroxyapatite Synthesis

The procedure currently used for the synthesis of HAp fibers was the following: Initially, the reagents are dissolved in tridistilled water at 60 °C with a magnetic stirrer for 2 h to obtain two independent solutions; one containing glutamic acid [$C_5H_9NO_4 \cdot H_2O$] and calcium nitrate [$Ca(NO_3)_2 \cdot 4H_2O$] and the other containing monobasic potassium phosphate [KH_2PO_4] mixed with potassium hydroxide [KOH].

Subsequently, both solutions were mixed with 2% of magnesium nitrate [$Mg(NO_3)_2$] was added to the chemical composition of the mixture and it was kept constant for the end of the chemical reaction. The reaction mixture was placed inside the quartz tubes. For the experimental setup, HAp synthesis was performed in a microwave oven (Synthos 3000 from Anton Paar) with the following parameters: heating rate of 7.5 °C/min up to 170 °C and final pressure of 80 kPa. The reaction was held for another 45 min for each experiment. After the completion of the reaction, the white crystalline solid obtained from the reaction mixture was filtered and washed with a cold 1:1 mixture of ethanol and water and dried at 50 °C in a light vacuum oven.

2.2 X-ray Diffraction Experiments

To identify the crystalline components contained in the final product, XRD was performed on all samples obtained from the synthesis reactions. A D8 Advance diffractometer manufactured by Bruker was used for the analyzes and the operating conditions in the equipment were 35 kV voltage and a current of 15 mA. A CuK_{α} radiation (wavelength of $\lambda = 1.5406 \text{ \AA}$) was used. All diffraction experiments were done from 10° to 90° on a 2 θ scale with a step size of 0.05°.

2.3 Scanning Electron Microscopy

A JEOL JSM-6390 LV scanning electron microscope (SEM) was used to observe the morphology and microstructure of all samples under the microscope. The voltage used was 20 kV and all images were formed from secondary electrons. The HAp-Mg sample was collected when the drying process finished. A small portion of the filtered solid was placed in a sample holder and covered with a charcoal paint. The specimens were then observed using a JOEL SEM (Model 6400F, JEOL, Tokyo, Japan). The samples used in the SEM study were 8.0 mm in diameter and 2.0 mm thick.

2.4 Culture and Treatment of Fibroblasts Obtained from Chicken Embryos

Primary cultures of chicken embryo fibroblasts were made, which were maintained in MEM medium with 10% inactivated fetal bovine serum (SBFi) and a mixture of 5% gentamicin, penicillin (100 u/mL) and streptomycin (100 ug/mL) in the presence of 5% CO₂ at 37 °C. Once 80% confluence was reached, the cells were treated with different concentrations of HAp (0.1, 1, 10 and 10 ug/ml) previously dissolved in DMSO. Treatments were started for 6 days under the aforementioned conditions. Untreated cells were used as control.

2.5 Cell Viability and Cytotoxicity Assays

To assess cytotoxicity, an MTT solution was prepared by dispersing 10 mg of the sample in 10 ml of Hank's balanced solution. Primary cultures of chicken embryo fibroblasts were made, which were maintained in a 96-well plate with MEM medium + 10% SBFi and a mixture of 5% antibiotics in the presence of 5% CO₂ at 37 °C for 6 days.

The *in vitro* growth inhibition effect of the test compound was evaluated by spectrophotometric determination of the conversion of MTT to "formazan blue" by living cells. To evaluate cell viability, the AlamarBlue Assay (Thermo Scientific, USA) was performed. Cells were harvested after 6 days of HAp treatment in 96-well plates. Subsequently, 10% of the volume of the AlamarBlue reagent medium was added, which is reduced by living cells to a blue compound. Cultures were incubated for 2 h and cytotoxicity was measured by spectrophotometry at 570 nm in a spectrophotometer (Multiskan SkyHigh, Thermo Scientific, USA).

3 Results

3.1 X-ray Diffraction Experiments

X-ray diffraction shows the production of highly crystalline HAp-Mg. Phase identification was made by comparison with ICDD PDF files [Brucker]. The diffractogram indicates the Miller indices for the main reflections, which correspond to planes 211 (more intense), 300, 120, 130, 100 and 002 of the HAp according to PDF 86-1199. Figure 1 shows narrow, well-defined Bragg reflections, which also exhibit high intensities.

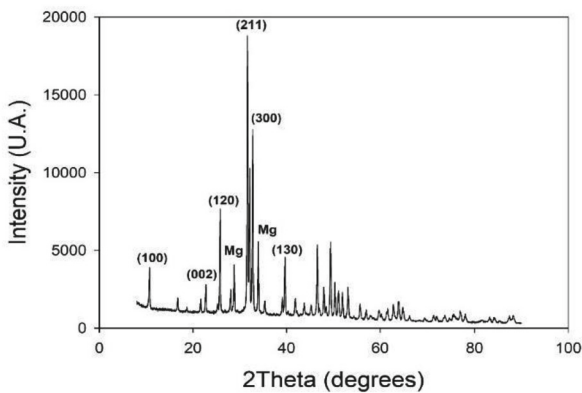


Fig. 1. Diffractogram of magnesium-doped hydroxyapatite.

3.2 SEM Experiments

Regarding the SEM, in the morphological and topological analysis of the HAp we can observe elongated crystalline nanofibers with a hexagonal structure which are grouped forming conglomerates (Fig. 2).



Fig. 2. Microphotographs of magnesium-doped hydroxyapatite obtained by SEM at different magnifications.

3.3 Cytotoxicity and Cell Viability Assays

In the morphological evaluation of the primary cultures of fibroblasts at 1–6 days of treatments, no changes in cell morphology or reduction in the number of cells were observed (Fig. 3a–f). The results of the Alamar Blue and MTT assays do not show a significant reduction in cell viability (Fig. 3g and Fig. 3h).

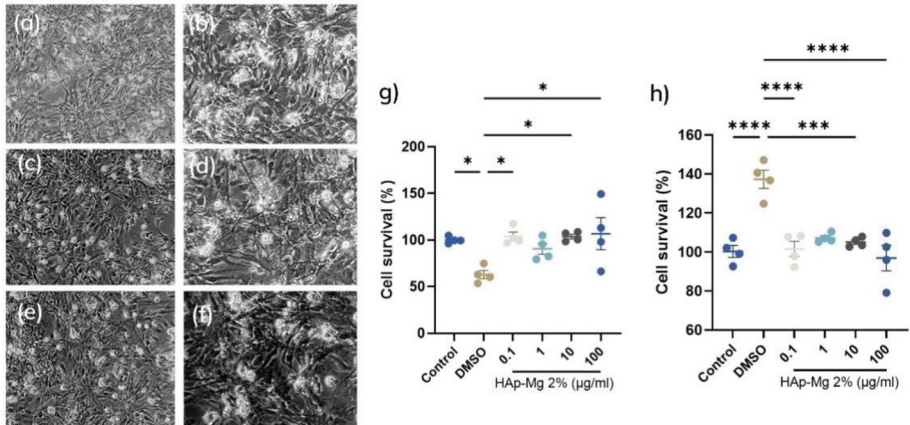


Fig. 3. Chicken embryo fibroblasts in culture treated with different concentrations of HAp. Treated cells: a) HAp-Mg 0.1 µg/ml b) HAp-Mg 1 µg/ml c) HAp-Mg 10 µg/ml d) HAp-Mg 100 µg/ml e) and f) Control cells without treatment. g) Results of MTT assay h) Results of Alamar-Blue assay.

4 Discussion and Conclusion

In this study, we successfully obtained magnesium-doped hydroxyapatite nanofibers with a unique highly crystalline hexagonal nanofiber structure. Our crystallographic data confirmed the successful doping of hydroxyapatite with magnesium, employing the previously described mechanism of ionic exchange with calcium. The resulting structure exhibited a remarkable resemblance to the mineral found in natural bone, implying a higher potential for interaction with the surrounding bone tissue and enhanced biocompatibility. Particularly, the hexagonal morphology of these nanofibers played a pivotal role in promoting the adhesion of bone cells and providing a three-dimensional surface for cell anchoring and proliferation, thereby facilitating bone tissue regeneration. Previous research has already established that hydroxyapatite with similar characteristics favors bone regeneration both in *in vivo* and *in vitro* settings [4–7]. Moreover, the highly crystalline structure of these nanofibers demonstrated increased long-term stability in animal models, which is crucial to ensure that implants or coatings maintain their properties throughout the regeneration process, alongside improvements in mechanical properties compared to commercial hydroxyapatites [1]. This morphology and crystalline structure enhance the potential of these nanofibers in the development of bone implants and replacements, owing to their increased mechanical strength, as we evidenced in previous tension-deformation assays [3]. In the biological realm, we evaluated the cell viability and cytotoxicity of the HAp-Mg nanofibers through MTT and AlamarBlue assays. The results indicated that cell viability does not decrease as the concentration of magnesium-doped hydroxyapatite increases. Specifically, at higher concentrations of hydroxyapatite, cells exhibited greater viability compared to control samples. This finding suggests promising potential for bone regeneration, which could significantly impact the field of regenerative medicine.






While we have established the induction of cell proliferation, especially in stem cells and osteocytes, delving into the molecular and cellular mechanisms associated with this inductive effect will be crucial in future studies. The process of ionic doping in hydroxyapatite has gained prominence in regenerative medicine and bone tissue regeneration, as it allows the adjustment of mechanical, biological, bioactive, and antimicrobial properties of pure hydroxyapatite through the incorporation of magnesium. This ion has the ability to stimulate bone mineralization and remodeling, playing a fundamental role in osteocyte proliferation, as previously mentioned [5, 7]. This observation aligns with our results from biological assays, where we demonstrated the inductive potential of HAp-Mg nanofibers in cell regeneration. To conclude, the resulting material, Mg-HAp, showcases considerable potential as a biomaterial in bone tissue engineering. The inclusion of magnesium can enhance the bioactivity and degradation of hydroxyapatites, while the unique morphology of nanofibers promotes cell adhesion and proliferation. The next crucial step lies in the *in vivo* evaluation of these HAp-Mg nanofibers, enabling a more comprehensive understanding of their effectiveness and applicability in real biological environments.

References

1. Bal, Z., Kaito, T., Korkusuz, F., Yoshikawa, H.: Bone regeneration with hydroxyapatite-based biomaterials. *Emergent. Mater.* **3**, 521–544 (2020)
2. Chetty, A., Wepener, I., Marei, M.K., Kamary, Y.El., Moussa, R.M.: *Hydroxyapatite: Synthesis, Properties, and Applications*. Nov Science Publishers, pp. 91–132 (2012)
3. Alanís-Gómez, J.R., et al.: Synthesis of micro and nano-sized hydroxyapatite fibers through the microwave assisted hydrothermal method. *J. Nanosci. Nanotechnol.* **16**, 7557–7566 (2016)
4. Wang, J.Y., et al.: Flame-sprayed strontium- and magnesium-doped hydroxyapatite on titanium implants for osseointegration enhancement. *Surf. Coat. Technol.* (2020). <https://doi.org/10.1016/j.surfcoat.2020.125452>
5. Predoi, D., Iconaru, S.L., Predoi, M.V., Stan, G.E., Buton, N.: Synthesis, characterization, and antimicrobial activity of magnesium-doped hydroxyapatite suspensions. *Nanomaterials* (2019). <https://doi.org/10.3390/nano9091295>
6. Nabiyouni, M., Brückner, T., Zhou, H., Gbureck, U., Bhaduri, S.B.: Magnesium-based bioceramics in orthopedic applications. *Acta Biomater.* **66**, 23–43 (2018)
7. Zhao, X., Wei, S., Yang, Z., Yang, P., Liu, A.: High-strength and tough bioactive Mg-doped hydroxyapatite bioceramics with oriented microchannels. *Ceramics Int.* **48**, 13494–13507 (2022). <https://doi.org/10.1016/j.ceramint.2022.01.227>



Voronoi 3D: A Novel Approach to Design 3D PLA/HAp Printed Scaffolds for Tissue Engineering Applications

Salgado-Alvarez Ana Paola¹ , Hernández-Vega Luis Alberto^{1,2,3} , Alanís-Gómez José Rafael^{1,2,3} , and Hernández-Rosas Fabiola^{1,2,3}  

¹ Faculty of Biomedical Engineering, Anáhuac Querétaro University, 76246 El Marqués, Mexico

fabiola.hernandez86@anahuac.mx

² Faculty of Architecture, Anáhuac Querétaro University, 76246 El Marqués, Mexico

³ Research Center, Anáhuac Querétaro University, 76246 El Marqués, Mexico

Abstract. Bone repair is one of the most studied fields within tissue engineering since it is one of the most affected structures in the human body. Biomaterials based on calcium phosphate such as hydroxyapatite (HAp) have demonstrated to be promising solutions, due to its capacity to mimic the mineral composition and/or its porous structure. Additionally, using additive manufacturing alongside Computer-Aided Design Software, has granted the opportunity to generate cellular scaffolds for replacement or bone grafts thanks to its controllable mechanical properties, porosity, pore size and structural form. For this reason, the aim of this project is to design, fabricate and characterize PLA/HAp 3D printed scaffolds for tissue engineering applications. For this, HAp was first synthesized through the Microwave-Assisted Hydrothermal Method using $\text{Ca}(\text{NO}_3)_2$, $\text{K}_2(\text{HPO}_4)$ and KOH as precursor and glutamic acid as growth inhibitor, obtaining HAp nanofibers with a hexagonal structure enhancing its mechanical properties. Furthermore, these HAp nanofibers were characterized by X-Ray Diffraction (XRD) and Scanning Electron Microscopy (SEM) to find out the dimension, morphology, topology, orientation, and crystalline structure of the nanofibers. In addition, a variety of 3D bone scaffolds with defined and interconnected pores mimicking the morphology and permeability of the trabecular bone, were designed using 3D Voronoi tessellation method through Rhinoceros 7 with Grasshopper. These scaffolds were fabricated using the extrusion method, where PLA was melted and extruded as a filament. Layer by layer the filament was deposited to create scaffolds with a controlled arrangement of struts and pore dimensions without the need for a binder.

Keywords: Hydroxyapatite · Bone Scaffolds · Biomaterial · 3D printing

1 Introduction

It is well known that bone is a fundamental structure in the whole body. It is a type of connective tissue constantly changing, due to its adaptability in shape, size, and the biomechanical forces it endures. Bone is arranged in two structures, cortical or

compact and trabecular or spongy bone [1]. Additionally, it is a composite material with both organic and inorganic components such as collagen type I fibers and hydroxyapatite (HAp) that are small crystals of mineral structures [2].

As it was previously mentioned, bone is a tissue in constant change, thus there has been a need to start looking for alternatives to keep the bone from breaking or to repair it more efficiently avoiding the usage of metals and other material that could cause cytotoxicity or rejection from the body. For that reason, tissue engineering is looking for that answer. This branch of engineering altogether with innovative biomaterials such as synthetic HAp, offer a variety of solutions including the usage of scaffolds to provide structural template to bear loads of the adjacent tissues, to guarantee support for the newly formed tissue and extracellular matrix. Nevertheless, the success each scaffold depends on its design, materials, and patient's activity [3].

In the present, several manufacturing technologies have emerged to try and improve past methods and 3D printing is a clear example of new techniques that have come to innovate this field [4]. These are techniques that apply computational modeling, such as Computational Assisted Design (CAD) software, allowing the designer to choose the size, morphology, number of pores, size of pores and percentage of porosity in each scaffold [3, 5]. Hence, the aim of this work is to design, fabricate and characterize 3D printed composite scaffolds of HAp and Polylactic Acid (PLA) to evaluate their properties and ability to mimic the spongy bone for tissue engineering applications. Also, our research question is: Do PLA/HAp 3D printed bone scaffolds possess unique structural and morphological properties and can they stimulate bone regeneration?

2 Methodology

2.1 Scaffold Design

In this investigation, a scaffold prototype was designed using the 3D Voronoi tessellation method [6] to simulate the trabecular-like human bone. As it is well described, the trabecular bone presents a porosity range from 50% to 90% depending on the bone type [1]. Additionally, prior authors have described that the suggested pore size goes between 200 μm and 1200 μm [3], therefore with this method, we can control two of the most important variants in tissue engineering scaffolds: pore size and porosity. The scaffolds were designed through a computer aided design (CAD) Rhinoceros 7 (Robert McNeel & Associates, WA, USA) with Grasshopper.

To begin with the design, the Bounding Box command was selected to create a solid region as a total volume of the scaffold. Then, a number of points, that will represent the center of each pore, were chosen and introduced with the command Populate 3D, inside the box previously created, these points will serve as seeds to generate the 3D Voronoi structure [7, 8]. After that, the 3D Voronoi command was used to create the organic porous structure we are looking for followed by Brep, which deconstructs the object in edges and vertices. Next Simplify Curve is used to takes the object's edges to shape them into geometric figures accompanied by the Duplicate Line remover command. Finally, those lines are used with Multipipe, as a track to determine the strut diameter of the cylinder to obtain the trabecular-like structure and create the porous scaffold, shown in a schematic design in Fig. 1. To prove that the porosity percentage and size of the pore

have a correlation between the input parameters such as the number of pores and the strut diameter, and the targeted parameters like porosity percentage the next equations described by Liu, et al. [8] were followed:

$$P\% = \frac{V_{\text{Bounding Box}} - V_{\text{scaffold}}}{V_{\text{Bounding Box}}} \times 100\% \quad (1)$$

$$V_{\text{void}} = V_{\text{Bounding Box}} - V_{\text{scaffold}} \quad (2)$$

$$V_{\text{void}} = V_{\text{Bounding Box}} \times P\% \quad (3)$$

Where $V_{\text{BoundingBox}}$ is the volume of the solid structure, $P\%$ is the porosity of the scaffold and V_{void} is the vacuous volume, that is, the pore volume and V_{scaffold} is the remnant structure after the Voronoi 3D method [8]. Hence, the porosity of the scaffold is directly related with the strut diameter and the number of pores.

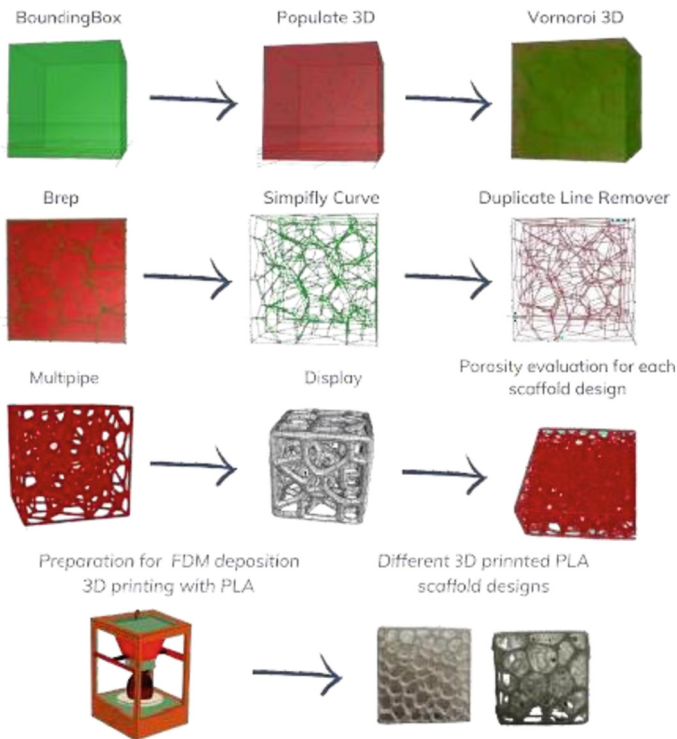


Fig. 1. Scaffold design process using a CAD software and promising results.

2.2 Fused Deposition Modeling (FDM) 3D Printing

For the FDM 3D printing, the porous scaffolds were converted into STL files and transferred into the UltiMaker Cura software for a rapid previsualization and evaluation. These

first designs were printed in a 2:1 scale to deeply observe the scaffold structure. Finally, they were fabricated in an UltiMaker S5 Model using the FDM process, as Winarso et al. [9], described consists of building 3D structures by depositing a thermoplastic material, such as PLA, into a substrate in finite and precise layers using a temperature-controlled printhead, for it to melt to form a thermoplastic filament obtaining a microscopic, printed layer of semi molten polymers.

2.3 HAp Synthesis by HAHM and Characterization

This procedure was realized by the Microwave Assisted Hydrothermal Method (MAHM) in a reactor Monowave [300] (Anton Paar, Austria), as it is described by Alanís-Gómez et al., [10] and shown in Fig. 2:

1. Prepare a solution with glutamic acid [$C_5H_9NO_4 \cdot H_2O$] and calcium nitrate [$Ca(NO_3)_2 \cdot 4H_2O$] in 250 ml of water, warmed ($40^\circ C$) and stirred.
2. Prepare a solution of potassium phosphate [KH_2PO_4] together with of potassium hydroxide [KOH] in 150 ml of water, heated and vigorously stirred. Then, mix both solutions.
3. Subsequently, the vials must be filled with the resulting solution heated in the microwave oven. To fill the vials, it is necessary to keep them vertical and add the solution, without exceeding the allowed volume limit. For this, the vials were open with the sealing device, and the vent screw was open. Next, the cap was snapped on, sealing the vial under pressure. Finally, the vent screw was closed and placed into the reactor.
4. The Microwave Reactor was programmed as follows: $170^\circ C$ of intern temperature, a reaction time of 45 min and a cooling time of 15 min.
5. After microwave synthesis, the HAp will be seen as a sediment in the bottom of the vial with a white powdery appearance, the supernatant liquid is discharged.
6. Finally, the HAp is collected in a sterile falcon tube and washed twice with isopropanol.

X-Ray Diffraction (XRD). XRD analysis was conducted on all samples obtained from the synthesis reactions to determine the crystalline components present in the final product. The analysis was performed using a Bruker-manufactured D8 Advance diffractometer to 30 kV. CuK_α radiation and $\lambda = 1.4406 \text{ \AA}$ was employed. The diffraction experiments covered a range of 10° to 90° on a 2θ scale, with a step size of 0.05° . Phase identification was accomplished by comparing the obtained diffractogram with ICDD PDF files from Bruker, particularly PDF 86–1199.

Scanning Electron Microscopy (SEM). SEM was conducted using a JEOL JSM-6390 to examine the morphology and microstructure of all samples. The SEM operated at a voltage of 25 kV, and the images were generated from secondary electrons. The HAp sample was obtained after the completion of the drying process. A small portion of the filtered solid was placed in a sample holder and coated with charcoal paint. The specimens were then observed using a SEM. Image capture was performed at 2.0 k and 20.0 k magnification.

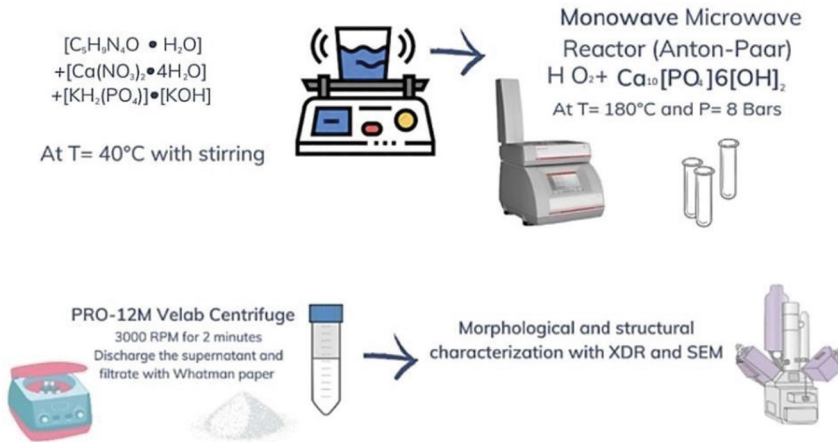


Fig. 2. HAp synthesis process and characterization.

3 Results

Highly crystalline HAp fibers were obtained by the Microwave-Assisted Hydrothermal Method (MAHM). The HAp samples analyzed by SEM presented a heterogeneous topology made up of elongated crystals with hexagonal prism shape and a cross-sectional diameter of $1.5 \mu m$, grouped in agglomerates between 500–1000 nm. As it is seen in the Fig. 3, showing a SEM micrograph at 10 k and 20 k magnification of HAp fibers synthesized by MHAM.

X-Ray Diffraction Analysis of HAp

XRD analysis confirms the successful production of HAp with a high degree of crystallinity. Phase identification was accomplished by comparing the obtained diffractogram with ICDD PDF files from Brucker.

The presence of specific signal in the XRD pattern at characteristic 2θ angles corresponding to hydroxyapatite allowed for the confident identification of the phase. The diffractogram reveals prominent signal corresponding to the Miller indices of major reflections, namely planes (211), (300), (120), (130), (100), and (002) of the HAp phase, as indicated by PDF 86-1199.

In our samples, the strongest Bragg reflection corresponds to the (211) plane. The intensity and position of these peaks provided information about the crystal.

structure and purity of the hydroxyapatite sample. Figure 4 showcases well-defined Bragg reflections that are narrow in width and exhibit strong intensities.

Finally, PLA 3D scaffolds of trabecular bone were designed and printed shown in Fig. 5, as a prototype for future biological assays of bioactivity, osteoinduction and osteoconduction of HAp nanofibers. The prototypes were made in Rhinoceros 7 and Grasshopper 7 (Robert McNeel & Associates, WA, USA) with a total of 250 pores and a porosity of the structure of 73%. Once optimal scaffolds for the tests have been obtained and approved, they will be coated with HAp synthesized in the laboratory by means of physical deposition techniques to be further tested in cell culture.

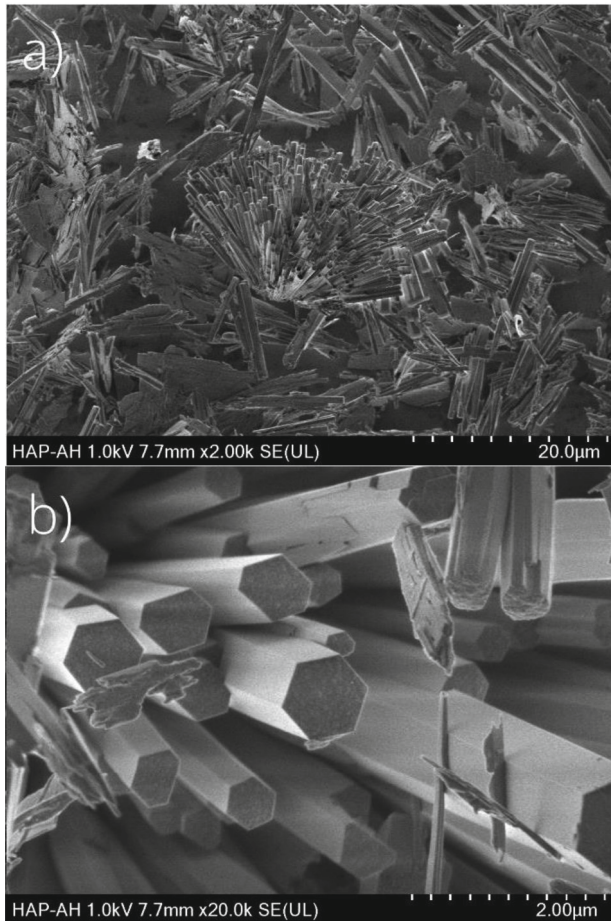


Fig. 3. Analysis of hydroxyapatite powder by SEM. a) 2.0 k magnification b) 20.0 k magnification.

4 Analysis

The successful synthesis of highly crystalline HAP fibers through the microwave-assisted hydrothermal method (MAHM) holds great promise for various biomedical applications. The unique morphology of the HAP fibers, characterized by elongated crystals with hexagonal shapes, offers several advantages in terms of bioactivity and mechanical properties [10]. The controlled synthesis of HAP fibers with specific dimensions and crystallographic orientations can play a crucial role in tailoring the material's properties for specific applications, such as bone tissue engineering [11].

The characterization of the synthesized HAP fibers using SEM analysis revealed a heterogeneous topology with elongated crystals. The presence of well-defined hexagonal morphology further supports the high degree of crystallinity achieved through the

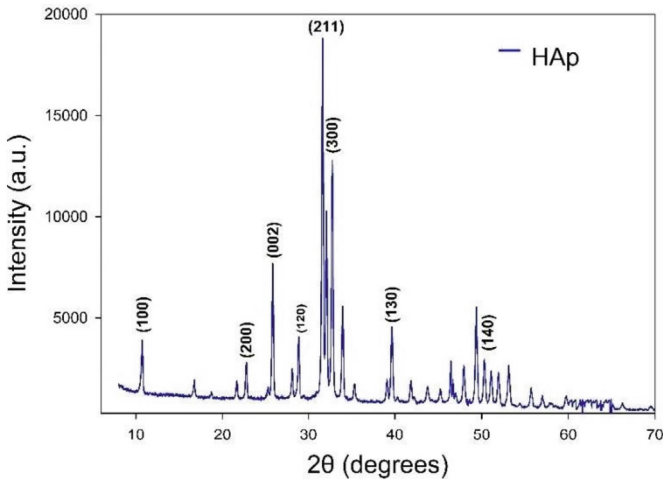


Fig. 4. Result of an X-ray diffraction experiment. Diffractogram of a HAp powder sample.



Fig. 5. 3D Scaffold proposal printed at a scale 2:1 for testing probes.

MAHM process. The clustering of fibers into aggregates indicates the formation of interconnected networks, which can potentially facilitate cellular adhesion, proliferation, and nutrient transport within the scaffolds [8].

The XRD analysis not only confirmed the successful production of HAp but also provided valuable information about the crystal structure and purity of the synthesized material. The comparison of the diffractogram with established ICDD PDF files allowed for phase identification, with the (211) plane of HAp showing the highest intensity. This finding aligns with previous studies highlighting the significance of the (211) plane in HAp crystal growth and mechanical properties. The highly crystalline nature of the HAp fibers is desirable for their effective integration into the mineralized matrix of natural bone [12].

The development of 3D-printed bone-like PLA scaffolds incorporating the synthesized HAp fibers represents a significant advancement in tissue engineering [7]. The design of the scaffolds, with their specific porosity and pore architecture, mimics the trabecular structure of natural bone, enabling cell infiltration, nutrient diffusion, and

vascularization [5]. The combination of the scaffold's structural properties and the bioactive nature of the HAp fibers can potentially enhance cellular responses, including cell attachment, proliferation, and differentiation, ultimately leading to improved tissue regeneration [13].

Future studies can focus on evaluating the biological performance of the HAp-coated scaffolds, such as conducting new assays of cell behavior, tissue integration, and bone regeneration capabilities. Additionally, the use of advanced surface modification techniques, such as physical deposition or biofunctionalization, can further enhance the bioactivity and osteoinductive properties of the HAp-coated scaffolds [14]. These advancements would pave the way for the translation of HAp-based scaffolds into clinical applications, addressing the challenges in bone defect repair and promoting tissue regeneration.

In conclusion, the successful synthesis of highly crystalline HAp fibers using the MAHM method, along with the characterization of their morphology and crystal structure, highlights their potential for various biomedical applications. The integration of these fibers into 3D-printed bone-like scaffolds opens new possibilities for bone tissue engineering and regenerative medicine. Further research and development are warranted to optimize the scaffold design, improve cellular responses, and assess the long-term performance of HAp-coated scaffolds in clinical settings.

5 Conclusions

This result is significant because the preferable crystalline orientation found in the X-Ray diffraction analysis, all together with the SEM results indicate that the HAp fibers grow in a [002] direction, together with the “c” axis of the hexagonal hydroxyapatite's structure. In addition, with the Microwave-Assisted Hydrothermal Method, HAp nanofibers with high purity and crystallinity were obtained. On top of that, the scaffold designed with the CAD software Rhinoceros 7 (Robert McNeel & Associates, WA, USA) and 3D printed in PLA shows promising results due to their high porosity percentage and pore interconnectivity, as well as their biocompatible properties with HAp. Furthermore, this type of design can be modified with a simple change in the variables given to the software to obtain a more porous structure or the other way around. These variables were considered for future calculations and design improvements.






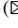

References

1. Lin, X., Patil, S., Gao, Y.G., Qian, A.: The bone extracellular matrix in bone formation and regeneration. *Front. Pharmacol.* **11**, 757 (2020). <https://doi.org/10.3389/fphar.2020.00757>
2. Wang, W., Yeung, K.W.K.: Bone grafts and biomaterials substitutes for bone defect repair: a review. *Bioact. Mater.* **2**, 224–247 (2017)
3. Tariverdian, T., Sefat, F., Gelinsky, M., Mozafari, M.: Scaffold for bone tissue engineering. In: *Handbook of Tissue Engineering Scaffolds: Volume One*, pp. 189–209. Elsevier (2019)
4. Fu, Q., Saiz, E., Rahaman, M.N., Tomsia, A.P.: Bioactive glass scaffolds for bone tissue engineering: state of the art and future perspectives. *Mater. Sci. Eng. C* **31**, 1245–1256 (2011)
5. Hollister, S.J.: Porous scaffold design for tissue engineering (2005)

6. Moreno Madrid, A.P.M., Vrech, S.M., Sanchez, M.A., Rodriguez, A.P.: Advances in additive manufacturing for bone tissue engineering scaffolds. *Mater. Sci. Eng. C* **100**, 631–644 (2019)
7. Zhao, H., et al.: Design and mechanical properties verification of gradient voronoi scaffold for bone tissue engineering. *Micromachines* (2021). <https://doi.org/10.3390/mi12060664>
8. Liu, S., Chen, J., Chen, T., Zeng, Y.: Fabrication of trabecular-like beta-tricalcium phosphate biomimetic scaffolds for bone tissue engineering. *Ceram. Int.* **47**, 13187–13198 (2021)
9. Winarso, R., Anggoro, P.W., Ismail, R., Jamari, J., Bayuseno, A.P.: Application of fused deposition modeling (FDM) on bone scaffold manufacturing process: a review. *Heliyon* (2022). <https://doi.org/10.1016/j.heliyon.2022.e11701>
10. Alanís-Gómez, J.R., et al.: Synthesis of micro and nano-sized hydroxyapatite fibers through the microwave assisted hydrothermal method. *J. Nanosci. Nanotechnol.* **16**, 7557–7566 (2016)
11. Alanís-Gómez, J.R., Rivera-Muñoz, E.M., Peza-Ledesma, C., Manzano-Ramírez, A., Velázquez-Castillo, R.: A comparison of mechanical properties of different hydroxyapatite (HAp) based nanocomposites: the influence of morphology and preferential orientation. *J. Nanosci. Nanotechnol.* **20**, 1968–1976 (2019)
12. Bal, Z., Kaito, T., Korkusuz, F., Yoshikawa, H.: Bone regeneration with hydroxyapatite-based biomaterials. *Emergent. Mater.* **3**, 521–544 (2020)
13. Domingos, M., Gloria, A., Coelho, J., Bartolo, P., Ciurana, J.: Three-dimensional printed bone scaffolds: the role of nano/micro-hydroxyapatite particles on the adhesion and differentiation of human mesenchymal stem cells. *Proc. Inst. Mech. Eng. H* **231**, 555–564 (2017)
14. Swetha, S., Balagangadharan, K., Lavanya, K., Selvamurugan, N.: Three-dimensional-poly (lactic acid) scaffolds coated with gelatin/magnesium-doped nano-hydroxyapatite for bone tissue engineering. *Biotechnol. J.* (2021). <https://doi.org/10.1002/biot.202100282>



Combating Prosthetic Infections: Synthesis, Characterization, and Evaluation of Magnesium-Doped Hydroxyapatite Nanofibers with Antibacterial Properties

Epsiba Lorena Marañón Romero¹ , Ricardo Pascual Alanís Gómez¹ ,
José Rafael Alanís-Gómez¹ , Kevin José Martínez Arellano¹ ,
Fabiola Hernández-Rosas³  , and Rodrigo Velázquez Castillo² 

¹ Escuela de Ingeniería Biomédica, Universidad Anáhuac Querétaro, Santiago de Querétaro 76246, México

² División de Investigación y Posgrado, Facultad de Ingeniería, Universidad Autónoma de Querétaro, Santiago de Querétaro, Querétaro 76010, México

³ Centro de Investigación, Universidad Anáhuac Querétaro, Santiago de Querétaro 76246, México

fabiola.hernandez86@anahuac.mx

Abstract. Hydroxyapatite (HAp) is one of the most important in the family of calcium phosphates since it is an inorganic component of bone and it has been proven to be a biocompatible, osteoconductive, and osteoinductive material. However, it presents low antimicrobial activity making it susceptible to infections. This work aimed first to synthesize and characterize HAp nanofibers doped with Mg nanoparticles with a growth-oriented crystalline structure and second to evaluate their antimicrobial activity. For this, we synthesized HAp nanofibers by microwave-assisted hydrothermal method and carried out the structural characterization using the X-ray powder diffraction method. The morphological, topological, and microstructural characterization was performed with scanning electron microscopy. Given the results, synthetic Mg-HAp nanofibers exhibited a hexagonal morphology and high purity and crystallinity. In addition, the nanofunctionality show of Mg-HAp exhibits good antimicrobial activity.

Keywords: Nanobiomaterial · Hydroxyapatite · Antimicrobial Activity

1 Introduction

Bone is a connective tissue formed by a mineralized extracellular matrix, which provides support to the body and protection to some organs [1]; This matrix is made up of an organic phase and an inorganic phase, which is mainly made up of CaPs in the form of HAp crystals. Factors that affect bone tissue have a significant impact on general health; and it is that when bone defects are critical, they require the addition of biomaterials with characteristics like the chemical and structural properties of the tissue for their repair

since otherwise their regeneration would not be carried out completely [2, 3]. It was decided to work with HAp due to its chemical composition very similar to the inorganic component of natural bone tissue, which provides great biocompatibility and bioactivity with surrounding tissues, facilitating the union, proliferation, and differentiation of bone cells [4, 5]. This makes it a very attractive biomaterial to use in grafts. Although HAp has these qualities, studies reveal that it has a low antibacterial property, a necessity for its clinical application [4]. To increase its physical-chemical, mechanical, and biological properties, it was decided to dope the HAp with nanoparticles of Mg, which has been reported in previous studies that Mg is a biodegradable, non-cytotoxic material that improves all the properties of the HAp and has an antimicrobial effect directly on bacteria, affecting their cell membrane [6–8].

There is limited research discussing the exact mechanism by which Mg acts against bacteria. Nevertheless, there are a few proposals that offer some clarity to the ongoing discussion. According to Robinson et al., the addition of Mg alone cannot be attributed to the antibacterial inhibition; instead, it is associated with changes in pH. In their in vitro study, they observed diminished growth of *Escherichia coli*, *Pseudomonas aeruginosa* and *Staphylococcus aureus* when reaching levels in pH of >9 [14]. This phenomenon finds support in the work of Nostro et al., who establish that an alkaline pH causes a lower adherence of bacteria due to bacterial surface hydrophobicity [15]. Additionally, a high alkalinity leads to an immoderate consumption of H^+ , which reduces ATP synthesis [6].

Another proposed mechanism of Magnesium revolves around the generation of reactive oxygen species (ROS), which can damage cells by disrupting bacterial proteins and DNA. This leads to reduced bacterial adhesion, subsequently reducing biofilm formation [6]. In a study by Sawai et al. the antibacterial attributes of magnesium oxide were investigated, leading to the conclusion that the ROS generation was responsible for the antibacterial effects against *E. coli* and *S. aureus* [16].

The factors mentioned above could be acting alone or together. However, it is crucial to acknowledge that most evidence has been derived from in vitro studies. Limited in vivo evidence only suggests that the behavior of the material varies under physiological conditions, opening the door to further research.

For this reason, the objective of this work was to synthesize Mg-doped HAp nanofibers with a crystalline growth orientation through MAHM, characterize the material, and evaluate its antimicrobial activity.

2 Materials and Methods

2.1 Synthesis of HAp by MAHM

HAp synthesis was performed according to Alanís-Gómez et al. [9], in a Monowave 300 (Anton Paar). The reaction mixture's temperature was $170\text{ }^{\circ}\text{C}$, with a pressure of 6–11 kPa. At the end of the reaction, a white crystalline solid was obtained, which was filtered and washed using H_2O . Finally, the dust was desiccated to $50\text{ }^{\circ}\text{C}$ inside a muffle.

2.2 Characterization of HAp Nanofibers

X-Ray Analysis. The analysis was made in a diffractometer D8 Advance [Bruker]. Sample preparation was not required. In the analysis, a Cu K radiation (to a wavelength of 1.54 Å) was used. The samples were scanned in a range of 2θ from 10° through 90° with a 0.05° step size.

Electron Microscopy. The morphological analyses of HAp were carried out using a JEO-JSM-6390-Scanning Electron Microscope (Jeol USA Inc). 20 kV was used in the acceleration voltage.

X-Ray Fluorescence Analysis. The X-Ray Fluorescence analysis (XRF) of the samples of HAp was made in X-ray fluorescence analyzer (AR Technologies, Inc.). All samples were distributed in 1 ml of ethanol as a dispersing agent.

2.3 Assessment of Antimicrobial Activity

Cultures of *Escherichia coli* (ATCC 25922), *Enterococcus faecalis* (ATCC 29212), *Staphylococcus aureus* (ATCC 23235) and *Candida albicans* (ATCC 96901) were grown on Mueller-Hinton (MH) agar plates. Once the colonies had grown, sample was collected and suspended in a tube with nutrient broth. A sterilized cotton swab was immersed in the resulting suspension, and a lawn of bacteria was applied to the agar plates. Covered the sample with a sterile cotton bud, and a layer of bacteria was applied to an MH agar plate.

The Mg-HAp suspension was placed on filter paper discs and applied to the *E. coli* cultures. The side containing the particles faced downwards to ensure direct interaction with the agar and the bacteria, and the samples were incubated at 37°C for 48 h. The inhibition zones around the filter are scarred every 24 h.

3 Results

3.1 X-ray Diffraction

For the analysis of the x-ray diffraction, our sample was compared to the powder diffraction file given by the International Center for Diffraction Data. The crystalline phases of our HAp-Mg sample corresponded to those of ICDD-PDF#86-1203. This indicates a consistency in the crystallography of the material and shows a successful synthesis method.

The X-ray diffraction image (Fig. 1) shows distinctive Bragg reflections corresponding to hydroxyapatite's crystallographic planes. We can also observe cleanliness in the pattern which demonstrates minimal noise interference.

The disposition of the Bragg reflexions are displayed as narrow bands with high intensities, which could signify high crystallinity and the presence of large crystals.

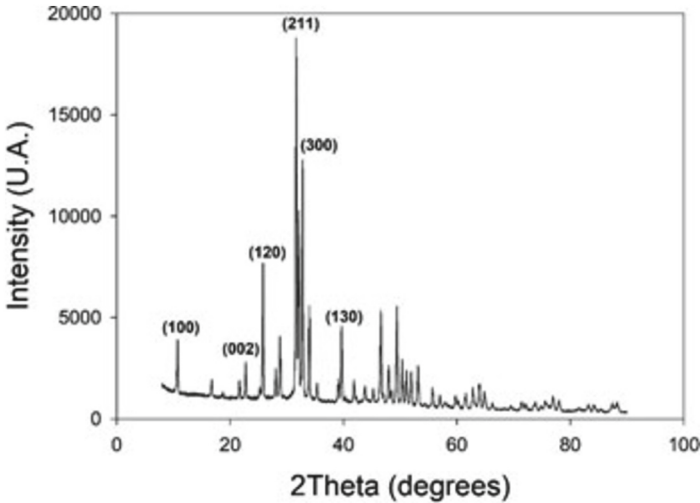


Fig. 1. X-ray analysis of Mg-HAp powder.

3.2 SEM

The SEM analysis captured a series of images at progressively closer magnifying intervals to examine the morphology of the fibers obtained. Figure 2a and 2b, taken at a moderate magnification, provide a general overview of the fibers' shape and arrangement. The images show a cluster of fibers that form a spherical structure.

Figure 2b, captured at a closer distance, reveals a clearer image of the fibers, providing more detail on their individual structure (15000x). However, it is until Fig. 2a with a magnification of 5000x that the hexagonal morphology of the fibers becomes evident, this being important since it improves its mechanical properties.

This image Fig. (2b) highlights their unique structural characteristics; attributed by the glutamic acid that adheres to phosphate groups and gives an acidic pH. This causes an intricate organized growth of the nanofibers in the c-direction, attributed by specific physical and chemical parameters used in the hydrothermal method: high temperatures, pressures and specific volume. These parameters are essential in providing an excellent medium for reaction speed and generation of smaller particles.

3.3 Energy Dispersive X-ray Spectroscopy

Figure 3 represents the elemental composition of our Mg-Hydroxyapatite sample, which is a crucial indicator to determine the relationship between phosphorus (P) and calcium (Ca). The most prominent peak in the Energy Dispersive X-ray Spectroscopy (EDS) spectrum corresponds to calcium (Ca) with an intensity of almost 16 (cps/eV), which indicates a significant amount of calcium within the sample. The spectrum also exhibits the presence of other elements such as phosphorus (P), magnesium (Mg), aluminum (Al), oxygen (O), and carbon (C).

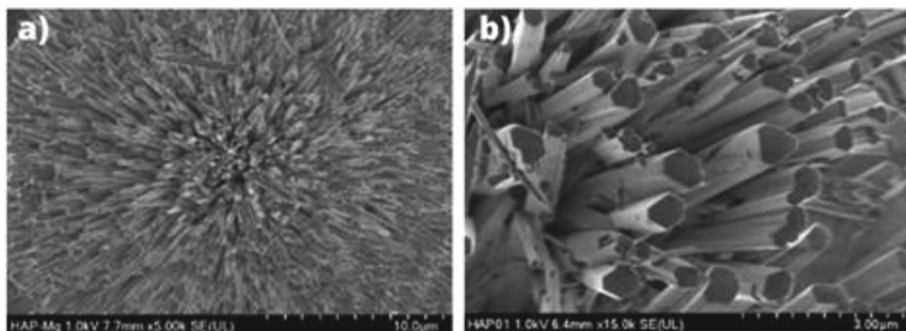


Fig. 2. SEM micrographs of Mg-HAp showcasing the fibers morphology. a) 5000 magnification b) 15000 magnification.

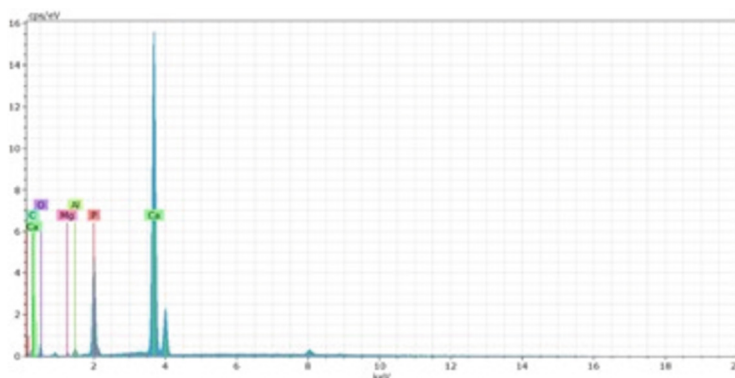


Fig. 3. EDS analysis of Mg-HAp powder

The concentration of the different elements in our HAp sample is shown on Table 1, providing more detail on major and minor constituents. Major elements are indicated by % and minor elements by ppm.

Table 1. Element concentration analysis.

Compound	Concentration	Unit
MgO	1.179	%
P2O5	40.326	%
SO3	0.101	%
K2O	0.171	%
CaO	58.137	%
Fe2O3	417.9	Ppm

3.4 Kirby Bauer Disk Diffusion Susceptibility Test

The antimicrobial activity of magnesium doped hydroxyapatite was tested in an *in vitro* model with a HAp-Mg concentration of 100 $\mu\text{g/ml}$ /DMSO, against *Escherichia coli* (Fig. 4a), *Enterococcus faecalis*, *S. aureus* and *Candida albicans*. The diameters of inhibition of three independent experiments by each microorganism vs positive control (sensible antibiotic) are shown in Fig. 4b, in which moderate inhibition of bacterial growth can be observed (Fig. 4b).

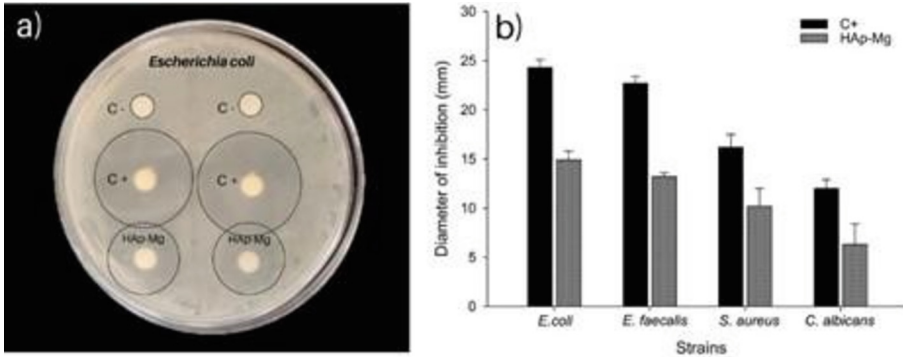


Fig. 4. HAp-Mg Antibiogram against *E. Coli* and inhibition diameters against different strains.

4 Analysis

Mg-HAp powder was synthesized through the microwave assisted hydrothermal method (MAHM), ensuring precision over parameters such as temperature and pressure. This method enabled us to produce nanofibers with superior crystallinity by initiating and guiding their growth. The high crystallinity in the resulting nanofibers Mg-HAp yielded a well-defined and organized structure, which led to the desired morphology [2, 11].

The powder obtained underwent X-ray analysis to provide more information about its composition and crystal structure. The crystallographic planes also allowed the identification of characteristic peaks and their corresponding Miller indices. The most intensive reflection occurred in the (211) crystallographic plane at $2\theta = 34$ degrees, which is characteristic of hydroxyapatite. We can observe a well-defined spectrogram with narrow peaks. The presence of amino acids, as it has been mentioned in several studies, modifies the morphology and crystalline structure of HAp [12]. Therefore, the glutamic acid within the reaction functioned as a growth orientator, yielding the formation of nanofibers with strong definition and direction [2, 12].

Through SEM images we could deepen our understanding about the fibers' morphology and structure. We can highlight the formation of spherical structures made up of HAp nanofibers and intermixed with Mg particles. This structure occurs as a result of the deformations that take place on the crystal lattice when Mg ions are involved in the structure due to the substitution of Ca^{2+} ions by Mg^{2+} ions [13]. The examination of

the fibers at different scales also revealed their hexagonal nature, which suggests a well-defined crystallographic structure. An EDS was then performed to obtain an elemental analysis, which offers data to analyze the P/Ca relationship within the sample. However, it is important to notice the significantly higher peak of calcium, which means there is a stronger presence of these atoms in comparison to phosphorus atoms.

Given that the calcium peak is 15.5 cps/eV and the phosphorus peak approaches 7 cps/eV, it is possible to calculate Ca/P (15.5 cps/eV/7 cps/eV) which is approximately 2.21. The higher concentrations of elements within our HAp powder were diphosphorus pentoxide with a concentration of 40.326% and calcium oxide with a concentration of 58.137%. This Ca/P relationship results in 1.64, approaching the relationship in human bone of 1.67 [2]. The antimicrobial analysis was carried out by using HAp-Mg as the test sample, with a negative control consisting only of dimethyl sulfoxide (DMSO) and a positive control consisting of DMSO with an antibiotic, in this case ciprofloxacin 10 µg. To precisely measure the sensibility of a microorganism, the diameter of the inhibition zones was utilized as an indicator of the antimicrobial activity. The Mg-HAp presented an inhibition ring of 14 units with a concentration of 2%. The control positive also demonstrated intense antimicrobial activity while control negative didn't show any bacterial inhibition. This only indicates that our results are reliable.

5 Conclusion

This study focused on the synthesis and characterization of magnesium doped hydroxyapatite using controlled temperature and pressure using the hydrothermal microwave assisted method. The resulting particles showed distinctive crystallographic peaks in the X-ray diffraction analysis, demonstrating the preservation of the hydroxyapatite structure despite the incorporation of Mg.

SEM analysis revealed a hexagonal and unique morphology of Mg-HAp fibers attributed by the influence of glutamic acid, as a growth orientator in the c direction. EDS analysis reassured the elemental composition of our HAp, with notable concentrations of Ca/P, reaching similarities with human bone composition.

Through the Kirby Bauer Disk Diffusion Susceptibility Test, we observed an inhibition of bacterial growth when exposed to Mg-HAp at a 100 µg/ml/DMSO. These results point to promising advances on the exploration of Mg-HAp as an antimicrobial strategy in diverse medical and biomaterials applications.








References

1. Lin, X., Patil, S., Gao, Y.G., Qian, A.: The bone extracellular matrix in bone formation and regeneration. *Front. Pharmacol.* **11**(May), 1–15 (2020)
2. Alanís-Gómez, J.R., Rivera-Muñoz, E.M., Peza-Ledesma, C., Manzano-Ramírez, A., Velázquez-Castillo, R.: A Comparison of Mechanical Properties of Different Hydroxyapatite (HAp) based nanocomposites: the influence of morphology and preferential orientation. *J. Nanosci. Nanotechnol.* **20**(3), 1968–1976 (2019)
3. Chetty, A., Wepener, I., Marei, M.K., Kamary, Y.El., Moussa, R.M.: Hydroxyapatite : Synthesis. *Polym. Compos. Mater. Sci. Manuf.* 1–57 (2018)

4. Franco, D., Calabrese, G., Petralia, S., Neri, G., Corsaro, C., Forte, L., et al.: Antimicrobial effect and cytotoxic evaluation of MG-doped hydroxyapatite functionalized with au-nano rods. *Molecules* **26**(4), 1–12 (2021)
5. Zastulka, A., Clichici, S., Tomoaia-Cotisel, M., Mocanu, A., Roman, C., Olteanu, C.D., et al.: Recent Trends in Hydroxyapatite Supplementation for Osteoregenerative Purposes. *Materials (Basel)* **16**(3) (2023)
6. Luque-Agudo, V., Fernández-Calderón, M.C., Pacha-Olivenza, M.A., Pérez-Giraldo, C., Gallardo-Moreno, A.M., González-Martín, M.L.: The role of magnesium in biomaterials related infections. *Colloids Surf. B Biointerf.* [Internet] **191**(March), 110996 (2020). <https://doi.org/10.1016/j.colsurfb.2020.110996>
7. Bedair, T.M., Heo, Y., Ryu, J., Bedair, H.M., Park, W., Han, D.K.: Biocompatible and functional inorganic magnesium ceramic particles for biomedical applications. *Biomater Sci.* **9**(6), 1903–1923 (2021)
8. Vimbela, G.V., Ngo, S.M., Frazee, C., Yang, L., Stout, D.A.: Antibacterial properties and toxicity from metallic nanomaterials. *Int. J. Nanomed.* **12**, 3941–3965 (2017)
9. Alanís-Gómez, J.R., Rivera-Muñoz, E.M., Cervantes-Medina, J.S., Almanza-Reyes, H., NavaMendoza, R., Cortes-Romero, C., et al.: Synthesis of micro and nano-sized hydroxyapatite fibers through the microwave assisted hydrothermal method. *J. Nanosci. Nanotechnol.* **16**(7), 7557–7566 (2016)
10. Maye, B.R., Guzmán, M.: El Antibiograma de discos. Normalización de la técnica de Kirby-bauer. *Biomédica* **4**(3–4), 112 (1984). <https://doi.org/10.7705/biomedica.v4i3-4.1891>
11. Ebrahimi, S., Sipaut, C.S., Arshad, S.E.B.: Hydrothermal synthesis of hydroxyapatite powders using Response Surface Methodology (RSM). *PLoS ONE* **16**(5), e0251009 (2021). <https://doi.org/10.1371/journal.pone.0251009>
12. Tavafoghi, M., Cerruti, M.: The role of amino acids in hydroxyapatite mineralization. *J. R. Soc. Interface* **13**(123), 20160462 (2016). <https://doi.org/10.1098/rsif.2016.0462>
13. Alioui, H., Bouras, O., Bollinger, J.: Toward an efficient antibacterial agent: Zn- and Mg-doped hydroxyapatite nanopowders. *J. Environ. Sci. Health, Part A* **54**(4), 315–327 (2019). <https://doi.org/10.1080/10934529.2018.1550292>
14. Robinson, D.A., Griffith, R.W., Shechtman, D., Evans, R.B., Conzemius, M.G.: In vitro antibacterial properties of magnesium metal against *Escherichia coli*, *Pseudomonas aeruginosa* and *Staphylococcus aureus*☆. *Acta Biomater.* **6**(5), 1869–1877 (2010). <https://doi.org/10.1016/j.actbio.2009.10.007>
15. Nostro, A., et al.: Effect of alkaline pH on staphylococcal biofilm formation. *APMIS* **120**(9), 733–742 (2012). <https://doi.org/10.1111/j.1600-0463.2012.02900.x>
16. Sawai, J., Kojima, H., Igarashi, H., Hashimoto, A., Shoji, S., Shimizu, M.: *World J. Microbiol. Biotechnol.* **16**(2), 187–194 (2000). <https://doi.org/10.1023/A:1008916209784>



Characterization and Antimicrobial Evaluation of Gadolinium- Doped Hydroxyapatite for Potential Use as Drug Carrier System

Cristhian Valencia Arreguin¹ , Luis Fernando Serna Maldonado¹ ,
Natalia Mora Padron² , Ramírez Ortiz^{1,2,3}, Fernando^{1,2,3},
Fabiola Hernandez Rosas^{1,2} , José Rafael Alanis Gómez¹ ,
and Rodrigo Velázquez Castillo³  

¹ Escuela de Ingeniería Biomédica, Universidad Anáhuac Querétaro, Santiago de Querétaro 76246, México

² Centro de Investigación, Universidad Anáhuac Querétaro, El Marqués 76246, México

³ División de Investigación y Posgrado, Facultad de Ingeniería, Universidad Autónoma de Querétaro, Querétaro 76010, México

rodrigo.velazquez@uaq.mx

Abstract. Hydroxyapatite, a ceramic material with similarity to natural human bone, finds applications in various medical fields. HAp-based nanocarriers, particularly in the form of polymeric nanoparticles, offer promising potential for targeted drug delivery and their investigation in biological systems. This study focuses on the synthesis of gadolinium-doped HAp nanofiber using the Microwave Assisted Hydrothermal Method (MAHM), aiming to assess their suitability as drug carriers. The morphological and topological analysis, as well as the elemental chemical composition of HAp-Gd nanofibers, were evaluated using SEM/EDS and crystallinity was evaluated by XRD. The antimicrobial activity of the biomaterial was tested against *Escherichia coli* using the disk diffusion method. The MAHM successfully synthesized HAp-Gd, as evidenced by the results from SEM and EDS, which confirmed the crystalline and pure nature of the synthesized HAp nanowires. Additionally, these results demonstrated a homogeneous chemical composition and effective integration of gadolinium into the HAp structure. Although gadolinium-doped hydroxyapatite exhibited limited antimicrobial activity against *Escherichia coli*, the findings provide valuable insights for further exploration and optimization of its drug delivery potential.

Keywords: Biomaterials · Doped Hydroxyapatite · Gadolinium · Drug Carrier

1 Introduction

In recent years, there has been a growing interest in developing biomaterials with specific drug release capabilities for biomedical applications [1]. Hydroxyapatite (HAp), a synthetic compound known for its biocompatibility and ability to mimic natural bone composition, has emerged as a promising candidate for drug delivery systems [2]. This

study focuses on the synthesis, characterization, and evaluation of hydroxyapatite doped with gadolinium (Gd) as an optimized drug carrier. Various characterization techniques, including X-ray diffraction, energy-dispersive spectroscopy (EDS), and scanning electron microscopy (SEM), were employed to assess the crystalline structure, elemental composition, and surface morphology of the composite material [3].

Gadolinium, a paramagnetic element, was incorporated into the hydroxyapatite structure to enhance its drug carrier capabilities. The successful integration of gadolinium into hydroxyapatite crystals has been demonstrated in previous studies. For instance, Somoza et al. (2023) reported the synthesis and characterization of hydroxyapatite-doped gadolinium nanoparticles, highlighting their potential for efficient drug delivery systems [4]. Additionally, Yuan et al. (2021) investigated the positive effects of gadolinium doping on biocompatibility in bone marrow stem cells [5].

The doping of hydroxyapatite with gadolinium offers several advantages, including improved drug loading, controlled release, and enhanced imaging capabilities. The composite material shows promise for applications in photodynamic therapy (PDT) and photothermal therapy (PTT). In PDT, hydroxyapatite-doped gadolinium can function as an imaging agent, emitting intense red light upon excitation with ultraviolet light, enabling precise localization of cancer cells [6]. This facilitates more effective subsequent treatment. Furthermore, hydroxyapatite-doped gadolinium is being investigated as a drug releaser in photothermal therapy, where selective heating and destruction of cancer cells are achieved using light [6]. The selective encapsulation and release of therapeutic drugs in malignant cells by hydroxyapatite-doped gadolinium enhance treatment efficacy and reduce associated side effects.

The objective of this study is to further investigate the synthesis, characterization, and antimicrobial evaluation doping of hydroxyapatite with gadolinium, focusing on its potential as an optimized drug carrier in the biomedical field. Through a comprehensive analysis of the material's crystalline structure, elemental composition, and surface morphology, we aim to determine the feasibility of this composite for target-ed drug delivery applications. By elucidating the potential of hydroxyapatite- gadolinium composites as efficient drug carriers, this research contributes to the advancement of biomaterials science and offers new avenues for personalized medicine and therapeutics.

2 Material and Methods

2.1 HAp Gd Synthesis

The procedure was carried out by means of the method determined by Alanís- Gómez et al. [7] on a Monowave 300 (Anton Paar). The calculations of the molar ratio of gadolinium nitrate were made to correspond to 2% with respect to calcium nitrate. The temperature of the reaction mixture was 170 °C, with a pressure between 6 to 11 kPa. In an intermediate process, gadolinium doping was added at a concentration of 2%. At the end of the reaction a white crystalline solid was obtained, which was filtered and left to dry at room temperature. And left to dry at room temperature, after which the solid was recovered from the filter.

2.2 Characterization of HAp-Gd Structures

Characterization by Scanning Electron Microscope (SEM). They were observed using two scanning electron microscopes (SEM), namely JEOL JSM-6060 LV from Jeol in Akishima, Tokyo, Japan, and Hitachi SU8200 from Hitachi High-Technologies in Tokyo, Japan. An accelerating voltage of 10 kV and 20 kV was applied to make the observations and secondary electrons were used to form all images.

Energy Dispersive X-ray Spectroscopy Analysis (EDS). It was carried out using EDS with an EDAX system. Pure and Gd-doped HAp specimens, which were sintered at 1300 °C for 6 h, were coated with gold/palladium for 1 min using a sputter-coating magnetron from Emitech Inc. Then, the gold-coated specimens were observed using a JOEL SEM (Model 6400F, JEOL, Tokyo, Japan) that was equipped with a Noran light element EDS X-ray detector.

X-ray Diffraction (XRD). The experiments were conducted using a Bruker D8 Advance diffractometer. The operational parameters for the equipment were set at an accelerating voltage of 35 kV and a current of 35 mA. All analyses employed Cu K radiation with a wavelength of 1.54 Å. Samples were scanned across a range of 10 to 80°. The crystalline phase identification was achieved by comparison with the powder diffraction file (PDF) database provided by the International Centre for Diffraction Data (ICDD).

Antimicrobial Activity. It was determined using the Kirby-Bauer disk diffusion technique, which is a widely accepted and used method to assess the susceptibility of microorganisms to antimicrobial agents. For this, a sterile HAp-Gd/H₂O suspension was prepared at a concentration of 0.1 mg/ml. Gadolinium-doped hydroxyapatite impregnated discs were then prepared using sterile discs which were allowed to dry at room temperature. In addition, disks with Ciprofloxacin 5 µg were used as a positive control and disks impregnated with sterile water as a negative control. Subsequently, the *E. coli* strain (ATCC 25922) was seeded with a sterile swab on Müller-Hilton agar under sterile conditions. The culture was incubated for a period of 24 and 48 h at 37 °C in an Ecoshell Incubator. After incubation, the formation of zones of inhibition around the impregnated discs was observed, indicating the antimicrobial activity of the HAp-Gd. Subsequently, the diameters of the inhibition zones formed around the impregnated discs were measured. Finally, data obtained were recorded and compared with positive and negative controls to determine the antimicrobial activity of HAp-Gd against *Escherichia coli*. This experiment was carried out in triplicate and the means of the inhibition halos at 24 and 48 h were plotted against the positive control at 48 h.

3 Results

3.1 SEM of HAp-Gd

For the morphological, topological, and microstructural analysis of the HAp-Gd, a Scanning Electron Microscopy was performed (Fig. 1). In general, nanowires and mixed structures similar to short and long needles are observed in SEM images approximately 4–6 µm wide by 20–40 µm long, which in turn are made up of horizontal nanofibers.

From 20 to 40 nm in its cross section. These structures form clumps in the shape of irregular needles. In addition, we observed that the crystallinity and homogeneity of the hydroxyapatite decreased as the gadolinium dopant was added, with the pure HAP observed in Fig. 1a and 1b being more crystalline and homogeneous compared to the HAp-Gd observed in Fig. 1c and 1d. Finally, the HAp-Gd crystallites showed anisotropic growth. The different morphologies can be attributed to the various phenomena involved during the different stages in the synthesis pathways.

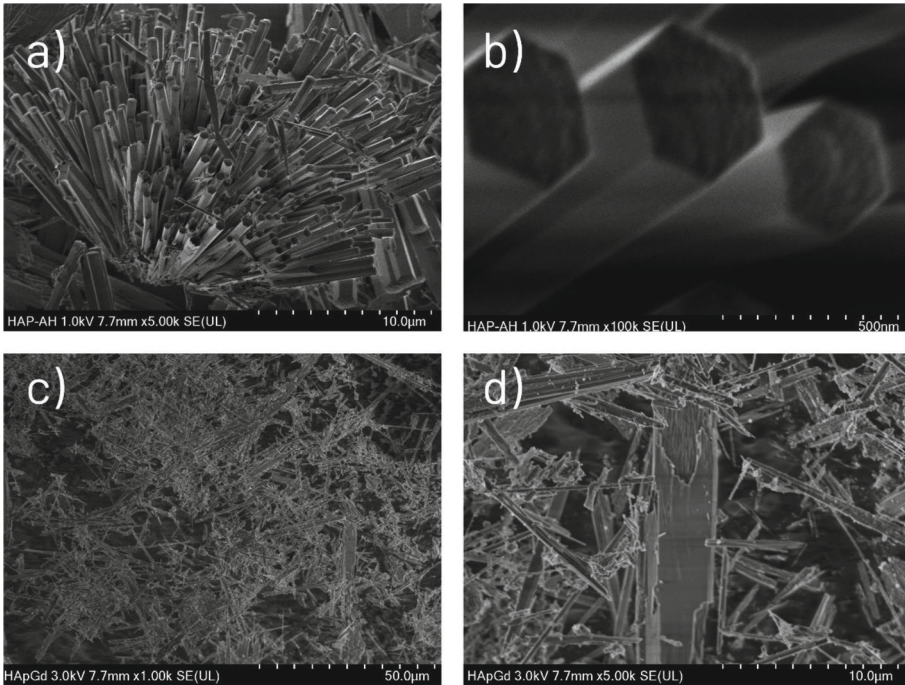


Fig. 1. Comparative SEM analysis of HAp (a) Nanofibers of pure HAp observed at 5000x magnifications. (b) Nanofiber of pure HAp observed at 100,000x magnification. (c) Nanowires of HAp-Gd observed at 1,000X magnification. (d) Nanowires of HAp-Gd observed at 3,000x magnifications.

3.2 EDS of HAp-Gd

The spectrogram shows information on the elemental chemical composition of the HAp-Gd sample, identifying the presence of gadolinium in the chemical composition of the hydroxyapatite. Figure 2 shows one of the 2 specific EDS analyzes that were carried out on the HAp-Gd1 and 2 samples. From this analysis, it was obtained that its main elements are Ca, P, C, O, Mg, Al, and Gd. The Ca/P atomic ratios were on average 1.62 and 1.59, respectively.

The identified HAp phase matched the powder diffraction file (PDF) PDF 09-0432, and no other crystalline components were detected. This suggests a high level of purity.

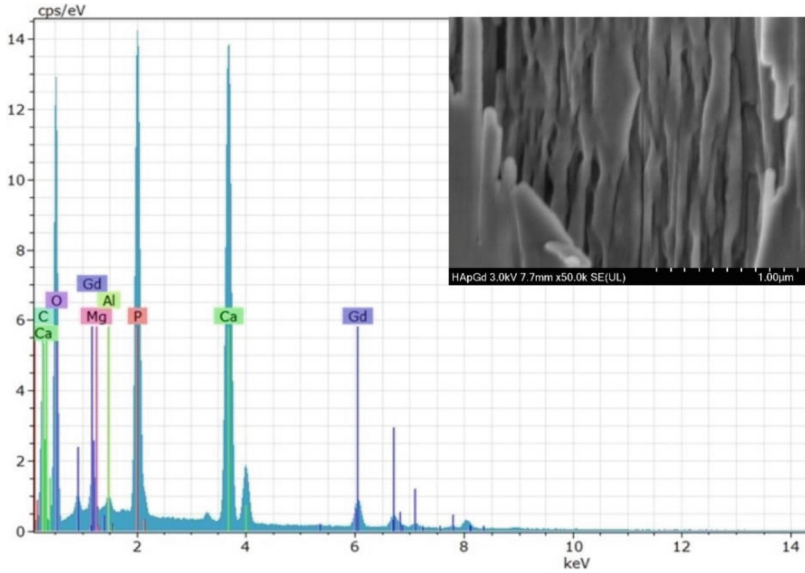


Fig. 2. EDS spectra obtained for the HAp-Gd samples.

The HAp-Gd exhibited a characteristic diffraction pattern with Bragg reflections positioned at 2θ values per the PDF mentioned. Moreover, these reflections displayed the

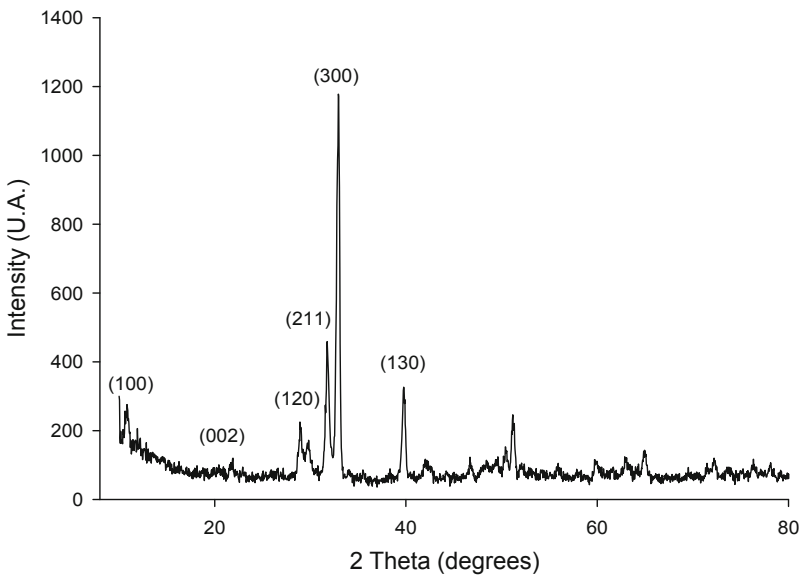


Fig. 3. Diffractogram obtained for the HAp-Gd sample.

expected intensities. Notably, the most prominent reflection occurred at 35.94° , corresponding to the (300) plane. However, the quality of crystallinity in this sample was found to be low (Fig. 3).

3.3 Antimicrobial Activity

Figure 4 shows the result of the antimicrobial susceptibility test, using discs impregnated with gadolinium-doped hydroxyapatite that were placed on an M.H. where the *Escherichia coli* strain was planted. After incubation, we observed zones of inhibition around the control (+) and HAp-Gd discs, indicating the antimicrobial activity of the biomaterial. Compared with the positive control of ciprofloxacin, which is a widely used antibiotic known for its activity against *Escherichia coli*, the inhibition halo observed around gadolinium-doped hydroxyapatite-impregnated discs was small. This suggests that the antimicrobial activity of the biomaterial against *Escherichia coli* is limited compared to ciprofloxacin. It is important to highlight that the size of the inhibition halo may be related to the concentration of the antimicrobial agent and its ability to diffuse in the agar. A small halo indicates that the biomaterial's ability to inhibit *Escherichia coli* growth may be less potent compared to ciprofloxacin.



Fig. 4. Result of the antimicrobial activity test by the disk diffusion method using HAp-Gd 0.1 mg/ml against the positive (ciprofloxacin) and negative (water) control.

The results of three independent experiments of the susceptibility test against *E. coli* at 24 and 48 h of treatment were plotted and compared with the result obtained by the positive control (Fig. 5). A significantly larger diameter ($p < 0.05$) of the inhibition halos of the positive control is observed compared to HAp-Gd at 24 and 48 h. The results indicate that while gadolinium-doped hydroxyapatite may exhibit some antimicrobial activity against *Escherichia coli*, its effectiveness is limited compared to a ciprofloxacin positive control.

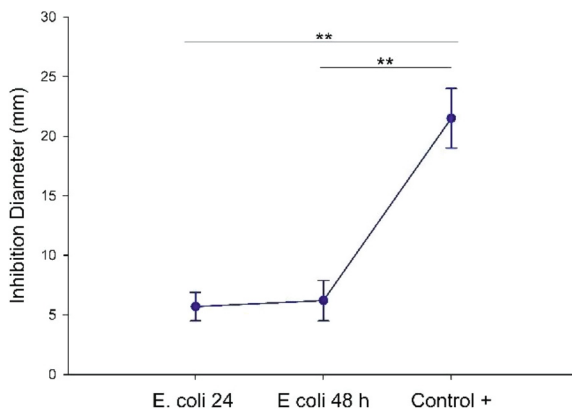


Fig. 5. Graph of the diameters of the inhibition halos obtained by the HAp incubated at 24 and 48 h versus the positive control. Mean values and standard deviation are shown. Student's t test was used to compare between groups.

4 Analysis

In the present study, the synthesis and characterization of HAp-Gd nanofibers was carried out with the purpose of later using this biomaterial as a drug transport system, due to the fact that the optical properties and controlled release of HAp-Gd make this material a promising candidate for use in photodynamic therapy and photothermal therapy [8]. The use of gadolinium in the manufacture of biomaterials such as HAp-Gd presents several advantages. First, gadolinium exhibits high pharmacological affinity, making it an effective drug delivery system [9]. Second, its ability to emit intense red light under ultraviolet excitation allows for precise localization of cancer cells [4]. In addition, HAp-Gd can also be investigated as a drug-releasing agent in photothermal cancer therapy, which uses light to selectively heat and kill cancer cells. By selectively encapsulating and releasing therapeutic drugs in malignant cells, HAp-Gd increases treatment efficacy and reduces associated side effects, which holds promise in the field of biomedical engineering.

In previous studies, gadolinium has been shown to be biocompatible and non-toxic to healthy cells, which is essential to minimize adverse effects in cancer drug therapy [5]. Therefore, we focus on the synthesis of this biomaterial through the microwave-assisted hydrothermal method, a method that our research group previously standardized and that generates nanofibers with good mechanical properties and high crystallinity. Characterization of the HAp-Gd nanofibers was performed using scanning electron microscopy (SEM) and energy dispersive spectroscopy (EDS) techniques. The SEM allowed us to obtain high-resolution images of the sample surface, observing structures in the form of nanowires, while the EDS provided information on the elemental composition of the sample and allowed us to confirm the correct integration of gadolinium in the hydroxyapatite structure.

The results revealed the formation and successful doping of the HAp-Gd. Furthermore, the HAp-Gd configured a different structure from the one we obtained in a previous

study where we synthesized pure hydroxyapatite [7] with a hexagonal cross-sectional structure. Therefore, the presence of gadolinium in the hydroxyapatite structure can confer unique properties to the material, such as improved optical properties for imaging or greater efficiency in the release and delivery of drugs. In addition, in the antimicrobial activity evaluation tests, a slight inhibition effect on the growth of *Escherichia coli* is shown, which is favorable since it adds an extra property to the biomaterial by reducing the risk of infection. In this sense, dual properties of calcium phosphate bioceramics have previously been demonstrated when they act as nanocarriers [10, 11].

Calcium phosphates (CaP) are commonly used for the treatment of bone infections associated with bone loss. This material can be used as a local antibiotic delivery agent for bone infections and can be substituted with antibacterial ions in its crystal structure to have sustained broad-spectrum antibacterial activity even against drug-resistant bacteria, some of the most tested ions and with a clear antimicrobial effect are zinc, silver, and strontium and the heavy metals gadolinium, rubidium, and samarium [11]. These findings are consistent with our results; however, future experiments are required to evaluate the antimicrobial activity of HAp-Gd. Against more microorganisms, including gram positive and negative bacteria and fungi.

Finally, the synthesis of gadolinium-doped hydroxyapatite nanofibers and their characterization proved to have a promising approach for the development of drug transport systems in cancer drug therapy. The next step is to explore the biological properties, cytotoxicity, and biocompatibility of this biomaterial in *in vitro* assays.





References

1. Bal, Z., Kaito, T., Korkusuz, F., Yoshikawa, H.: Bone regeneration with hydroxyapatite-based biomaterials. *Emergent Mater* **3**, 521–544 (2020)
2. Chetty, A., Wepener, I., Marei, M.K., Kamary, Y.El., Moussa, R.M.: Hydroxyapatite: synthesis, properties, and applications. In: Nov Science Publication, pp. 91–132 (2012)
3. Wang, W., Yeung, K.W.K.: Bone grafts and biomaterials substitutes for bone defect repair: a review. *Bioact. Mater* **2**, 224–247 (2017)
4. Somoza, M., et al.: Microfluidic fabrication of gadolinium-doped hydroxyapatite for therapeutic applications. *Nanomaterials* **13**(3), 501 (2023). <https://doi.org/10.3390/nano13030501>
5. Yuan, S.J., Qi, X.Y., Zhang, H., Yuan, L., Huang, J.: Doping gadolinium versus lanthanum into hydroxyapatite particles for better biocompatibility in bone marrow stem cells. *Chem. Biol. Interact.* **346**, 109579 (2021). <https://doi.org/10.1016/j.cbi.2021.109579>
6. Mueller, R., et al.: Imaging and characterization of sustained gadolinium nanoparticle release from next generation radiotherapy biomaterial. *Nanomaterials* **10**, 1–13 (2020)
7. Alanís-Gómez, J.R., et al.: Synthesis of micro and nano-sized hydroxyapatite fibers through the microwave assisted hydrothermal method. *J. Nanosci. Nanotechnol.* **16**, 7557–7566 (2016)
8. Alanís-Gómez, J.R., Rivera-Muñoz, E.M., Peza-Ledesma, C., Manzano-Ramírez, A., Velázquez-Castillo, R.: A comparison of mechanical properties of different hydroxyapatite (HAp) based nanocomposites: the influence of morphology and preferential orientation. *J. Nanosci. Nanotechnol.* **20**, 1968–1976 (2019)
9. Liu, Y., et al.: Gadolinium-doped hydroxyapatite nanorods as T1 contrast agents and drug carriers for breast cancer therapy. *ACS Appl. Nano Mater* **2**, 1194–1201 (2019)

10. Sampath Kumar, T.S., Madhumathi, K., Rubaiya, Y., Doble, M.: Dual mode antibacterial activity of ion substituted calcium phosphate nanocarriers for bone infections. *Front. Bioeng. Biotechnol.* **3**, 59 (2015)
11. Kamphof, R., et al.: Antimicrobial activity of ion-substituted calcium phosphates: a systematic review. *Heliyon* **26**, e16568 (2023)



Wrist-Forearm Differential Kinematics Using Monocular Vision Capture

Alejandro Pescador-Salas^{1,2} , Juan Pablo Rosales-Huie² ,
Dulce Martinez-Peon^{1,2} , and Ernesto Olgún-Díaz³ 

¹ Faculty of Graduate Studies, National Technological Institute of Mexico,
Guadalupe, Nuevo León 67170, Mexico

alejandropescador.sa@gmail.com

² Department of Electrical and Electronic Engineering, National Technological
Institute of Mexico, Guadalupe, Nuevo León 67170, Mexico

³ Robotics and Advanced Manufacturing Group, Research Center for Advanced
Studies (CINVESTAV), Ramos Arizpe, Coahuila 25900, Mexico

Abstract. Each year the number of patients requiring motor rehabilitation for the upper limb, particularly for the wrist and forearm, increases, due to a loss in their fine motor skills. Although physiotherapists assist them, the progress evaluation remains subjective. Modern technology can be used to create solutions to provide a quantitative description allowing objective metrics evaluations for motor recovery of the patients, which typically yield complex and expensive solutions.

This paper presents a methodology to obtain the differential kinematic trajectories of the wrist and forearm performed by a patient, through video capture of its movement, using the open-source MediaPipe library. The angles of the wrist and forearm are obtained through inverse kinematics analysis using hand-specific landmarks. A second-order filter estimates the angular trajectories for position, velocity, and acceleration. The study was performed with basic movements used in rehabilitation: adduction-abduction, flexion-extension, pronation-supination, and complex movements such as circumduction with the participation of six healthy patients. The results show that it is possible to obtain estimates of differential wrist trajectories. The applications of this methodology in the fields of biomechanics and rehabilitation are discussed.

Keywords: Wrist and forearm motion · Monocular vision capture · Differential kinematics

1 Introduction

Advances in modern technology and medical research have led to an increase in the population's life expectancy. However, this extension has also led to increased disabilities and chronic conditions, particularly in the elderly, often due to cognitive and motor impairments. The World Health Organization estimates that approximately 2.4 billion people require rehabilitation [1], resulting in a growing

demand for physical therapists [2]. Specifically, pathologies related to the wrist and forearm, including fractures, stroke, arthritis, and tendonitis, have become increasingly important in medical care [3, 4].

Despite improvements in the methods used by healthcare professionals to assess the progress of their patients, there remains a reliance on subjective criteria and imprecise tools. For example, assessment of fine motor skills often relies on inaccurate instruments such as the grooved pegboard test [5]. In addition, the goniometer traditionally used to measure joint flexion relies on clinician interpretation and placement to achieve effective results.

Although robotic technology has emerged as a promising avenue to improve patient recovery with reduced supervision [6], vision-based solutions have emerged as an economically viable and accurate substitute for objectively assessing motor recovery [7]. Vision-based systems have been used to approximate limb and joint positions, primarily in whole-body configurations [8].

Existing systems, such as Vicon, use multiple camera configurations to achieve accurate results using information redundancy but become expensive, [9, 10]. On the other hand, up-to-date monocular systems capture body motion but do not focus specifically on hand movements, [11]. The sensor glove CyberGlove addresses hand motion tracking, but requires calibration for each patient, [12]. Recently, the open-source MediaPipe Hands library (MPHL) has come to the fore [13], which uses hand detection techniques to localize hand landmarks on 2D images and neural networks to estimate and transform these 2D coordinates into geometry- and depth-dependent 3D coordinates. Furthermore, this system integrates temporal tracking techniques to provide real-time and accurate results as the hand navigates through space. It has been employed in [14] as a tool for measuring tremors in Parkinson's patients. This raises the question of whether it is possible to derive wrist joint trajectories and their temporal derivatives using this motion capture tool.

This paper presents a methodology to capture hand motion vis-à-vis the forearm, employing a monocular camera in conjunction with the open-source MediaPipe Hands library. The approach focuses on the estimation of the wrist-forearm trajectory, implementing the wrist functional range of motion, [15], on the three basic motions: 1) flexion-extension (FE), 2) abduction-adduction (AA) and 3) pronation-supination (PS). Moreover, we have added a circumduction (CIR) motion involving FE and AA carried out during therapy.

2 Methods

2.1 Material

- Laptop with an i5 processor and 16 GB of RAM, operating on Windows 10 64-bit.
- Python 3.8.8 and MPHL 0.9.1.0. was used for image processing.
- MATLAB 2015 software to process landmarks associated with each frame.
- Simulink 8.5 to construct a second-order filter.

- Recorded videos using a Samsung S20FE camera 12 MP lens featuring an aperture of f/1.7, mounted on a tripod.
- FHD Video quality at 30 FPS, with a 1:1 aspect ratio.
- Forearm support base.

2.2 Participants

Six healthy volunteers participated in the study, three males and three females (aged $22.66 \text{ years} \pm 4.84$, height of $1.70 \text{ m} \pm 0.10$, weight of $73 \text{ kg} \pm 7.00$). Volunteers were made known for detailed information about the experimental procedure and provided informed consent following the principles outlined in the Declaration of Helsinki.

2.3 Assessment Procedure

Participants were instructed to perform the exercises presented in a video guide using the right hand, following the order of AA, FE, PS, and CIR. A physiotherapist assessed the video guide. Each exercise was repeated three times, with a 2-second rest period between repetitions. Two videos were recorded for each participant for which an $\mathcal{L}_2(e) = \left(\int_{t_0}^{\infty} \|e(t)\|^2 dt \right)^{\frac{1}{2}}$ (Euclidian Lebesgue norm) of the error trajectory $e(t) = y(t) - r(t)$ (difference of participant's motion wrt the reference guide video) has been computed along the experiment, and the one with the minimum norm value was selected. Figure 1 illustrates the general procedure, which consists of six steps described below:

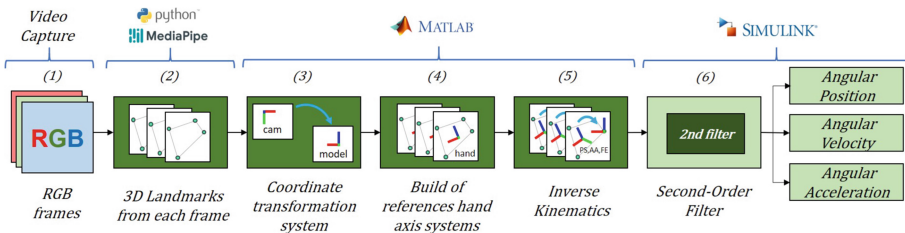


Fig. 1. General scheme of the methodology

1. Recording videos using the next conditions:
 - Lux level: $364 \text{ lx} \pm 3.39$.
 - Position the camera at 50 cm concerning the hand and parallel to the palmar surface.
 - Elbow flexed at 90° and neutral hand position.
2. Getting the landmarks frame-by-frame using Python and MPL with the following library settings: num-hands=1, min-hand-detection-confidence=0.5, min-hand-presence-confidence=0.5 and min-tracking-confidence=0.5.

3. Obtaining the position of each landmark point in the coordinate system of the wrist model:

$$\vec{p}_{L_i}^{(w)} = R_c^{wT} \left(\vec{p}_{L_i}^{(c)} - \vec{p}_{w/c}^{(c)} \right), \quad (1)$$

where $\vec{p}_{L_i}^{(w)}$ represents the position of the i^{th} landmark concerning the position of the wrist landmark in wrist model coordinates, $\vec{p}_{L_i}^{(c)}$ denotes the position of the i^{th} landmark, and $\vec{p}_{w/c}^{(c)}$ represents the position of the wrist landmark, both with respect to camera coordinates, R_c^{wT} refers to the transpose of the rotation matrix from the camera to the wrist model axis system, defined as:

$$R_c^w = \begin{bmatrix} -1 & 0 & 0 \\ 0 & 0 & -1 \\ 0 & -1 & 0 \end{bmatrix}.$$

4. Obtaining the hand axis system frame following the next steps:
- Creation of a plane in the palm using the landmarks of the wrist, the base of the index finger, and the base of the little finger; and using the position vectors $\vec{p}_{L_5}^{(w)}$ and $\vec{p}_{L_{17}}^{(w)}$ that denote respectively the positions of the index and little finger bases, with respect to the wrist.
 - Unit *approach vector* calculation:

$$\vec{a} = \frac{\vec{p}_a^{(w)}}{\left| \vec{p}_a^{(w)} \right|}, \quad (2)$$

where $\vec{p}_a^{(w)} = \frac{1}{2} \left(\vec{p}_{L_5}^{(w)} + \vec{p}_{L_{17}}^{(w)} \right)$ denotes the vector from the wrist to the midpoint between the index finger base and little finger base, laying in the palm plane.

- Unit *normal* (to the palm) *vector* calculation :

$$\vec{n} = \frac{\vec{p}_{L_5}^{(w)} \times \vec{p}_{L_{17}}^{(w)}}{\left| \vec{p}_{L_5}^{(w)} \times \vec{p}_{L_{17}}^{(w)} \right|}, \quad (3)$$

- Unit *lateral vector* calculation:

$$\vec{l} = \vec{a} \times \vec{n}. \quad (4)$$

- Rotation between the hand axis system frame with respect to the wrist axis system frame (see Fig. 3) can be constructed simply as:

$$R_h(k) = \left[\vec{a}, \vec{n}, \vec{l} \right] = \begin{bmatrix} a_x & n_x & l_x \\ a_y & n_y & l_y \\ a_z & n_z & l_z \end{bmatrix}. \quad (5)$$

5. Calculation of the wrist angles (ps , aa , fe), defined respectively as pure basic rotations around the x , y and z -axes of the wrist axis system frame, arise after the complex rotation matrix produced after the above mention angles, getting the following expression:

$$R(\theta) = R_x(ps) R_y(aa) R_z(fe) = \begin{bmatrix} C_{aa}C_{fe} - C_{aa}S_{fe} & S_{aa} & \\ a_{21} & a_{22} & -C_{aa}S_{ps} \\ a_{31} & a_{32} & C_{aa}C_{ps} \end{bmatrix}, \quad (6)$$

where $C_x = \cos(x)$ and $S_y = \sin(y)$ stand for the basic trigonometric functions and $a_{21} = C_{ps}S_{fe} + S_{ps}S_{aa}C_{fe}$, $a_{22} = C_{ps}C_{fe} - S_{ps}S_{aa}S_{fe}$, $a_{31} = S_{ps}S_{fe} - C_{ps}S_{aa}C_{fe}$, $a_{32} = S_{ps}C_{fe} + C_{ps}S_{aa}S_{fe}$. Therefore the anatomical angles that match the basic movements of the wrist with respect to the forearm can be computed after the elements of (6) with the values of (5), using the 4-quadrant inverse tangent function $arctan2$, defining the order zero inverse kinematics:

$$aa = \arcsin(l_x) \quad \in [-\pi/2, \pi/2], \quad (7a)$$

$$fe = -\arctan 2(n_x, a_x) \quad \in [-\pi, \pi], \quad (7b)$$

$$ps = -\arctan 2(l_y, l_z) \quad \in [-\pi, \pi]. \quad (7c)$$

6. Estimation of differential kinematics, *ie*: the velocity and acceleration trajectories, a second-order filter was implemented and is shown in Fig. 2, with coefficients $\omega_n = 5rad/sec$ and $\xi = 1$.

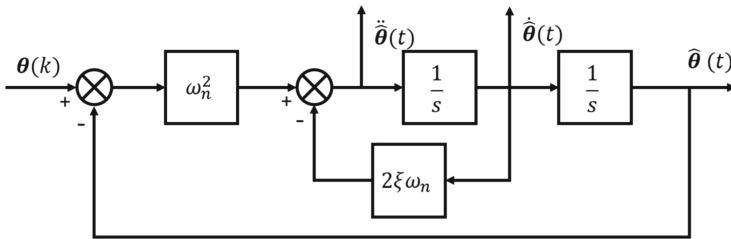


Fig. 2. Schematic of the second-order filter implementation.

The graphical process of this study is shown in Fig. 3, with a video version available at <https://www.youtube.com/watch?v=5sEv1w0kW8E>. Image c) shows a hand model created specifically to visualize and compare the trajectories generated by the proposed method. This was modeled using an alternative methodology to define the reference frames of each body, different to the traditional Denavit-Hartenberg (DH) method used in the formulation of direct kinematics in robotics and biomechanics. The adoption of this alternative methodology, described in [16], represents a novel approach to addressing hand kinematics.

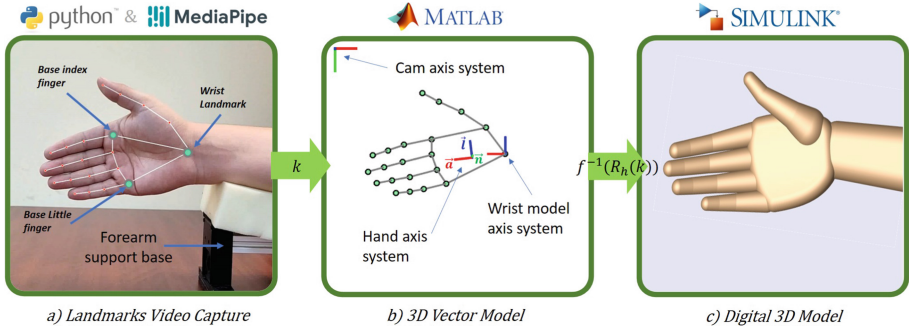


Fig. 3. Algorithm pipeline

3 Results

The graphs presented in Figs. 4, 5, 6 and 7 display the variables ps , aa , and fe , which represent the angles acquired through the employed method, along with their filtered versions, accompanied by their respective velocity and acceleration profiles. Figure 4 displays the overall trajectories for volunteer 6, while Figs. 5, 6 and 7 depict the results of comparing trajectories for each exercise across the six participants. The figures are segmented by vertical dashed lines, corresponding to intervals dedicated to the exercises mentioned above. Exercise was executed in the intervals: AA in $t = (0 - 11)$, FE in $t = (11 - 22)$, PS in $t = (22 - 34)$ and CIR in $t = (34 - 42)$.

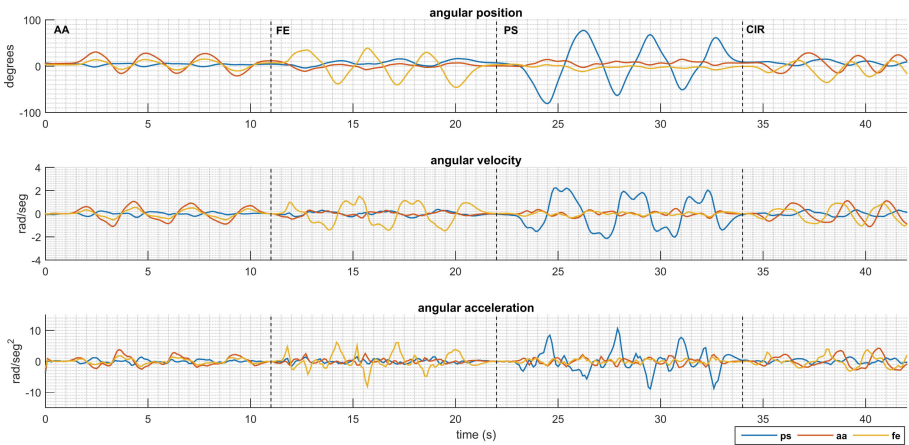


Fig. 4. Trajectories of subject 6 of their angular positions, velocities, and accelerations captured for the movements of AA, FE, PS and CIR.

It is vital to acknowledge that the inherent limitations of participants during the execution of the three primary natural motions (PS, AA, FE) can result in disturbances in the other angular variables (ps , aa , fe). The trajectory associated with each specific exercise in Fig. 4 shows heightened activity compared to other curves, facilitating the identification of the particular motion. For instance, the involvement of the ps variable is notable during the CIR exercise. However, it's important to highlight that the curves showing the most pronounced activation correspond to the aa and fe angles, consistent with the anticipated outcomes of this exercise. Notice that zero in all angular position graphs represents the neutral position of the movement. Positive values correspond to supination, adduction, and flexion, while negative values relate to pronation, abduction, and extension movements, respectively to the ps , aa , and fe variables.

The dissimilarities in the trajectories showcased in the figures stem from individual participants executing the movements according to their capacities, thereby revealing distinct movement patterns. Importantly, Participant 3 displayed comparatively lower performance than other participants, particularly concerning tracking errors wrt the guidance video. This discrepancy is evident in the comparative analysis.

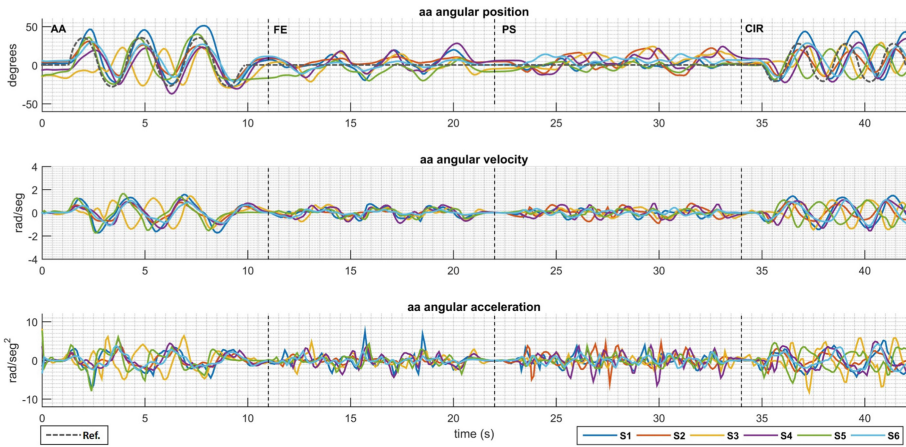


Fig. 5. Comparison of the aa trajectories among the 6 participants

4 Discussion

This study's results are significant for physical therapists, as they provide a potential method to objectively assess the efficacy of wrist and forearm therapies. This tool effectively measures motor function, coordination, and movement patterns, and can evaluate the efficacy of therapeutic interventions. Moreover, estimating velocity and acceleration trajectories could lead to novel objective metrics, which may enhance the accuracy of patient recovery assessment. These

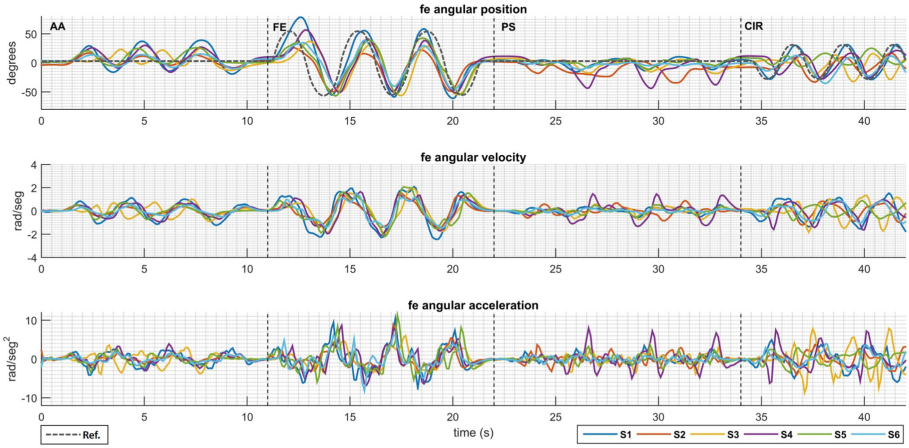


Fig. 6. Comparison of the fe trajectories among the 6 participants

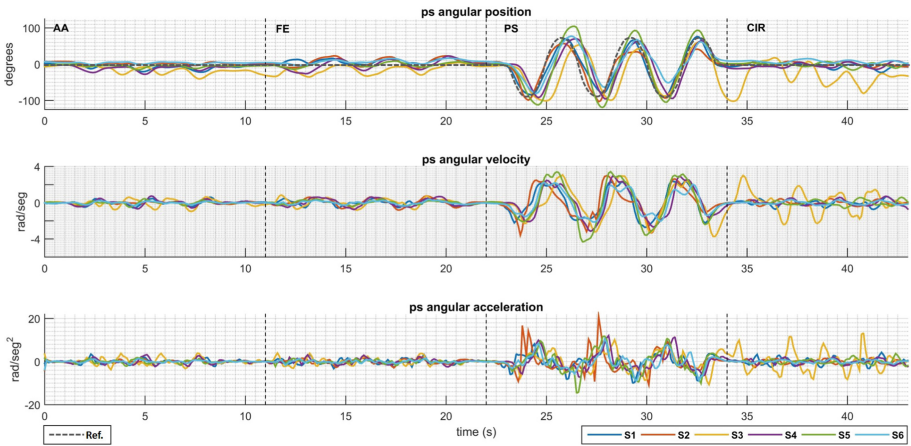


Fig. 7. Comparison of the ps trajectories among the 6 participants

trajectories play a crucial role in generating inverse dynamics models of the upper limb in biomechanics.

It should be noted that the results derived from MPHL have inherent limitations due to its method of estimating 3D landmarks. This limitation arises due to the derivation of landmarks from the perspective and depth of the 2D landmarks extracted from the video. Additionally, determining the Z-axis coordinate based on the wrist landmark limits the participants' wrist movement during recording.

This proposed solution provides a cost-effective alternative to existing methodologies like Vicon systems [9,10] or CyberGlove [12], necessitating software and hardware acquisition. Integrating the MPHL decreases financial burdens for healthcare professionals and enhances access to objective assessment

tools in various settings. This approach's ease of use and scalability promotes broad adoption, leading to large-scale studies that benefit both patients and healthcare professionals.

Additional research is crucial in objectively quantifying the accuracy attained through this solution. Another limitation exists due to the latency introduced by the second-order filter, which hinders real-time implementation. Future research recommends integrating a robust differentiator that can provide real-time derivatives to overcome this limitation.

5 Conclusions

The methodology presented in this study allows us to obtain trajectories of wrist and forearm movements of the right hand using a monocular vision-based motion capture system and MDHL. Using a second-order filter enables the analysis of signals in the time domain and the estimation of the first and second derivatives corresponding to the velocity and acceleration trajectories of the wrist and forearm. The obtained trajectories offer valuable insights into the behavior of each hand movement, particularly concerning the orientation angles presented. In turn, this facilitates the study of specific exercises targeting the wrist and forearm. The movements' amplitudes fall within the known and reported ranges in the literature. However, evaluating the tool's precision remains a necessary task for future studies.

References

1. Rehabilitation. <https://www.who.int/news-room/fact-sheets/detail/rehabilitation>. Accessed 28 June 2023
2. Jesus, T.S., Landry, M.D., Hoenig, H.: Global need for physical rehabilitation: systematic analysis from the global burden of disease study 2017. *Int. J. Environ. Res. Public Health* **16**(6), 980 (2019)
3. Erickson, M., Lawrence, M., Jansen, C.W.S., Coker, D., Amadio, P., Cleary, C.: Hand pain and sensory deficits: carpal tunnel syndrome. *J. Orthop. Sports Phys. Therapy*. **49**(5), CPG1–CPG85 (2019)
4. Stefanou, N., Kontogeorgakos, V., Varitimidis, S., Malizos, K., Dailiana, Z.: Spaghetti wrist: transverse injury, axial incision, layered microsurgical reconstruction. *Injury* **52**, 3616–3623 (2021)
5. Tolle, K.A., Rahman-Filipiak, A.M., Hale, A.C., Andren, K.A.K., Spencer, R.J.: Grooved pegboard test as a measure of executive functioning. *Appl. Neuropsychol. Adult*. **27**(5), 414–420 (2020)
6. Ranzani, R., et al.: Towards a platform for robot-assisted minimally-supervised therapy of hand function: Design and pilot usability evaluation. *Front. Bioeng. Biotechnol.* **9**, 652380 (2021)
7. Feingold Polak, R., Tzedek, S.L.: Social robot for rehabilitation: expert clinicians and post-stroke patients' evaluation following a long-term intervention. In: *Proceedings of the 2020 ACM/IEEE International Conference on Human-Robot Interaction, Series, HRI 2020*. New York, NY, USA, pp. 151–160. Association for Computing Machinery (2020)

8. Azhand, A., Rabe, S., Müller, S., Sattler, I., Heimann-Steinert, A.: Algorithm based on one monocular video delivers highly valid and reliable gait parameters. *Sci. Rep.* **11**(1), 14065 (2021)
9. Pfister, A., West, A.M., Bronner, S., Noah, J.A.: Comparative abilities of microsoft kinect and vicon 3d motion capture for gait analysis. *J. Med. Eng. Technol.* **38**(5), 274–280 (2014)
10. Kidziński, L., Yang, B., Hicks, J., Rajagopal, A., Delp, S., Schwartz, M.: Deep neural networks enable quantitative movement analysis using single-camera videos. *Nat. Commun.* **11**(1), 4054 (2020)
11. Hesse, N., Baumgartner, S., Gut, A., van Hedel, H.J.A.: Concurrent validity of a custom method for markerless 3d full-body motion tracking of children and young adults based on a single rgb-d camera. *IEEE Trans. Neural Syst. Rehabil. Eng.* **31**, 1943–1951 (2023)
12. Wang, Y., Neff, M.: Data-driven glove calibration for hand motion capture. In: Kim, T., Sumner, R. (Eds.) *Eurographics/ ACM SIGGRAPH Symposium on Computer Animation*, ACM SIGGRAPH/Eurographics Association (2013)
13. Zhang, F., et al.: Mediapipe hands: on-device real-time hand tracking. arXiv preprint [arXiv:2006.10214](https://arxiv.org/abs/2006.10214) (2020)
14. Güney, G., et al.: Video-based hand movement analysis of Parkinson patients before and after medication using high-frame-rate videos and mediapipe. *Sensors*. **22**(20), 7992 (2022)
15. Brigstocke, G., Hearnden, A., Holt, C., Whatling, G.: The functional range of movement of the human wrist. *J. Hand Surg. (Eur. Vol.)* **38**(5), 554–556 (2013)
16. Hernández-Hernández, B., et al.: An alternative method for kinematic modelling applied to the human joint position. In: *Proceedings of the 6th International Congress on Sport Sciences Research and Technology Support - Volume 1: icSPORTS*. SciTePress, pp. 139–144 (2018)



Knee Osteoarthritis Therapy Assistance Software

Pérez Alvarado Oscar Eduardo^(✉), Solís López Daniel^{ORCID},
and Vargas Martinez Darien Gustavo^{ORCID}

Ingeniería Biomédica, Universidad Politécnica de Quintana Roo, Cancún Quintana Roo,
Benito Juárez 77539, México
202000327@estudiantes.upqroo.edu.mx

Abstract. This work focuses on effectively exploring the application of computer vision technology in the field of healthcare. In this context, the research aims to address the limitations present in the traditional method of physiotherapy and how these can be overcome through the integration of advanced technology, revealing an opportunity to tackle these shortcomings. Computer vision technology, using OpenCV and MediaPipe in Python, is responsible for detecting key points on the human body and calculating internal angles when extending or flexing the knee. This approach aims to provide valuable support in the treatment of patients diagnosed with knee osteoarthritis, one of the primary conditions affecting individuals over the age of 45.

The implementation of this work results in harnessing this technology to develop a tool for precise and objective measurement of the range of motion, presenting itself as an alternative to the current procedure. This leads to an increase in measurement reliability, benefiting a more accurate assessment of patient progress during treatment. Simultaneously, it optimizes the customization of treatment plans, surpassing the limitations of traditional methods.

Keywords: Osteoarthritis · MediaPipe · OpenCV · Assistance Software

1 Introduction

This project presents software whose main objective is to provide help in the treatment of one of the most common diseases among the population over 45 years of age. Its purpose is to overcome the current limitations of the analog tools used in disease measurement, which affect their precision.

The project is divided into several phases. In the first phase, the general aspects of the problem were addressed, the objectives were established and a detailed action plan was designed. Next, a comprehensive investigation of the disease was carried out, identifying its characteristics and limitations.

With all the information collected and considering the established objectives, we proceeded to develop the software. Articulation recognition technology was used through tools such as OpenCV and MediaPipe in Python. This made it possible to accurately measure the angle of motion of the knee in patients with osteoarthritis.

One of the main advantages of this approach is that it can be applied in a virtual environment and at a distance, which prevents patients from abandoning their therapies and especially benefits those with mobility difficulties. In addition, the software provides remote assistance tools that simplify the work of the physiotherapist.

In short, a project that uses state-of-the-art technology to improve the measurement and monitoring of knee osteoarthritis treatment. Providing a more accurate, accessible and convenient solution for patients, while facilitating the work of healthcare professionals

1.1 Problem Statement

Measurement of the range of motion of a joint using a goniometer and visual assessment by the physical therapist have certain limitations that make it difficult to obtain accurate measurements. These traditional methods can be subject to human errors and subjective variations, which compromises the objectivity of the results. This lack of precision can affect the effectiveness of the treatment and the evaluation of the patient's progress. These challenges underscore the need to develop solutions that allow for more accurate and objective measurement of joint range of motion.

Objective

Develop accurate and reliable software that allows the precise measurement of the flexion-extension angle of the knee joint, acquiring said information in real time during therapy sessions. This will improve the quality of care provided by physiotherapists, will facilitate the assessment and monitoring of the patient's progress, and will allow the performance of remote therapies, thus optimizing the fluidity and effectiveness of the treatment.

2 Theoretical Framework

2.1 Osteoarthritis

The International Osteoarthritis Foundation (FIO) defines osteoarthritis, also known as osteoarthritis (OA), as a degenerative joint disease that affects both the cartilage and the bone and soft tissues of the joint (see Fig. 1). It is classified within rheumatic diseases and, within this classification, it is a type of arthritis. It can occur in the hip, knees, hands, feet and spine, the first three being the most frequent [1].

The treatment recommended by the American College of Rheumatology (ACR), the American Academy of Orthopedic Surgeons (AAOS) and the European League Against Rheumatism (EULAR) for non-pharmacological osteoarthritis includes low-impact aerobic exercises, aquatic exercises and/or resistance training, physiotherapy, maintaining a healthy body weight ($BMI \leq 25 \text{ kg/m}^2$) and the use of supportive and orthopedic devices [2].

Knee and hip osteoarthritis show a higher incidence in men under 50 years of age, while after 50 years of age the prevalence is higher in women. The risk of developing osteoarthritis in these joints increases in women after menopause. Also, the disease

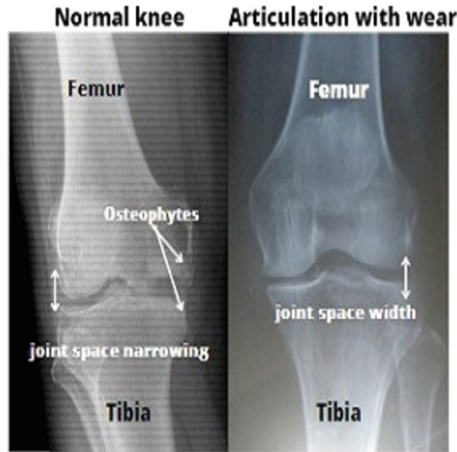


Fig. 1. Comparison between a healthy knee and one with joint wear, according to the evaluation by radiologists, the most prominent pathological feature in osteoarthritis is joint space narrowing.

progresses faster in women than in men. Globally, osteoarthritis of the knee and hip ranks fourth as a cause of disease in women over 60 years of age and eighth in men [3].

In Mexico, a prevalence of 2.3% in adults is estimated, being one of the main causes of medical consultation and disability. According to a study carried out at the IMSS, a prevalence of knee osteoarthritis of 11.7% in women and 8.71% in men was found, with notable variability in different parts of the country [4].

In summary, physiotherapy plays a crucial role in the treatment of arthritis, aiding in symptom relief, delaying disease progression, and enhancing patients' quality of life. Through stretching and strengthening exercises, the use of orthopedic devices, and joint rest as recommended by physiotherapists, these goals are achieved. They often use tools like the goniometer to measure joint movement angles; however, they tend to encounter measurement errors stemming from human errors, variability among physiotherapists, and variations in measurement techniques [5].

In order for goniometric techniques to provide meaningful and reliable data, measurements must be valid and reliable. In terms of validation, as stated by Currier, "validity refers to the degree to which a measuring instrument accurately measures what it intends to measure and approaches its intended purpose." In the context of this project, validity ensures that range of motion measurements accurately reflect the actual angle of the evaluated joint [5].

On the other hand, reliability, a pivotal component for assessing measurement quality, focuses on the consistency and coherence of results obtained through different measurements carried out by various physiotherapists or at different times. Specifically, the study of goniometric reliability seeks to mitigate the impact of systematic and random errors that may arise during the measurement process. By addressing reliability, the goal is to ensure that measurements are not only precise on a single occasion, but also consistent and reproducible across various circumstances, contributing to a more accurate assessment and monitoring of patient progress during rehabilitation treatment [6].

3 Methodology

To fulfill the proposed objectives, the Anaconda programming environment was implemented, as it includes all the necessary basic packages, which facilitates work organization and libraries. Similarly, for code writing, the JupyterLab IDE was used to maintain a dynamic development environment that enhances the efficiency of testing and project changes.

From the MediaPipe library, the modules “drawing” was used to draw reference points on the image. Likewise, “pose,” a pre-trained model, was used to perform detection, segmentation, and localization of the reference points.

To conduct program testing, images were captured in a posture similar to that of the therapy in which it will be applied, with the goal of detecting reference points on the ankle, knee, and shoulder (see Figs. 2 and 3).



Fig. 2. Capture for extension test

Subsequently, we obtained the key reference points – shoulder, hip, and ankle – which are essential for the calculation of the desired angle. This was achieved by accessing these points through an indicator defined by MediaPipe. The indicator provides a standardized and consistent method for identifying these specific anatomical landmarks, ensuring accuracy and reliability in the measurement process. This approach not only streamlines the data collection procedure but also enhances the precision of angle calculation. By using these reference points as guided by MediaPipe’s defined indicator, we established a robust foundation for accurate angle measurement in our project (see Fig. 4).

Using the reference points, we proceed to connect them and create an imaginary line that touches the second point (the hip) and the last point (the ankle). This configuration forms a triangle, allowing us to easily obtain the internal angle of the knee. This entire process is automated and carried out in real-time, enhancing the therapy experience by providing a smoother and more fluid measurement procedure. This automated angle calculation eliminates the need for manual measurements, reducing the potential for human error and ensuring consistent and accurate results (see Fig. 5).



Fig. 3. Capture for flexion test.

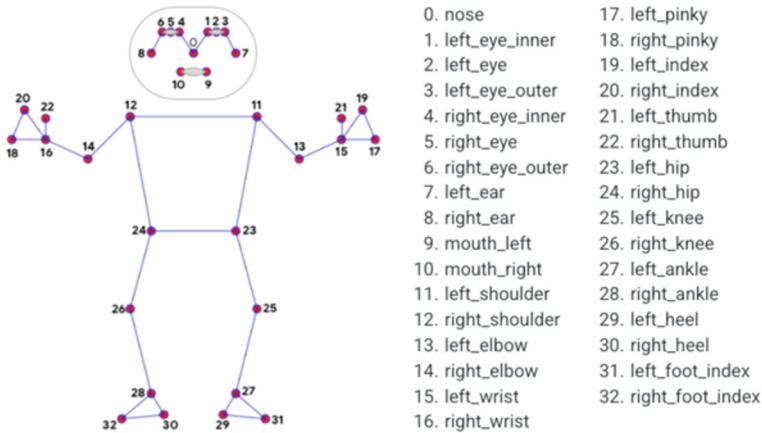


Fig. 4. Figure 4 illustrates the points detected by MediaPipe which enables us to access the reference points. This connection ensures that we can accurately identify and utilize the detected points for further analysis and calculations.

Lastly, to validate the results and ensure the software’s reliability, several tests were conducted involving different patients and various physiotherapists. This approach aimed to establish a comprehensive comparison among different techniques and measurement methods. Additionally, it accounted for variations in body types and the achievable range of angles. By doing so, a mean measurement error was obtained, allowing for the assessment of the extent to which the project successfully reduced this margin of error. This meticulous testing process contributes to the software’s credibility and confirms its capability to consistently provide accurate and dependable knee angle measurements.



Fig. 5. Figure 5 displays a preliminary result of the key point detection, their connection, and the corresponding angle calculation. The calculated angle provides valuable insights into the knee joint's range of motion during the therapy session.

The collected data from these tests serves as a foundation for assessing the software's performance across a diverse range of scenarios and individuals, ultimately solidifying its potential as an innovative tool in enhancing knee osteoarthritis therapy, see Table 1.

At the same time the same measurements were taken with the software to compare errors and measurements, see Table 2.

For a better result the measurements of a second therapist were analyzed and processed, and these were their results, see Table 3 and 4.

With the measures taken we managed to make a realistic comparison between the different processes for calculating the angle.

Table 1. The following table shows the results obtained in measuring the internal angle of the knee with the traditional methods of a physiotherapist in a sample of 5 people who perform the leg extension in sitting position.

First physiotherapist								
5 successive amplitude measurements in degrees obtained in five individuals								
Person	Measure 1	2	3	4	5	All	average	Global average
1	176	164	175	170	172	857	171.4	170.04
2	175	172	171	177	177	872	174.4	
3	176	172	170	172	174	864	172.8	
4	170	168	165	165	170	838	167.6	
5	168	160	160	165	167	820	164	

Table 2. The following table shows the results obtained in the measurement of the inner angle of the knee with the use of the software with the same people and the same posture.

Software measurements in comparison of the first physiotherapist								
Person	Measure 1	2	3	4	5	All	average	global average
1	168	170	170	171	173	852	170	164.88
2	163	166	166	164	161	820	164	
3	165	169	166	161	169	830	166	
4	168	171	172	165	163	839	167	
5	164	152	156	153	156	781	156.2	

Table 3. 5 successive amplitude measurements in degrees obtained in five individuals.

Second physiotherapist								
Person	Measure 1	2	3	4	5	All	average	Global average
1	179	178	175	172	176	880	176	170.72
2	168	175	175	169	168	855	171	
3	170	173	165	163	168	839	167.8	
4	168	169	166	167	167	837	167.4	
5	164	165	175	177	176	857	171.4	

Table 4. The following table shows the results obtained with the use of the software in comparison with the measures of the second physiotherapist.

Software measurements in comparison of the second physiotherapist								
Person	Measure 1	2	3	4	5	All	average	Global average
1	172	170	172	171	173	858	171.6	165.88
2	166	163	163	161	165	818	163.6	
3	167	163	167	171	169	837	167.4	
4	163	171	171	165	163	833	166.6	
5	160	160	159	161	161	801	160.2	

4 Results

Initially, the standard deviation calculation was performed, indicating the biological variation in degrees using traditional methods, resulting in a biological variation of 4.21° for the measurements of the first physiotherapist, as seen in Table 5.

Continuing with traditional methods, the measurement error was calculated in degrees, resulting in a measurement error of 3.2332° with the first 5 samples, as seen in Table 6.

For the calculations of measurement errors made by the software, a significantly similar error to that of the current methods was obtained as Table 7 shows.

Calculated the measurement error in degrees of the software in a sample of 5 individuals indicated in Table 8.

Comparison measurements with the second physiotherapist, shown in Table 9.

With traditional methods, the measurement error was calculated in degrees, resulting in a measurement error of 3.52° with the second 5 samples, shown in Table 10.

Finally, we proceed to compare the measurements of the second physiotherapist with the measurements of the software as Table 11 shows.

With the use of the software, the measurement error was calculated in degrees, resulting in a measurement error of 2.19° with the second 5 samples, summarized in Table 12.

Table 5. Calculation of standard deviation indicating biological variation in degrees with traditional methods.

Measurements of the first physiotherapist		
Person	(x)	Biological variance
1	171.4	4.21°
2	174.4	
3	172.8	
4	167.6	
5	164	

Table 6. Measurement error.

Person	$(x_1 - X)^2$	$(x_2 - X)^2$	$(x_3 - X)^2$	$(x_4 - X)^2$	$(x_5 - X)^2$	Σ	average	Measurement error
1	21.1599	54.76	12.96	1.96	0.3599	91.02	4.7749	3.2332°
2	0.3599	5.76	11.56	6.7599	6.7599	31.2	2.7928	
3	10.2399	0.64	7.84	0.64	1.4399	20.08	2.2803	
4	5.76	0.16	6.7599	6.7599	5.76	25.2	2.5099	
5	16	16	16	1	9	56	3.8078	

Table 7. Calculation of standard deviation indicating variation in degrees.

Software calculations compared to the first physiotherapist		
Person	(x)	variance
1	170.4	5.3937°
2	164	
3	166	
4	167.8	
5	156.2	

Table 8. Measurement error.

Person	$(x_1 - X)^2$	$(x_2 - X)^2$	$(x_3 - X)^2$	$(x_4 - X)^2$	$(x_5 - X)^2$	Σ	average	Measurement error
1	5.76	0.16	0.16	0.3599	6.7599	13.2	1.8165	3.16°
2	1	4	4	0	9	18	2.1213	
3	1	9	0	25	9	44	3.3166	
4	0.0399	10.2399	17.6399	7.84	23.04	58.8	3.8340	
5	60.84	17.6399	0.0399	10.2399	0.0399	88.8	4.7116	

Table 9. Results with the second physiotherapist.

Measurements of the second physiotherapist		
Person	(x)	Biological variance
1	176	3.46°
2	171	
3	167.8	
4	167.4	
5	171.4	

Table 10. Measurement error with second physiotherapist.

Person	$(x_1 - X)^2$	$(x_2 - X)^2$	$(x_3 - X)^2$	$(x_4 - X)^2$	$(x_5 - X)^2$	Σ	Average	Measurement
1	9	4	1	16	0	30	2.73	3.52°
2	9	16	16	4	9	54	3.67	
3	4.83	27.03	7.84	23.04	0.03	62.8	3.96	
4	0.035	2.55	1.96	0.16	0.16	5.2	1.14	
5	54.76	40.96	12.96	31.35	21.15	161.2	6.34	

Table 11. Comparison of the measurements of the second physiotherapist with the measurements of the software.

Software calculations compared to the second physiotherapist		
Person	(x)	variance
1	171.6	4.27°
2	163.6	
3	167.4	
4	166.6	
5	160.2	

Table 12. Error of measurement with the software in the measurements of the second physiotherapist.

Person	$(x_1 - X)^2$	$(x_2 - X)^2$	$(x_3 - X)^2$	$(x_4 - X)^2$	$(x_5 - X)^2$	Σ	Average	Measurement
1	0.16	2.55	0.16	0.35	1.96	5.2	1.14	2.19°
2	5.76	0.35	0.35	6.75	1.96	15.2	1.94	
3	0.16	19.36	0.16	12.96	2.55	35.2	2.96	
4	12.96	19.36	19.36	2.55	12.96	67.2	4.09	
5	0.03	0.03	14.43	0.64	0.64	2.8	0.83	

5 Conclusions

In conclusion, this project represents a significant advancement in enhancing knee osteoarthritis therapy through the application of computer vision technology. The effective exploration and utilization of tools like OpenCV and MediaPipe in Python have showcased their capacity to overcome limitations of traditional methods for measuring joint angles in physiotherapy.

The implementation of this software has enabled precise and automated detection of key points on the human body, facilitating the calculation of relevant joint angles. The ability to measure in real-time and non-invasively provides a crucial advantage by offering continuous and personalized tracking of patients' progress during rehabilitation.

Thoughtful consideration of concepts such as validity and reliability has been essential in validating the project. The pursuit of valid and consistent measurements has been substantiated through comprehensive tests with patients and physiotherapists, allowing for result comparisons and validation of the software's reliability across various clinical scenarios.

By reducing measurement errors and providing more accurate and objective joint range measurements, this project offers a tangible solution to enhancing knee osteoarthritis therapy. The capability to customize treatment plans and provide ongoing monitoring





strengthens the patient-centric approach. Ultimately, this innovation holds the potential to significantly impact the quality of life for individuals grappling with this condition, paving the way for more effective and tailored therapy in the field of physiotherapy.

References

1. Osteoarthritis Foundation International. <https://www.oafifoundation.com/que-es-la-artrosis/#:~:text=La%20artrosis%2C%20tambi%C3%A9n%20conocida%20como,tejidos%20blandos%20de%20la%20articulaci%C3%B3n>
2. Meza, G., Aldrete, J., Espinosa, R., Torres, F., Díaz, A., Robles, M.: Osteoarthrosis: implementation algorithms diagnostic y therapeutic. Revista Médica del Instituto Mexicano del Seguro Social, <https://www.redalyc.org/articulo.oa?id=457749297019>. Accessed 18 Aug 2323
3. Rosales Pérez, G.J., Hernández Izurieta, J.P., Jaramillo Villalobos, J.S., Cortés Naranjo, C.W., et al.: Sociedad Cubana de Reumatología FJ, Grupo Nacional de Reumatología (Cuba) DA, Osteoarthrosis. Revista Cubana de Reumatología. Sociedad Cubana de Reumatología (2019). http://scielo.sld.cu/scielo.php?script=sci_arttext&pid=S181759962019000200009&lng=es&nrm=iso&tlng=es. Accessed 18 Aug 2323
4. CENETEC. Prevención, Diagnóstico y Tratamiento de Rehabilitación en el Paciente Adulto con Osteoarthrosis de Rodilla en los Tres Niveles de Atención, México (2014). <https://www.actuamed.com.mx/informacion-medica/prevencion-diagnostico-y-tratamiento-de-rehabilitacion-en-el-paciente-adulto-con>. Accessed 18 Aug 2323
5. Norkin, C.C., White, D.J.: Goniometria. Marban Libros (2006). Accessed 18 Aug 2323
6. Junquera, R. (n.d.): Goniómetro o instrumento de valoración en fisioterapia. Fisioterapia-online.com; FisiOnline. <https://www.fisioterapia-online.com/glosario/goniometro-o-instrumento-de-valoracion-en-fisioterapia>. Accessed 18 Aug 2323



Hand Assessment Device Prototype

Sabrina Sofía Prieto Salazar^(✉) , Guadalupe Karla Velasco Gómez ,
Perla Vanessa Aguilar Mejía , and Marisol Martínez-Alanís 

School of Engineering, Universidad Anahuac Mexico, 52786 Huixquilucan, Mexico
sofi.prieto.salazar@gmail.com

Abstract. The assessment done during physiotherapy is a critical step, since it provides information needed to determine the best possible treatment for the patient. Specifically, hands are essential tools for humans; reason for which developing limitations causes a significant drop in patients' quality of life. As a result, it is necessary to have tests that record patients' development in quantitative terms, independent of the physiotherapists' interpretation.

Nevertheless, the instruments used for the task possess limitations that lead to errors during the assessment. Hence, the aim of this work was to develop a device capable of measuring the range of motion (ROM) and grip strength, simultaneously.

To fulfil the project's objective, force and position sensors were analysed, resulting in the selection of the FSR400 for strength and P090 for ROM measurements. All sensors were calibrated to obtain the correct units (Newtons and degrees). Subsequently, the interface was developed using NI LabVIEW. This software allows for fast analog data input and processing, using specialised data acquisition devices (DAQ).

Tests for adjustability and accuracy were taken to ensure the correct behaviour of the prototype. Accuracies of 81.62% in ROM and 52.47% in grip strength were found, demonstrating its overall functionality and possibility for improvement.

Keywords: Hand Assessment Device · ROM · grip strength · sensors

1 Introduction

Rehabilitation is the process that allows patients to recover, maintain or improve their basic abilities to perform daily activities that have been diminished as a result of an accident, disease or as a side effect of medical treatment. Physiotherapists are the health professionals that provide patients with these rehabilitation processes and their corresponding assessments, assisted by diverse devices and equipment as needed [1].

In physiotherapy, the initial assessment refers to the dynamic process [3] implemented before starting the patient's rehabilitation. During this stage, all the information required to determine an adequate rehabilitation process is acquired through anamnesis and physical exploration [2]. The developed process must be customised to the patient's needs and objectives, based on realistic goals that suit the patient's lifestyle and context [4].

This is why it is essential to have updated functional testing according to the patient's pathologies, particular needs and characteristics, as well as adapted in order to make comparisons among devices and to analyse their progress based on the treatment provided [5].

On the other hand, human beings are in constant use of their hands, since these are indispensable to perform basic daily activities. Consequently, if there is a problem in one or both hands, their quality of life will be negatively affected.

There are various pathologies that affect the hand's motricity, the most frequent ones being tendonitis, rhizarthrosis, hand arthrosis and sprains, carpal tunnel syndrome, as well as traumas, concussions, arthritis and cardiovascular accidents (CVA) [6]. Any of these can have a detrimental effect on the way hands function, mainly changing their range of motion (ROM) and the amount of pressure that can be exerted.

As a result, there are several assessment devices that can be used to evaluate both measures, such as the dynamometer, the pinch meter, the vigorimeter and the goniometer. Nevertheless, these tools depend on the physiotherapists' ability to use and read them, therefore causing a lack of precision and continuity during the rehabilitation process [7].

Consequently, there is an increasing necessity of developing new devices that satisfy the acquisition of these measurements while providing an increased accuracy and a shorter evaluation time, improving the overall process, for both patients and health professionals. Some devices have been developed that aim to measure either force or ROM separately [8–10]. However, there is no device capable of obtaining both measures simultaneously at low cost.

Due to this, the Hand Assessment Device prototype (HAD) was developed.

2 Materials and Methods

2.1 Materials

For the development of the HAD prototype, two sensors were used. Firstly, to measure force, it was determined that the appropriate sensors, due to their characteristics, would be the Force Resistive Sensors FSR400 (Interlink Electronics, California, USA), which meet the maximum dimensions considered to be placed on the fingertips (10 mm). These sensors cover the needed measuring range, with a resolution of 0.1 N and maximum sensitivity of 10^2 N, allowing force to be measured by decreasing electrical resistance as more pressure is applied. In addition, they have force detection resistors at their core, which are responsible for producing the reduction of the electrical resistance as they detect variations in pressure. Its operation is based on applying pressure in the measuring area so that the conductor allows the flow of electricity from one cable to another. Additionally, when the sensor is in a neutral state, the circuit will remain at rest and electrical current cannot pass [11, 12].

On the other hand, the choice of sensors for the measurement of ROM was the P090 rotatory linear potentiometers (TTI Electronics, Texas, USA). These sensors have an ideal size for being attached to the fingers (since the movements made by the joints of the hands are very small), as well as having a wide measuring range, and having the terminals in a lateral position (beneficial for the design of the device). In addition, the

slot on the knob will help in the adaptation of the sensor, allowing it to move at the same time and angle as the finger joints.

LabVIEW (National Instruments, Texas, USA) was used as the programming language.

2.2 Prototype Development

In order to develop the prototype, the methodology shown in Fig. 1 was followed. Firstly, a previous investigation was carried out to determine the needs of patients and professionals and existing commercial products. Subsequently, for the construction of the device, the sensors that would make the desired measurements were chosen, and the circuit and source code were built (Figs. 2 and 3). The sensors were calibrated, and the structure that would support the sensors was designed. Likewise, the materials were chosen to build said structure, and the components assembled. Finally, the prototype was tested and the necessary corrections were made.

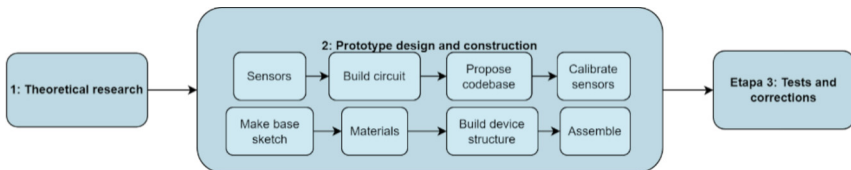


Fig. 1. Methodology followed for the development of the Hand Assessment Device prototype.

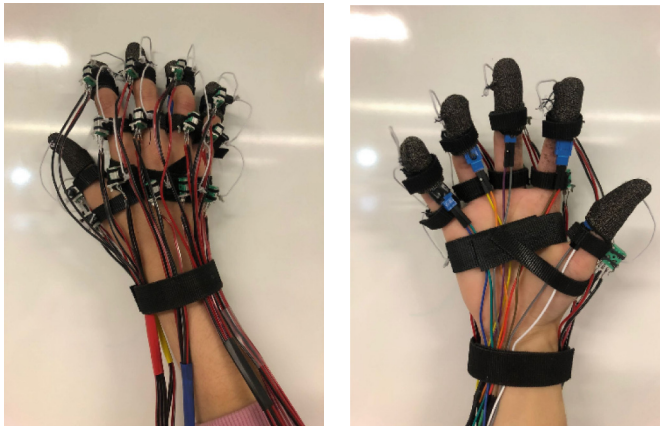


Fig. 2. Final assembly of the Hand Assessment Device prototype; back of the hand (left) and palm (right).



Fig. 3. User interface (LabVIEW).

2.3 Data Collection

To test the device's adjustability and accuracy, 10 subjects of different ages and sexes were asked to use the HAD in order to compare the results with those given by the references used to calibrate the sensors. Each one of them used the device on their dominant hand (all of which were measured), providing the ROM of three fingers (thumb, index, and middle) and digital strength of one pinch (thumb+index pinch).

Furthermore, the data obtained with the HAD and stated instruments was analysed in order to calculate the standard deviation to determine the device's accuracy. Additionally, a comparison of the measured hands was made with known data to determine the device's adjustability to adult hands.

3 Results

A total of 10 volunteers were tested in order to obtain the accuracy of the hand assessment device (Tables 1 and 2) and its adjustability to different hand sizes (Table 3).

The device's accuracy was determined by the following Eq. (1), based on a statistical analysis of the data.

$$\text{accuracy} = (1 - \sigma z) \times 100 \quad (1)$$

where,

σz = standard deviation of z.

$z = (h_n - x_n)/x_n$.

x_n = goniometer/GFT measurements.

Table 1. Accuracy and average data obtained from 10 different subjects using the Hand Assessment Device vs a goniometer.

Finger	Hand Joint	HAD [°]	Goniometer [°]	Accuracy [%]
Thumb	IP	36.85	43	83.62
	MP	11.993	16.8	61.52
Index	DIP	37.12	35.2	93.43
	PIP	61.28	58.2	90.47
	MP	8.23	10.9	71.45
Middle	DIP	37.23	36.4	91.78
	PIP	50.33	53	90.39
	MP	12.22	14.6	70.27

IP: interphalangeal, DIP: distal interphalangeal, PIP: proximal interphalangeal, MP: metacarpophalangeal.

hn = HAD measurements.

Table 1 shows the average degrees measured with the HAD compared with the average degrees measured with the goniometer. These averages were taken from each of the three fingers' joints.

Based on these data, it was possible to determine the accuracy presented by the device. The average accuracy for all joints in all three fingers was 81.62%. Said number presents the overall accuracy of the HAD in terms of ROM measurement, but as it can be seen, it varies depending on which joint is analyzed. These variations are expected since the HAD is still a prototype, with structural vulnerabilities that can affect the way in which it measures finger movement. Still, despite said area of improvement, the device proves to be accurate for ROM measurements.

Moreover, the device eliminates the inter-rater reliability, which may be poor depending on the physiotherapists' abilities when assessing the same individual, since it will perform consistently for each individual.

A similar prototype implemented inertial measurement units (IMUs) to measure ROM. Even though this device reported a small error rate ($\leq 2^\circ$) [8], the IMUs are more complex to calibrate and more expensive, making the potentiometers better to replicate the device at a low cost while maintaining a good accuracy level. In addition, this prototype does not include any force measurements. Another similar device uses the ROM for a motion capture device [9]. Since the objective of this prototype was motion capturing, there are no ROM measurements, making it difficult to evaluate if its performance would allow a better assessment for the rehabilitation process.

As shown in Table 2, the accuracy corresponding to the force measurements is globally barely over 50%. This can be improved by ensuring the FSRs have a correct connection, since faulty connections were detected on them during testing. Another issue was that the available sensors were not as accurate as expected. Therefore, if replaced, the device's accuracy for grip strength measurement will improve exponentially.

Table 2. Data comparison obtained from 10 subjects using the Hand Assessment Device vs the Grip Force Transducer

Finger-pulp pinch (thumb+index)		
HAD [N]	Grip Force Transducer [N]	Accuracy
17.31	33.11	52.74%

The data obtained in Table 3 correspond to three hand measurements that provide a global view of a patient's hand size. This was done in order to determine whether the HAD has enough versatility to be used on any adult patient, regardless of their hand size. The device evaluation was performed using a total of 10 subjects, 5 men and 5 women. In this case, the male subjects largest hand length was 21 cm, while for the female subjects was 18.40 cm. Comparing these values with the average hand size for males (19.30 cm) and females (17.27 cm), it can be ensured that the HAD has enough adaptability to be used in any adult patient [13].

Table 3. Subjects' hand size

Subject	Hand length ^{b)} [cm]	Hand width ^{b)} [cm]	Thumb length ^{c)} [cm]
11	18	8.5	11.4
2	19.3	8.2	11
3	18.4	7.5	11.7
4	17	8	11.5
5	16.8	8.0	11
6	21	10.4	16.5
7	18.4	8.9	10.3
8	16.8	7.6	11.6
9	17.5	7.5	12
10	18	8.7	14.3

a) Hand length: measured from the tip of the longest finger to the crease under the palm.

b) Hand width: measured below the knuckles excluding the thumb.

c) Thumb length: measured from the tip of the thumb to the crease under the palm.

4 Conclusions

Knowing the range of motion and pressure applied by the hand is fundamental in order to prescribe an ideal rehabilitation process, thus allowing patients the best opportunity to recover their functionality. Therefore, the HAD is an innovative tool that will allow physiotherapists to perform detailed, accurate and quantifiable assessments on patients that are in need of hand rehabilitation, providing the best outcome possible.







The prototype fabricated presented an average accuracy of 81.62% in ROM measurement and 52.47% in grip strength measurement. These results will be improved by replacing the selected sensors and modifying the design vulnerabilities that were detected during the testing process. Even though these limitations were detected, the HAD is an excellent start for a device that can measure both instantaneously. Moreover, the HAD's adjustability has been ensured thanks to the comparison made with the average hand size for males and females, ensuring that it can be used to assess any adult hand.

References

1. Rehabilitación. MedlinePlus (2022) <https://medlineplus.gov/spanish/rehabilitation.html>
2. Ramos, A., Ruiz, F.: La importancia de una valoración en fisioterapia (2022). <https://vitalclinic.es/valoracion-fisioterapia/>
3. Maya Hijuelos, L.: Importancia del proceso de evaluación fisioterapéutica en neurorehabilitación. *Revista Colombiana de Rehabilitación*, vol. 16 (2017)
4. Sierra Martín, M.: La importancia de una valoración fisioterapéutica (2019). <https://clinicaso hail.com/blog/valoracion-fisioterapeutica/>
5. Díaz Arribas, M.J., Fernández Serrano, M., Polanco Pérez-Llantada, J.: La valoración del funcionamiento a través de test validados. *Revista Iberoamericana de Fisioterapia y Kinesiología*, vol. 8, pp. 28–35 (2005)
6. Equipo Farmalastic: Conoces las principales patologías de la mano? Te lo contamos (2022). <https://farmalastic.cinfa.com/blog/patologias-de-la-mano-como-tratarlas>
7. Escalona D'Angelo, P., Jeannette Naranjo, O., Lagos, S.V., Fresia Solis, F.: Parámetros de normalidad en fuerzas de prensión de mano en sujetos de ambos sexos de 7 a 17 años de edad. *Revista Chilena de Pediatría* **80**, 435–443 (2009)
8. Lin, B.S., Lee, I.J., Chiang, P.Y., et al.: A modular data glove system for finger and hand motion capture based on inertial sensors. *J. Med. Biol. Eng.* **39**, 532–540 (2019). <https://doi.org/10.1007/s40846-018-0434-6>
9. Fang, B., Sun, F., Liu, H., Guo, D.: Development of a wearable device for motion capturing based on magnetic and inertial measurement units. *Sci. Program.* (2017). <https://doi.org/10.1155/2017/7594763>
10. Austin, E.F., Jr., Kearney, C.P., Chacon, P.J., Wings, S.A., Acharya, P., Choi, J.-W.: A fabricated force glove that measures hand forces during activities of daily living. *Sensors* **22**, 1330 (2022). <https://doi.org/10.3390/s22041330>
11. Force Sensing Resistor® (FSR) Sensor Series. Interlink Electronics (2022). <https://www.interlinkelectronics.com/force-sensing-resistor>
12. Ada, L.: Force Sensitive Resistor (FSR). Adafruit (2022). <https://learn.adafruit.com/force-sensitive-resistor-fsr/overview>
13. Roland, J.: Average hand size: for adults, children, athletes, and more. Healthline (2019). <https://www.healthline.com/health/average-hand-size#:~:text=Hands%20come%20in%20all%20different>



Determination of the Survival of Recellularized Primary Hepatocytes in a Wistar Rat Liver Extracellular Matrix

Nelly A. Morales-Guerrero¹ [✉], Alfredo Varela-Echavarría² ,
Carlos Lozano-Flores² , Francisco G. Vázquez-Cuevas² ,
Esperanza Mata-Martínez² , and Hebert Luis Hernández-Montiel³ 

¹ School of Medicine, Autonomous University of Queretaro, 76170 Queretaro City, Mexico
draneliamg@gmail.com

² Institute of Neurobiology, National Autonomous University of Mexico, 76230 Queretaro City, Mexico

³ Faculty of Natural Sciences, Autonomous University of Queretaro, 76230 Queretaro City, Mexico

Abstract. Introduction: Liver diseases in Mexico are the fifth cause of mortality and it involves a limited donation culture. Currently, alternatives such as the use of extracellular matrix (ECM) are developed to solve this health problem. Tissue engineering works on recellularization techniques to combine cells, biomolecules, and bioscaffolds and thus create functional organs because they do not generate an antigenic response. Objective: To determine the survival of the recellularized primary hepatocytes in a Wistar rat liver extracellular matrix (ECM) in 7 days *in vitro* culture. Material and methods: Experimental and longitudinal study, five Wistar rats weighing 300 g were used. Once extracted, the livers were decellularized with the process of Morales-Guerrero et al. in 2022 through a gravity perfusion system (GPS) using washes in series of 3 h each one with no ionic and anionic detergents, subsequently, tissue sections from the MECs were sliced and used for *in vitro* cultures with GFP primary hepatocytes in 7 days. The evaluation was with histological stains. Results: After 7 days, cell proliferation was observed, with preserved morphology. Conclusions: the hepatic ECM allowed the survival of the recellularized hepatocytes and cell proliferation processes. This promotes the development of studies about the recellularization of extracellular matrices.

Keywords: Liver · Recellularization · Extracellular Matrix

1 Introduction

Liver diseases in Mexico are the fifth cause of mortality and it involves a limited donation culture [1, 2]. Currently, alternatives such as the use of extracellular matrix (ECM) are being developed to solve this health problem [3, 4, 5]. Tissue engineering works on recellularization techniques to combine cells, biomolecules, and bioscaffolds (ECM) and thus create functional organs since it has been described that these constructs preserve

proteins and growth factors that can guide the cellular union and proliferation processes in an organ-specific way for their repopulation [6, 7, 8, 9]. Thus, the recellularization requires three main characteristics: cells from appropriate sources, an optimal method of cell seeding, and an adequate repopulation method to achieve functional remodeling [10, 11]. In addition, a very important characteristic of the scaffolds is the null immune response to their transplant, which represents a great advantage over conventional methodology [5, 12, 13]. This would improve the prognosis of patients, a shorter waiting time for the recipient and a decrease in treatment costs [14]. Therefore, this study aims to determine the survival of the recellularized primary hepatocytes cultured in a Wistar rat liver ECM.

2 Material and Methods

An experimental and longitudinal study, in which five Wistar rats' livers weighing approximately 300 g were used. Once extracted, the livers were decellularized with no ionic and anionic detergents for 12 h based on Morales-Guerrero et al., 2022 technique through a GPS (Triton x-100 at 1%, 2%, and 3% followed by SDS at 1% and finally, a PBS buffer) [15, 16]. Subsequently, tissue sections from the acellular MECs obtained were sliced and used for *in vitro* cultures with green fluorescent protein labeled (GFP) primary hepatocytes in 7 days. Finally, the tissues were processed for evaluation with Hematoxylin and eosin (HyE) and Hoechst 33342 staining to identify cell morphology, also used the F-ara-EdU to identify cell proliferation processes.

3 Results

H&E staining allowed evaluation of the characteristics of the nucleus and cytoplasm of the hepatocytes during culture, which remained unchanged during culture (Fig. 1). On the other hand, staining with Hoechst 33342 facilitated the identification of superimposed nuclear DNA in GFP hepatocytes after one week of culture, which did not represent degenerative changes (Fig. 2). Finally, staining with F-ara-EdU allowed us to appreciate cells with nuclear DNA synthesis after 7 days (Fig. 2).

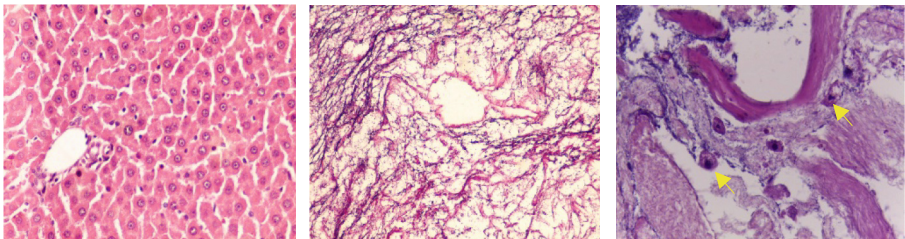


Fig. 1. Morphological evaluation of the recellularized liver matrix (40×). Microphotographs of staining for HyE showed a liver section of the control (left), decellularized (center), and recellularized (left) which can observe primary hepatocytes (arrows).

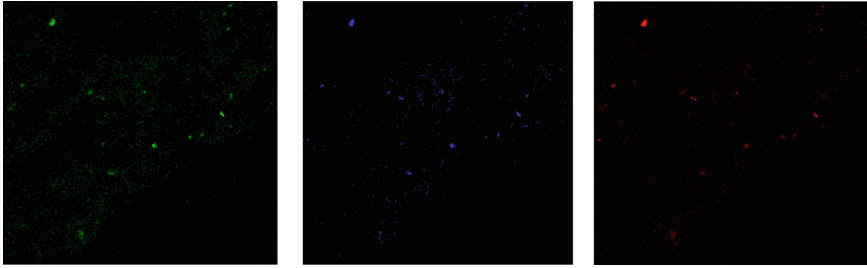


Fig. 2. *In vitro* cultures of hepatocytes on the recellularized liver matrix (62×). The microphotographs can show the GFP primary hepatocytes (green), the nuclear components with Hoechst 33342 staining (blue) and proliferating DNA nuclear component with F-ara-EdU staining (red) (Color figure online).

4 Conclusion

In this work, a successful recellularization technique was developed, and it was possible to demonstrate cell survival in 7 days. Specifically, it was possible to identify that cell morphology is preserved, which coincides with studies such as that of Uygun et al. in 2010. In addition, a proliferation marker identificatory alludes to the cell's ability to identify an optimal environment that can be repopulated. This information promotes further studies about the scaffold-specific metabolic and repopulation processes. As reported, hepatocyte transplantation is a potential therapy for numerous diseases, but its survival remains challenging [8]. Although there are different challenges concerning the possible interactions between different cell lines, vascularity, oxygenation, and thrombosis *in vivo* studies [6, 8, 14], this work adds efforts to find new therapeutics to the organ's scarcity for transplants.

References



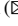


1. INEGI: Estadística de defunciones registradas de enero a junio del 2021 (Preliminar) (1), 12 (2021)
2. OPS: Ministros de Salud acuerdan plan para aumentar la donación de órganos y los trasplantes, que son insuficientes para la demanda - OPS/OMS—Organización Panamericana de la Salud (2019). <https://www.paho.org/es/noticias/2-10-2019-ministros-salud-acuerdan-plan-para-aumentar-donacion-organos-trasplantes-que-son>
3. Caralt, M., Velasco, E., Lanas, A., Baptista, P.M.: Liver bioengineering: from the stage of a liver decellularized matrix to the multiple cellular actors and bioreactor special effects. *Organogenesis* **10**(2), 250–259 (2014)
4. Shirakigawa, N., Ijima, H., Takei, T.: Decellularized liver as a practical scaffold with a vascular network template for liver tissue engineering. *J. Biosci. Bioeng.* **114**(5), 546–551 (2012)
5. Scarritt, M.E., Pashos, N.C., Bunnell, B.A.: A review of cellularization strategies for tissue engineering of whole organs. *Front. Bioeng. Biotechnol.* **3**, 43 (2015)
6. Baptista, P.M., Siddiqui, M.M., Lozier, G., Rodriguez, S.R., Atala, A., Soker, S.: The use of whole organ decellularization for the generation of a vascularized liver organoid. *Hepatol. Baltim. Md.* **53**(2), 604–617 (2011)

7. Ren, H., Shi, X., Tao, L., Xiao, J., Han, B., Zhang, Y., et al.: Evaluation of two decellularization methods in the development of a whole-organ decellularized rat liver scaffold. *Liver Int.* **33**(3), 448–458 (2013)
8. Dai, Q., Jiang, W., Huang, F., Song, F., Zhang, J., Zhao, H.: Recent advances in liver engineering with decellularized scaffold. *Front. Bioeng. Biotechnol.* **10** (2022). <https://www.frontiersin.org/article/https://doi.org/10.3389/fbioe.2022.831477>
9. Willemse, J., Versteegen, M.M.A., Vermeulen, A., Schurink, I.J., Roest, H.P., van der Laan, L.J.W., et al.: Fast, robust and effective decellularization of whole human livers using mild detergents and pressure controlled perfusion. *Mater. Sci. Eng. C* **108**, 110200 (2020)
10. Ahmed, E., et al.: Micro and ultrastructural changes monitoring during decellularization for the generation of a biocompatible liver. *J. Biosci. Bioeng.* **128**(2), 218–225 (2019). <https://doi.org/10.1016/j.jbiosc.2019.02.007>
11. Moulisová, V., et al.: Novel morphological multi-scale evaluation system for quality assessment of decellularized liver scaffolds. *J. Tissue Eng.* **11**, 2041731420921121 (2020). <https://doi.org/10.1177/2041731420921121>
12. Caires-Júnior, L.C., et al.: Pre-coating decellularized liver with HepG2-conditioned medium improves hepatic recellularization. *Mater. Sci. Eng. C Mater. Biol. Appl.* **121**, 111862 (2021). <https://doi.org/10.1016/j.msec.2020.111862>. Epub 2021 Jan 7 PMID: 33579511
13. Antarianto, R.D., Pragiwaksana, A., Septiana, W.L., Mazfufah, N.F., Mahmood, A.: Hepatocyte differentiation from iPSCs or MSCs in decellularized liver scaffold: cell-ECM adhesion, spatial distribution, and hepatocyte maturation profile. *Organogenesis* **18**(1), 2061263 (2022). <https://doi.org/10.1080/15476278.2022.2061263>. PMID:35435152;PMCID:PMC9037523
14. Dai, Q., Jiang, W., Huang, F., Song, F., Zhang, J., Zhao, H.: Recent advances in liver engineering with decellularized scaffold. *Front. Bioeng. Biotechnol.* **10**, 831477 (2022). <https://doi.org/10.3389/fbioe.2022.831477>. PMID:35223793;PMCID:PMC8866951
15. Morales-Guerrero, N.A., et al.: A new strategy for the decellularization of whole organs by hydrostatic pressure. *Biotechnol. Prog.* **38**, e3248 (2022). <https://doi.org/10.1002/btpr.3248>
16. Uygun, B.E., et al.: Organ reengineering through development of a transplantable recellularized liver graft using decellularized liver matrix. *Nat. Med.* **16**, 814–820 (2010). <https://doi.org/10.1038/nm.2170>

**Clinical Engineering, Regulations
and Innovation and Development
of Technologies for Health, Medical
Physics**



An Experimental Study of Induced Maculopathy in Ex-Vivo Tissue by Laser Pointers

Aurora-Yunuen Cardiel-Espino¹ , Galilea-Fernanda Corral-Valencia¹ ,
Manuel Vázquez-Nambo¹ , Carlos-Alberto Trejo-Seráfico¹ ,
and Joaquin Esteves-Delgado² 

¹ División de Estudios de Ingeniería Biomédica, Tecnológico Nacional de México/Instituto Tecnológico Superior de Pátzcuaro, Avenida. Tecnológico 1, Tzurumútaró, Pátzcuaro C. P. 61615, Michoacán, México

manuelvn02@gmail.com

² Facultad de Ciencias Físico Matemáticas, Universidad Michoacana de San Nicolas de Hidalgo, Avenida Francisco J. Múgica S/N Ciudad Universitaria, Morelia C.P. 58030, Michoacán, México

Abstract. In recent years, the sales of laser pointers have not been regulated, which represents a public health hazard due to their close relationship with induced maculopathy cases. The lack of knowledge about the damage caused by the direct exposure of the eye to laser pointers is a common practice among children and teenagers. Attractive factors include the intensity and bright color of the light, so they forget about the exposure risk. The light emitted by a laser pointer can cause everything from mild retinopathy or maculopathy to total vision loss. The present work shows an experimental study with pig eyes to compare the healthy macula, cornea, and retina with exposure to laser pointers. The length of exposure was 15 cm for all samples, varying the time between 15 and 60 s. For 15 and 60 s, the cornea showed slight injury from the three laser pointers; however, the macula and retina presented damage. At 60 s, the macula and retina showed severe lesions, including burns.

Keywords: Maculopathy · Laser pointer · Exposure damage

1 Introduction

The increasing number of cases of loss of vision in children and teenagers is commonly associated with the use of laser pointers. Regardless of the time exposure, the retina and macula can be injured, and loss partial or total vision [1]. A laser is a device that creates a single-color, magnified source of light that does not get wider or weaker as with other sources. The fundamental principle for producing laser light is based on the mirror array's ability to intensify a hue and direct it in one direction [2]. Furthermore, it should be monochromatic, coherent, and collimated (see Fig. 1).

The correlation between the signal's amplitude and phase times is referred to as temporal coherence, thus, a high level of coherence thus characterizes laser light (Eq. 1).

$$\tau \approx \frac{1}{2\pi \Delta \nu} \quad (1)$$

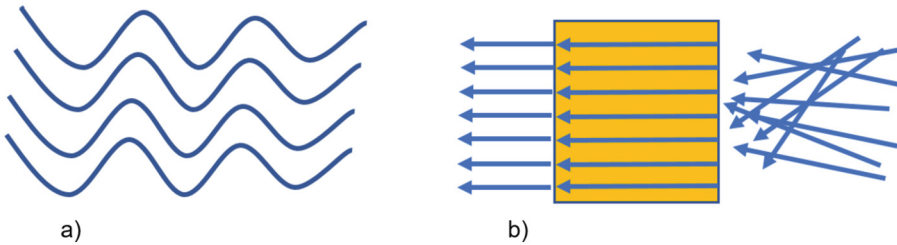


Fig. 1. Schematic diagram for a) coherent light and b) collimated light.

where $\Delta\nu$ is the varying frequency. The length of time that this beam remains collimated is given by:

$$b \approx \frac{2\pi\omega_0^2}{\lambda} \quad (2)$$

where λ is the wave length and ω the radius of laser beam that correspond to photon flux propagated through a medium with velocity v , speed light in the vacuum c and refraction index n (Eq. 3) [3].

$$v = \frac{c}{n} \quad (3)$$

Laser devices have been used by most of the population; children and teenagers are the main users, with a high risk of retinal injury [4]. A possible cause is their natural curiosity to watch the light emitted from the laser pointer, which is considered harmless, increasing the number of induced maculopathy cases that represent a public health problem [5].

The macula is a small tissue surrounding the fovea and allows to see fine details of the outside and includes an important number of retinal cells (see Fig. 2) [6].

The macula can be injured by multiple mechanisms such as photochemical, thermal, and ablative, in particular by high-intensity light [8]. A work published in 1999 mentioned the appropriate use of laser pointers as not being a hazard [9]. Nevertheless, there is a currently debate about the risks of these devices. Among the articles published, Sanches et al. reported a 9-year-old child with visual loss from the exposure of a laser pointer in his right eye and feasible irreversible damage [10]. Thomse studied the laser-tissue interactions to understand the photochemical, photothermal, and photomechanical pathobiological effects; she mentioned the lethal effects on the cornea by laser exposure devices [11]. Raevis and Shrier published a work about a 12-year-old boy with maculopathy induced by a blue laser pointer [12]. Additionally, Gonzáles mentioned the hazards of unaware use of laser pointers when the eye is exposed to high-intensity light [13]. The purpose of this paper is to present an experimental study with exvivo tissues to quantify the damage to the cornea, macula, and retina of healthy and exposed eyes exposed to lasers of different wavelengths.

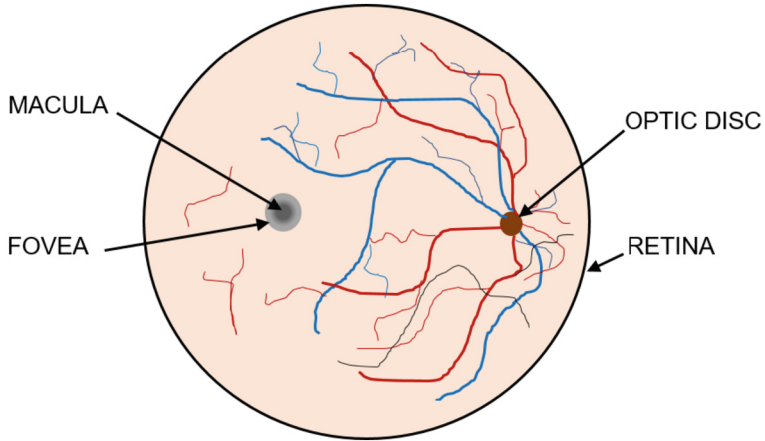


Fig. 2. Schematic diagram of human eye anatomy.

2 Materials and Methods

The work constitutes an experimental study with pig eyes exposed to four laser pointers, in order to obtain a description of the cornea, macula, and retinal damage. The used devices were a green laser with item model number LJK DT-8008-30 and a wavelength of 532 nm, two red lasers of 630–650 nm, and a blue laser with a wavelength of 405 nm. Output power was 5 W and 5 mW, respectively, a microscope model Olympus CX31RTSF and pig eyes (see Fig. 3).

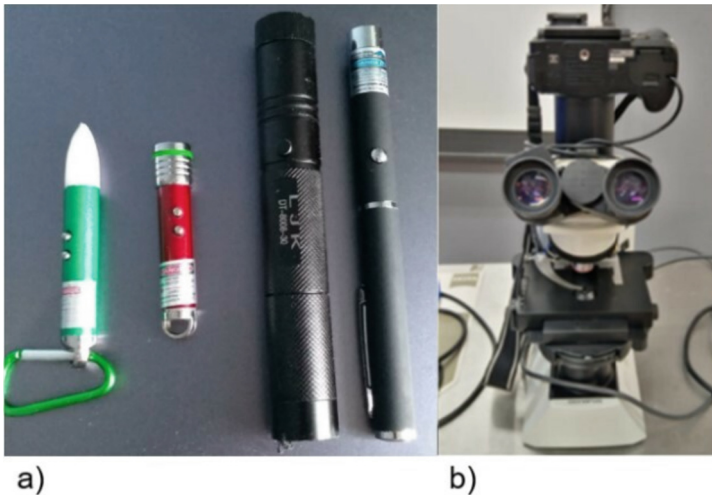


Fig. 3. a) Laser pointers used on experimental array and b) Microscope model Olympus.

The length from the laser beam to the eyes was 15 cm for all samples with time exposure was between 10 and 60 s for each trial. The test was repeated twice to decrease the measuring error (see Fig. 4).

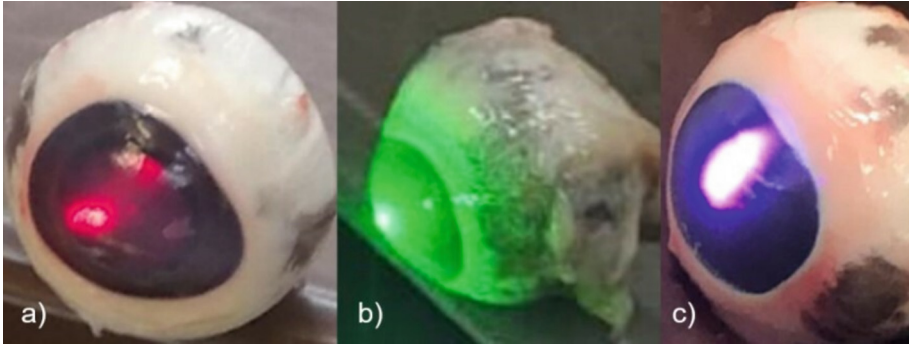


Fig. 4. Exposure of pig eyes to laser pointers a) Red laser, b) Green laser c) Blue laser for 15 cm. (Color figure online)

The cornea, macula, and retina were separated from the eye and located on a sample holder to evaluate the injury to tissue. The severity of the lesion was quantified through a light microscope coupled to a digital camera (see Fig. 5).

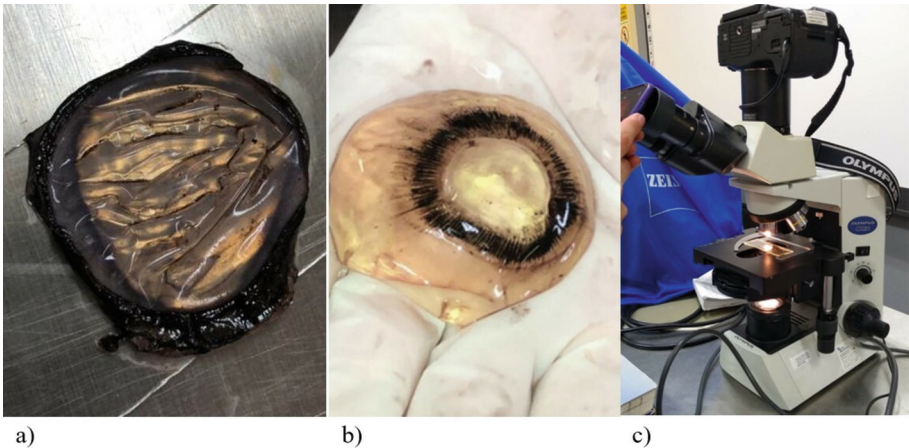


Fig. 5. a) Cornea, b) Crystalline section and c) Observed samples.

The samples exposed to the laser beam were compared with healthy images to identify the lesions that are associated with pigmentation changes. All irradiated tests showed significant alterations in color; however, the increased time exposure was a determining factor for macula and retinal damage.

3 Results and Discussion

Corneal images showed pigmentary changes that include hyperreflectivity due to damage to the retina and macula, as a result of laser light penetrating deep into the eye [14, 15]. A possible answer for the injury is related to thermal damage and photochemical impacts as a consequence of the time exposure for durations longer than 10 s [16]. The degree of damage from laser irradiance on the eyes after 15 s also depend on the wavelength that corresponded to the laser color.

All exposed corneas were affected. Even though the literature said that the biggest damage could be caused by exposure to blue lasers, in the present work the greatest lesion corresponds to the red laser. The injury of cornea has a dendritic region in all samples that don't appear defined but instead showed to be radiated or branching (see Fig. 6b).

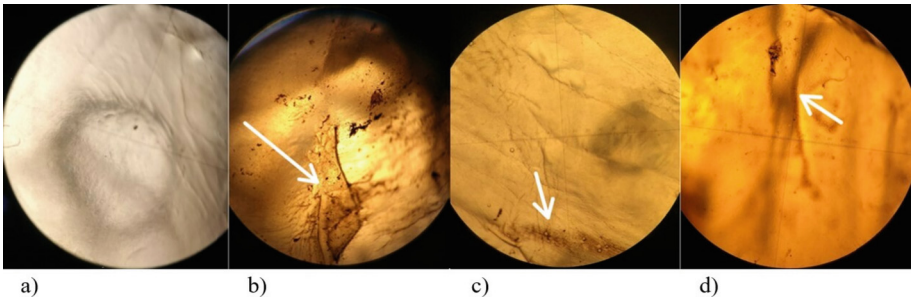


Fig. 6. a) Healthy cornea, b) Red, c) Green and d) Blue laser, for exposure time of 15 s. (Color figure online)

In regards to the macula, all samples presented remarkable lesions that may be related to the foveal damage. Red laser lesion area (see Fig. 7b) is more defined than green (see Fig. 7c) and blue laser (see Fig. 7d).

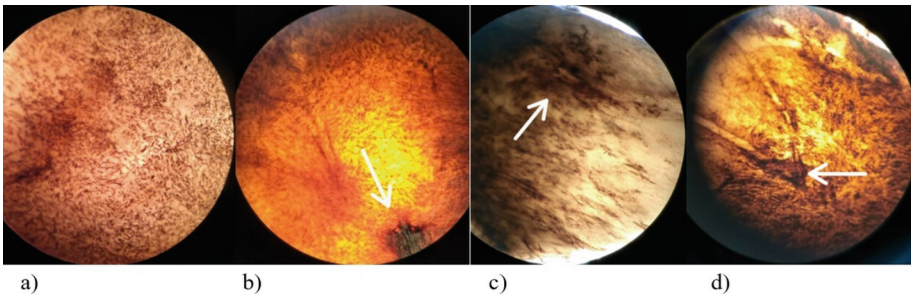


Fig. 7. a) Healthy macula, b) Red, c) Green and d) Blue, for exposure time of 15 s. (Color figure online)

Although high-power laser injuries may result in macular holes, there have been reports of retinal hemorrhages as a result of direct exposure [17]. Thus, it is probably true that the retina shows damage in different areas by prolonged time exposure.

In particular, the retina exposed to the red and green laser (see Fig. 8b and c) presents damage in different zones and a more defined area for the blue laser (see Fig. 8d).

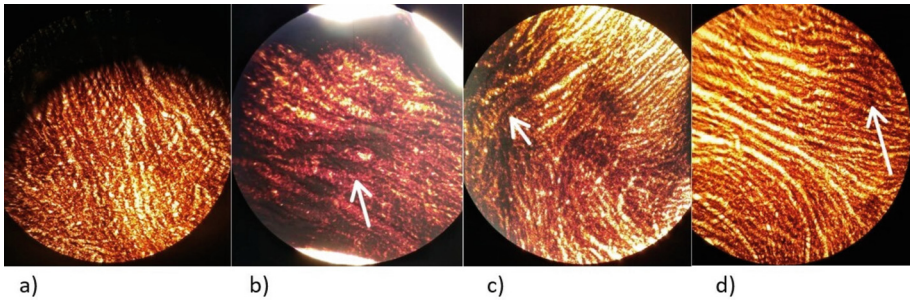


Fig. 8. a) Healthy retina, b) red, c) green and d) blue laser, for an exposure time of 15 s. (Color figure online)

The cornea exposed to the green laser for one minute (see Fig. 9a) shows a geometry dendritic lesion similar to (Fig. 6c). Despite the increased exposure time, it presented minimal damage, probably by material transparency, as the wavelengths can pass freely (see Fig. 9a) [18].

On the other hand, the macula featured severe injuries, although the lesion shape is irregular, the appearance evinces the severity of the damage (see Fig. 9b).

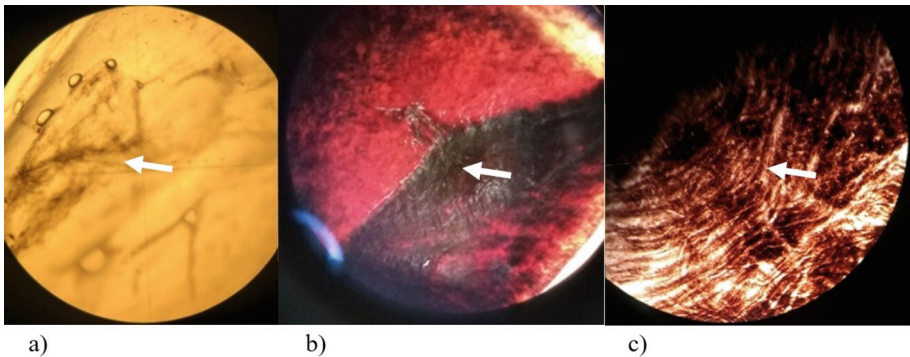


Fig. 9. a) Cornea, b) Macula and c) Retina for time exposure of a minute.

According to Birtel et al. the degree of retinal damage depends on the laser wavelength, exposure time, spot size, and power [13]. Thus, there is probably harm induced owing to photocoagulation. Although the retina lesion shape does not have a defined geometry, the severe harm caused by the portable green laser pointer can be seen by visual inspection.

Neffendorf et al. declared that laser output powerful of 5 mW does not permanently harm the retina when the eye is exposed to a laser pointer for a few seconds [15]. However, the exposure effects may cause blinding bursts or glare, as the retina is a tissue especially susceptible to laser lesions, resulting in loss of vision.

4 Conclusions and Future Work

The unregulated sale of laser pointers on the internet and local stores has increased the number of cases of induced maculopathy. Usually, children and teenagers are the most vulnerable to laser light exposure, as their natural curiosity for things discovery leads them to watch the light for long periods of time. Although the material transporence rarely causes damage to the ocular surface, it is probably a cause of lesions in the macula and retina, as the retina's ability to amplify irradiance makes it particularly vulnerable to injuries, that include damage in the fovea.

The test tissues were quantified comparing a healthy cornea, macula, and retina with those exposed for 15 and 60 s. The corneas irradiated showed slight burns for 15 s; this also happened for 60 s, and in both cases, the damage was similar, probably because of the cornea's similarity to a crystal, which involves the light can freely pass.

The irradiated cornea with the red laser showed the biggest injury compared with its exposure with the green and blue lasers. An essential factor in increasing the lesions on the eye parts was the time exposure, as the macula showed the biggest damage at 60 s.

In regards to the retina, it is evident that the harm occurs for both times, however, it is most severe at 60 s. In conclusion, the sale of laser pointers should be controlled according to international standards. Moreover, children and teenagers should be supervised to avoid possible see sense damage.

The future work will be focused on the analysis of lens damage and intraocular fluid, called aqueous humor, that is produced by the ciliary body.

References

1. Thomsen, S.: Pathologic analysis of photothermal and photomechanical effects of laser-tissue interactions. *Photochem. Photobiol.* **53**(6), 825–835 (1991)
2. Farkas, J.P., Hoopman, J.E., Kenkel, J.M.: Five parameters you must understand to master control of your laser/light-based devices. *Aesthetic Surg. J.* **33**(7), 1059–1064 (2013)
3. Goldman, L.: Laser light. A new visual art and a new occupational hazard. *Arch. Environ. Health.* **20**(2), 5411377 (1970)
4. Xu, K., Chin, E.K., Quiram, P.A., Davies, J.B., Wilkin, P.D., Almeida, D.R.P.: Retinal injury secondary to laser pointers in pediatric patients. *Pediatrics* **138**(4), 9–16 (2016)
5. Rusu, I., Sherman, J., Gallego-Pinazo, R., Lam, M., Freund, K.B.: Spectral-domain optical coherence tomography and fundus autofluorescence findings in a case of laser pointer-induced maculopathy. *Retin. Cases Br Reports* **7**(4), 371–375 (2013)
6. Neffendorf, J.E., Hildebrand, G.D., Downes, S.M.: Handheld laser devices and laser-induced retinopathy (LIR) in children: an overview of the literature. *R. Coll. Ophthalmologists* **33**(8), 1203–1214 (2019)
7. Eagle, R.C.: Mechanisms of maculopathy. *Ophthalmology* **91**(6), 613–625 (1984)

8. Patrick, W.C., Curtis, J.H., Yannis, M.P.: Non-therapeutic laser retinal injury. *Int. J. Ophthalmic Res.* **5**(1), 321–335 (2019)
9. Sánchez-Barahona, C., González-Martín, M.J., Zarallo-Gallardo, J., Lozano, E.I., Cobo-Soriano, R.: Cambios precoces en la tomografía de coherencia óptica en un niño con maculopatía inducida por puntero láser. *Arch. Soc. Esp. Oftalmol.* **92**(1), 33–36 (2017)
10. Carroll, L., Humphreys, T.R.: LASER-tissue interactions. *Clin. Dermatol.* **24**(1), 2–7 (2006)
11. Raevis, J., Shrier, E.: Pediatric bilateral blue laser pointer-induced maculopathy. *Case Rep. Ophthalmol.* **8**(1), 152–156 (2017)
12. González-Martín, M.J., Hernández-Verdejo, J.L., Zarallo-Gallardo, J.: Maculopathy: A review of the literature (II). *Arch. Soc. Esp. Oftalmol.* **93**(11), 542–550 (2018)
13. Birtel, J., Harmening, W.M., Krohne, T.U., Holz, F.G., Issa, P.C., Herrmann, P.: Retinal injury following laser pointer exposure—a systematic review and case series. *Dtsch. Arztebl. Int.* **114**(49), 831–837 (2017)
14. Xu, L., Knox, W.H., DeMagistris, M., Wang, N., Huxlin, K.R.: Noninvasive intratissue refractive index shaping (IRIS) of the cornea with blue femtosecond laser light. *Investig. Ophthalmol. Vis. Sci.* **52**(11), 8148–8155 (2011)
15. Neffendorf, J.E., Hildebrand, G.D., Downes, S.M.: Handheld laser devices and laser-induced retinopathy (LIR) in children: an overview of the literature. *Eye* **33**(8), 1203–1214 (2019)
16. Zhang, L., et al.: Laser-induced photic injury phenocopies macular dystrophy. *Ophthalmic Genet.* **37**(1), 59–67 (2016)
17. Sethi, C.S., Grey, R.H.B., Dean, H.C.: Laser pointers revisited: a survey of 14 patients attending casualty at the Bristol Eye Hospital. *Br. J. Ophthalmol.* **83**(10), 1164–1167 (1999)



Innovation of Sanitization Procedures for Mechanical Ventilators Using Six Sigma Methodology

Ana Bertha Pimentel-Aguilar¹  and Martha Refugio Ortiz-Posadas² 

¹ Biomedical Engineering Department, National Institute of Respiratory Diseases, Mexico City, Mexico

² Electrical Engineering Department, Universidad Autónoma Metropolitana Iztapalapa, Mexico City, Mexico
posa@xanum.uam.mx

Abstract. During the years 2018, 2019 and 2020, the National Institute of Respiratory Diseases (INER, its acronym in Spanish) had an increase in ventilator-associated pneumonia of 12%, 53%, and 77%, respectively. In the last year, the increase was much higher due to the care of critically ill COVID-19 patients who required mechanical ventilation. Currently, INER has 292 mechanical ventilators from 16 different brands, with varying ages. Therefore, the objective of this study was to analyze and improve the sanitization procedures of these medical devices using the Six Sigma methodology. Three procedures were studied: 1) Ventilator cleaning; 2) Disinfection of reusable accessories, and 3) High-level disinfection for mechanical ventilators. In total, five non-value-added activities and four areas of opportunity were identified. Seven innovations were proposed and implemented in a four-week pilot program, resulting in an average improvement of 76% in procedure execution.

Keywords: Mechanical Ventilator Disinfection · Procedures Innovation · Six Sigma Methodology

1 Introduction

The National Institute of Respiratory Diseases (INER, its acronym in Spanish) is a third-level public hospital whose main objective is to address respiratory diseases, scientific research, training of qualified human resources, and the provision of highly specialized medical care services, covering the entire national territory [1]. It has 273 beds and over six thousand diagnostic, treatment, and rehabilitation medical devices to provide patient care. The department responsible for managing these devices is the Biomedical Engineering Department (BED).

During the years 2018, 2019, and 2020, INER had an increase in Ventilator-Associated Pneumonia (VAP) of 12%, 53%, and 77%, respectively. In 2020, there was a much higher increase due to the high demand of patients with critical COVID-19 cases

requiring mechanical ventilation [2]. Currently, INER has 292 mechanical ventilators from 16 different brands with varying ages.

To carry out the sanitization procedures of the mechanical ventilators, INER has the Respiratory Therapy Service (RTS) and a Biosafety Committee. Additionally, the Biomedical Engineering Department assists in executing these procedures through medical technology management. Therefore, the objective of this study was to analyze and improve the sanitization procedures of the mechanical ventilators by applying the Six Sigma methodology.

2 Methodology

Three procedures were studied: 1) Ventilator cleaning; 2) Disinfection of reusable accessories, and 3) High-level disinfection for the ventilators [3]. The Six Sigma methodology [4] was used, following these stages:

1. *Analysis*: The non-value-added activities (activities that do not contribute to customer satisfaction, do not improve the perception of service, and do not meet process requirements) and the associated waste were identified. There are seven types of waste: motion, waiting time, overproduction, overprocessing, quality defects, inventory, and transportation [4]. The areas of opportunity were also identified to discover cause-and-effect relationships.
2. *Innovation*: Using Lean tools [4], various innovations were proposed to make the execution of the procedures more effective.
3. *Implementation*: The innovations were implemented in the three studied procedures during a four-week pilot program.

3 Results

3.1 Cleaning Procedure

Analysis. The cleaning procedure for the ventilators, when they have been connected to a patient, is carried out four days a week in three shifts: Tuesday, morning shift; Thursday, afternoon shift; and Saturdays and Sundays, special shift. The ventilator is superficially cleaned using towels soaked in isopropyl alcohol, with random motions covering the entire screen. Afterwards, using towels soaked in hydrogen peroxide, the casing, humidifier, nebulizer, and cables are cleaned, as well as the rails for mobilization, the respiratory circuit arm, the transport cart, and the wheels. The coordinator of the Respiratory Therapy Service (RTS), who is a pulmonologist, assigns the number of ventilators to be cleaned to the inhalation therapy technician.

Opportunity Areas. Two areas of opportunity were identified:

- *Respiratory circuit control.* The respiratory circuit should be changed every week or when visibly dirty (with organic matter or condensed fluid). Mechanical filters are changed every third day. However, there is no control over these activities, so it is unknown how many days each accessory has been on the mechanical ventilator.

- *Respiratory circuit replacement.* These circuits are disposable and should be used for no more than 96 h or 4 days [5]. It is crucial to have control over the usage time. After the cleaning procedure, new disposable accessories are placed on a ventilator, but sometimes it may remain unused for several days until a patient who needs it arrives. Consequently, the accessories are exposed to environmental contamination during that period.

Innovation. Two innovations were developed for the aforementioned areas of opportunity. The Lean tool called Kanban (a visual tool) [4] was used. The following are the proposed innovations:

- *Disposable accessories control.* To control the expiration period of disposable accessories in accordance with the manufacturer’s recommendations stating that respiratory circuits are for short-term use (four to seven days) and electrostatic filters (three days), a visual tool was designed for each of these accessories (Fig. 1). These tools are placed on the support arm of the mechanical ventilator after the cleaning procedure, and the information is completed by the inhalation therapy technicians. The card contains the identification number of the ventilator, the date, and the shift when the disposable accessory was placed.



Fig. 1. Visual tools for disposable accessories.

- *Completion of the cleaning procedure.* To verify compliance with the ventilator cleaning procedure, a visual tool was designed to be placed at the end of the ventilator cleaning procedure, which the inhalation therapy technician completes the information (Fig. 2). The card contains the day on which the cleaning is performed (Tuesday,

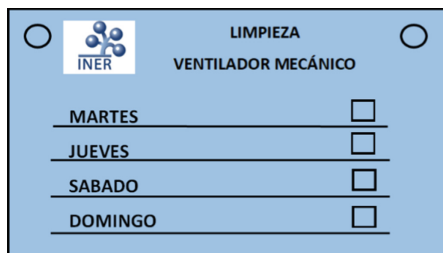


Fig. 2. Card to conclude the cleaning procedure.

Thursday, Saturday, and Sunday). The corresponding checkbox is marked according to the case.

3.2 Disinfection Procedure for Accessories

Analysis. There are three types of reusable accessories that require disinfection:

- Type A: Masks for non-invasive mechanical ventilation (NIMV), flow sensors, exhalation filter housings, headgear, expiratory valve, micro-pumps and their “T” piece, ventilator chamber, and nebulizer head circuits.
- Type B: Heating cable/warmer, temperature sensor cable, exhalation filters.
- Type C: Exhalation valves.

Non-value-added Activities. In relation to the disinfection procedure for accessories, two non-value-added activities were identified. These are associated with waste of quality defects:


- *Disinfection Time.* The Respiratory Therapy Service procedures manual [6] specifies that the accessories should remain submerged in each of the disinfectant solutions (CIDEX OPA and Endozime) for 40 min, but this time is not being measured.
- *Sealing Machine.* Accessories that are packaged in medical-grade bags should be sealed, but the sealing machine has been out of service for months. Currently, only a fold is made in the bag, which poses a biological risk to the disinfected accessories.

Opportunity Areas. Two opportunity areas were identified:

- *Control of Accessories.* Some criteria for discarding accessories include visible damage or obvious dirt, which depend on the personnel evaluating the accessory. However, there is no control over the quantity and type of accessory that is discarded.
- *Biological risk.* According to the procedures manual of the Respiratory Therapy Service [6], biological cultures should be performed on each accessory to control the quality of the disinfection process. However, it is unknown how frequently the cultures are performed, which accessories are selected for testing, how many accessories are tested, and what the results of the cultures are.

Innovation. Three innovation proposals were generated:

- *Timer for measuring disinfection time.* A timer was provided to the Respiratory Therapy Service assistant to measure the 40 min that reusable accessories should be immersed in the disinfectant solutions.
- *Quick user guide.* A quick guide for the disinfection procedure of each disposable accessory was designed, based on the procedures manual of the Respiratory Therapy Service [6]. The infographic describes all the steps of the process (Fig. 3).
- *Accessories control.* A digital logbook was designed to record information regarding the disposal of mechanical ventilator accessories. Additionally, a printed and laminated QR code is displayed in the Respiratory Therapy washing unit. The QR code



INSTITUTO NACIONAL DE ENFERMEDADES RESPIRATORIAS ISMAEL COSÍO VILLEGAS

INSTITUTO NACIONAL DE ENFERMEDADES RESPIRATORIAS ISMAEL COSÍO VILLEGAS
SERVICIO DE TERAPIA RESPIRATORIA—AREA DE LAVADO

PROCEDIMIENTO PARA EL LAVADO, DESINFECCIÓN, SECADO Y EMPAQUETAMIENTO DE LOS ACCESORIOS DESECHABLES DEL VENTILADOR MECÁNICO

PROCEDIMIENTO I :

1. Lavar el contenedor (1) con una mezcla de detergente y agua. Posteriormente enjuagar con agua corriente.
2. En el contenedor (1) se prepara el **Endozime** a una dilución de 4 ml por cada litro de agua corriente tibia. (Cambiar cada 24 horas).
3. En el contenedor (2) se prepara el **Cidex Opa** sin diluir.
4. Con guantes desechables sumergir el equipo durante **40 minutos** en el contenedor (1).
5. Realizar cambio de guantes desechables para extraer el equipo del contenedor (1).
6. Enjuagar el equipo con agua corriente asegurándose que no queden restos de Endozime.
7. Secar equipo con gasas estériles.
8. Con guantes desechables sumergir el equipo durante **40 minutos** en el contenedor (2).
9. Realizar cambio de guantes desechables para extraer el equipo del contenedor (2).
10. Enjuagar el equipo con agua corriente asegurándose que no queden restos de Cidex Opa.
11. Secar equipo con gasas estériles.
12. Empaquetar equipo en bolsas plástico, papel grado médico y rotular con fecha del procedimiento.

PROCEDIMIENTO II :

1. Con guantes desechables limpiar el equipo con gasas impregnadas de agua con jabón.
2. Aclarar con gasas húmedas de agua.
3. Limpiar con gasas impregnadas de agua clorada.

PROCEDIMIENTO III :

1. En un contenedor (1) preparar una mezcla de agua clorada en una dilución de 10 ml de **cloro** por cada litro de agua.
2. En otro contenedor (2) se prepara **agua corriente**.
3. Con guantes desechables sumergir el equipo durante **40 minutos** en el contenedor (1).
4. Sumergir el equipo en agua corriente en el contenedor (2) . (Hacer aproximadamente 10 repeticiones en un lapso de 24 horas).

EQUIPO REUSABLE PARA PROCEDIMIENTO I:

- Mascarilla de ventilación no invasiva.
- Sensores de flujo Hamilton G5 y C2
- Cascos cefálicos.
- Vasos de precipitación del ventilador 840.
- Microbombas y su pieza en "T" aerogen.
- Válvulas de exhalación del Monal y Hamilton G5 y C2.
- Circuitos del IPV.
- Cabezal Nebulizador del IPV.

EQUIPO REUSABLE PARA PROCEDIMIENTO II:

- Cable calefactor MR-850.
- Cable de temperatura MR850.
- Filtros de exhalación Avea. 840.

EQUIPO REUSABLE PARA PROCEDIMIENTO III:

- Válvulas de exhalación del Engstrom


Fig. 3. Quick guide for disinfecting mechanical ventilator accessories.

redirects to a digital form (Fig. 4) with fields such as date, accessory type, clinical service, brand, reason for disposal, and observations. This information is automatically stored in a database (Excel®) accessible to any user in real-time.

Desecho de accesorios del Ventilador Mecánico

Descripción del formulario

Fecha *

Día, mes, año 

Accesorio

- Mascarilla
- Sensor de flujo
- Carcasa de filtro
- Casco cefálico
- Microbombas
- Válvula de exhalación
- Válvula de inhalación
- Otra...




Fig. 4. Digital form for accessories control

3.3 High-Level Disinfection Procedure for Mechanical Ventilators

Analysis. The High-Level Disinfection (HLD) procedure is performed only for ventilators at risk of contamination with highly infectious microorganisms, such as those with multidrug-resistant pathogens. The process begins after the thorough cleaning procedure, verified by the janitorial staff, ensuring proper cleanliness of the entire space and the elements within the enclosure. For infusion pumps and vital signs monitors, a medium-level cleaning and decontamination are carried out by a specialized external company. This process involves applying vapor pressure with a disinfectant to the medical devices.

Subsequently, the HLD is performed by personnel from the Biosecurity Committee, covering the entire enclosure, including the mechanical ventilator. The HLD procedure depends on the microorganisms the patient has been exposed to. For Type 1 microorganisms (*Clostridium difficile* and *Acinetobacter*), a vaporized hydrogen peroxide (H_2O_2) gasifier and an aeration system are used to remove excess H_2O_2 after the appropriate exposure time. For Type 2 microorganisms (*Pseudomonas*, *Aspergillus*, *Escherichia coli*, *Staphylococcus aureus*, and *Mycobacterium tuberculosis*), ultraviolet type C (UVC) light is irradiated from different angles using a system equipped with ten lamps arranged in a circular manner.

Non-value-added Activities. Three activities that do not add value were identified:

- *Ventilator Control.* There is no control over which ventilators require HLD because the associated microorganism is unknown. This activity is associated with the waste of quality defects.
- *Communication Flow.* The completion of the thorough cleaning procedure by the janitorial staff and the cleaning by the external company is not known. This means that the Biosecurity Committee personnel may arrive to perform the HLD, but sometimes the previous procedures have not been completed. Consequently, the HLD needs to be rescheduled. This activity is associated with wastes called waiting time and motion due to the resulting delays and staff relocation.
- *Identification of ventilators requiring high-level disinfection (HLD).* Occasionally, several ventilators are stored in one enclosure without knowing which ones require HLD. This activity is associated with the waste of quality defects.

Innovation. Two innovation proposals were generated:

- *Digital logbook:* A digital logbook was designed for the Biosecurity Committee personnel to record information about ventilators requiring HLD, the corresponding microorganism, and the type of disinfection required. Any user can access this information. A QR code was designed to redirect to a digital record (Fig. 5) for recording the date, ventilator identification number, microorganism type, time, and the status of the ventilator (if contaminated). The information is automatically stored in a digital spreadsheet database that can be shared with any user and accessed in real-time. An example of how the stored information would look is shown in Fig. 6.
- *Identification of contaminated ventilators.* With the aim of communicating to the staff about the type of disinfection required for the mechanical ventilator, and whether it is contaminated with any microorganism, two visual tools were designed. Their dimensions are 13.0 cm × 18.5 cm and are printed on opaline paper in two different colors. The pink color (Fig. 7a) is used for a ventilator contaminated with Type 1 microorganisms (*Clostridium difficile* and *Acinetobacter*). In this case, decontamination needs to be performed using ultraviolet lamps. The blue color (Fig. 7b) is used for a ventilator contaminated with Type 2 microorganisms (*Pseudomonas*, *Aspergillus*, *Staphylococcus aureus*, *Mycobacterium tuberculosis*, and *Escherichia coli*). In this case, decontamination needs to be performed using hydrogen peroxide (H_2O_2). The green color is used to indicate that the ventilator has been disinfected (Fig. 8). These

Ventiladores mecánicos - DAN

Descripción del formulario

Fecha *

Día, mes, año 📅

Cubículo *

Cubiculo donde está ubicado el ventilador.

Texto de respuesta breve

ID Ventilador *

Número de identificación del ventilador.

Texto de respuesta breve



Fig. 5. Digital record.

DESINFECCIÓN DE ALTO NIVEL (DAN) - VENTILADORES MECÁNICOS							
Marca temporal	Fecha	Cubículo	ID Ventilador	Microorganismo	Tipo de DAN	Hora	Estado
26/7/2022 20:47:14	26/7/2022	4	5	Clostridium Difficile	H2O2	12:30:00 p. m.	CONTAMINADO
26/7/2022 21:09:39	26/7/2022	4	5	Staphylococcus Auerus	UV	5:00:00 a. m.	DESCONTAMINADO
26/7/2022 21:23:58	27/7/2022	3	8	Clostridium Difficile	H2O2	4:00:00 p. m.	CONTAMINADO
26/7/2022 21:28:39	27/7/2022	1	2	Pseudomona Aspergillus	UV	4:40:00 p. m.	CONTAMINADO
26/7/2022 21:30:01	28/7/2022	7	9	Acinetobacter	H2O2	5:50:00 p. m.	DESCONTAMINADO
27/7/2022 10:01:02	27/7/2022	6	5	Clostridium Difficile	H2O2	10:00:00 p. m.	DESCONTAMINADO
1/8/2022 11:42:36	1/8/2022	7	123	Escherichia Coli	UV	11:42:00 a. m.	CONTAMINADO

Fig. 6. Example of shared digital spreadsheet visualization

signs are placed on the mechanical ventilator after the completion of the High-Level Disinfection (HLD) procedure by the Biosafety Committee staff.

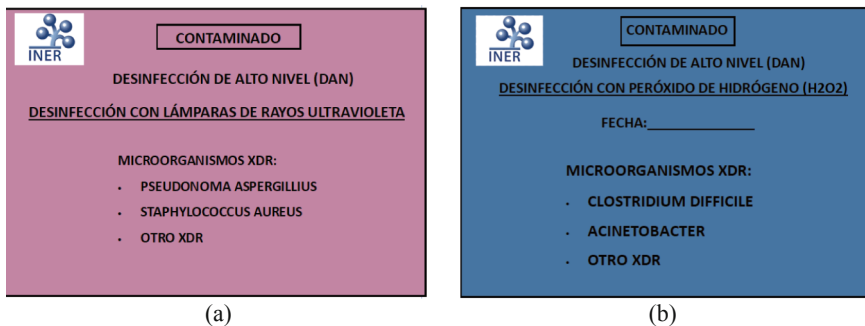


Fig. 7. Visual tools for the identification of contaminated ventilators

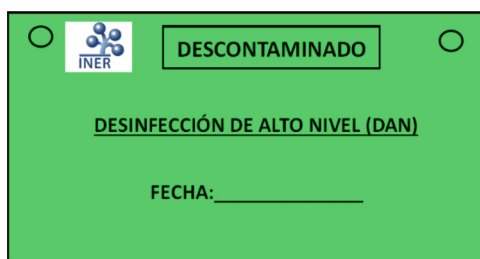


Fig. 8. Visual tools for the identification of decontaminated ventilators.

4 Implementation of Innovations (Pilot Program)

During a four-week period (from August 29th to September 24th, 2023), a pilot program was implemented in the Clinical Pulmonology Service of the INER. Five innovation proposals were implemented, and training was provided to seven users from the Respiratory Therapy Service (RTS): six inhalation therapy technicians and one assistant from the washing area, who work in three different shifts (morning, evening, and special). Additionally, shadowing (a qualitative research technique conducted on a small scale where the researcher acts as an observer of the real-life situations of a research subject for a set period [7]), was conducted with the seven RTS users. The implemented innovations are described below.

4.1 Control of Disposable Accessories

Sixteen cards, like those shown in Fig. 1, were generated to identify the accessories of eight ventilators. Seven inhalation therapy technicians were trained in the use of these cards across the three shifts (morning, evening, and special). During the first three weeks, there was low compliance with this activity. Feedback was provided to the technicians, and the cards were replaced with adhesive labels. During the fourth week when these labels were used, the activity showed a 50% improvement in response from the technicians, both in controlling the respiratory circuit and the ventilator filters. It

should be noted that for electrostatic filters, it was observed that writing the date and shift on the filter housing is more effective.

4.2 Control of Completion of Mechanical Ventilator Cleaning Procedure

Eight cards, as shown in Fig. 2, were generated, and placed on eight ventilators. Seven inhalation therapy technicians were trained across the three shifts (morning, evening, and special) on how to fill out these cards. This activity had a compliance rate of 78%.

4.3 Measurement of Disinfection Time

A stopwatch was provided to the accessory disinfection area for mechanical ventilators. The staff was trained to time the 40 min required for immersing the accessories in each of the disinfectant solutions (CIDEX OPA and Endozime). Through shadowing, compliance with the required time for the disinfection process was evaluated. This activity had a compliance rate of 100%.

In the three procedures analyzed (cleaning ventilator, control accessories and disinfection time) there were an improvement in the performance of 78%, 50%, and 100% (Fig. 9).

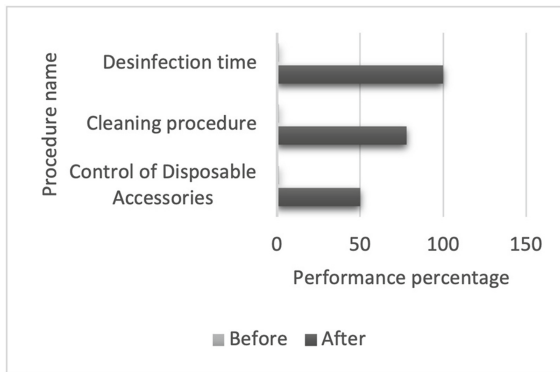


Fig. 9. Improvement percentage for the three processes studied

5 Conclusion

In this study, the Six Sigma methodology was employed to analyze three sanitization procedures at the National Institute of Respiratory Diseases: 1) Mechanical ventilator cleaning; 2) Disinfection of reusable accessories; and 3) High-Level Disinfection (HLD) for mechanical ventilators. A total of five non-value-added activities and four areas of opportunity were identified, and seven innovations were proposed.

Forty visual tools were implemented. For the cleaning procedure, 32 cards were placed on the support arm of eight mechanical ventilators, and eight cards were used for the HLD procedure.

Training was provided to seven users from the Respiratory Therapy Service (six inhalation therapy technicians and one assistant from the washing area) across three different shifts (morning, evening, and special).

In all cases, there was an improvement in the performance of the procedures. Cleaning of mechanical ventilators increased by 78%, control of disposable accessories increased by 50%, and the 40-min time stipulated for disinfecting accessories was achieved with 100% compliance.

Finally, it is important to say that, in Mexican hospitals, in general, the clinical processes have a high variability in the results obtained, since they are executed according to the expertise of the medical/paramedical staff. The Six Sigma methodology has the objective of minimizing the execution of processes through five stages (define, measure, analyze, innovate, control —DMAIC—). In particular, the last stage allows establishing control measures to know the performance of the processes studied and, where appropriate, apply DMAIC again to develop new improvements. In this sense, Six Sigma is a continuous improvement methodology that allowed unifying criteria among all the actors involved in the execution of the disinfection processes of mechanical ventilators, obtaining effective and efficient results in their performance, as well as the contribution in reducing the incidence of nosocomial infections. Finally, Six Sigma is a methodology that can be used to improve any process that is of interest in health services.

References

1. National Institute of Respiratory Diseases. Home page: <https://www.gob.mx/salud/iner>
2. Salas Hernández, J.: Informe Anual de Autoevaluación del Director General del Instituto Nacional de Enfermedades Respiratorias. Secretaría de Salud, México (2021). <https://www.gob.mx/cms/uploads/attachment/file/716841/InformeAnualdeAutoevaluacion2021.pdf>
3. Jaimes Rodríguez, A.G.: Innovación de los procedimientos de limpieza y desinfección de los ventiladores mecánicos del Instituto Nacional de Enfermedades Respiratorias. Tesis de Licenciatura en Ingeniería Biomédica. Universidad Autónoma Metropolitana Iztapalapa, México (2022)
4. Hadfield, D., Holmes, S.: *The Lean Healthcare Pocket Guide: Tools for the Elimination of Waste in Hospitals, Clinics and Other Healthcare Facilities*, 2nd edn. MCS Media Incorporated, Chelsea (2009)
5. Lei, Y.: *Medical Ventilator System Basics: A Clinical Guide*. University Press, Oxford (2017)
6. Instituto Nacional de Enfermedades Respiratorias. *Manual de Procedimientos del Servicio de Terapia Respiratoria*. INER, México (2017)
7. Czarniawska, B.: *Shadowing, and Other Techniques for Doing Fieldwork in Modern Societies*. Bussines School Press, Copeenhagen (2007)



A Technical Assessment Tool to Prioritize Medical Devices Replacement

María de Lourdes Cruz-Hernández , Beatriz Gutiérrez-Sánchez ,
and Martha Refugio Ortiz-Posadas  

Electrical Engineering Department, Universidad Autónoma Metropolitana Iztapalapa,
Mexico City, Mexico
posa@xanum.uam.mx

Abstract. The objective of this work was to develop a technical evaluation tool (related to the state of operation) to prioritize the replacement of medical devices. The result was a technical indicator with which 608 medical devices of nine different technologies were evaluated, from the National Institute of Respiratory Diseases (INER, its Spanish Acronym). This evaluation provided auxiliary criteria for the Department of Biomedical Engineering (DIB, its Spanish Acronym) to make decisions based on evidence, and to plan the replacement of the medical devices. The replacement priority distribution was as follows: 398 devices must be replaced in a period not longer than six years (medium priority); 127 obtained a low priority (replacement in 10 years); and the smallest percentage of medical devices (14%) must be replaced in the next three years (high priority). This evaluation provided an auxiliary criterion to the INER DIB staff, to make decisions about the replacement of medical devices, based on evidence.

Keywords: Technical Evaluation · Medical Equipment Replacement · Replacement Priority

1 Introduction

Health technology assessment (HTA) is a systematic and multidisciplinary evaluation of the properties of health technologies and interventions covering both their direct and indirect consequences. It is a multidisciplinary process that aims to determine the value of a health technology and to inform guidance on how these technologies can be used in health systems around the world. HTA is a transparent and accountable process that can be used by decision makers and other stakeholders to support the decision-making process in health care at the policy level by providing evidence about given technologies [1].

In general, public hospitals in Mexico have a very old inventory of medical devices and there is great interest in developing evaluation tools that can provide auxiliary criteria based on evidence to prioritize the replacement of medical technology and make a rational investment of financial resources. In this sense, different evaluation tools have been developed, such as an indicator to determine the surplus or deficit of the medical

equipment in critical care units [2]; a comparative analysis of two indicators of technical evaluation for the replacement of medical equipment [3]; the use of pattern recognition techniques for supporting the replacement of medical equipment [4]. The present work was supported by the technical indicators reported in the last two works, and new variables, that were of interest to the staff of the Department of Biomedical Engineering, were incorporated.

Knowing the technical state of the equipment allows having a criterion to know the period of replacement, therefore, the objective of this work was to develop a technical evaluation tool to assist and prioritize the replacement of medical devices which is related to the state of operation. The result was a technical indicator used to evaluate 608 medical devices of nine different technologies from the National Institute of Respiratory Diseases (INER, its Spanish Acronym) [5]. This evaluation provided an auxiliary criterion to the staff of the Department of Biomedical Engineering (DIB, its Spanish Acronym) of INER, to make decisions on the replacement of medical devices, based on evidence.

2 Methodology

2.1 Definition of Variables

Eight variables defined in previous technical indicators [3, 4] were considered, and two new variables were defined in conjunction with the staff of Department of Biomedical Engineering (DIB) of the institute: equipment type (x_5), and failure cause (x_{10}). In total, ten variables were defined (x_i) with their relevance factor (ρ_i), related to the performance and operation of medical devices (Table 1). Observe that the most relevant variables ($\rho_i = 15$) are those related to the availability of spare parts and consumables for the next five years (x_1 and x_2). The least relevant variables are x_9 , corresponding to maintenance requirement, and x_{10} , the cause of failure, Both with $\rho = 12$. The variables have a qualitative domain (q_i) with which the dib staff works.

Table 1. Variables and weights defined for the technical indicator

x_i	Variable	ρ_i
x_1	Spare parts available next 5 years	15
x_2	Consumables available next 5 years	15
x_3	Equipment age	14
x_4	Out of service days of the equipment	14
x_5	Equipment type	13
x_6	Equipment function	13
x_7	Equipment failure frequency	14
x_8	Physical risk	13
x_9	Maintenance requirement	12
x_{10}	Failure cause	12

To develop the assessment tool, a mapping was done to have a quantitative domain (M_i) (Table 2). Notice that there are two boolean variables (x_1 and x_2). All other variables have at least three values in their domain. In all cases, the domain of the variables is in the interval $M_i = [0, 15]$.

Table 2. Qualitative (Q_i) and quantitative (M_i) domain of the variables x_i

x_i	Q_i	M_i
x_1	yes/no	[0,15]
x_2	yes/no	[0,15]
x_3	[0, 5] years	3
	[6, 10] years	6
	[10, 15] years	9
	[15, 20] years	12
	>20 years	15
x_4	0 days	0
	[1, 5] days	3
	[6, 30] days	6
	>30 days	15
	Life support	15
x_5	Surgical and intensive care	14
	Surgical sterilization	13
	Monitoring of physiological variables	10
	Analytical lab	8
	Physiotherapy and treatment	7
	Lab accessories	6
	Medical equipment accessories	4
Computer and related	2	
x_6	Diagnostic	15
	Therapeutic	12
	Rehabilitation	9
	Other	3
x_7	Without failures	0
	[1, 2] failures	4
	[3, 4] failures	8
	[5, 6] failures	12
	>6 failures	15
x_8	Patient/operator dead	15
	Patient/operator partial damage	12
	Inappropriate treatment/misdiagnosis	9
	Equipment damage	6
	No significant risk	3
x_9	Security tests	15
	Calibration	12
	Preventive maintenance	9
	Function check	6
	Visual inspection	3
x_{10}	Hardware failure	15
	Software failure	10
	External failure	3

2.2 Technical Indicator

The Technical Indicator (I_T) was defined by expression (1).

$$I_T = \frac{\sum_{i=1}^{10} \rho_i x_i}{N} = \frac{\sum_{i=1}^{10} \rho_i x_i}{2025} \tag{1}$$

where: x_i , is variable i ; $i = \{1, \dots, 10\}$

ρ_i : relevance factor for x_i ;

N , normalization factor so that the value of $I_T = [0, 1]$ defined by (2).

$$N = \sum_{i=1}^{10} \rho_i M_{imax} \tag{2}$$

Qualitative Scale for I_T Interpretation. The qualitative scale allows an interpretation of the numerical result obtained with the technical indicator (I_T). This scale was defined with three intervals that indicate the priority and replacement time of the medical device (Table 3).

Table 3. Qualitative scale for the replacement of medical devices

I_T	Priority	Replacement (years)
[0, 0.25]	Low	10
[0.26, 0.55]	Medium	6
[0.56, 1]	High	3

2.3 Application of the Technical Indicator

To illustrate the application of the technical indicator (I_T), a volumetric ventilator located in the Intermediate Therapy Unit was evaluated with the data shown in Table 4. Observe the qualitative domain (Q_i) of each variable and its respective quantitative domain (M_i). It is a mechanical ventilator that is 17 years old and was out of service for more than a month due to software failures.

Substitute the quantitative value of each variable in (1):

$$I_T = \frac{\sum_{i=1}^{10} \rho_i x_i}{2025} = \frac{15(0) + 15(0) + 15(12) + 14(15) + 13(15) * 13(12) + 14(4) + 13(15) + 12(15) + 12(10)}{2025}$$

$$I_T = 0.6$$

According to the qualitative scale (Table 3), this volumetric ventilator needs to be replaced in a period not longer than 3 years, since it obtained a high replacement priority.

Table 4. Description of a volumetric ventilator in terms of the ten variables defined in the qualitative (Q_i) and quantitative domain (M_i).

Variable	Q_i	M_i
x_1	yes	0
x_2	yes	0
x_3	17 years	12
x_4	> 30 days	15
x_5	Life support	15
x_6	Therapeutic	12
x_7	2 failures	4
x_8	Patient dead	15
x_9	Security tests	15
x_{10}	Software failure	10

3 Results

In total, 608 medical devices distributed in nine types of technology (anesthesia machine, defibrillator, electrocardiograph, mechanical ventilator, mobile Rx, oximeter, spirometer, tomography scan, and vital signs monitor) were evaluated. For the application of the Technical Indicator (I_T), the information registered in the physical and functional inventory of the equipment during the year 2022 was used. The information of the first two variables: x_1 and x_2 (availability of spare parts and consumables the next five years), it was requested directly from the suppliers of each brand. The data for the variables: x_4 (days out of service), x_7 (failure frequency) y x_{10} (failure cause) were obtained from the corrective maintenance orders from the Department of Biomedical Engineering (DIB, its Spanish Acronym). The tool was developed in Excel and the result is displayed in a visualizer that shows the name of the device, the inventory number, the medical service where the medical device is located, the I_T result and the replacement time in years. A fragment of the result obtained for twelve volumetric ventilators is shown in Table 5.

The replacement priority results for each device are shown in Table 6. Notice that in the replacement priority column, it shows how many devices got the corresponding priority (in parentheses). For anesthesia machines, tomographs, portable Rx and spirometers, in all cases, a result was obtained in the interval $I_T = [0.26, 0.55]$, which corresponds to a medium replacement priority, that means the replacement of these devices should be done in a period not longer than six years. 97% of the vital signs monitors (127) obtained a low replacement priority (10 years). On the other hand, most of the remaining devices:

49 defibrillators (94%), 24 ECGs (96%), and 53 oximeters (98%), must be replaced within 6 years.

In the case of mechanical ventilators, it should be mentioned that due to the re-conversion of INER to COVID-19 Hospital, in 2020 there was an acquisition of 228 devices. The Institute currently has 310 ventilators of two types (volumetric and transfer), of 16 different brands with different ages.

Table 5. Visualization of the result obtained with the technical indicator and the replacement period

Equipment name	No. Inventory	Medical service	I_T	Replacement
Mechanical ventilator	570416	Intermediate therapy	0.63	3 years
	570417	Intermediate therapy	0.63	
	570457	Sleep clinic	0.66	
	570458	Sleep clinic	0.66	
	570490	Respiratory therapy	0.79	
	570489	Respiratory therapy	0.80	
	570506	Pulmonary rehab	0.42	6 years
	571265	Emergency room	0.42	
	570459	Sleep clinic	0.44	
	570472	Respiratory therapy	0.44	
	570462	Sleep clinic	0.44	
	570471	Respiratory therapy	0.53	

The oldest ventilator is from 1998 (25 years), and the most recent ventilators are from 2020 (3 years). The technical indicator was applied and it was obtained that 75% of these ventilators, the replacement priority is medium; which means they have to be replaced in a period not longer than 6 years. The remaining 25% got a high priority (replacement in 3 years). This last percentage corresponds to the 78 oldest ventilators acquired before 2020.

Table 6. Replacement priority for 608 medical devices evaluated with the technical indicator

Medical equipment	Amount	I_T	Replacement priority	Replacement period (years)
Anesthesia machine	9	[0.38, 0.46]	Medium	6
Tomography scan	3	[0.33, 0.35]	Medium	6
Mobile x ray	5	[0.26, 0.48]	Medium	6
Spirometer	19	[0.27, 0.36]	Medium	6
Defibrillator	52	[0.36, 0.60]	Medium (49) High (3)	6 3
Electrocardiograph	25	[0.31, 0.58]	Medium (24) High (1)	6 3
Vital signs monitor	131	[0.25, 0.27]	Low (127) Medium (4)	10 6
Oximeter	54	[0.27, 0.58]	Medium (53) High (1)	6 3
Mechanical ventilators	310	[0.38, 0.82]	Medium (232) High (78)	6 3
Total	608			

As mentioned, 608 medical devices of nine types were evaluated. The distribution of the replacement priority in each case is shown in Fig. 1. Observe that 65% of the devices must be replaced in a period not longer than six years (medium priority). 21% scored low priority (replacement in 10 years), and the lowest percentage of medical devices (14%) must be replaced within the next three years (high priority).

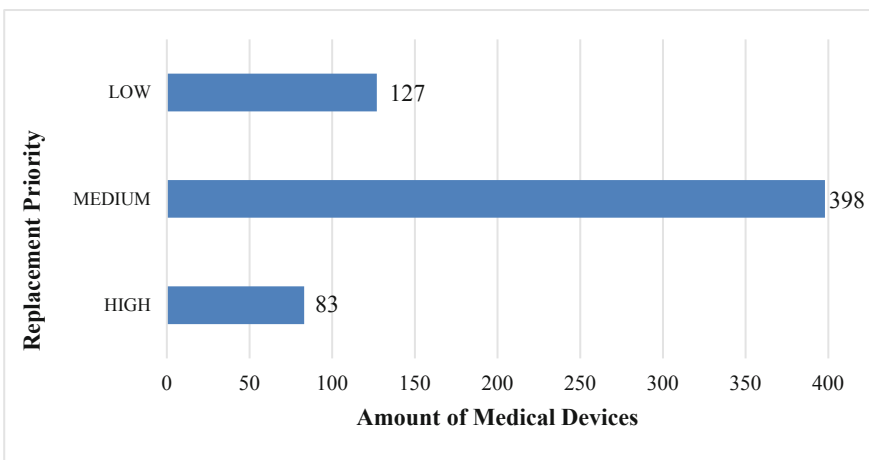


Fig. 1. Distribution of the replacement priority of the 608 medical devices evaluated

4 Conclusion

A technical indicator (I_T) was developed to evaluate the state of operation of medical devices. For the interpretation of the numerical result obtained with I_T , a qualitative scale was designed with three intervals that indicate the replacement priority: high, medium or low; with its replacement period of 3, 6 and 10 years respectively.

A sample of 608 medical devices of nine different technologies from the National Institute of Respiratory Diseases was evaluated. 389 devices obtained a medium priority and must be replaced in a period not exceeding six years. 127 devices got a low priority, and need to be replaced in 10 years. The fewest number of medical devices (83), need to be replaced in the next three years, as they got a high priority.

The technical evaluation instrument presented in this paper provides evidence to develop a technology substitution program and make a rational exercise of the financial resources available at INER. In other words, it helps to acquire the most necessary medical devices, according to the replacement priority obtained.

Finally, the methodology with which the indicators are developed allows for the incorporation of other variables that are of interest to the user, since they are mathematical models based on knowledge. In this case, the staff of the Biomedical Engineering Department of the National Institute of Respiratory Diseases incorporated two more variables (type of equipment and cause of failure) that are using to assess the technical status of medical equipment. The flexibility of these evaluation instruments lies in the fact that they are based on the expertise of the users and can be modeled according to the interests of the evaluator. Evaluation instruments with these characteristics provide evidence-based auxiliary criteria for technical decision-making regarding the performance of installed medical devices.

Acknowledgement. The authors would like to thank the students of the Hospital Programs 22-P course of the Biomedical Engineering Degree at UAM-Iztapalapa, as well as the staff of the Department of Biomedical Engineering of INER, because without their collaboration the development of this work would not have been possible.

References

1. WHO home page, https://www.who.int/health-topics/health-technology-assessment#tab=tab_1. Accessed 04 May 2023
2. Mora-García, T., Piña-Quintero, F., Ortiz-Posadas, M.: An indicator to determine the surplus or deficit of the medical equipment in critical care units. In: VIII Latin American Congress on Biomedical Engineering, CLAIB 2019. IFMBE Proceedings, vol. 75, pp. 1357–1364, Springer, Cham (2019). https://doi.org/10.1007/978-3-030-30648-9_176
3. Mora-García, T.R., Hernández-López, L.A., Piña-Quintero, M.F., Pimentel-Aguilar, A.B., Ortiz-Posadas, M.T.: Comparative analysis of two indicators of technical evaluation for the replacement of medical equipment. In: VIII Latin American Congress on Biomedical Engineering, CLAIB 2019. IFMBE Proceedings, vol. 75, pp. 1365–1372, Springer, Cham (2019). https://doi.org/10.1007/978-3-030-30648-9_175

4. Mora-García, T.R., Piña-Quintero, F., Ortiz-Posadas, M.R.: Pattern recognition for supporting the replacement of medical equipment at mexican institute of pediatrics. In: Ortiz-Posadas, M. (ed) Pattern Recognition Techniques Applied to Biomedical Problems. STEAM-H: Science, Technology, Engineering, Agriculture, Mathematics & Health, pp. 197–215. Springer, Cham (2020). https://doi.org/10.1007/978-3-030-38021-2_9
5. National Institute of Respiratory Diseases (INER, its Acronym in Spanish) Home page, <https://www.gob.mx/salud/iner>. Accessed 04 May 2023



Innovation of Pre-surgical Orthopedics Process for Patients with Cleft Lip and Palate Using the Six Sigma Methodology

Alitzel Munguía-Crisóstomo¹  and Martha Refugio Ortiz-Posadas^{1,2}  

¹ Departamento de Ingeniería Eléctrica, Universidad Autónoma Metropolitana Iztapalapa, Ciudad de México 09340, México

posa@xanum.uam.mx

² Centro Integral de Labio y Paladar Hendido “Centro SUMA”, Ciudad de México 03100, México

Abstract. The SUMA Center of Cleft Lip and Palate Comprehensive Care is a non-profit civil association whose mission is to provide care to patients with cleft lip and palate in vulnerable conditions. The comprehensive care protocol involves 16 medical specialties, including Dentistry. Dental treatment for patients begins with Pre-surgical Orthopedics, which consists of reorienting the anatomical structures that affect the cleft, to reduce the amplitude and improve the effectiveness of the first surgical intervention. The objective of this work was to innovate the process of Pre-surgical Orthopedics care of the Dental Department of the SUMA Center, using the Six Sigma methodology. Non-added-value activities, areas of opportunity were identified, and some innovation related to the management of information in the medical record were proposed. The innovations were implemented in a pilot program by four weeks.

Keywords: Cleft Lip and Palate · Pre-surgical Orthopedics · Six Sigma Methodology · Process Innovation

1 Introduction

The congenital malformation of cleft lip and palate (CLP), clinically called primary and secondary cleft palate respectively, not only brings aesthetic consequences, but also affects different functions in the patient, such as feeding, hearing, nasal breathing, and language, among others. Ideally, patients should be comprehensively evaluated during the first month of life by different specialists (plastic surgeon, dentist, pediatrician, geneticist, among others) to specify the diagnosis, and to verify the existence of other pathologies associated, and where appropriate, the performance of additional diagnostic studies [1]. The multidisciplinary team must attend to the patient early, in accordance with a treatment protocol with a defined schedule for each type of cleft lip and palate.

SUMA, the cleft lip and palate comprehensive care center is a non-profit civil association whose mission is to care patients with cleft lip and palate (CLP) in vulnerable

conditions, from the prenatal stage to the end of their life [2]. It is the first Cleft Lip and/or Palate Leadership Center in Mexico endorsed by the Smile Train Foundation, which is an international humanitarian organization focused on providing solutions to cleft lip and palate in a sustainable manner [3]. The care protocol involves 16 clinical specialties, among which is Dentistry [4]. The clinical processes of the SUMA Dental Department involve the areas of General Dentistry, Maxillofacial Surgery, Orthodontics, Pediatric Dentistry and Pre-surgical Orthopedics. In general, the specialists assess the patient and decide the treatment according to their expertise. This implies that there are no unified criteria nor standardized processes in patient care.

Pre-surgical Orthopedics is a treatment that consists of reorienting the anatomical structures that affect cleft palates, to reduce the width of the cleft and improve nasal deformation before the first surgical intervention. Using several orthopedic devices, it allows an adequate development of the gums and teeth, a better feeding of the newborn, and helps the result of the surgery to be much better. The patient undergoes this treatment for three months, on average. The objective of this work was to innovate the process of Pre-surgical Orthopedics care of the Dental Department of the SUMA Center, using the Six Sigma methodology.

Six Sigma is a methodology for quality improvement that measures how many defects there are in a current process and seeks to systematically eliminate them. This methodology has been used successfully in the innovation and control of several health technology management processes [5–7]; as well as for improving the drug dispensing process [8].

2 Methodology

Six Sigma is a method that provides organizations tools to improve the capability of their processes. This increase in performance and decrease in process variation helps lead to defect reduction and improvement in profits, employee productivity, and quality of products or services. This is achieved by using a structured approach called DMAIC (Define, Measure, Analyze, Innovation, and Control) to identify and eliminate causes of variation and improve processes [9]. For the study of the Pre-surgical Orthopedics process, the Six Sigma methodology was used as follows:

1. *Analysis*. Non-added-value activities (activities that do not contribute to patient satisfaction, do not improve the perception of the clinical service, and do not meet the process requirements), and the associated waste were identified. According to the methodology, there are seven types of waste: movement, waiting time, overproduction, overprocessing, quality defect, inventory and transportation [9]. Areas of opportunity to discover cause-effect relationships were also identified.
2. *Innovation*. Innovations were proposed to improve the performance of the process through Lean tools [9].
3. *Implementation*. The innovations were implemented in the SUMA Dental Department's Pre-Surgical Orthopedics process in a four-week pilot program.

3 Results

3.1 Pre-surgical Orthopedics Medical Devices

Pre-surgical Orthopedics treatment consists of the use of various orthopedic devices for the stimulation and bone remodeling of cleft nasal, alveolar and palatal segments, to reduce the size of the cleft before surgery. In this sense, considering the anatomical characteristics of the fissure, and the type of medical device used, the management of the patient's was analyzed. The most widely used medical devices in Presurgical Orthopedics [10, 11] are:

- Lip taping. It is medical adhesive tape such as foam or surgical silk tape across the upper lip.
- Naso-alveolar Molding (also known as NAM). It is a passively therapy repositions both the alveolar segments and nasal cartilages prior to cleft lip repair.
- Nasal conformers (or retainers). There are typically used to correct or retain the nostril shape after primary cheiloplasty surgery (lip surgery). The main difference between NAM and nasal conformers is that the nasal conformers do not have an alveolar molding effect.
- Nasal elevator. It is a premade nasal and alveolar molding device which can be used to successfully mold the upper lip, alveolus, and nose prior to cleft lip repair.
- Feeding obturator. It is a device that creates a seal between the oral and nasal cavities and controls the flow of milk.
- Friedman's stimulation palate. It is used to confront the alveolar ridges less than 5mm to continue subsequently with the formation of the nasal wings which were depressed.
- Micro-implants. There are small titanium pins 1-2mm in diameter, and 6mm in length. They allow absolute or skeletal anchorage.

The most used medical devices in SUMA patients are shown in Table 1. Note that for cleft lip (unilateral or bilateral), the same devices are used. In the case of cleft palate, an obturator plate is used to help better feeding the patient. For labial-palatal clefts (clefts that occur in both lip and palate simultaneously) the same treatment is also carried out, regardless of whether the primary cleft palate is unilateral or bilateral.

According to the management of Pre-surgical Orthopedics analyzed, it was observed that in 53 records of patients treated at SUMA chosen at random, the distribution of the use of these orthopedic devices was as follows:

- Naso-alveolar Molding (NAM): 39.6% (21 patients)
- Friedman's stimulation plate: 7.5% (4 patients)
- Feeding obturator: 7.5% (4 patients)
- Nasal conformer: 50.9% (27 patients)
- Lip taping: 33.9% (18 patients)
- Nasal elevator: 22.6% (12 patients)
- Micro-implants: 3.8% (2 patients)

Table 1. Medical devices for Pre-surgical Orthopedics management.

Case	Medical devices
1. Unilateral cleft lip	Lip taping Nasal elevator or nasal conformer
2. Bilateral cleft lip	Lip taping Nasal elevator or nasal conformer
3. Cleft palate	Feeding obturator or Friedman palate
4. Unilateral cleft lip + cleft palate	Lip taping Nasal elevator Nasoalveolar Molding (NAM)
5. Bilateral cleft lip + cleft palate	Lip taping Nasal elevator NAM (If the patient is older than 4 months, and the bone is no longer malleable, only micro-implants are placed)

Most of the patients used a NAM plate (almost 40%) and the device that was used the least was the micro-implant, since it is generally applied in outdated patients (when Pre-surgical Orthopedics is not applied before three months of age), or patients are older than 6 months of age. Therefore, micro-implants have a lower incidence use in the SUMA Center.

Analyzing the type of orthopedic device used in patients treated at the SUMA Center, makes it possible to identify those with the greatest demand and provides auxiliary criteria for making decisions on the rational investment of the budget. The latter is very useful in invest financial resources in a non-profit organization that works from donations (as SUMA Center).

3.2 Analysis of the Pre-surgical Orthopedics Process

The execution of the Pre-surgical Orthopedics Process is shown in the flowchart of Fig. 1. There are five actors involved: patient, dentist, pediatrician, geneticist, and surgeon. The patient who arrives for the first time at the SUMA Center, photos of the original fissure are taken, and a file is opened. Subsequently, he/her has a pre-consultation with the medical specialties of pediatrics and genetics. If the patient is diagnosed with an additional disease, is not accepted and is referred to another public health institution.

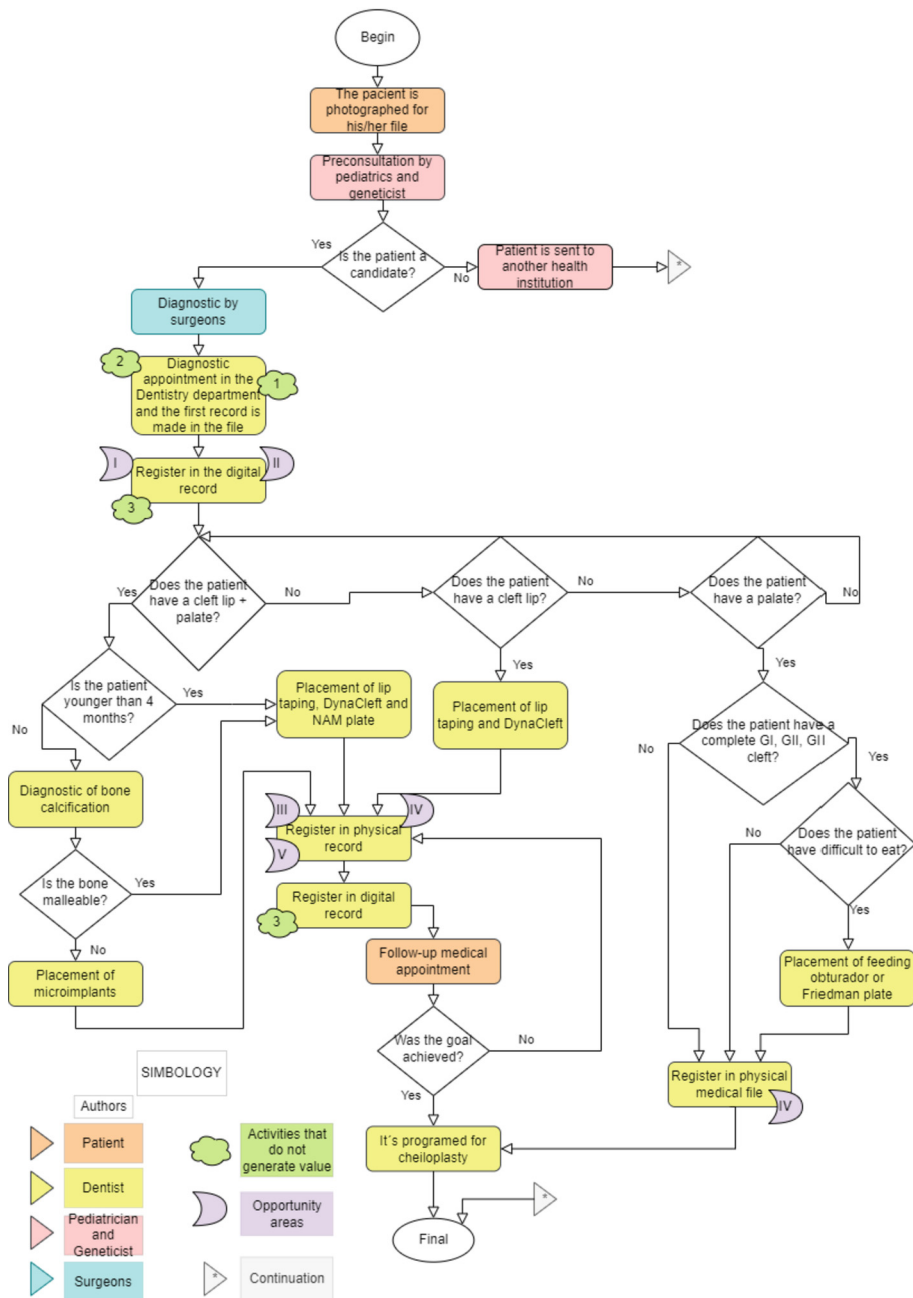


Fig. 1. Pre-surgical Orthopedics Process

Non-added-value Activities. During the analysis of the Pre-Surgical Orthopedics process, three activities that do not add value were found (Table 2). Note that the associated waste was overprocessing/rework for activities 1 and 3, and for activity 2, it was associated with wasted inventory.

Table 2. Activities that do not generate value and waste associated in the Pre-Surgical Orthopedics process.

No	Non-added-value activities	Associated waste	Innovation
1	Duplicate diagnosis by surgical and dental specialists	Overprocessing/Rework	Make a single joint diagnosis with both specialists involved
2	Unused format “Historia Dental” (dental record)	Inventory	Eliminate this format and, where appropriate, design the new format
3	Medical record on paper and digital	Overprocessing/Rework	Use only digital record

Opportunity Areas. Five areas of opportunity were found and for each one an improvement was also proposed (Table 3). Observe that the computer is affecting the registration of the digital records because it requires modifying the software and hardware, in addition to the fact that the registration is not complete. For example, it is necessary to incorporate information about who is responsible for the patient in the consultation correspondent.

Table 3. Opportunity areas in the Pre-surgical Orthopedics

No	Areas of opportunity	Improvement proposal
I	Incomplete record	Update registration system
II	Outdated computer	It is suggested to update the work teams
III	Clinical history without notes of medical evolution	In all cases a medical note must be made
IV	Messy medical notes timeline	Propose a chronological order of the medical notes within the file
V	Medical notes without author	Use a color code by specialty

3.3 Innovation of the Pre-surgical Orthopedics Process


The innovations proposed for the three wastes (Table 1) are related to the management of information in the patient’s record. For the five areas of opportunity (Table 2), some improvements imply updating the software and hardware of the computer equipment.

In both cases, the innovations aim to optimize the patient record and the follow-up information and increase the effectiveness of dental process.


3.4 Implementation of the Innovations

The innovations that were implemented were those related to the handling of information in the patient’s file, which are described below.

Patient Follow-up. The format called “Monitoring Sheet” was updated (Fig. 2). The following fields were added: patient name, file number, date of birth and dates of admission. Twelve Treatment Phases were included in which the patient can be placed and the start and end dates of each stage. A section was also included to record the initial diagnosis of the patient (original cleft) and another called “Alert” for specific observations by the specialist. The printed format is currently in use at the SUMA Dental Department.



SUMA
CENTRO INTEGRAL
DE CLEFT PALADARIO



Smile Train
CLEFT LEADERSHIP CENTER
CENTRO DE LIDERAZGO EN CLEFT PALADARIO

Departamento Dental

Hoja de Seguimiento

Nombre: _____

N. de Expediente: 1183

Fecha de nacimiento: 26/10/2022

Fechas de ingreso: _____

Fase de Tratamiento	Fecha de inicio	Fecha de fin
Ortopedia Prequirúrgica		
Queiloplastía		
Seguimiento pos queiloplastía		
Palatoplastía		
Tubos de Ventilación		
Seguimiento preventivo		
Ortopedia de los maxilares		
Máscara de Protracción		
Preparación para Injerto Alveolar		
Injerto Alveolar		
Aparatología Fija y Ortodoncia		
Rinoseptoplastía		
Otra:		

¡¡ALERTA!!

Diagnóstico

Fig. 2. Monitoring sheet

Record of Medical Evolution Notes. This section of the file was also updated (Fig. 3). A color was assigned to identify each specialty of the Dental Department that made the medical note. For Pre-surgical Orthopedics, the mint blue color was chosen; for Pediatric Dentistry, the orange color; and for Orthodontics, purple. For example, in Fig. 3 the date of the medical note was highlighted with mint blue, which means that it is a Pre-Surgical Orthopedics note. Additionally, the patient’s dental laboratory order may be attached containing the following information: patient’s name, file number, name of the requesting doctor, medical devices to be made, and the date of delivery.

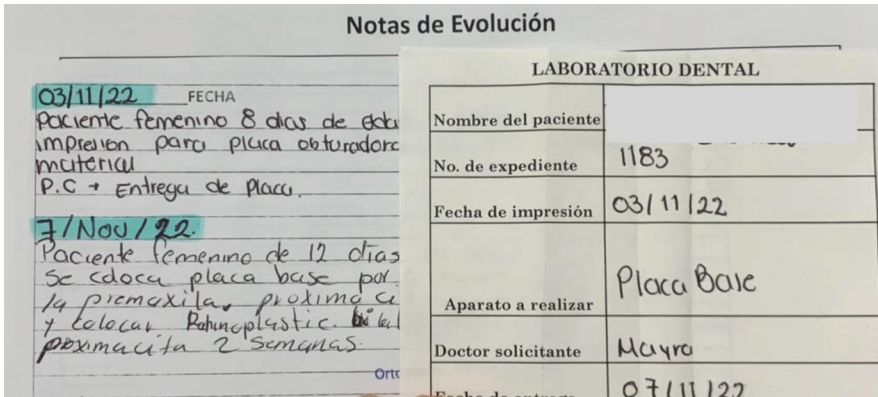


Fig. 3. Record of medical evolution notes

Record of Anthropometric Measurements of the Cleft. New formats were designed and implemented for including anthropometric measurements of unilateral clefts (Fig. 4) and bilateral clefts (Fig. 5). These request the patient’s name, the patient’s file number, and the date of the record of the information. The format considers information on the extraoral and intraoral characteristics of the cleft. Measurements of the different anatomical structures affected by the fissure are recorded. In each case, a photo of the corresponding anatomical structure is presented, a section to indicate which is the cleft side (unilateral cleft); and another to indicate the non-cracked side. Both formats serve to assess and diagnose the fissure more objectively.

Departamento Dental

Medidas Antropométricas	Esquema	Lado fisurado	Lado no fisurado	Medidas Antropométricas	Esquema	Lado fisurado	Lado no fisurado
1.- Longitud de la columela				6.- Longitud del segmento alveolar mayor y menor			
2.- Proyección de longitud alar				7.- Amplitud posterior de la fisura palatina			
3.- Ángulo de la columela				8.- Amplitud del arco			
4.- Segmento de la fisura labial				9.- Rotación del segmento alveolar mayor			
5.- Distancia Intersegmental				10.- Rotación del segmento alveolar menor			

Medidas Antropométricas del Paciente Unilateral

Paciente: _____

Exp. : _____

Fecha: _____

Inicial/Final

Fig. 4. Format for anthropometric measurements of the unilateral patient.

Departamento Dental

Medidas Antropométricas	Esquema	Lado izquierdo	Lado derecho	Medidas Antropométricas	Esquema	Lado izquierdo	Lado derecho
1.- Longitud de la columela				6.- Amplitud de fisura alveolar			
2.- Proyección de longitud alar				7.- Protrusión de la premaxila			
3.- Ángulo nasolabial				8.- Amplitud de la fisura palatina posterior			
4.- Segmento de la fisura labial				9.- Distancia intercanina			
5.- Longitud del prolabio				10.- Rotación de la premaxila			

Medidas Antropométricas del Paciente Bilateral

Paciente: _____

Exp. : _____

Fecha: _____

Inicial/Final

Fig. 5. Format for anthropometric measurements of the bilateral patient.

4 Conclusion

The process of Pre-surgical Orthopedics of the Dental Department of the SUMA Center was analyzed using the Six Sigma methodology. Three non-added-value activities related to inventory and overprocessing (re-work) wastes were identified; and five areas of opportunity. To improve the performance of the process, five innovations were proposed.

Together with the Pre-surgical Orthopedics specialists, the follow-up formats and medical notes were updated. Additionally, to provide more evidence for making an accurate and timely diagnosis, a new format was designed to record the anthropometric measurements of the anatomical structures affected by the fissure. These three formats are currently being used for the registration and follow-up of patients in the SUMA Dental Department. The evaluation of the impact of these improvements will be done in six months.

It is important to say that it is imperative that the Dental Department eradicate the use of paper in patient records and migrate to digital tools to perform these tasks. That is why, it is necessary to have updated computers and software, as well as the training of specialists to use these digital tools.

Finally, although in this work the Six Sigma methodology was applied to innovate pre-surgical orthopedic processes, it is important to say that this methodology can be used to improve any type of process related to health care.

Acknowledgement. The authors want to thank Doctors Scarlett Escobar and Mayra Álvarez from the Dental Department of the SUMA Center, because without their collaboration the development of this work would not have been possible.

References

1. Monasterio, L., Ford, A., Tastets, M.: Fisuras Labio Palatinas. Trabajo Multidisciplinario. Revista Médica Clínica Las Condes, 27, 14–21 (2016). <https://docplayer.es/82085837-Fisuras-labio-palatinas-tratamiento-multidisciplinario.html>
2. Centro SUMA, <https://www.centrosuma.org/>. Accessed 16 May 2023
3. Smile Train, <https://www.smiletrain.org/cleft-leadership-centers/suma>. Accessed 16 May 2023
4. Maya-Behar, J., Morales de la Cerda, R., Cabal-Jiménez, K.E., Ortiz-Posadas, M.R.: Labio Y Paladar Hendido ¿Qué Es Y Cómo Se Trata?, 125, 52–63 (2022). <https://contactos.izt.uam.mx/index.php/contactos/issue/view/16/16>
5. Navarro-Arcos, Y.J., Aguilar-Pimentel, A.B., Ortiz-Posadas, M.R.: Innovation and control of health technology management procedures applying six sigma methodology. In: XLV Mexican Conference on Biomedical Engineering. CNIB 2022. IFMBE Proceedings, 86 (2): 793–804 (2022). Springer, Cham. https://doi.org/10.1007/978-3-031-18256-3_83
6. Becerril-Alquicira, A., Ortiz-Posadas, M.R.: Improvement of the health technology management process of the public health services in morelos using the six sigma methodology. In: Proceeding of 32nd Annual International Conference of the IEEE Engineering in Medicine and Biology Society, pp. 450–453 (2010)
7. García-Porres, J., Ortiz-Posadas, M.R., Pimentel-Aguilar, A.B.: Lean six sigma applied to a process innovation in a mexican health institute's imaging department. In: Proceeding of 30th Annual International Conference of the IEEE Engineering in Medicine and Biology Society, pp. 5125–5128 (2008)

8. Pimentel-Aguilar, A.B., Aguilar-Adaya, M.K., Sánchez-Castillo, E.I., Ortiz-Posadas, M.R.: Improving the drug dispensing process at the national institute of respiratory diseases by applying the six sigma methodology. In: Proceeding of 33rd Annual International Conference of the IEEE Engineering in Medicine and Biology Society, pp. 1185–1188 (2011)
9. Hadfield, D., Holmes, S.: *The Lean Healthcare Pocket Guide: Tools for the Elimination of Waste in Hospitals, Clinics and Other Healthcare Facilities*. 2nd ed. MCS Media Incorporated, Chelsea (2009)
10. Alzain, I., Batwa, W., Cash, A., Murshid, Z.: Presurgical cleft lip and palate orthopedics: an overview. *Clin. Cosmet. Investig. Dent.* **9**, 53–59 (2017). <https://doi.org/10.2147/CCIDE.S129598>
11. Vinson, L.A.: Presurgical orthopedics in cleft lip palate care. *J. Dentistry Oral Med.* **4**, 14–19 (2016). <https://doi.org/10.13189/ojdom.2016.040102>



Permanent Changes in Clinical Engineering Procedures Since COVID-19 in OECD Countries

Valeria Chico¹ , Nelly Gordillo-Castillo¹  , Ana Luz Portillo¹ ,
and Yara Villalobos² 

¹ Department of Electrical and Computer Engineering, University of Ciudad Juarez, Ciudad Juarez, Mexico
nelly.gordillo@uacj.mx

² Health Services Jalisco, Ciudad Juarez, Mexico

Abstract. The COVID-19 pandemic has impacted clinical engineering procedures, including medical technology management, training and technical support, quality risk management, and research and development. This research aims to highlight the permanent changes in clinical engineering practices that emerged due to the pandemic in OECD member countries. By analyzing sources of information, this study examines how the adoption of technologies and digitization of healthcare have been accelerated during the pandemic. The findings are presented in implementations focused on telemedicine, big data, and digital health while also identifying areas of opportunity and challenges for the ongoing adoption of these measures. This abstract provides a succinct summary of the research's focus, objectives, and key findings related to the impact of COVID-19 on clinical engineering procedures and the consequent transformations in healthcare practices.

Keywords: clinical engineering · COVID-19 · OECD

1 Introduction

In December 2019, a cluster of pneumonia cases with an unknown cause was observed in Wuhan, China, leading to an increasing number of reported human infections [1, 2]. It was later confirmed as a novel coronavirus, SARS-CoV-2 (severe acute respiratory syndrome coronavirus 2) [1]. On March 11, 2020, the World Health Organization declared the disease caused by SARS-CoV-2 as coronavirus disease 2019 (COVID-19) and classified it as a pandemic [2].

COVID-19 generated significant stress within various healthcare services due to its high contagion rate, leading to an overload of the healthcare system and demanding organizational changes. Throughout the pandemic, healthcare professionals acquired the knowledge and skills required to manage patients infected with COVID-19, utilizing the available resources at the time. These workers faced numerous challenges since the onset of the pandemic, including adapting hospitals for the treatment of SARS-CoV-2-infected patients, limited availability of protective equipment for staff, and inadequate

clinical protocols [3]. The surge in demand for medical services caused by the pandemic prompted healthcare managers to focus on implementing actions to maximize the efficient utilization of limited resources [4].

Griffin *et al.* [5] list the initial challenges arising from COVID-19 and the corresponding solutions. These include expanding service capacity, ensuring employee well-being, addressing clinical challenges, and providing education on the subject. Based on these issues, contingency plans, ethical recommendations, guidelines on ventilation systems, and resource and patient redistribution strategies were developed [6].

Observing the healthcare system's response to the increased demand for medical care and recognizing the emerging medicolegal and ethical aspects faced by health professionals, consensus documents were developed, incorporating medical criteria and fundamental ethical values [7]. To mitigate the spread of the virus within healthcare facilities, measures such as audits, training, and continuous supervision were implemented [8].

The digitalization of healthcare emerged as a potential solution to transform healthcare delivery during the pandemic [9]. Telehealth, for instance, proved to be a valuable tool for COVID-19 patients, enabling remote assessment and care delivery. Conversely, telehealth provided convenient access to routine care without exposure in crowded hospitals for uninfected individuals at higher risk, such as older adults with pre-existing conditions [10]. The application of intelligent technologies or systems to control and manage SARS-CoV-2 infection offered various advantages, ranging from the rapid production of 3D-printed medical products to the timely assessment of hospital activities using artificial intelligence and machine learning [11].

According to the adaptations, changes, and regulations implemented in hospitals to provide care for COVID-19 patients in member countries of the Organization for Economic Cooperation and Development (OECD), this paper aims to investigate the long-term impact of these measures on clinical engineering procedures.

2 Methods

A comprehensive search was conducted to identify scientific articles, reports, and documents that discussed the implementations resulting from the COVID-19 pandemic and their impact on clinical engineering. These sources were gathered from various databases and subsequently compiled for further analysis. The acquired information was tabulated, and inclusion and exclusion criteria were applied to refine the data.

Inclusion criteria:

- Information collected from scientific articles and reports from OECD member countries.
- The articles had to be published in English or Spanish.
- The articles had to evaluate the impact or permanence of adaptations, changes, and regulations implemented in hospitals to care for patients with COVID-19.
- The timeframe for inclusion was from 2020 to 2022.

Exclusion criteria:

- Information from books and other systematic or state-of-the-art reviews was excluded.

2.1 Document Search

To align with the definition of clinical engineering as the application of engineering knowledge and health technology management to support patient care, a list of relevant terms associated with the topic was generated. These terms created Boolean equations that enhanced the search for relevant information. The search equation was employed in the following databases: EBSCO, PubMed, and ScienceDirect. The University of Ciudad Juarez provided direct access to these databases. The search Eq. (1) used was formulated in English and Spanish.

((coronavirus OR COVID-19 OR SARS-Cov-2 OR pandemic OR post-covid-19) NOT (allergic OR vaccination OR during)) AND (hospitals OR "health facilities" OR "medical equipment" OR healthcare OR "biomedical engineering" OR "clinical engineering") AND ("internet of things" OR telemedicine OR "patient monitoring" OR "electronic health records" OR "medical technology" OR "big data") (protocols OR normative OR regulations OR "government policy") (1)

2.2 Classification of Information Sources

An Excel file was created to facilitate the organization of the collected information. The file consisted of four different sheets: title, DOI, inclusion/exclusion/revision, and reason. Each sheet corresponded to a specific database where the results were obtained. Documents meeting the inclusion criteria, as determined by the content of their abstracts and titles, were added to the inclusion section of the Excel file. The DOI of each included document was recorded for identification purposes.

2.3 Content Analysis and Identification of Adaptations

The selected information sources from the initial stage were subjected to a detailed content analysis based on the established guidelines. A table was created to identify the title of each article, provide a summary of its content, specify the implemented change or adaptation, describe how the implementation was carried out, identify the specific area where it was implemented, and include an inclusion/exclusion condition section to filter further and categorize the obtained results effectively.

2.4 Categorization of Identified Changes

To ensure a structured view of the identified implementations or adaptations, the search terms associated with clinical engineering were utilized to define categories for classifying the selected information sources. This categorization process aimed to present the gathered information clearly and organized. The articles and reports were categorized into the following fields: telemedicine, microdata, and eHealth. Once the categories were established, the obtained information was presented through tables, focusing on visualizing the implemented actions and their applications in various medical areas rather than sorting them by specific medical fields.

3 Results

This section presents the findings, synthesizes, and discusses the identified areas of opportunity or challenges associated with the obtained results.

3.1 Document Search

Equation 1 was utilized in the search engines to retrieve relevant information. However, the search conducted using the equations in Spanish did not yield significant results. As a result, only the equations in English were applied. Figure 1 shows the PRISMA 2020 flow diagram for identifying of studies via databases and registers.

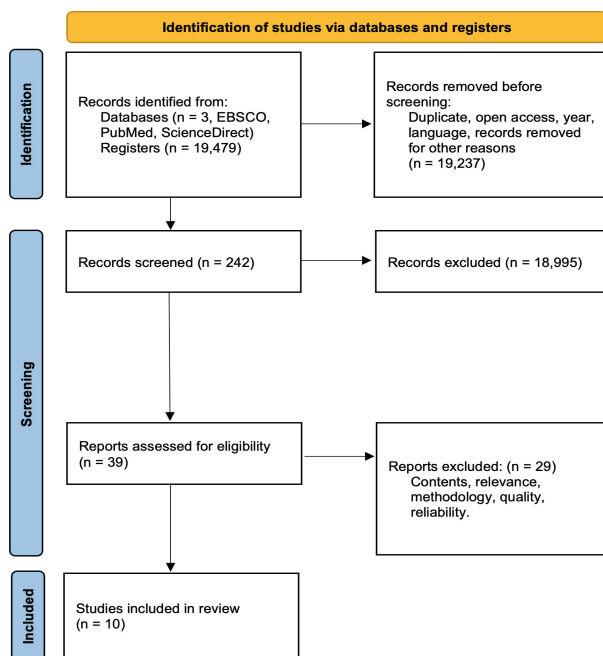


Fig. 1. Prisma 2020 flow diagram.

3.2 Summary of Selected Sources

Out of the initial 39 documents, a final selection of 10 documents was made as information sources. This reduction was made with the specific aim of highlighting real-world project implementations. The following tables present the categorization of the identified implementations. Table 1 showcases implementations centered around telemedicine; Table 2 focuses on implementations related to big data, and Table 3 highlights implementations in the realm of digital health.

Table 1. Implementations focused on telemedicine.

Article	Health area	Situation to be addressed	Summary of contents
[12]	Neurology	Amyotrophic Lateral Sclerosis Clinical Trials	Telemedicine requirements for supporting clinical trials in recruitment, consent, screening, and evaluation, such as investigator compliance with FDA-1572. Remote tests, like the ALSFRS-R, are performed for ALS treatment
[13]	Orthopedics	Remote patient care in surgical orthopedics	Identifying the benefits and challenges of remote care became necessary during the COVID-19 pandemic. Benefits include increased access to healthcare and decreased provider spending. The challenge to address: Cost management for technology implementation and maintenance
[14]	General Practice	Two-way communication systems linked to the patient's medical record	Existing patient portals are being improved to allow online interfaces for patients to monitor certain aspects of their health remotely, such as blood sugar levels or blood pressure
[15]	Otolaryngology	Digital assessment and care	Shift towards using virtual platforms for patient care that comply with HIPAA requirements, including platforms like "Skype for Business," "Zoom for Healthcare," "Google G Suite Hangouts Meet," "Doxy.me," "Updox," and "Vsee"
[16]	Neurology / Neurophysiology	Development of guidelines in Italy for clinical teleneurophysiology	Use of secure VPN connections and remote desktop programs to establish both in-hospital and out-of-hospital computer networks, ensuring compliance with patient privacy legislation

Table 2. Implementations focused on big data.

Article	Health area	Situation to be addressed	Summary of contents
[17]	N/A	Secure informed consent of personal data provided by individuals	Research on synthetic data, generated by artificial intelligence algorithms trained on real-world data, aiming to address the issue of miscommunication regarding informed consent and the abuse of personal data
[18]	Oncology, General Medicine, Gynecology, and Obstetrics	Measuring the performance of healthcare innovations	Use of dashboards to present key performance indicators and enable performance management in hospitals. Example applications in pilot projects include deploying a tracking interface for locating medical equipment and utilizing big data to identify workflow bottlenecks within the hospital
[19]	N/A	Unfalsifiability and anonymity of patient information	Proposing a secure and privacy-preserving authentication system, known as SEAPA, based on Lattice's approach, to meet the data security requirements of cyber-physical healthcare systems

3.3 Summary of Findings

Although the articles were classified based on the primary implementation identified, they have a close relationship. Telemedicine in clinical engineering is connected to managing big data, and digital health is linked to artificial intelligence, cybersecurity, and big data. An example of this relationship is in reference [22], where inter-societal recommendations by the Italian Society of Neurophysiology and the Italian Society of Telemedicine are mentioned. These recommendations involve using computer networks, secure VPN connections, and remote desktop software to enable remote control of electro-medical equipment by physicians.

Table 3. Implementations focused on digital health.

Article	Health area	Situation to be addressed	Summary of contents
[20]	N/A	Investing in new information and communication technologies, such as artificial intelligence, cybersecurity, and high-performance computing	The new European interoperability framework was announced in 2017, and research work has been conducted to implement it as a strategy within the timeframe of 2020–2025
[21]	N/A	Modernize the information system with the purpose of guaranteeing reliable information that anticipates the needs of the population and favors the National Health System	Policy guidelines related to e-health are mentioned, including coordinating measures to prevent and combat diseases, particularly during pandemics, focusin on utilizing digital media. Emphasis is placed on improving communication, databases, and digitizing records in the healthcare sector

Compliance with General Data Protection Regulation (GDPR) requirements, such as appointing a data protection officer, maintaining a register of processing activities, obtaining signed consent, and conducting data protection impact assessments, is necessary for health institutions.

Critical data management and control are often outsourced to external providers. Patient rights regarding access, deletion, and transfer of personal data should be respected.

During the COVID-19 crisis, big data technology was used to support virus control, and it continues to be used for performance management in hospitals. Integrated management tables and pilot projects were utilized to analyze their functionality.

The pandemic has led to the adoption of medical technologies in most of the OCDE countries, particularly in private health institutions. Digital health has been incorporated to improve administrative management, with logic/benefit measures applied to laboratory information systems and medical imaging. Laboratory chains are more advanced in medical technology and telemedicine services, allowing for experience and quality to be gained before implementing them in more extensive settings like hospitals.

3.4 Limitations and Future Areas of Opportunity

Although the benefits of clinical engineering strategies during the pandemic have been discussed, there are also areas of opportunity for further improvement and their continued implementation in clinical practices.

Reference [17] highlights a limitation related to users not always limiting the use of their personal data to the original purpose for which consent was given. In one example,

private information collected for tracking purposes during the pandemic was used in a murder investigation, indicating a need to address mishandling of patient data.

Other limitations identified in the investigation include the time range of the search, with many articles focusing on pandemic mitigation strategies rather than future applications or potential long-term implementation in clinical engineering.

Member countries face various limitations in achieving permanent implementations, such as the absence of interoperable platforms, inadequate regulatory frameworks for digital health, limited budgets, and operational capabilities.

The Mexican Health Sector Program proposes six action plans to address these limitations and promote digital health:

1. Create a Health Intelligence Center to standardize information recording and storage.
2. Utilize existing information systems to create platforms and databases.
3. Digitize records or promote interoperability across different levels of care.
4. Strengthen mechanisms for recording personal data to avoid duplication.
5. Implement telemedicine in marginalized populations.
6. Improve the evaluation and management of Information and Communication Technologies in healthcare to enhance service quality.

4 Conclusions

The investigated implementations played a significant role in mitigating the spread of the SARS-CoV-2 virus and have found additional applications in healthcare and health management practices, leading to their permanent use.

The categorized applications and changes highlight the interconnectedness between different functions, such as the need for interoperability to support patient information management, closely related to digital health.

While the adoption of technologies for risk management during the pandemic was accelerated, the permanent implementation of these technologies in clinical engineering procedures requires careful consideration of various factors, including technology costs, legal agreements, the appointment of data protection officers, and ongoing data protection assessments.

The research needs to be more transparent regarding whether healthcare managers comply with the necessary agreements, training, regulations, and standards to establish the permanence of technologies in different healthcare areas officially. The need for written agreements, training, and regulatory frameworks is discussed, as well as the potential reliance on temporary consents and permits, which may indicate the current state of the permanence of these technologies in clinical engineering procedures.

References

1. Pallarés Carratalá, V., Górriz-Zambrano, C., Llisterri Caro, J.L., Górriz, J.L.: The COVID-19 pandemic: an opportunity to change the way we care for our patients (2020). <https://doi.org/10.1016/j.semerg.2020.05.002>
2. El Zowalaty, M.E., Järhult, J.D.: From SARS to COVID-19: a previously un-known SARS-related coronavirus (SARS-CoV-2) of pandemic potential infecting humans – Call for a One Health approach. *One Health*. 9 (2020). <https://doi.org/10.1016/j.onehlt.2020.100124>

3. Esquivel-Chirino, C., et al.: The effects of covid-19 on healthcare workers and non-healthcare workers in Mexico: 14 months into the pandemic. *Medicina (Lithuania)*. 57 (2021). <https://doi.org/10.3390/medicina57121353>
4. Maylevis, A., Valdés, M., Felipe Ramírez Pérez, J., Contreras, E.V., Sebastian, P., Ritchie, H.: CONTRIBUCIÓN DE LOS INDICADORES DE GESTIÓN EN LA EFICIENCIA ORGANIZACIONAL Y LA ADMINISTRACIÓN HOSPITALARIA EN INSTITUCIONES DE SALUD. *UNESUM-Ciencias: Revista Científica Multidisciplinaria*. 5, 109–122
5. Griffin, K.M., Karas, M.G., Ivascu, N.S., Lief, L.: Hospital preparedness for COVID-19: a practical guide from a critical care perspective (2020). <https://doi.org/10.1164/rccm.202004-1037CP>
6. Ballesteros Sanz, M., et al.: Recommendations of the Working Groups from the Spanish Society of Intensive and Critical Care Medicine and Coronary Units (SEMICYUC) for the management of adult critically ill patients in the coronavirus disease (COVID-19). *Med Intensiva*. 44, 371–388 (2020). <https://doi.org/10.1016/j.me-din.2020.04.001>
7. Arimany-Manso, J., Martín-Fumadó, C.: Medico-legal issues regarding from the COVID-19 pandemic. *Med. Clin. (Barc.)* 155, 344–346 (2020). <https://doi.org/10.1016/j.medcli.2020.06.010>
8. Xu, C., et al.: Application of refined management in prevention and control of the coronavirus disease 2019 epidemic in non-isolated areas of a general hospital. *Int. J. Nurs. Sci.* 7, 143–147 (2020). <https://doi.org/10.3761/j.issn.0254-1769>
9. Assaye, B.T., Shimie, A.: Worku: telemedicine use during COVID-19 pandemics and associated factors among health professionals working in health facilities at resource-limited setting 2021. *Inform. Med. Unlocked*. 33 (2022). <https://doi.org/10.1016/j.imu.2022.101085>
10. Smith, A.C., et al.: Telehealth for global emergencies: Implications for coronavirus disease 2019 (COVID-19). *J. Telemed. Telecare* 26, 309–313 (2020). <https://doi.org/10.1177/1357633X20916567>
11. Rudrapati, R.: Using industrial 4.0 technologies to combat the COVID-19 pandemic (2022). <https://doi.org/10.1016/j.amsu.2022.103811>
12. Govindarajan, R., Berry, J.D., Paganoni, S., Pulley, M.T., Simmons, Z.: Optimizing telemedicine to facilitate amyotrophic lateral sclerosis clinical trials. *Muscle Nerve* 62, 321–326 (2020). <https://doi.org/10.1002/mus.26921>
13. Makhni, M.C., Riew, G.J., Sumathipala, M.G.: Telemedicine in orthopaedic surgery. *J. Bone Joint Surg.* 102, 1109–1115 (2020). <https://doi.org/10.2106/JBJS.20.00452>
14. Casillas, A., et al.: Portals of change: how patient portals will ultimately work for safety net populations. *J. Med. Internet Res.* 22, e16835 (2020). <https://doi.org/10.2196/16835>
15. Faden, D.L., Chang Sing Pang, K., Hildrew, D.M.: The age of telemedicine is upon us. *Laryngoscope Investig Otolaryngol.* 5, 584–585 (2020) <https://doi.org/10.1002/lio2.391>
16. Stipa, G., et al.: The Italian technical/administrative recommendations for telemedicine in clinical neurophysiology. *Neurol. Sci.* 42, 1923–1931 (2021). <https://doi.org/10.1007/s10072-020-04732-8>
17. Andreotta, A.J., Kirkham, N., Rizzi, M.: AI, big data, and the future of consent. *AI Soc.* 37, 1715–1728 (2022). <https://doi.org/10.1007/s00146-021-01262-5>
18. van Elten, H.J., Sülz, S., van Raaij, E.M., Wehrens, R.: Big data health care innovations: performance dash boarding as a process of collective sense making. *J. Med. Internet Res.* 24, e30201 (2022). <https://doi.org/10.2196/30201>
19. Liu, J., Yu, Y., Wang, H., Zhang, H.: Lattice-based self-enhancement authorized accessible privacy authentication for cyber-physical systems. *Secur. Commun. Netw.* 2022, 1–9 (2022). <https://doi.org/10.1155/2022/8995704>
20. Kouroubali, A., Katehakis, D.G.: Policy and Strategy for Interoperability of Digital Health in Europe. Presented at the June 6 (2022). <https://doi.org/10.3233/SHTI220209>

21. Fernández-Tapia, J.: Avances y limitaciones en las políticas públicas de e-Salud en México. *RCH* **12**, 152–178 (2021)
22. Stipa, G., et al.: The Italian technical/administrative recommendations for tele-medicine in clinical neurophysiology. <https://doi.org/10.1007/s10072-020-04732-8/Published>



Relationship Between Neuroarchitecture and Stress Reduction Compared to Conventional Architecture in Healthcare Personnel

Mauricio Baez¹  , Sergio Camacho¹ , Bersain Reyes¹ , Antonio Morante¹ ,
and Miguel Fuentes² 

¹ School of Sciences, Autonomous University of San Luis Potosi, 78295 San Luis Potosi, San Luis Potosi, Mexico

A280193@alumnos.uaslp.mx

² Biomedical Engineering Department, Guadalupe Victoria Maternal and Child Hospital, 52918 Atizapan de Zaragoza, Mexico State, Mexico

Abstract. This study investigates the influence of hospitals built with conventional architecture compared to those built using neuroarchitecture, a branch of architecture that considers the impact of design on cognitive and emotional responses. Neuroarchitecture merges architectural design and brain science, crafting environments optimized for human well-being. It encompasses factors like spatial layout, colors, textures, and acoustics to shape cognitive and emotional responses positively. This interdisciplinary approach aims to create spaces that promote relaxation, focus, and overall mental health. A device sensitive to skin impedance was used to measure symptoms of stress. A total of 28 participants were shown two videos, one featuring conventional architecture and the other showcasing neuroarchitecture. Additionally, the Depression, Anxiety and Stress Scale - 21 Items (DASS-21) questionnaire was administered to assess the symptomatology of stress, depression, and anxiety. Significant differences in skin impedance were found between subjects exposed to Neuroarchitecture and Conventional Architecture environments. In the Tococirugía data, Neuroarchitecture showed an average impedance of 355 K Ω compared to 287 K Ω in the conventional environment. Similarly, in the UCIN data, Neuroarchitecture had an average impedance of 302 K Ω while the conventional environment had 230 K Ω . For the UTIN data, Neuroarchitecture exhibited an average impedance of 377 K Ω , whereas the conventional environment had 235 K Ω . The DASS-21 questionnaire results indicated higher levels of moderate stress (53.5%) compared to mild anxiety (46.4%) and mild depression (50%) among medical personnel in the evaluated clinical services.

Keywords: Neuroarchitecture · Stress reduction · Skin impedance · Stress Scale-21 · Medical personnel

1 Introduction

Stress is a significant factor that impacts individuals' health and well-being, with the brain playing a crucial role in our stress response. Chronic or excessive stress can have negative effects on health, while moderate stress can have positive effects on adapt-ability.

© The Author(s), under exclusive license to Springer Nature Switzerland AG 2024

J. de J. A. Flores Cuautle et al. (Eds.): CNIB 2023, IFMBE Proceedings 97, pp. 232–240, 2024.

https://doi.org/10.1007/978-3-031-46936-7_25

Stress activates the hypothalamic-pituitary-adrenal and sympathetic-adrenomedullary axes, triggering physiological responses to maintain homeostasis. Disruptions in these axes are associated with psychological disorders and health problems [1]. Stress also affects memory, behavior, and overall health. The American Psychiatric Association (2017) points out anxiety and depression disorders can lead to suicidality, increased cardiovascular risk, sleep problems, and other symptoms [2].

In Mexico, occupational stress affects 63% of workers, the highest percentage globally [3]. Healthcare professionals are particularly vulnerable due to overwhelming demands [4]. Environmental demands impact satisfaction, well-being, and functioning [5]. Neuroarchitecture explores design's influence on cognitive and emotional responses. Some elements define this field: spatial layout and flow impact navigation and comfort; lighting influences circadian rhythms and mood; color palette evokes emotional responses; materials and textures affect tactile experiences; acoustics and noise control influence stress levels and concentration; biophilic design connects to nature, reducing stress; and environmental comfort, including temperature and air quality, impacts well-being. These elements play a crucial role as they interact with sensory perceptions and cognitive processes, enabling architects and designers to craft spaces that optimize cognitive function and emotional well-being by aligning with the brain's innate tendencies and capacities [7]. Research demonstrates Neuroarchitecture's benefits in healthcare, reducing pain, stress, and anxiety medication use, and enhancing patient and staff satisfaction [8, 9]. Neuroimaging reveals the Para-hippocampal place area's role in processing and storing information, intensifying in response to specific places and visual scenes [6].

As mentioned above, the occupational stress among healthcare workers is a significant concern [10], and the situation in our country is not an exception. Hence, this study aims to corroborate the following hypothesis: "There are differences in psychological stress among medical personnel, as measured by skin impedance when observing Neuroarchitecture in comparison to Conventional Architecture at the Guadalupe Victoria Maternal and Child Hospital in Atizapan de Zaragoza". To achieve this, measures regarding stress response through galvanic skin impedance (GSR), aka electrodermal activity (EDA), and Likert-type questionnaires like Depression, Anxiety and Stress Scale - 21 Items (DASS-21) were employed as they have shown to provide valuable insights into anxiety, depression, and stress levels.

2 Materials and Methods

A system was developed to measure skin impedance using an impedance sensor as well as to showcase virtual reality videos created with Conventional Architecture and Neuroarchitecture, aiming to provide visual representation of the investigated environments. At the end the DASS-21 questionnaire was administered to obtain levels of depression, anxiety, and stress experienced by the medical personnel at the Guadalupe Victoria Maternal and Child Hospital in Atizapan de Zaragoza. The following sections details the developed system, data acquisition and data analysis performed in this study.

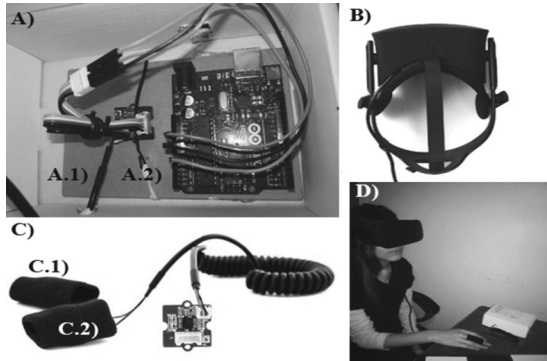


Fig. 1. In section A, the sensor (Grove - GSR Sensor) connected to the Arduino is observed. Section B shows the virtual reality glasses (Oculus Rift), section C displays the sensor with electrodes, and section D depicts the sensor and VR glasses placed on the user.

2.1 System Development

Skin impedance measurement was conducted using the Grove - GSR sensor (Seed Studio, Shenzhen, China), which measures skin impedance connecting two electrodes to different fingers. It is well-known that skin conductance, or impedance, directly provides information about human emotional behavioral regulation, justifying its use for stress detection applications. The sensor sends the signal as voltage to an Arduino UNO board (Arduino, New York, USA), where the voltage is converted into impedance.

Physically, the used Grove - GSR sensor, shown in Fig. 1A, was connected to two nickel electrodes (labels A.1 and A.2). Additionally, as shown in Fig. 1B, virtual reality goggles (Oculus Rift, California, USA) were used to show a video of Conventional Architecture and a video with Neuroarchitecture in hospitals. To conduct the study, the nickel electrodes were inserted into a pair of elastic garments, shown in Fig. 1C and labels C.1 and C.2, to ensure contact with the fingers. Finally, during the study, the sensor electrodes were placed on the middle and ring fingers to measure skin impedance while videos were presented.

To create the architectural environments, virtual reality videos were download, showcasing Neuroarchitecture and Conventional Architecture in hospitals. The videos were sourced from the websites of Hospital Serena del Mar in Colombia (Fig. 2, labels A, C, E, G) and Hospital General 450 in Mexico (Fig. 2, labels B, D, F, H). The videos were randomly played for participants using the virtual reality headsets, and the skin impedance measurements were taken while they were exposed to each environment.

2.2 Data Acquisition

This non-randomized experimental study compares the psychological stress response of medical personnel when observing Neuroarchitecture in hospitals versus Conventional Architecture. Three physicians and 25 nurses ($N = 28$) aged between 25 and 45 years, who are part of the medical staff at Guadalupe Victoria Maternal and Child Hospital in Atizapan de Zaragoza, with an 8-h work shift from 7:00 am to 3:00 pm, Monday to

Friday, and with 2 to 10 years of work experience at the hospital, were selected. The medical staff from the Neonatal Intensive Care Unit (known as UCIN in Mexico), Neonatal Intermediate Care Unit (known as UTIN in Mexico), and Labor and Delivery (known as Tococirugía in Mexico) provided their support. Inclusion criteria were the acceptance and signing of the informed consent letter by the medical personnel. Exclusion criteria included individuals who were unable to tolerate the test. Ethical considerations were addressed throughout the study, ensuring the dignity and rights of the subjects. Confidentiality of information and data was guaranteed, and informed consent was obtained from the medical personnel. The study adhered to the standards established in the General Health Law for Health Research in Mexico.

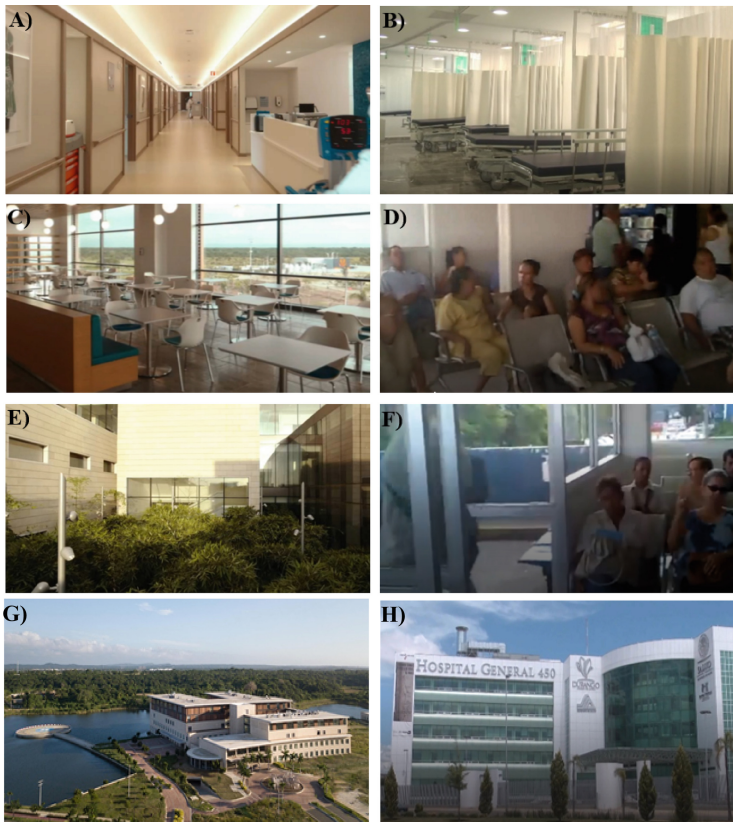


Fig. 2. Hospitals with Neuroarchitecture and Conventional Architecture: A), B) Hospitalization Spaces; C), D) Waiting Areas; E), F) Green Areas; G), H) Exterior Views of Both Hospitals, Serena del Mar Healthcare Center (A), C), E), G)) and Hospital General 450 in Durango (B), D), F), H)).

2.3 Data Analysis

The collected data were analyzed using descriptive statistics, including box plots to visualize the distribution of skin impedance data. The data from the DASS-21 questionnaire were also analyzed to determine the levels of depression, anxiety, and stress in the medical personnel. This analysis provided information on the impact of Neuroarchitecture on the mental health of medical staff. Statistical analysis was performed using R Studio Ver. 1.4.1703 (RStudio, Inc., Boston, MA, USA), to evaluate the difference in skin impedance levels between the two hospital environments. For each impedance signal, the last 30 s of each signal were analyzed, considering that a transition from one psychological state to another had already occurred at that point. Finally, these values were averaged for each subject. An unequal variance t-test was conducted on dependent samples with a significance level of $p < 0.05$, and a left-tailed hypothesis to determine whether the two groups had a statistically significant difference in terms of their mean skin impedance values.

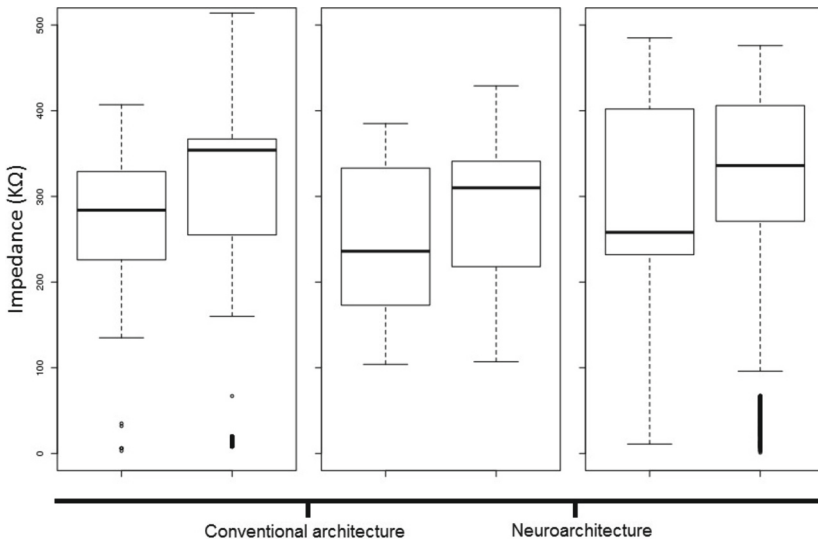


Fig. 3. Mean differences obtained in: A) Tococirugía, B) UCIN, and C) UTIN. All graphs (x-axis) depict the comparison between conventional architecture and neuroarchitecture, while the y-axis represents the change in impedance, using the same scale for all graphs.

3 Results

The results of the test to verify if there was a difference in skin impedance between subjects exposed to Neuroarchitecture and Conventional Architecture environments were found to be the following.

For the Tococirugía data, as shown in boxplots from Fig. 3A, a statistically significant difference was observed ($t = -64.699, p = [2.2 \times 10](-16)$) in the average

skin impedance between neuroarchitecture and conventional environments. The average impedance in the Neuroarchitecture environment was $355K\Omega$, while in the conventional environment, it was $287K\Omega$.

Regarding the results for the UCIN data, shown in Fig. 3B, a significant difference ($p = [2.2 \times 10](-16)$) in the average skin impedance between the two environments was also found. In this case, the average impedance in the Neuroarchitecture environment was $302K\Omega$, while in the conventional environment, it was $230K\Omega$.

Finally, for the UTIN data, shown in Fig. 3C, a statistically significant difference ($p = [2.2 \times 10](-16)$) in the average skin impedance was also observed between the neuroarchitecture and conventional environments. The average impedance in the Neuroarchitecture environment was $377K\Omega$, while in the conventional environment, it was $235K\Omega$.

Table 1 summarizes the results regarding the DASS-21 questionnaire. They indicate that 14.3% of the medical personnel in the Hospital presented normal levels of stress, followed by 21.5% for mild, 53.5% for moderate, and 10.7% for severe. Also, they indicate that 14.3% of the medical personnel in the Hospital presented normal levels of anxiety, followed by 46.4% for mild, 35.8% for moderate, and 3.5% for severe. Finally, for the depression section of the DASS-21 questionnaire indicates that 21.5% of the medical personnel presented normal levels of depression, followed by 50% for mild, 25% for moderate and 3.5% for severe. These results suggest a higher stress prevalence than anxiety and depression in the three evaluated clinical services.

Table 1. DASS-21 scores.

Percentage of Incidents					
Symptomatology	Normal	Mild	Moderate	Severe	Extremely severe
Stress	14.3%	21.5%	53.5%	10.7%	0
Anxiety	14.3%	46.4%	35.8%	3.5%	0
Depression	21.5%	50%	25%	3.5%	0

4 Discussion

This study examined the relationship between hospital architecture and the physiological response of healthcare workers using skin impedance measurements. The results indicated that Neuroarchitecture environments influenced the psychological stress and average skin impedance in the Tococirugá subjects. The higher impedance observed in the Neuroarchitecture environment may be attributed to its design factors aligned with Neuroarchitecture principles [10]. These findings align with previous studies suggesting that Neuroarchitecture-built environments positively impact sensory experience and well-being [11, 12].

However, this study had limitations, including a small sample size and focus on a single Tococirugá service in a specific hospital. Factors such as age, specific medical conditions, and patient stress were not evaluated, which could influence skin

impedance. Further research should assess each Neuroarchitecture factor independently and explore whether their combination contributes to the observed statistical difference. Larger-scale investigations in diverse hospitals, considering these factors, are recommended to enhance understanding of the influence of Neuroarchitecture environments on psychological stress and their potential association with skin impedance.

Furthermore, the results in subjects working in UCIN and UTIN services were very similar to those obtained in Tococirugía. Therefore, we believe that regardless of the clinical area in which this study is conducted, the results will be consistent with our findings in Tococirugía. It worths noting that, we believe that the results of UCIN and UTIN present the same limitations as the Tococirugía study.

The results of the DASS-21 questionnaire highlight the importance of addressing psychological stress in healthcare personnel in the UCIN, UTIN, and Tococirugía services. However, particularly in the UCIN, the results showed a higher prevalence of psychological stress. We believe that the stress experienced by the subjects in this service is due to the emotional burden of caring for critically ill patients, as well as the physical demands involved [13], which may contribute to higher levels of stress compared to other areas. Therefore, since these hospitals are unlikely to change their architecture from conventional to Neuroarchitecture, we believe it is necessary to implement stress management strategies and provide appropriate psychological support to ensure the well-being of healthcare personnel.

Moreover, it worths highlighting that, although the results showed that stress was the most prevalent condition in all three services, significant levels of anxiety and depression were also observed. Therefore, we believe that it is necessary to comprehensively address the mental health of healthcare professionals by offering courses and workshops that address psychological stress, anxiety, and depression in this population. Finally, we acknowledge that a limitation of the study with the DASS-21 questionnaire is the lack of a control group, and we believe it is necessary to include one in future studies.

Results emphasize addressing stress, anxiety, and depression through tailored interventions and psychological therapies to improve mental health [14]. Additionally, we believe it is necessary to provide Special attention needed for individuals with severe conditions.

5 Conclusion

This study provides evidence that Neuroarchitecture can have a positive impact on reducing stress among healthcare personnel compared to a hospital with conventional architecture. These findings are important as stress can significantly affect the quality of care provided by medical staff to patients.

Moreover, building on the Neuroarchitecture perspective, a set of overarching recommendations comes to the fore. These recommendations, guided by the essence of Neuroarchitecture, have the potential to reshape hospital spaces. Ranging from the incorporation of calming design elements, such as nature-inspired motifs and aesthetically pleasing color palettes, to optimizing spatial arrangements that promote relaxation.

Furthermore, this study suggests that biomedical engineers, architects, and designers involved in hospital construction should consider incorporating Neuroarchitecture principles when designing a hospital.

References

1. Osorio, J.E., Cárdenas Niño, L.: Estrés laboral: estudio de revisión [Work stress: a review study]. *Diversitas: Perspectivas en Psicología*, 13(1) (2017). <https://doi.org/10.15332/s1794-9998.2017.0001.06>
2. Thase, M.E., Weisler, R.H., Manning, J.S., Trivedi, M.H.: Utilizing the DSM-5 anxious distress specifier to develop treatment strategies for patients with major depressive disorder. *academic highlights. J. Clin. Psychiatry* (2017). <https://www.psychiatrist.com/jcp/psychiatry/utilizing-the-dsm-anxious-distress-specifier-to-develop-treatment-strategies-for-patients-with-major-depressive-disorder/>
3. Villavicencio, E.: Work overload is a product of the work culture that prevails in the country, as stated by Erika Villavicencio, a researcher at the highest school of studies. En *Breaking News*. Recuperado de (2022). <https://www.infobae.com/en/2022/04/15/unam-mexicans-are-the-most-stressed-people-in-the-world-unam/>
4. Joshi, K., Modi, B., Singhal, S., Gupta, S.: Occupational Stress among Health Care Workers. Submitted: August 22nd, 2022. Reviewed: August 25th, 2022. Published: October 3rd, 2022 (2022). <https://doi.org/10.5772/intechopen.107397>
5. Schneiderman, N., Ironson, G., Siegel, S.D.: Stress and health: psychological, behavioral, and biological determinants. *Annu. Rev. Clin. Psychol.* **1**, 607–628 (2005). <https://doi.org/10.1146/annurev.clinpsy.1.102803.144141>. PMID:17716101.PMCID:PMC2568977.NIHMSID:NIHMS70622
6. Ghamari, H., Golshany, N., Naghibi Rad, P., Behzadi, F., Trousselard, M., Barragán Martín, A.B.: Neuroarchitecture assessment: an overview and bibliometric analysis. *Eur. J. Investig. Health Psychol. Educ.* **11**(4), 1362–1387 (2021). <https://doi.org/10.3390/ejihpe11040099>. PMID:34842658.PMCID:PMC8628715
7. García Espinosa, S., García Aguilar, A.E.: Neuroarquitectura: Un campo fértil, más allá de las fronteras disciplinares. *Milenaria, Ciencia y Arte*, 9(14), julio-diciembre. Recuperado de file:///C:/Users/TanyRocio/Downloads/Milenaria14_Art11_27-29.pdf (2019)
8. Kellert, S.R.: Building for health: implications of neurobiological research for architectural design. *J. Biourban.* **1**(1), 5–18 (2012)
9. Ulrich, R.S., et al.: A review of the research literature on evidence-based healthcare design. *HERD: Health Environ. Res. Des. J.* **1**(3), 61–125 (2008). <https://doi.org/10.1177/193758670800100306>
10. Martínez, R.J.: Aplicación de los principios de la neuroarquitectura para el diseño de un centro de atención para dependiente a sustancias psicoactivas en la provincia de Trujillo en el 2019 (Tesis de licenciatura). Repositorio de la Universidad Privada del Norte. Recuperado de (2020). <https://hdl.handle.net/11537/2432311>
11. Guzmán Vergara, D.P.: Vivienda Psicológicamente Saludable para Ciudades Más Humanas: Luz Natural en Espacios Emocionantes, Enfoque Desde la Neuroarquitectura [Psychologically Healthy Housing for More Human Cities: Natural Light in Exciting Spaces, an Approach From Neuroarchitecture]. (Doctoral dissertation). Pontificia Universidad Católica de Chile, Chile. (ProQuest Dissertations Publishing No. 30160018)12 (2022)
12. Mora Atehortúa, M.P.: Arquitectura Hospitalaria un Renacer Sensorial desde la Neuroarquitectura. *Hospital Architecture: A Sensory Rebirth from Neuroarchitecture* (Master's thesis). Universidad Piloto de Colombia, Facultad de Arquitectura, Programa de Arquitectura y Artes, Bogotá, Colombia (2021). Retrieved from <http://repository.unipiloto.edu.co/handle/20.500.12277/11336> 13
13. Acosta Arista, J.M.: Criterios de la Arquitectura Biofílica: Opción para el bienestar de los pacientes del Área de Internamiento del Hospital Regional Eleazar Guzmán Barrón–Nuevo Chimbote [Biophilic Architecture Criteria: an Option for the Well-being of Patients in the

- Inpatient Area of the Eleazar Guzmán Barrón Regional Hospital-Nuevo Chimbote] (Master's thesis) (2021). Retrieved from <https://hdl.handle.net/20.500.12692/68607>
14. Tolsa, M.D., Malas, O.: COVID-19: Impacto Psicológico, Factores de Riesgo e Intervenciones Psicológicas en el Personal Sanitario. *Revista Iberoamericana de Psicología y Salud*, **12**(2), 58–75 (2021). <https://doi.org/10.23923/j.rips.2021.01.045>



Implementation of QR Codes on Medical Equipment as a Tool for Hospital Management

Quetzalli Hidalgo¹(✉), Sergio Camacho¹, Bersain Reyes¹, and Miguel Fuentes²

¹ School of Sciences, Autonomous University of San Luis Potosí, 78295 San Luis Potosí, Mexico
A281054@alumnos.uaslp.mx

² Biomedical Engineering Department, Guadalupe Victoria Maternal and Child Hospital, 52918
Atizapan de Zaragoza, Mexico State, Mexico

Abstract. This work focused on enhancing the management of medical equipment in a hospital by utilizing Quick Response (QR) codes and a customized database. For this purpose, a MySQL database was established, containing comprehensive information about the available medical equipment within the hospital. Additionally, a Graphical User Interface (GUI) connected to the database was developed, enabling data editing, maintenance date updates, and QR code generation for each individual equipment. These QR codes were affixed to the medical equipment to facilitate easy tracking and organization. An experiment was conducted to demonstrate the efficiency of QR code utilization as compared to manual information retrieval. Throughout the experiment, challenges such as limited knowledge regarding equipment location and restricted database access were also identified. Technical solutions were proposed to enhance the connectivity between mobile devices and the hospital's database. Overall, the implementation of the QR code and database-driven approach significantly improved the medical device management system's organization, enabling efficient maintenance and precise tracking of equipment locations.

Keywords: Health Technologies · Medical Equipment · QR Code

1 Introduction

Proper management of medical equipment is crucial to ensure the safety and effectiveness of healthcare services. Improper use of these equipment can have serious consequences and impact the quality of medical care. In Mexico, there is a need to improve the management of medical equipment, as risks such as equipment unavailability, safety issues, and their incorrect location have been identified. To address these challenges, technological solutions such as the use of QR codes and NFC chips have been proposed [1].

QR (quick response) codes are information carriers that can be scanned using a camera-enabled mobile device, making them practical and cost-effective. On the other hand, NFC (near field communication) chips enable short-range wireless communication and are considered secure for transmitting data between devices. These technologies can enhance the management of medical equipment by providing detailed information and

facilitating staff training [2]. In an experiment conducted at the Medical University of Shanxi in Taiyuan, China, it was demonstrated that the use of electronic manuals with QR codes improved data search and training, as well as equipment utilization and satisfaction by healthcare personnel. This finding suggests that QR codes are a viable and cost-effective option when compared to NFC chips [3].

In this study, research was conducted on the implementation of a medical equipment management system using QR codes at a Hospital in Atizapán de Zaragoza, Mexico, with an inventory of 408 medical equipments. The aim of the study was to improve organization and prevent adverse events and was prompted by recognizing issues with the manual and impractical process of information retrieval for order filling. The Biomedical Engineering Department (BMED) oversaw the implementation of a computerized management graphical user interface (GUI) to handle medical equipments, including the incorporation of new equipment, maintenance, and inventory control.

2 Materials and Methods

2.1 Design and Implementation of the System

The implemented medical equipment management system consisted of a database, a GUI, and QR codes affixed to the medical equipment. The relationship between these three components is shown in the flowchart of Fig. 1, and their design and implementation are described below.

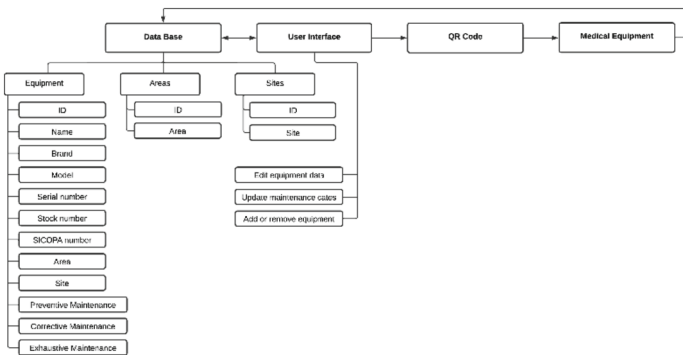


Fig. 1. Flowchart illustrating the components and workflow of the proposed medical equipment management system, showcasing the database, GUI, and QR code integration for efficient equipment tracking and maintenance.

First, a Structured Query Language (MySQL) database, managed using the php-MyAdmin software tool (PhpMyAdmin, Gifhorn, Germany), was established to gather information about medical equipment within the hospital. The database contained essential details of each of the 408 registered medical equipments, including their ID, name, brand, model, serial number, inventory number, asset control number (SICOPA number from the State of Mexico’s web-based asset control system), area, and location. Additionally, it recorded the scheduled dates for upcoming preventive or corrective maintenance

or, alternatively, the date of the most recent maintenance performed on the respective equipment. The database was designed with three tables: 1) Equipment, 2) Areas, and 3) Sites. As medical equipment is assigned to specific areas and sites, the Areas and Sites tables were created to track existing areas and sites. These tables were interconnected with the Equipment table, as depicted in Fig. 1, as each piece of equipment must be associated with a designated area and site.

Regarding the GUI, it was developed using the Java programming language and the NetBeans platform (NetBeans, Menlo Park, CA, USA). The GUI was linked to the aforementioned database, enabling access to and modification of stored information. Functionalities of the GUI encompassed editing medical equipment data, updating maintenance schedules, adding or removing equipment, and generating QR codes. Illustrated in Fig. 1, the bidirectional connection between the database and the GUI facilitated information retrieval from the database and allowed data modification within the GUI.

The GUI's distinctive feature involved generating a unique QR code for each medical equipment. These QR codes encapsulated information authorized by the Biomedical Engineering Department (BMED) is head to be easily displayed to hospital personnel, including ID, name, brand, model, serial number, inventory number, SICOPA number, area, and location. These generated QR codes consisted solely of text. When scanned using a QR code reader application, the text within the code appeared on the device's screen (be it a smartphone or tablet) without necessitating an internet connection. It is noteworthy that the QR code implementation aimed to enhance medical equipment organization and tracking within the hospital. Consequently, generating unique QR codes for each medical equipment facilitated straightforward scanning using any mobile phone or tablet, eliminating the requirement for an internet connection (Wifi, GSM, 3G, 4G, or 5G). This proves particularly advantageous within a hospital environment where consistent access to a stable internet signal might be restricted.

Ultimately, the QR codes generated by the GUI were printed and affixed to each medical equipment using label paper, and an additional transparent adhesive protective layer was applied to prevent damage during cleaning.

Access to the GUI is exclusively granted to the BMED personnel. They are authorized to generate QR codes for any hospital equipment and update the database. The GUI is accessible solely from the BMED computer and is supervised by the department head.

2.2 Experiment

A randomized experiment was conducted to test whether the time taken to complete a service order using the implemented system via QR code offers an advantage compared to manual filling, that is, without using the implemented system. For this purpose, fifteen volunteers ($n = 15$) from the BMED were recruited. Inclusion criteria were subjects involved in preventive and corrective maintenance services for medical equipment, with 3 to 5 months of work experience, on the morning shift, as the hospital's BMED operates only during the morning shift, and all participants were interns. Exclusion criteria were subjects not involved in these services, and non-inclusion criteria were subjects who had to withdraw from the experiment for any reason. No personal information was requested from them. For each volunteer, the time required for each procedure, that is, information retrieval with and without QR codes, was measured. Finally, the obtained data were

compared using a Welch’s t-test ($\alpha = 0.05$), using R Studio software Ver. 1.4.1703 (RStudio, Inc., Boston, MA, USA).

3 Results

3.1 Implemented System

The final database comprises three tables: Equipment, Areas, and Sites. These tables store pertinent details about each piece of equipment, including the scheduled date for its next preventive and comprehensive maintenance. Figure 2 illustrates the connection between the Areas and Sites tables to the Equipment table, allowing the creation of a dropdown menu that enables users to choose from existing areas and sites within the hospital. This functionality streamlines the process of selecting and associating equipment with specific areas and sites within the hospital.

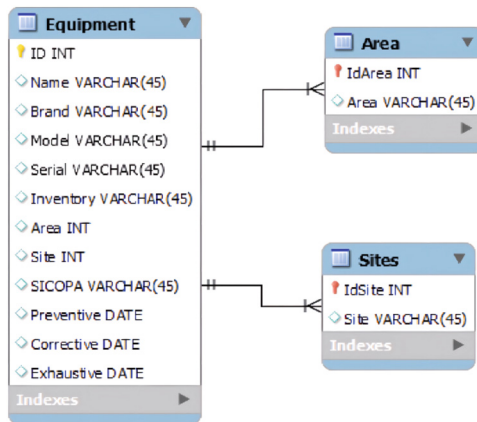


Fig. 2. Diagram illustrating the structure and relationships of the database, showcasing the Equipment, Areas, and Sites tables.

Regarding the implemented GUI via NetBeans, it offered seamless and efficient access to the information stored in the database. The bidirectional connection between the database and the user interface allows for timely updates of the information. Figure 3 displays a screenshot of the implemented GUI, showcasing the interface design and the buttons utilized for various functionalities.

Hospital Inventory

ID	Name	Brand	Model	Serial	Inventory	Area
338	MONITOR DESFIBRILADOR	WEINMANN	MEDUCORE STA...	3671	1E216960642017	AMB...
339	NEBULIZADOR ULTRASONIC...	SAN-UP	3060	62891	1E216960642017	AMB...
348	OXIMETRO DE PULSO	NONIN	2500	502112249	1E216960642017	AMB...
373	TERIOMETRO	MICROLIFE	FR1DM1	291609263	1E216960642017	AMB...
1	AGITADOR DE PLAQUETAS	I SERIES	HELMER	999582	2E7960642011	BAN...
36	BASCULA MECANICA CON ES...	SECA	700	5700112112694	2E140860642011	BAN...
105	CENTRIFUGA REFRIGERADA ...	THERMO SCI...	CRYOFUGE 5500I	41167185	2E11460642011	BAN...
106	CENTRIFUGA SEROLOGICA P...	CLAY ADAMS	SERO-FUGE 2002	4780039	2E11560642011	BAN...
113	CONGELADOR DE PLASMA	SMEG	C25V140C6/C3PL...	C3PL92	2E526460072012	BAN...
118	CONGELADOR PARA PLASMA	THERMO SCI...	FORMAFFFF123...	117591501101...	2E11760642011	BAN...
171	ESFIGMOMANOMETRO ANER...	RIESTER	BIG BEN SQUARE	90622457	2E8560642011	BAN...
187	ESFIGMOMANOMETRO ANER...	WELCH ALLYN	TYCO	90723080436	2E85260642011	BAN...
361	REFRIGERADOR PARA BANC...	REFRIMED	RBACDV-12	1210-198-03-0...	2E37260642011	BAN...
363	REFRIGERADOR PARA MEDI...	REFRIMED	RVCCDV-10	1210-198-03-0...	2E143180642011	BAN...
368	REFRIGERADOR VERTICAL I...	METALFRIO	REB250	2117873	2E175960642011	BAN...

ID:
 QR Code:

Equipment:

Brand:

Model:

Serial:

Inventory:

Area:

Site:

SICOPA:

Preventive Maintenance:

Last Corrective Maintenance:

Exhaustive Maintenance:

Fig. 3. GUI showcasing the intuitive design and user-friendly interface. The GUI provides seamless navigation and access to various functionalities, including equipment registration, and maintenance scheduling.

Implementation and deployment of QR codes generated from the database information has allowed for more precise tracking of medical equipment. Figure 4 illustrates how QR codes were applied to each piece of medical equipment, enabling easy scanning and retrieval of relevant information. This implementation has streamlined the tracking process, improving efficiency and accuracy in equipment management.



Fig. 4. Deployment of implemented QR codes. Left: The application of QR codes to each piece of medical equipment. Right: The QR code visibly applied on a vital signs monitor, ready for use.

An example of information retrieval using QR codes is depicted in Fig. 5, where the smartphone camera is seen reading the QR code and the obtained information is displayed directly in the mobile device. This information includes all relevant details about the medical equipment. Each QR code can be scanned by any medical staff member to review the equipment's information.

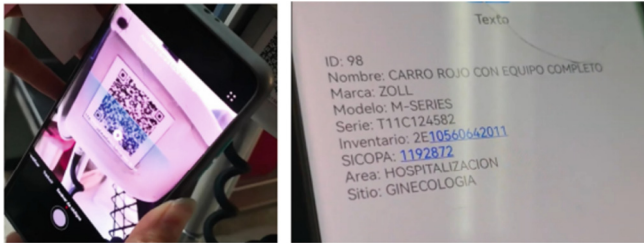


Fig. 5. Scanning of QR codes and information retrieval. Left; The camera of the cellphone scanning the QR code. Right: The information displayed upon scanning the QR code.

3.2 Hypothesis Testing

The resulting data about times required to fill out an order both with and without the use of QR codes is summarized in the box plot of Fig. 6. Statistical analysis via Welch's t -test, considering a 95% confidence level, revealed a mean difference ($t = 2.79$) with a statistically significant difference ($p = 0.0099$) in time taken to fill out a maintenance request form in the experimental group ($\bar{x} = 58.73s$) compared to the mean value in the control group ($\bar{x} = 76.33s$). Additionally, there was less dispersion in the experimental group ($\sigma = 13.57s$) compared to the control group ($\sigma = 20.29s$), as can be noted from

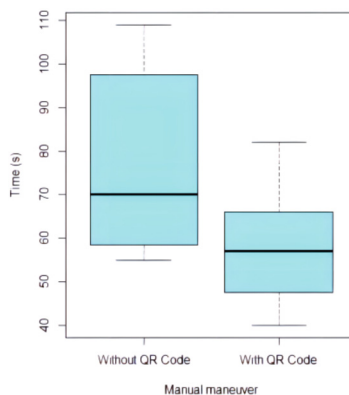


Fig. 6. Distribution of the search times for equipment information without using the QR code and using the QR code strategy. Statistically significant differences ($p = 0.0099$) were observed between the two samples.

Fig. 6. The analysis reveals significant differences between the two samples, indicating that the utilization of QR codes substantially reduces the time required to retrieve equipment information.

4 Discussion

The implementation of QR codes has proven to be effective in improving the efficiency of medical equipment management by providing easy access to relevant information and avoiding confusion [4]. This is particularly relevant for Biomedical Engineering Departments, nurses, and physicians who often struggle with knowing the location of each medical equipment.

The development of the database revealed inconsistencies and missing data in the hospital's inventory, which is a common issue in many hospitals [5]. A thorough inventory review was necessary to determine which equipment was decommissioned, operational, or in storage, among other details. Once the information was correctly established, each medical equipment was registered in the database, including its name, brand, model, ID, inventory number, serial number, asset control number, area, and location.

Regarding the comparison between retrieval information times without QR codes versus with QR codes, the results showed that the use of QR codes significantly improved the speed of recording preventive and corrective maintenance services in the BME Department ($p = 0.0099$). This solution can be particularly beneficial for BME workers as it allows faster and more efficient access to relevant information.

Additionally, the implementation of QR codes has been found to increase accuracy in service order completion. Previously, personnel had to physically search for equipment details or check computer records, which was a time-consuming process prone to errors. By utilizing QR codes, the probability of human errors is reduced as information is directly scanned from the equipment, resulting in less time spent ($\bar{x} = 58.73$ s vs. $\bar{x} = 76.33$ s). Furthermore, the Deputy Head of the BME Department does not have to allocate additional time and resources to review and correct incorrect orders, thereby improving process efficiency. This can have a positive impact on the quality of preventive and corrective maintenance of medical equipment, indirectly affecting patient care. A study published, in the Medical Journal of the Mexican Social Security Institute in 2016, found that delays in maintenance can lead to increased patient waiting times, appointment cancellations, and decreased diagnostic and treatment quality [6]. Thus, timely and efficient maintenance services are crucial to ensure medical equipment is in optimal condition for patient care.

Moreover, it was observed that the personnel in the hospital's BME Department easily adapted to the use of QR code technology to access equipment information. This suggests that implementing this solution can be relatively easy and quick in other hospitals aiming to improve their equipment management.

Despite the advantages of the developed system, two significant obstacles were encountered during the research. First, the hospital did not allow a connection to the database via mobile devices within its network. Additionally, the hospital management objected to the disclosure of maintenance information to avoid potential conflicts with the staff.

We consider that establishing a connection between mobile devices and the hospital's database is feasible. Solutions such as implementing a virtual private network (VPN), using remote access software, or establishing a secure internet connection can be employed. These solutions have been widely used in healthcare environments to ensure data privacy and security [7]. However, implementing the QR code program in the hospital where the internet connection was unstable, and administration personnel did not approve granting access to certain information was not a viable option. Therefore, only the use of QR codes without internet access was implemented at this stage, and the GUI with database connection remained exclusively for the use of the BME Department. Hence, addressing of the main obstacles of this study remains to be explored as future work and represent areas of opportunity for the BME Department.

The promising results of this study suggest that implementing QR codes in the process of completing preventive and corrective maintenance orders can significantly improve efficiency, accuracy, and speed. This solution can be valuable in many hospitals, enhancing the management of medical equipment and positively impacting the quality of preventive and corrective maintenance, ultimately benefiting patient health.

5 Conclusion

The implemented database represents a significant advancement in the management of the hospital's Biomedical Engineering department. Prior to its implementation, the hospital lacked proper organization in its medical equipment records. The database's structure also seamlessly facilitated the integration with the QR code implementation. The utilization of QR codes streamlined data accessibility, enabling efficient tracking of equipment location, and leading to a reduction in maintenance order filling time. This enhancement significantly improved the management and organization of medical equipment within the hospital.

The ability to swiftly access detailed information about each equipment considerably enhanced the accuracy and speed of carrying out preventive and corrective maintenance orders. Additionally, the developed graphical interface is expected to contribute to avoiding confusion and errors during equipment use by offering precise and up-to-date location information.

The comparison between equipment management before and after the implementation of the database and QR code system revealed a clear improvement in the swiftness and accuracy of the process. These implemented solutions enabled a straightforward and swift tracking of equipment. The convergence of the medical equipment database and QR code application seems to be a promising and practical solution for medical equipment management within hospital settings.



References

1. Kruk, M.E., et al.: High-quality health systems in the Sustainable Development Goals era: time for a revolution. *Lancet Glob. Health* **6**(11), e1196–e1252 (2018). [https://doi.org/10.1016/S2214-109X\(18\)30386-3](https://doi.org/10.1016/S2214-109X(18)30386-3)

2. Lee, S.H., Jung, S.H., Lim, K.Y., Kim, S.W., Hong, J.H.: Practical application of QR code electronic manuals in equipment management and training. *J. Biomed. Res.* **16**(2), 82–87 (2015)
3. Ma, L., Mu, Y., Wei, L., Wang, X.: Practical application of QR code electronic manuals in equipment management and training. *Front. Public Health* **9** (2021). <https://doi.org/10.3389/fpubh.2021.726063>
4. Mishra, D., Mishra, A.: Access control mechanism for healthcare information system. *Int. J. Comput. Sci. Inf. Technol.* **6**(3), 3033–3036 (2015). <https://doi.org/10.5281/zenodo.1071594>
5. Adams, R.J., Smart, P., Huff, A.S.: Improving inventory accuracy in hospitals. *Int. J. Oper. Prod. Manag.* **37**(3), 301–322 (2017). <https://doi.org/10.1108/IJOPM-08-2015-0465>
6. Gómez Moreno, F.C., Márquez Vega, M.C., Martínez Martínez, A.: Importance of maintenance of medical equipment in healthcare institutions. *Revista Científica de la Sociedad de Enfermería Neurológica de la Asociación Madrileña de Enfermería* **44**(3), 39–45 (2016)
7. Wong, M.C., Gao, R.X.: Remote access to healthcare databases: a review of existing technologies and their potential security implications. *J. Med. Syst.* **39**(9), 88 (2015). <https://doi.org/10.1007/s10916-015-0288-8>



Examining the Impact of Academic Degree Level on Misinformation Levels Regarding the COVID-19 Pandemic in Mexico: A Social Media Perspective

Sarahi Alvarez^(✉) , Sergio Camacho , and Bersain Reyes 

School of Sciences, Universidad Autónoma de San Luis Potosí, 78295 San Luis Potosi, Mexico
A282737@alumnos.uaslp.mx

Abstract. The dissemination of misinformation on social media during the pandemic has had a significant impact on people's perception, leading to misconception in terms of healthcare actions and treatments. This study is aimed to investigate the relationship between academic degrees and the level of misinformation on social media during the COVID-19 pandemic. A scientifically validated survey was used to evaluate data from $N = 101$ volunteer participants on aspects such as monthly income, academic degree, internet, and social media usage habits, as well as true and false questions about COVID-19 facts. The results revealed a relationship between academic degree level and the belief in false news related to the pandemic; where 75% of the doctoral level population identified fake news in contrast to those at the primary and secondary levels, which obtained 37.5% and 39.58% respectively. Ultimately, this study could provide insights about how the Mexican population learn on social media and how strategies can be implemented to foster a better understanding of the COVID-19 pandemic, and more importantly in future ones.

Keywords: Fake News · COVID-19 · misinformation · academic degree

1 Introduction

Currently, access to health information is relatively easy, but the spread of fake news on social media has led to a decline in the quality of such information [1]. During the COVID-19 pandemic, an “infodemic” occurred where a large amount of true information and rumors were disseminated, making it difficult for the population to make accurate decisions [1].

Society behavior and decision-making are influenced by emotions, and in the context of the infodemic generated by COVID-19, the excess of data and images on social

Sarahi Alvarez—Collected and interpreted the results

Sergio Camacho—Devised and designed the study

Bersain Reyes—Writing review and analyzed the data

© The Author(s), under exclusive license to Springer Nature Switzerland AG 2024

J. de J. A. Flores Cuautle et al. (Eds.): CNIB 2023, IFMBE Proceedings 97, pp. 250–256, 2024.

https://doi.org/10.1007/978-3-031-46936-7_27

media instilled fear in people worldwide [2, 3]. Individuals tend to acquire and share the information they find appealing, which may include false information. Over the years, information manipulation has established behavioral patterns in society, and during the pandemic, the flow of manipulated information destabilized society and generated panic [4, 5].

On social media, persuasive ideas and false rumors related to COVID-19 were widely spread, e.g., ineffective home remedies and conspiracy theories about vaccines. It is worth highlighting that some individuals considered these irrational ideas as true, leading to vaccine hesitancy once vaccines became available [6–8].

Several studies in different countries, such as Mexico, Peru, and Brazil, have identified social media as the main means to spread misinformation, especially through images. Particularly in Mexico, UNAM carried out an investigation where they conducted a survey, and participants indicated that their information-seeking arose from the uncertainty generated by their lack of knowledge about the virus [9]. They also mentioned that they shared the information with their acquaintances to keep them informed. In Peru, a similar study was conducted, in which it was discovered that misinformation originated on social media [3]. In Brazil, it was found that even before a positive case was reported in the population, they were already seeking answers about what was happening in China [10]. For instance, on the YouTube platform, a wide variety of content related to vaccine development was shared, leading to vaccine hesitancy in some individuals. Unfortunately, society tends to pay more attention to content produced by artists rather than the content shared by health authorities [11].

The lack of effective connection between public institutions and the media caused people to seek alternative sources of information, where they found content opposing health measures and generating a rejection of health recommendations [12].

This study is aimed to explore the possible relationship between individuals with different academic degrees and their belief in false information, and thus shedding light on the understanding about how these factors can influence the dissemination and acceptance of misinformation. To this end, a survey-based study was conducted to determine if there was an influence of the information presented on social media on the perception of the COVID-19 pandemic. The survey was applied to $N = 101$ volunteers with a vast diversity of academic degrees.

2 Materials and Methods

The abovementioned questionnaire was structured as follows (Fig. 1). First, a question was asked about age with four possible answers (Fig. 1a). Next, a question was posed regarding the academic degree level, ranging from primary education to doctorate degree (Fig. 1b). Then, a question about monthly income (MI) was asked, considering the three types of income that subdivide the economic classes according to the National Institute of Statistic and Geography of Mexico, INEGI (Fig. 1c).

Subsequently, information about the participants' work sector was obtained, including the type of job and income (Fig. 1d). Following that, a question about the source of information was asked (Fig. 1e), a question to determine if participants use the internet (Fig. 1f), and further inquiries were made about their use of social media and which platforms they use (Fig. 1g).

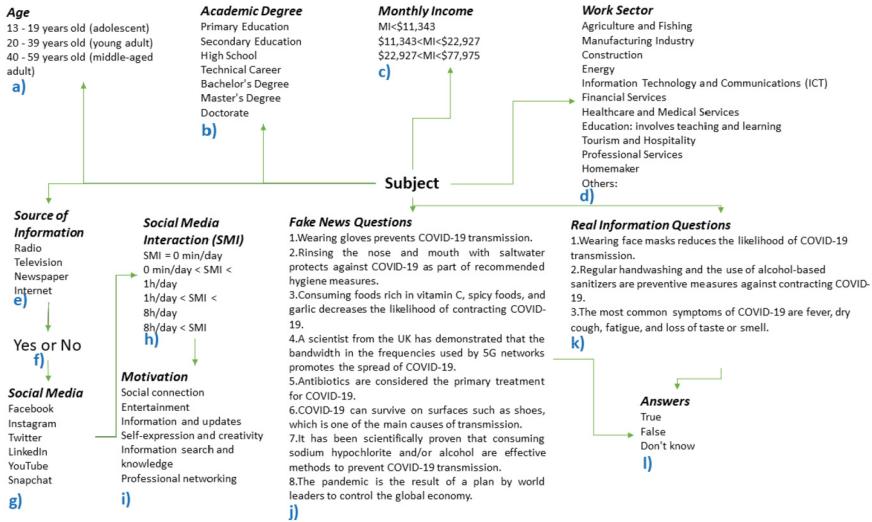


Fig. 1. Questionnaire related to fake news.

Afterwards, participants were asked about their daily interaction time spent on social media (Fig. 1h). Then, a question was posed about the motive behind their social media interaction (Fig. 1i). Finally, at the end of the questionnaire, eight false questions (Fig. 1j) and three true questions (Fig. 1k) about COVID-19 were included, for which the response options were “true,” “false,” or “I don’t know” (Fig. 1l).

The validation of the survey involved five experts with a doctoral degree in medical sciences who had worked with patients affected by COVID-19 during the pandemic. This validation process consisted of sending them the survey after designing and developing it, for them to make corrections. These corrections included modifications, deletions, and even the addition of clauses and questions. After receiving the initial feedback, adjustments were made, and the survey was sent back to them for final approval.

The survey was conducted using the digital platform Google Forms (Google LLC, Mountain View, CA, USA) and was distributed across different groups through the messaging application WhatsApp (Meta, Menlo Park, CA, USA). A total of $N = 101$ volunteers participated in this study, and their responses were captured and stored for subsequent analysis. During the analysis, the data were categorized by age, economic level, and academic degree of the participants. “False,” “true,” and “do not know” responses were grouped and organized considering the economic level and academic degree. Finally, percentages were calculated, and the results were summarized in tables.

3 Results

The survey results showed the participation of nine adolescents (aged 13–19 Y.O.), 70 young adults (aged 20–39 Y.O.), 19 middle-aged adults (aged 40–59 Y.O.), and three elderly adults (over 60 Y.O.) who completed the survey; of which the participation of 1 person with primary education, 6 of secondary education, 11 of upper secondary

education, 3 of technical career, 58 of bachelor's level, 11 of master's level and 11 of doctoral level was registered. Economic income was grouped into three proposed salary ranges; where 45 subjects reported earning $MI < \$11,343/\text{month}$, 24 subjects reporting income $\$11,343 < MI < \$22,927/\text{month}$, 26 subjects had a salary range of $\$22,900 < M < \$77,975/\text{month}$, and 6 subjects who did not provide income information. All the MI are reported in Mexican peso. These findings demonstrate the diversity of the participant group in terms of age, academic degree, and income, providing a broad and representative view of the analyzed sample.

Table 1 summarizes the survey results about the interaction of subjects by academic degree with social media. These findings highlight the significance of the internet as an information source and the engagement of the study participants on social media, with notable variations in the percentage based on the subjects' academic degree; the groups ranging from primary school, secondary school, high school, technical career, bachelor's, master's, to doctorate (100%, 66.6%, 100%, 0%, 93.1%, 70%, and 90% respectively) interact on social media. Additionally, these results reveal that the use of social media during work hours is common among participants, with entertainment being the primary motive for social media browsing across most academic degree levels. However, notable differences are observed, such as the use of social media for information seeking, particularly among participants with a doctoral degree.

Table 1. Interaction of subjects by academic degree with social media ($N = 101$).

Academic Degree	Sources of information				Interaction on social networks		Time on social networks			Reason for browsing social media						
	Radio	Television	Internet	Newspaper	Yes	No	Does not use them	t<1h	1h<t<8h	8h<t	SC	E	I	SE&C	KSR	PN
Elementary school	0	0	1	0	1	0	0	0	1	0	0	0	1	0	0	0
Middle school	0	0	6	0	4	2	0	1	4	1	2	4	0	0	0	0
High school education	0	0	11	0	11	0	0	1	8	2	1	9	0	0	1	0
Technical career	0	0	3	0	0	3	0	0	3	0	0	1	2	0	0	0
Bachelor's degree	0	0	58	0	54	4	1	6	45	6	2	39	9	1	6	1
Master's degree	1	0	10	0	7	4	3	2	6	0	0	5	3	0	2	1
Doctorate	0	2	9	0	10	1	1	6	4	0	0	3	5	0	3	0

SC = Social Connection, E = Entertainment, I = Information, SE&C = Self-expression and Creativity, KSR = Knowledge Seeking and Research, PN = Personal Networking.

The results from Table 2 indicate association between economic incomes and responses to true and false questions about Covid-19, with notable performance among those with medium and high incomes. It is important to highlight that there was a percentage of participants who did not provide information about their salary, and also a percentage of participants who did not respond to certain questions.

Finally, the comparison between the level of academic degree and the responses related to COVID-19 is presented in Table 3. It can be observed that in the responses to false questions, no discernible trend is apparent among those who answered "true" or indicated not having knowledge. However, a significant upward trend is evident from elementary education to doctoral level in the false responses. On the other hand, regarding the responses to true questions, no visible trend is observed in any of the categories: true, false, or unknown.

Table 2. Comparison by economic income vs. responses to COVID-19 questions ($N = 101$).

Income per month	Responses to false questions				Responses to true questions			
	True	False	Don't know	Did not answer	True	False	Don't know	Did not answer
MI<\$11,343	19.67	61.50	18.56	0.28	97.04	2.22	0.74	0.00
\$11,343<MI<\$22,927	10.42	75.52	13.54	0.52	87.50	11.11	1.39	0.00
\$22,927<MI<\$77,975	10.58	74.04	14.90	0.48	69.23	3.85	26.92	0.00
Did not answer	25.53	40.43	34.04	0.00	88.89	5.56	5.56	0.00

Table 3. Comparison by academic degree vs. responses to COVID-19 questions ($N = 101$).

Academic degree	Responses to false questions				Responses to true questions			
	True	False	Don't know	Did not answer	True	False	Don't know	Did not answer
Elementary school	25.00	37.50	37.50	0.00	100.00	0.00	0.00	0.00
Middle school	20.83	39.58	39.58	0.00	88.89	5.56	5.56	0.00
High school education	22.22	56.94	20.83	0.00	100.00	0.00	0.00	0.00
Technical career	22.50	62.50	15.00	0.00	100.00	0.00	0.00	0.00
Bachelor's degree	15.86	71.37	12.33	0.44	99.43	0.57	0.00	0.00
Master's degree	5.68	72.73	21.59	0.00	96.97	3.03	0.00	0.00
Doctorate	6.82	75.00	17.05	1.14	93.94	3.03	3.03	0.00

4 Discussion

The results of this study showed the perception of different demographic groups regarding health information related to the COVID-19 pandemic. These results could inform and serve as a basis for generating communication and health education strategies between health authorities and the population to provide adequate and reliable dissemination of information to all segments of the population.

Additionally, the results of this study seem to emphasize the role of the internet and social media as sources of information in the current context [13]. The findings are partially conclusive regarding internet usage based on participants' academic degrees; the results indicated that using social media during work hours is common, with entertainment being the main motive for browsing social media platforms across most academic degree levels. Therefore, we believe that the findings of this study could contribute to providing a clearer understanding of how people use information during a pandemic situation, which is important for authorities to design communication and education strategies tailored to different educational groups [14].

Regarding the comparison of economic incomes with responses to false questions about COVID-19, the results showed a potential association between economic incomes and responses to both false and true questions about COVID-19. Specifically, it was expected that the group of individuals with lower incomes would answer a higher number of false questions as true, and the other two groups exhibited very similar patterns. Additionally, in responses to false questions marked as false, those with lower incomes

provided the fewest correct answers. Subjects with middle incomes, similar to those with high incomes, responded similarly. These latter two groups exhibited similar response levels. We believe that this is due to the fact that individuals from the middle and upper class possess a higher level of academic education.

In relation to the results indicating that individuals with a elementary school academic degree were more likely to answer false questions as true about COVID-19, we believe that participants at this educational level have less exposure to reliable sources of information, such as official health websites or even research articles, as well as a lower capacity to analyze and evaluate the accuracy of the information they receive. Similarly, the findings showing that participants with a elementary school academic degree answered false questions to a greater extent could be attributed to a lack of knowledge and skills necessary to identify misinformation. Individuals with lower academic degrees may have limited access to formal education, which restricts their ability to develop critical thinking and discernment skills [15]; however, a study with a larger number of subjects at this level is necessary. Additionally, the results seem to demonstrate a decreasing trend in the percentage of false responses to false questions as the educational level increases. This pattern could be attributed to the development of higher levels of critical thinking and the acquisition of competencies that facilitate the ability to distinguish between false and true information. Participants with higher levels of education may possess greater skills to analyze and evaluate the accuracy of information, as reflected in their ability to correctly identify false responses [15].

Regarding responses to true questions, the results seem to show that participants with a primary academic degree, secondary academic degree, and technical career level obtained a 100% correct response rate. This may be related to the content of the questions and the familiarity of these groups with the topic. On the other hand, the groups that answered the true questions as false seem to exhibit an ascending pattern according to the academic degree, with primary, high school, technical career, bachelor's degree, master's degree, and doctoral degree; except at the secondary level, where they answered false to a greater extent to the true questions. This trend may be related to the level of knowledge and analytical skills developed at each academic degree [16].

The results found allowed us to establish that the academic degree is a factor that influences the identification of fake news, however, the lack of answers to some questions posed in the survey limits the interpretation of the results. The sample size is significant, however, if we seek to reach specific population sectors, we could obtain a clearer idea of the impact that the academic degree has on the identification of false news.

It is important to highlight that a fundamental aspect in future work will be to present the participants with real information based on reliable evidence and then administer the same questionnaire again to determine if this modifies their responses.

5 Conclusion

The vast amount of information circulating during the COVID-19 pandemic continues to be bewildering for society. The lack of regulation of content disseminated on social media platforms has generated confusion regarding COVID-19.

This study aimed to highlight the relationship between educational attainment and responses to true and false questions about the COVID-19 pandemic, as well as the crucial

role that critical thinking, access to reliable information, and discernment play in individuals' ability to correctly identify answers. These findings underscore the importance of promoting education and the development of critical skills in society through critical thinking training programs from early stages of education, and by encouraging access to trustworthy sources of information. These measures would contribute to enhancing understanding and response to crisis situations, such as the COVID-19 pandemic, empowering individuals with tools to make informed and well-founded decisions.

References

1. Safarnejad, L., Xu, Q., Ge, Y., Krishnan, S., Bagarvathi, A., Chen, S.: Comparación de las estructuras de difusión de información errónea y verídica en las redes sociales durante una emergencia de salud pública. *Rev. Panam. Salud Publica* **45**, 1–8 (2021)
2. Triviño, N.A.A., Freire, V.M.Z.: Impacto de Twitter en el proceso de construcción de la opinión pública: Pandemia COVID-19 entre marzo y diciembre 2020 en Ecuador. *Rev. Internacional de Cultura Visual* **9**(3), 1–8 (2022). <https://doi.org/10.37467/revvisual.v9.3518>
3. Pichahua, S.: Tipología de los contenidos virales de desinformación durante los primeros meses de emergencia sanitaria por la COVID-19 en el Perú. *Rev. Com.* **21**(2), 197223 (2022)
4. Ramon, F.: Comunicación y noticias falsas en relación al COVID-19: algunas reflexiones sobre la información, la desinformación y propuestas de mejora. *Rev. Esp. Comun. Salud* 253264 (2020)
5. Wanying, X., Yuzhu, T., Zeshui, X., Zhang, X., Dengling, L.: The impact of the infodemic on the stock market under the COVID-19: taking the investors' information infection index as the intermediary variable. *Rev. Tec. Ec. Dev. Eco.* **29**(2), 653–676 (2023)
6. Pérez, C., Velasco, A.M.: Impacto del discurso político en la difusión de bulbos sobre Covid19. Influencia de la desinformación en públicos y medios. *Rev. Lat. Comun. Soc.* 86–119 (2020)
7. Organización Mundial de la Salud. Consejos para la población acerca de los rumores sobre el nuevo coronavirus (2019-nCoV) (2019). <https://www.who.int/es/emergencias/diseases/novel-coronavirus-2019/advice-for-public/myth-busters#cms>
8. Sharma, L.D., Joshi, K.J., Acharya, T.A., Dwivedi, M.G., Sethy, G.B.: Infodemics during era of COVID-19 pandemic: a review of literature. *J. Fam. Med. Prim. Care* **11**, 4236–4239 (2022)
9. González, M.A., Díaz, D., Maldonado, B.V.: Percepción social del manejo informativo en los medios sobre COVID-19 en México. *Rev. Mex. Inv. Psicol.* **14**(1), 13–28 (2022)
10. Alcántara, J., Ferreira, R.R.: A infodemia da “gripezinha”: uma análise sobre desinformação e coronavirus no Brasil. *Rev. Lat. Comun.* **1**(145), 137–162 (2020)
11. Manco, A.: Análisis de los discursos médicos vertidos en Twitter sobre la validez de posibles tratamientos contra la COVID-19. *Rev. Esp. Comun. Salud.* **12**(1), 75–88 (2021)
12. Sued, G.E.: El algoritmo de YouTube y la desinformación sobre vacunas durante la pandemia de COVID-19. *Rev. Lat. Común.* **1**(145), 163–180 (2023)
13. Secretaría de Comunicaciones y Transportes. ¿Cuántos usuarios de internet somos en México? (2020). <https://www.gob.mx/sct/articulos/cuantos-usuarios-deinternet-somos-en-mexico>
14. Limas, S.J., Vargas, G.: Redes sociales como estrategia académica en la educación superior: ventajas y desventajas. *Rev. Educ. Educ.* **23**(4), 559–574 (2020)
15. Tamayo, O.E., Zona, R., Loaiza, Y.E.: El pensamiento crítico en la educación. Algunas categorías centrales en su estudio. *Rev. Lat. Est. Educ.* **11**(2), 111–133 (2015)
16. Ramirez, A.G.: Estudios de posgrado y elaboración de artículos científicos. *Utopía Praxis Lat.* **25**(11), 300–315 (2020)



Design Thinking Methodology Applied for the Development of Remote Teaching Models in Biomedical Engineering

Jorge Luis Rodríguez-Medina^(✉) , Guadalupe Dorantes-Méndez ,
and Aldo Rodrigo Mejía-Rodríguez 

Facultad de Ciencias, Universidad Autónoma de San Luis Potosí, San Luis Potosí,
San Luis Potosí 78295, Mexico
jorgerodriguez5tos@gmail.com

Abstract. The Design Thinking (DT) methodology is a creative and human-centered approach based on a deep understanding of the user's needs and challenges in order to define a problem and develop specific solutions. In the case of remote teaching of practical lessons for Biomedical Engineering, the use of DT emerges as a facilitator to identify and understand specific needs and challenges of students and teachers. In this work we propose several remote teaching models based on DT, particularly created for practical sessions of a Medical Imaging Systems course (lightboard, online and offline modalities classes). These models received positive evaluations from students, highlighting their ability to maintain attention, aid in concept comprehension, and provide high-quality audiovisual resources. These results showcased how DT proved to be an effective tool in addressing the demands of remote teaching and improving the learning experience.

Keywords: design thinking · audiovisual · remote education · biomedical engineering teaching

1 Introduction

In recent years, due to the massive closure of face-to-face activities in educational institutions to mitigate the impact caused by the COVID-19 pandemic, most countries have opted to guarantee educational continuity through distance resources, with the Internet being an optimal option, since it provides various communication tools, ideal for bringing schools and learning processes closer to students' homes. [1].

However, when restructuring and migrating the educational model to the field of online education several difficulties arose, due to technology does not replace the role of teachers, nor the areas of development that a school implies as a space for meeting and social coexistence [2]. Therefore, many educational institutions that relied mainly on a traditional face-to-face approach for the learning process, were not prepared for this urgent transition.

Besides, in the field of biomedical engineering, the use of hands-on sessions is essential to properly achieve the learning process related to medical technology, and the migration of these practical activities to a virtual scenario is still an open problem for biomedical engineering students, teachers and professionals. Therefore, the use of Design Thinking (DT) to identify and understand the specific challenges and needs of students and teachers or trainers in this situation makes it a suitable methodology to develop effective remote teaching models that translate into a better experience and improved learning outcomes, that might lead to unique solutions that would otherwise have been ignored.

DT could be defined as a five-stages design approach that aims to address complex problems by generating innovative solutions. The DT concept was developed over several decades [3]. In the 1960s, in the United States, approaches such as “Design Science” and “Industrial Design” emerged, which were mainly based on quantifiable facts and on improving the efficiency and functionality of products. Designers worked in university laboratories or factories, and focused on aspects such as ergonomics and the science of design. Buckminster Fuller was one of the pioneers of Design Science, seeking to apply scientific principles to design an environment that would meet the needs of humanity without harming the planet. Both approaches were characterized by specialization and measurement of results [3].

At the same time, in Scandinavia, the “Cooperative Design” approach was emerging, inviting all participants, from experts to workers and users, to co-design products and services. Tools such as cooperative prototyping, ethnographic research and democratic dialogue were used to generate ideas and improve designs. This approach focused on user participation for the co-creation of systems, services and policies [3].

These two approaches laid the foundation for what we know today as Design Thinking, emerging as a way to creatively address and solve complex problems in a user-centered and creative way through a collaborative and iterative approach. Being popularized in the 1990s by IDEO, a design firm that played a pivotal role in human-centered design education [3].

In the field of biomedical engineering, the DT methodology has been used successfully to address challenges in healthcare services and improving the patient experience. For example, in a large healthcare provider such as Kaiser Permanente, a multidisciplinary team from IDEO collaborated with professionals in several hospitals to identify and address problems at shift changes. Through observation and collaboration with nurses, it was discovered that information sharing was occurring inefficiently, leading to gaps in patient care [4, 5]. Using the ideas gained during the observation, the innovation teams explored potential solutions through brainstorming and rapid prototyping techniques. In the case of the Shift Change Project, a working prototype was developed that included new procedures and a simple software that allowed nurses to access previous shift change notes and add new ones. This improved knowledge transfer and reduced preparation time, allowing earlier and more informed contact with patients [4, 5]. The implementation of this change had a significant impact on the quality of

patient care and the work experience of nurses. The average time between a nurse's arrival and first interaction with a patient was cut in half, resulting in a considerable increase in the amount of nursing time available in hospitals. In addition, nurses experienced a higher level of job satisfaction. This success led to the implementation of Kaiser's new system-wide shift changes and the integration of the ability to reliably record critical patient information [4,5].

The use of DT can provide new alternatives to face a problem, such as virtual teaching approaches, and analyze and determine the option that best suits the needs of a particular problem [6,7]. In this context, the aim of this work is to use DT to develop remote teaching models as a complement for practical sessions for the Medical Imaging Systems course of the Biomedical Engineering program at UASLP, Mexico.

2 Methodology

The DT methodology followed in this work was proposed by the Stanford's Hasso-Plattner Design Institute, and it consists of five stages: Empathize, Define, Ideate, Prototype, and Test. In the next sections, a brief description of each stage is presented [7,8].

2.1 Empathize

Empathy is the first stage of the DT methodology and is the core element of a human-centered design process. Empathizing is the work that goes into understanding people within the context of the design challenge. It is the effort to understand how they do things and why, their physical and emotional needs, what is meaningful to them [7,8].

To perform this step, a survey was conducted to students from different generations of the Bachelor's Degree in Biomedical Engineering about their experience in virtual classes during the semesters of the period from August 2020 to July 2021.

2.2 Define

The goal of the Define stage is to craft a meaningful and actionable problem statement. This should be a guiding statement that focuses on the ideas and needs of a specific user or composite persona. Ideas do not usually appear suddenly; rather, they emerge from a process of synthesizing information to discover connections and patterns. In a simply way, Define is a way of giving meaning [7,8].

For this step, we developed a User Persona (UP), as it allowed us to gain a deeper understanding of the users and their needs. A UP is a design tool that consists of the creation of a fictitious profile, based on the data collected in the empathy process, which helped us to understand and represent the characteristics, behaviors, needs, frustrations and motivations of, in this case, the student.

2.3 Ideate

Ideation is the stage of the design process focused on the generation of ideas. Mentally, it represents a process of “scaling up” in terms of concepts and outcomes. Ideation provides both the approach and the material to build prototypes and bring innovative solutions to students [7, 8].

For this step, we use the “inverse brainstorming” technique, which consists of a reverse exploration for problem solving, i.e., we identify barriers and obstacles that must be avoided in order to find effective solutions. By questioning assumptions or approaches that highlight the problem, creative thinking is encouraged and new perspectives are discovered to solve the problem in an innovative way.

2.4 Prototype

This step is characterized for accelerating the innovation process, as it is when we shape our idea and begin to understand its strengths and weaknesses, and the faster we do this, the faster our ideas evolve [6, 7].

For this step, we established three proposals to cover the solutions established in the ideation stage. We did their layout and then developed a prototype of each proposal to apply them in practical classes and thereby discover their usefulness in satisfying the solutions proposed in the ideation phase.

2.5 Test

The last stage of DT is to acquire feedback on the prototypes created from the users, in this case the students. This stage gives another opportunity to understand the user experience and point out the path for the next iterations of the prototypes [7, 8].

To accomplish this step, students of the Medical Imaging Systems course who experienced the two lectures were asked to complete a survey regarding the quality of the lectures. Attention to the class, understanding of the concepts addressed and the quality of the audiovisual resources used were evaluated.

Additionally, two open questions were asked with the intention of understanding what advantages students find in the virtual practical sessions compared to the face-to-face practical sessions, and with which elements and tools applied to the distance classes they believe could improve their learning.

3 Results and Discussion

The results of each stage of the process of DT applied to develop models of practical distance learning classes in the field of Biomedical engineering and the corresponding discussion are presented below.

3.1 Empathy

In the empathy phase, 58 students were interviewed to understand their general experience with distance education and to gather their opinions and suggestions.

Some of the multiple choice questions of the survey, as well as the results are presented in Table 1.

Table 1. Online classes experience survey results

Questions	Answers				
	Excellent	Good	Average	Below average	Deficient
What is your general opinion about remote education?	0%	33%	45%	19%	3%
What has been your experience with the quality of your internet connection during online learning?	3%	38%	40%	16%	3%
How would you rate the audiovisual resources used in your distance learning classes?	9%	55%	34%	2%	0%
How do you rate the student-teacher interaction in online learning?	2%	37%	44%	16%	2%
How would you rate the attention you give to the remote classes?	2%	24%	50%	24%	0%
What do you think of the teaching and learning processes established in your online classes?	0%	50%	45%	5%	0%

They were also asked to evaluate their general satisfaction with the distance learning classes, both practical and theoretical. These results can be seen in Fig. 1

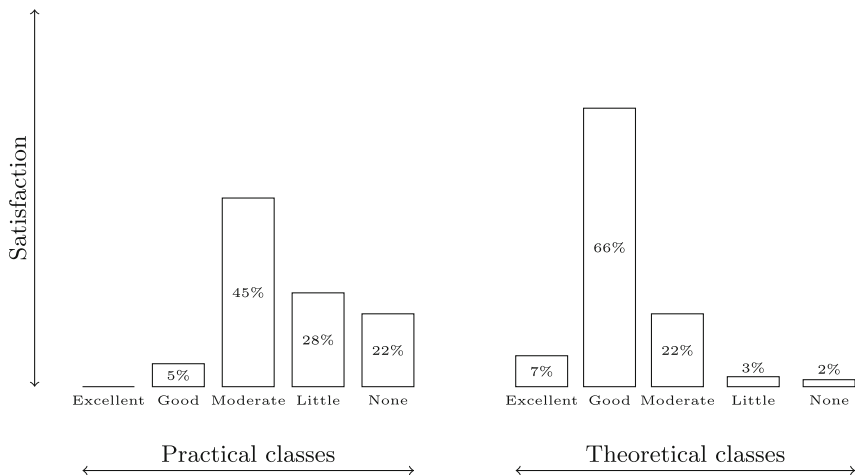


Fig. 1. Comparative satisfaction graph in distance learning classes.

In general, students considered distance education to be average, as well as the quality of their internet connection, the attention given to classes and the student-teacher interaction in online learning. The audiovisual resources used in the classes were rated as good. In terms of satisfaction with the distance classes, the students preferred the theoretical classes over the practical classes.

In addition, students were asked an open-ended question in which they were invited to propose elements and tools to improve the online learning experience. From the answers obtained, the most frequently addressed concepts were: improved practical classes, better material, more interaction, more adaptation and better internet connection.

3.2 Definition

Based on the information gathered in the empathy phase, a User Persona was developed that highlighted the needs, characteristics, motivations and frustrations of the students. This helped define the main problem to be addressed in the design of the practical distance learning classes. The created UP can be visualized in Fig. 2

Gabriela
 Age: 22
 Gender: Female
 Location: San Luis Potosí
 Occupation: Student
 Status: Taking classes remotely due to the pandemic

Gabriela is a Biomedical Engineering student at UASLP. Due to the global pandemic, face-to-face classes have been suspended and Gabriela has had to adapt to distance learning, using online platforms and videoconferencing tools to continue her learning.

⊙ Needs

- Improved interaction and communication with teachers.
- Access to quality materials and resources.
- Increased emphasis on practical classes and hands-on elements.
- More attention to doubts and feedback.

⊙ Motivations

- Gabriela feels a genuine passion for the opportunity to learn and apply concepts related to biomedical engineering, which motivates her and gives her a sense of purpose in her education.
- Gabriela is motivated by the opportunities her career can offer her in the future. She envisions a fulfilling and successful career path, which drives her to strive to make the most of her education.

⊙ Frustrations

- Gabriela is frustrated by the lack of personal interaction with her classmates and teachers. She misses the exchange of ideas experienced in a face-to-face setting.
- Gabriela is frustrated by the limitations of hands-on distance learning classes. She may feel that she does not get the same hands-on experience as she would in a face-to-face setting, which may affect her understanding and application of concepts.
- Gabriela may feel frustration if she experiences connection quality issues during distance classes. These problems can affect the learning experience and make it difficult for her to actively participate in academic activities.

Fig. 2. User persona created with the data collected in the empathy process.

User Persona problem definition. The problem faced by Gabriela is how to improve her online learning experience to effectively develop her skills and knowledge in the field, overcoming the limitations of face-to-face interaction,

the restrictions in the practical distance classes, the difficulty to solve doubts immediately, the possible difficulties with the quality of internet connection and the feeling of not being fully adapted to the virtual environment.

3.3 Ideation

In the ideation phase, the inverse brainstorming technique was applied to generate potential solutions to the defined problem. The result of the application of this technique for our problem can be seen in Fig. 3

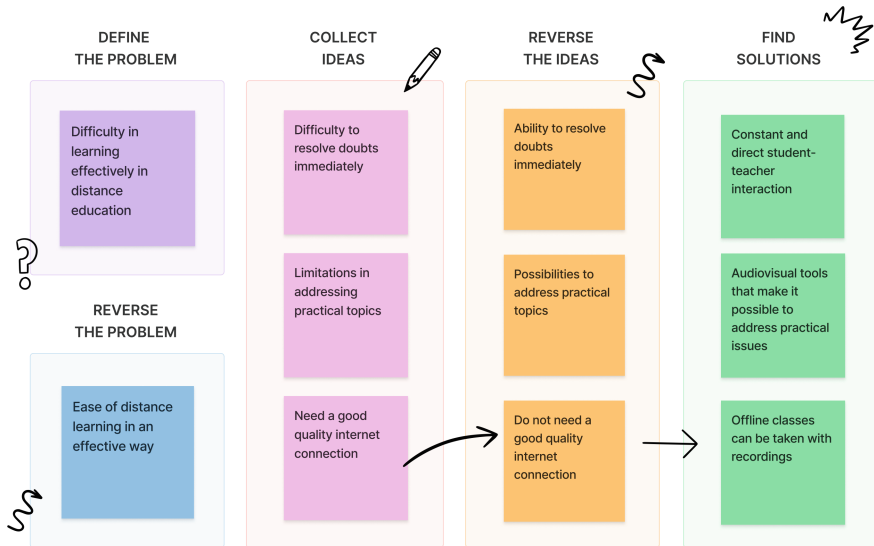


Fig. 3. Application of inverse brainstorming to find solutions to our problem.

As a result, three possible solutions were identified: 1) constant and direct student-teacher interaction, 2) audiovisual tools to address practical issues, and 3) the possibility of taking classes offline through recordings.

3.4 Prototyping

With the solutions proposed in the Ideation phase, three approaches were prototyped:

Lightboard Class. Our first proposal was the use of a lightboard with the intention of resembling as much as possible a classroom with the use of a whiteboard. We were able to implement it successfully, as can be seen in Fig. 4. However, we had to discard its use for the practical classes, because although it is very useful when we want to present a topic on the board, it does not offer any advantage when we need to present or demonstrate equipment for practical classes. However, it is

a great way to explain theoretical topics in recorded classes, due to its similarity to the approach that would be taken in a classroom.

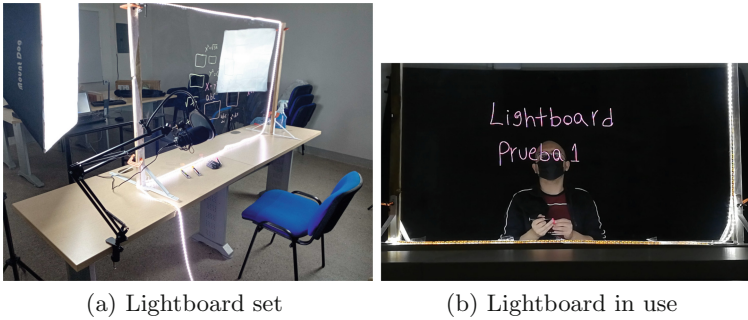
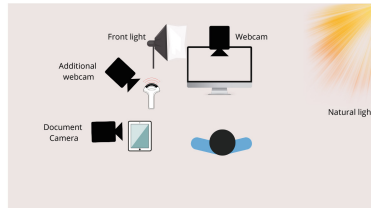
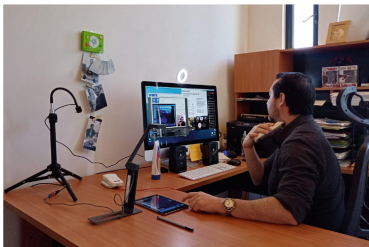


Fig. 4. Demonstration of the use of the lightboard.

Online Modality. Our second proposal was built with the intention of allowing the student to maintain an active participation, with real time feedback from the teacher during the session, and the possibility of re-watch the class in the subsequent recording of the lesson. This modality was applied for a practical class for the use of a wireless ultrasound in the Medical Imaging Systems course. Therefore, it was necessary to visualize the transducers, the acquisition interface and the real-time acquisition. The layout with the material used and the actual application of the class is presented in Fig. 5.



(a) Layout of the online modality.



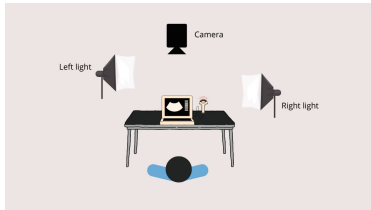
(b) Online demonstration class of wireless ultrasound.



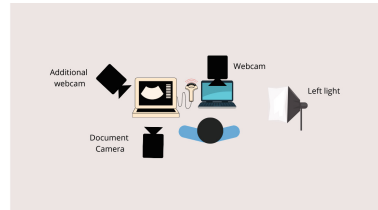
(c) Online class visualization in real time.

Fig. 5. Layout and application of the online modality. [9].

Offline Modality. Our last proposal had the goal to provide students and professors the possibility of maintaining an asynchronous and timeless class, since it can be visualized at any time and place, solving the common problem of a poor internet connection for online classes. However, it is important to mention that this modality requires a later accompaniment by the teacher to confirm and reinforce the content seen in the class. The application of this modality was for the use of a CHISON ECO1 ultrasound. The layout of the scenes with the material used and its application in the class is shown in Fig. 6.



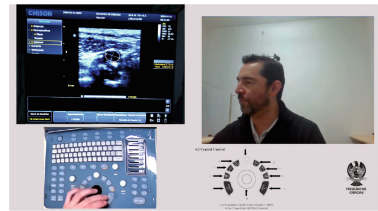
(a) First layout of the offline modality



(b) Second layout of the offline modality



(c) Offline class recording of the CHISON ECO1 ultrasound demonstration class.



(d) Edited offline class.

Fig. 6. Layout and application of the offline modality. [9].

3.5 Testing

In the testing phase, 26 students from the 2022 Medical Imaging Systems course were interviewed to evaluate the quality of the proposed prototypes. The results can be seen in Table 2.

Table 2. Satisfaction survey results [9]

Question	Online Class					Offline Class				
	<i>Excellent</i>	<i>Good</i>	<i>Moderate</i>	<i>Little</i>	<i>None</i>	<i>Excellent</i>	<i>Good</i>	<i>Moderate</i>	<i>Little</i>	<i>None</i>
How do you rate the attention you had in the class?	0%	33%	56%	11%	0%	22%	45%	22%	11%	0%
How do you rate your understanding of the concepts covered during the session?	0%	67%	33%	0%	0%	45%	33%	11%	11%	0%
How do you consider the audiovisual resources used in the class?	33%	45%	22%	0%	0%	22%	67%	11%	0%	0%

The results of the survey were as follows: in terms of attention in class, most of the students considered it “moderate” in online classes and “good” in offline classes. Regarding the understanding of the concepts addressed, most of the students considered it “good” in the online classes and “excellent” in the offline classes. As for the quality of the audiovisual resources, most of the students considered it “good” in both cases.

Additionally, another survey was conducted with 22 students, in which they were asked two open-ended questions: 1) The advantages of virtual practical sessions compared to face-to-face sessions, the most frequent answers included: possibility of recording, flexibility on time and valid long-term option; 2) What elements and tools could improve learning in distance classes, the most frequently addressed concepts were: use of games, active participation of teachers, more practical sessions and rest time.

3.6 Discussion

The results obtained throughout the DT methodology provided valuable information for the design of practical distance classes in Biomedical Engineering. The solutions proposed in the ideation phase, such as improve student-teacher interaction and possibility of offline classes, represented promising approaches to address the identified problem. The prototypes developed, online and offline modalities, were positively evaluated by students in terms of understanding of concepts and quality of the audiovisual resources.

The responses to the open-ended questions in the post-test surveys revealed that students find advantages in virtual practical sessions, such as the possibility of accessing recordings, saving time and having a valid long-term option. Elements and tools that could enhance learning in distance classes were also identified, such as the use of games, active participation of teachers and more practical sessions.

4 Conclusions

The results obtained demonstrate that the application of DT methodology in Biomedical Engineering for the design and improvement of practical distance learning classes offers an effective framework for understanding the needs and expectations of students, identifying problems and generating innovative solutions.

The application of DT allows the adoption of a user-centered approach, which ensures that solutions developed are designed to meet the real needs of students. In addition, it promotes empathy and a deep understanding of the challenges and constraints faced by students in the distance learning environment. In addition, it is possible to transfer these solutions to a professional scenario where online and offline training sessions could be achieved efficiently in a user-center way.

As Biomedical Engineering continues to evolve, it is important to consider the potential that DT presents as a tool to address future challenges, and provide new opportunities for innovative medical device design, improvement in healthcare processes, and the development of more effective educational solutions.

References

1. ECLAC-UNESCO. Education in the time of covid-19. COVID-19 report. 1, pp. 1–5 (2020)
2. Aragón Hernández, M.: Ser docente, ser estudiante en tiempos de contingencia sanitaria. Enseñar y aprender en tiempos de pandemia. **4**(11), 9–18 (2021)
3. Szczepanska, J.: Design thinking origin story plus some of the people who made it all happen. *Med. Corp. Inc.* **1**, 1–7 (2017)
4. Brown, T.: Design thinking. *Harv. Bus. Rev.* **86**(6), 84–92 (2008)
5. Jain, D.: Design thinking as an approach to innovation in healthcare at the bottom of the pyramid. Ph.D. thesis, University of Porto (2022). <https://repositorio-aberto.up.pt/bitstream/10216/145662/2/592866.pdf>
6. Brown, T.: Tim brown urges designers to think big (2009)
7. Grönman, S., Lindfors, E.: The process models of design thinking a literature review and consideration from the perspective of craft, design and technology education. *Techne serien-Forskning i slöjdpedagogik och slöjdvetenskap.* **28**, 110–118 (2021)
8. Hasso Plattner Institute of Design: An introduction to design thinking: Process guide. Institute of Design at Stanford, pp. 1–6 (2010)
9. Rodríguez-Medina, J.L., Dorantes-Méndez, G., Mejía-Rodríguez, A.R.: Use of audiovisual strategies as a complementary resource for practical courses in biomedical engineering. In: Trujillo-Romero, C.J., et al. (Eds.) XLV Mexican Conference on Biomedical Engineering. CNIB 2022. IFMBE Proceedings, vol. 86, pp. 860–870. Springer, Cham (2023). https://doi.org/10.1007/978-3-031-18256-3_90

Author Index

A

- Aguilar, Erick Ramírez 33
Alanis-Gómez, José Rafael 131
Alberto, Hernández-Vega Luis 122
Almanza-Martínez, Dorothy Alejandra 68
Álvarez-Nanguce, Wendy Meliza 80
Alvarez, Sarahi 250
Ana Paola, Salgado-Alvarez 122
Arellano, Kevin José Martínez 131
Arreguin, Cristhian Valencia 139

B

- Baez, Mauricio 232
Barrios, Carlos Orozco 108

C

- Camacho, Sergio 232, 241, 250
Cardiel-Espino, Aurora-Yunuen 183
Castillo, Rodrigo Velázquez 131, 139
Cedillo-Cruz, Edith 80
Chico, Valeria 222
Corral-Valencia, Galilea-Fernanda 183
Cortez, Ricardo 87
Cruz, Guillermo Jesús 108
Cruz-Hernández, María de Lourdes 202
Cuellar, Carlos 15, 25

D

- Daniel, Solís López 158
De León Cuevas, Alejandro 3
De Luna-García, Ángel Iván 87
Díaz-Ruiz, Araceli 108
Dorador-González, Jesús Manuel 99
Dorantes-Méndez, Guadalupe 257
Duarte, Isamar 25

E

- Eduardo, Pérez Alvarado Oscar 158
Esteves-Delgado, Joaquin 183

F

- Fabiola, Hernández-Rosas 122
Fernando 139
Fuentes, Miguel 232, 241

G

- Gómez, Guadalupe Karla Velasco 169
Gómez, José Rafael Alanis 115, 139
Gómez, Ricardo Pascual Alanis 131
González, Leonel 15, 25
González, Ximena Berenice Guzmán 57
González-Carbonell, Raide Alfonso 99
González-Navarrete, Roberto 68
Gordillo-Castillo, Nelly 222
Gustavo, Vargas Martinez Darien 158
Gutiérrez-Sánchez, Beatriz 202

H

- Hernández, Juan David Olivares 115
Hernández-Córdova, Roberto 80
Hernández-Montiel, Hebert Luis 176
Hernández-Rosas, Fabiola 115, 131
Hidalgo, Quetzalli 241

I

- Ibarra, Rafael Rangel 115
Ituarte, Arantza 15, 25

J

- Jiménez, Adrian Jefe Elías 3

L

- León, Felix 15, 25
Lozada-Castillo, Norma 87
Lozano-Flores, Carlos 176
Luviano-Juárez, Alberto 87

M

- Maciel-Cerda, Alfredo 80
Maldonado, Luis Fernando Serna 139

Martínez, Karla 48
 Martínez-Alanís, Marisol 169
 Martínez-Peon, Dulce 148
 Mata-Martínez, Esperanza 176
 Mejía, Perla Vanessa Aguilar 169
 Mejía-Rodríguez, Aldo Rodrigo 257
 Mendoza-Lorenzo, Patricia 80
 Mondragon-Lozano, Rodrigo 108
 Montes, Armando Ladislao López 3
 Morales-Guerrero, Nelly A. 176
 Morante, Antonio 232
 Munguía-Crisóstomo, Alitzel 211

O

Olayo, María Guadalupe 108
 Olguín-Díaz, Ernesto 148
 Ortiz, Ramírez 139
 Ortiz-Posadas, Martha Refugio 191, 202,
 211

P

Padron, Natalia Mora 139
 Pareja, Elizabeth 48
 Pescador-Salas, Alejandro 148
 Pimentel-Aguilar, Ana Bertha 191
 Portillo, Ana Luz 222

R

Rafael, Alanís-Gómez José 122
 Reyes, Bersain 232, 241, 250
 Reyes-Lagos, José Javier 15
 Rodríguez-Medina, Jorge Luis 257

Romero, Epsiba Lorena Marañon 131
 Romero, Rafaella 15
 Romo, María Fernanda Toledo 33
 Rosales-Huie, Juan Pablo 148
 Rosas, Fabiola Hernandez 139
 Ruiz, Antonio Gómez 3

S

Salazar, Sabrina Sofía Prieto 169
 Salazar, Tania Pérez 3
 Salgado, Angelica Coyoy 108
 Salgado-Ceballos, Hermelinda 108
 Salinas-Sánchez, Igor 99
 Sánchez, María Flores 33
 Sánchez-Torres, Stephanie 108
 Sandoval-Chileño, Marco 87
 Sierra, Hipólito Aguilar 33
 Soto, Isabel C. 48
 Sustaita, Yael Osmar Bravo 57

T

Trejo-Seráfico, Carlos-Alberto 183
 Trujano, Eva González 108

V

Varela-Echavarría, Alfredo 176
 Vázquez-Cuevas, Francisco G. 176
 Vázquez-Nambo, Manuel 183
 Vera, Juan Carlos 15, 25
 Vidal-Lesso, A. 57
 Vidal-Lesso, Agustín 68
 Villalobos, Yara 222